COUPLING CELLS COMPETITION, GROWTH AND REMODELLING IN MECHANICS OF BIOLOGICAL SYSTEMS

ANGELO ROSARIO CAROTENUTO

PhD in Materials and Structures Engineering

Cycle XXVIII

Department of Chemical, Materials and Production Engineering (DICMaPI)

School of Polytechnic and Basic Sciences
University of Naples Federico II

PhD Coordinator: *Ch.mo* Prof. Giuseppe Mensitieri

Tutor: *Ch.mo* Prof. Massimiliano Fraldi

Academic Year 2015/2016

To my family

ABSTRACT

The biomechanical behavior and the mechanobiology of cells, tissues and organs have been intensively investigated in the last decades, with the aim of discovering the key feedback mechanisms governing the ways in which cascades of chemical signals are transmitted within the hierarchically organized living structures and interplay with physical events at different scale levels. Continuum Mechanics has deeply contributed to develop this research area and to meet related challenges, by creating the physically and mathematically consistent ground on which large deformation, stresses, evolving constitutive laws, growth, remodeling and morphogenesis do interact. The needed multiphysics vision in analyzing the complex behavior of the living matter has in particular consolidated Tissue Mechanics theoretical approaches and related modeling strategies which are currently recognized as indispensable tools for explaining experimental evidences, for predicting dynamics of living systems as well as for supporting the design of prostheses for both soft and hard tissues. Further impulse to these studies is then given by the rapidly growing advances of the research in tissue engineering which continuously redraw new scenarios for applications in medicine and lead to envisage innovative drug delivery systems and biomaterials. Within this vivid multidisciplinary debate, an increasing interest has been recently registered in the Literature for the mechanical properties of living cells –and for the understanding of the dynamics to which they obey at different scale levels– also motivated by some recent discoveries which seem to allow to envisage new horizons for therapy and diagnosis of human diseases like cancer, by for example exploiting the different in-frequency response of single healthy and tumor cells stimulated by Ultrasound. However, at the macroscopic scale –say at the tissue level– the feedback mechanisms and the cascade of bio-chemical and physical signals characterizing the complex interaction of dynamics occurring at different scales significantly complicates the biomechanical response of living matter and growing tumor masses, thus requiring enriched models which incorporate the mechanobiology at the micro- and meso-scale levels. Cancer diseases in fact occur when in a healthy tissue the cell-cell and cells-ECM (the Extra-Cellular Matrix) interactions are altered, and hyperplasia is generated as effect of sudden and often unforeseeable genetic modifications followed by a cascade of biochemical events leading to abnormal cell growth, lost of apoptosis, back-differentiation and metastasis. As a consequence, the determination of models capable to macroscopically describe how tumor masses behave and evolve in living tissues by embodying tumor invasion dynamics determined by cell-cell and cells-environment to date still remains an open issue. Growth of biological tissues has been recently treated within the framework of Continuum Mechanics, by adopting heterogeneous poroelastic models where the interaction between soft matrix and interstitial fluid flow is additionally coupled with inelastic effects *ad hoc* introduced to simulate the macroscopic volumetric growth determined by cells division, cells growth and extracellular matrix changes occurring at the micro-scale level. These continuum models seem to overcome some limitations intrinsically associated to other alternative approaches based on mass balances in multiphase systems, because the crucial role played by residual stresses accompany-

ing growth and nutrients walkway is preserved. Nevertheless, when these strategies are applied to analyze solid tumors, mass growth is usually assigned in a prescribed form that essentially copies the *in vitro* measured intrinsic growth rates of the cell species. As a consequence, some important cell-cell dynamics governing mass evolution and invasion rates of cancer cells, as well as their coupling and feedback mechanisms associated to *in situ* stresses, are inevitably lost and hence the spatial distribution and the evolution with time of the growth inside the tumor –which would be results rather than input– are forced to simply be data. In order to solve this sort of paradox, the present Thesis work, within a consistent thermodynamic framework, builds up an enhanced multi-scale poroelastic model undergoing large deformation and embodying inelastic growth, where the net growth terms directly result from the "interspecific" predator-prey (Volterra/Lotka-like) competition occurring at the micro-scale level between healthy and abnormal cell species. In this way, a system of fully-coupled non-linear PDEs is derived to describe how the fight among cell species to grab the available common resources, stress field, pressure gradients, interstitial fluid flows driving nutrients and inhomogeneous growth do all simultaneously interact to decide the tumor fate. The stability of the predator-prey dynamics and some original theoretical results for the non-linear mechanics of growing media are also developed and discussed in detail. The general approach –that is the coupling of growth, large deformation and competitive cell dynamics– is therefore applied to actual biomechanical problems (in particular analyzing growth and stress in tumor spheroids and arterial walls) and the theoretical outcomes are finally compared with *in vivo* experiments and animal models to validate the effectiveness and the robustness of the proposed strategy.

INTRODUCTION

In the framework of Tissue Mechanics the contribution of the biomechanics and, more in general, of the mechanics of materials and structures, to complement biomedical know-how and support clinical and surgical choices is currently recognized as a successful approach in practical applications. The engineering standpoint often determines a deeper understanding of the complex behavior related to the physical interaction between tissues and their constituents, as well as between tissues and synthetic materials, this in turn giving the possibility to obtain better clinical outcomes and to gain some new insights into the basic understanding of the phenomena that hide behind physiological events, in health or disease. To investigate the key feedback mechanisms regulating the transmission of chemical signals within the hierarchically organized living structures and their connection with physical events at different scale levels, Continuum Mechanics provides a well-established theoretical framework in which hyperelasticity and evolving constitutive laws can be additionally enriched by growth, remodeling and morphogenesis.

With focus on the present Research work, one of the arguments treated regards the characterization of vascular systems – and more specifically pulmonary autograft transposed into aortic position– through nonlinear anisotropic elasticity and large deformation theories, additionally including a full coupling of these laws with specific evolution equations, in order to predict growth and remodeling in blood vessels, and analyze the effects that altered physiological conditions and interactions with synthetic materials can induce into the evolving living structures, in term of tissue morphology and histology as well as with reference to structural integrity and mechanical stability. However, needed physiological processes, aside from the impairment between the mechanical properties of the PA vessels with respect to the aortic systemic pressure, can be compromised by the arising of problems mainly related to two choices: the material(s) constituting the prosthesis and the microstructure of the device itself. The consequences deriving from these choices in terms of potential unfavorable remodelling have been in detail analyzed by means of simple analytical considerations. Furthermore, to overcome these issues, recent advances have been done on both biomechanical theoretical investigation and on in vivo experimentation of newly assembled co-polymer scaffolds for the reinforcement of PA in Ross operation. The proposed biomechanical model in fact provided positive effects coming from the synergy between the transposed vessel and the composite polymer scaffold, demonstrating the ability of this implant to accommodate mechanical loads guaranteeing graft integrity, controlling the progressive graft dilation, allowing regional somatic growth and preventing dilative degeneration.

However, the phenomenological description of the growth and remodelling capabilities of a biological system can be complicated by the necessity of including further aspects, which take into account the interactions between the tissue elementary constituents at the cells scale, since these dynamics are then inexorably connected to the macroscopic fate of the system itself.

Therefore, in order to catch the sometimes extremely complex functional relation-

ships and multi-physical interactions governing the organization of a growing tissue, the sole mechanical considerations can be no more exhaustive, and a multidisciplinary approach is necessary to take into account other leading aspects related to biochemical nature of the interplays at basis of the growth and remodelling processes. However, especially in dealing with the modelling of living structures, it can result sometimes advantageous to hazard to describe such phenomena by means of a more eclectic point of view, adopting approaches that are ordinarily not associated to that physical framework, but instead belong to other disciplinary areas. Nevertheless, the direct observation of some common elementary, characteristic properties of the natural phenomenon under study and an open-minded attitude allow to transpose some "foreign" logics to the mechanical problem at hand, opportunely integrating all the building-blocks in order to furnish a comprehensive description of all the interactions governing the behavior of the living structures.

In particular, in the present Research work, these strategies have been harnessed to model the growth of living tumors: the mechanics of the tumor growing mass has been explicitly modeled by considering the host tumor-host interactions interpreted in the light of behavioral sciences, and, in particular, by means of the Volterra-Lotka competitive logics. With the aim of predicting cancer fate, the growth of solid tumors can be in fact treated physically as a mechanical process according to which a heterogeneous tissue expands within a surrounding medium. Tumor expansion is controlled by some internal driving stresses, which are counterbalanced by mechanical resistance provided by the surrounding environment. Internal stresses are mostly generated by cells proliferation dynamics, which is influenced by the diffusion of nutrients within the tumor. This implies that the physical forces pushing the tumor ahead do not involve the sole surface tension and the pressure of the surrounding medium, but also the explicit active cellular forces deputy in the momentum balance that, in turn, retrospectively activate mechanosensitive cellular processes. To gain new insights into the basic understanding of the complex machine of the host-tumor interaction, a heterogeneous poroelastic model of tumor spheroid can be helpfully constructed taking into account the mechanically activated stress fields, fluid pressure and nutrient walkway all coupled with spatially inhomogeneous and time-varying bulk growth. Actually, the growth is seen as a result of competitive-cooperative dynamics occurring at the microscopic scale level among healthy cells, cancer cells and extra-cellular matrix (ECM) that —in principle-– cannot be assumed *a priori*. Nevertheless, these dynamics are generally neglected in engineering models, as a consequence of both the difficulty of mathematically describing them with sufficient accuracy and the problems arising from the coupling of competition equations with the mechanical ones. To try to overcome these limits –limits which significantly reduce the aptitude of the mathematical models to predict the destiny of tumor masses-– the idea is to macroscopically model the dynamics occurring at microscopic scales by introducing ad hoc nonlinear Volterra/Lotka-like equations (VL), extensively utilized to describe ecological systems as well as several population dynamics which involve psychological and collective behaviors of social communities. In brief, the present PhD thesis is organized as follows. Chapter 1 recalls the fundamentals of nonlinear solid mechanics, with insights into the mechanics of growth and remodelling, that will be exploited in the biomechanical models successively proposed. Chapter 2 presents the basic notion of Volterra-Lotka system, starting from the original predator-prey logic to the most general form. In

Chapter 3, some simple uncoupled biomechanical models will be presented with the aim to gain insight into the understanding of key aspects concerning the growth and remodelling of living tissues in physiological and non-physiological conditions. Chapter 4 applies a weak coupling strategy in order to investigate the previously described problem of somatic growth and remodelling of pulmonary autografts in Ross operations, while Chapter 5 is entirely dedicated to the full coupling strategy in which mechanical aspects, fluid walkways with nutrient transport, cells-cells and cells-ECM VL-interactions are simultaneously taken into account to characterize the growth multicellular tumor spheroids.

CONTENTS

Part I

T H E O R E T I C A L   F R A M E W O R K

The aim of the following two chapters is to introduce the basic concepts of Continuum Mechanics and Volterra-Lotka dynamical systems, that will be afterward coupled in order to model growth and remodelling processes of biological systems.

FUNDAMENTALS OF CONTINUUM SOLID MECHANICS

The Biomechanics of *growth* and *remodelling* is formulated within the framework of Continuum Mechanics. Solid mechanics provides in fact a macroscopic description of the material bodies kinematics and deformation, the stress concept and of the constitutive framework, as well as the statement of the fundamental balance principles (mass conservation, balance of momentum, balance of energy and entropy inequality). Also, growth (or conversely, resorption) implies that systems are open with respect to the mass. Remodelling, which is related to microstructural changes, can be itself described through the introduction of macroscopic quantities, such as internal stress and material properties. These widely known evidences are all taken into account in describing *continua* conservation equations, and suitable growth and remodelling-related specific terms are introduced. This chapter recalls some fundamental concepts of continuum mechanics of solids, with attention on those notions that will be successfully encountered in the following chapters dealing with specific biomechanical applications. For an exhaustive treatment of these arguments, the reader is invited to the inspiring books by Holzapfel [87], Ogden [148], Bigoni [22], Gurtin [79] and Cowin [46], as well as to the works by Lubarda et al. [127, 128], Garikipati [74], Schmid et al. [176] and Cowin [48], on which the most of these notions largely draws from.

1.1 MOTION OF CONTINUA AND DEFORMATION

The characterization of the motion, deformation and stress of a solid body subject to prescribed loading and constraint is the focus of solid continuum mechanics. The model of continuum body was introduced by the French mathematician Augustin-Louis Cauchy in the 19th century. It ignores the atomistic and molecular, and so discrete (discontinuous), nature of matter, and considers a body as a continuous (or at least piecewise continuous) distribution of matter in space and time, at a macroscopic scale. Therefore, a body $\mathcal{B}$ can be defined as a continuous set of material points [87]. Let this body be embedded in a frame $\{\mathbb{R}^d, t\}$, with d denoting the Euclidean space dimension (in what follows, a three-dimensional space is considered). The geometrical regions of the Euclidean space occupied by the body at a certain time t –say $\Omega_t \subset \mathbb{R}^d$– is called *configuration*. Each configuration is determined uniquely at any time. A specific configuration can be fixed in order to set timeline, at a conventional starting time $t_i = 0$, which is denoted as *initial time*. Consequently, the region Ω_0 can be identified as *initial configuration*. Similarly, one can fix a *reference configuration* as a particular region Ω_t in which body particles $P \in \mathcal{B}$ occupy position denoted by a position vector $\mathbf{X}$, this configuration being then considered as *undeformed* (with respect to which motion is described). It is convenient in the most of cases to make reference configuration and initial configuration actually coincide (hereinafter, this hypothesis will be held). Therefore, let the region Ω_0 move to a new region Ω at a time $t > 0$. In this configuration, material particles $P \in \mathcal{B}$ will be denoted by a certain position $\mathbf{x}$. This new configuration is called a *current* or *deformed configuration*.

The material and spatial position vectors $\mathbf{X} = X_I \mathbf{E}_I$ and $\mathbf{x} = x_i \mathbf{e}_i$ are respectively described by means of material basis $\{\mathbf{E}_I\}$ and a current basis $\{\mathbf{e}_i\}$, with X_I and x_i indicating the corresponding components. Starting from these initial considerations, there exist a one-to-one correspondence between each particle of the body $P \in \mathcal{B}$ and the position $\mathbf{X} \in \Omega_0(\mathcal{B})$ at $t = 0$, defining the map $\mathbf{X} = \kappa_0(P,t)$. A similar correspondence can be established for a current position vector $\mathbf{x}$ mapping P onto Ω, say $\mathbf{x} = \kappa(P,t)$. Then, since material points P are described by means of the reference undeformed configuration, an uniquely invertible correspondence between the current position and the material position can be introduced, which is called *motion*:

$$\mathbf{x} = \kappa\left[\kappa_0^{-1}\left(\mathbf{X},t\right),t\right] = \boldsymbol{\chi}\left(\mathbf{X},t\right) \tag{1.1}$$

$$\mathbf{X} = \boldsymbol{\chi}^{-1}\left(\mathbf{x},t\right) \tag{1.2}$$

This notion let to introduce two different ways to describe motion. The *material description* or *Lagrangian description* characterizes motion with respect to the material coordinates X_I and time t, so serves to describe what happens to the particle as it moves (the observer moves solidarily with the body particle). The *spatial description* or *Eulerian description* characterizes motion with respect to the spatial coordinates x_i and time t motion by fixing the attention on a region point.

A body $\mathcal{B}$ modifying its shape during motion is called a deformable body. Hence, deformation is related to the change of body particles reciprocal distances during motion. If inter-particales distances do not vary, motion is rigid. Assuming as coincident the reference systems for the reference and the current configurations, to adequately describe the movement of body particles, a displacement field can be introduced, connecting body particles material position $\mathbf{X}$ in the undeformed configuration to their current position $\mathbf{x}$. By adopting a Lagrangian description, it results

$$\mathbf{x} = \mathbf{X} + \mathbf{u}\left(\mathbf{X},t\right) \tag{1.3}$$

In order to exclude translations, equation (1.4) can be differentiated with respect to $\mathbf{X}$, in this way obtaining a direct relation between the infinitesimal line element $d\mathbf{x}$, $d\mathbf{X}$ and the differential $d\mathbf{u}$:

$$d\mathbf{x} = d\mathbf{X} + d\mathbf{u}\left(\mathbf{X},t\right) = \left[\mathbf{I} + \mathbf{u} \otimes \nabla_{\mathbf{X}}\right] d\mathbf{X} \tag{1.4}$$

where $\mathbf{I}$ is the identity second-order tensor in the reference configuration, $\nabla_{\mathbf{X}}$ is the vector differential operator $\{\partial/\partial X_1, \partial/\partial X_2, \partial/\partial X_3\}^{\mathsf{T}}$ and $\otimes$ is the standard tensor product between two vectors, defined in a way to give $\left[\mathbf{a} \otimes \mathbf{b}\right]_{ij} = a_i b_j$. Therefore, $\mathbf{u} \otimes \nabla_{\mathbf{X}} = \nabla_{\mathbf{X}}\mathbf{u}$, the latter operator indicating the material displacement gradient. The deformation process can be characterized by using *transport theorems*. They describe the mapping from the reference to current configuration of infinitesimal line, area, and volume elements, respectively. To do this, we introduce a fundamental kinematic quantity: the *deformation gradient* $\mathbf{F}$, which represents a linear transformation generating the current infinitesimal line elements $d\mathbf{x}$ through the action of the second-order tensor $\mathbf{F}$ on the reference infinitesimal line elements $d\mathbf{X}$ ([26]):

$$d\mathbf{x} = \mathbf{F}\left(\mathbf{X},t\right) d\mathbf{X} \tag{1.5}$$

Clearly, it readily follows from the direct differentiation of equation $(1.1)_1$ and the comparison with (1.4) that the deformation gradient $\mathbf{F}$ admits two alternative representations, namely:

$$\mathbf{F} = \nabla_{\mathbf{X}}\boldsymbol{\chi} = \frac{\partial \mathbf{x}}{\partial \mathbf{X}}, \qquad \mathbf{F} = \mathbf{I} + \mathbf{u} \otimes \nabla_{\mathbf{X}} \tag{1.6}$$

The elements of $\mathbf{F}$ are called *stretches* and represent the relative change in length between a spatial line element and a material line element. More precisely, the expression of $\mathbf{F}$ reads:

$$\mathbf{F} = \frac{\partial x_i}{\partial X_J}\mathbf{e}_i \otimes \mathbf{E}_j = F_{ij}\mathbf{e}_i \otimes \mathbf{E}_j \tag{1.7}$$

from which we see that $\mathbf{F}$ is a two-point tensor: one base vector is defined with respect to the Eulerian configuration and the other is defined with respect to the Lagrangian configuration, i.e. *it is a geometric object having its two feet on different manifolds* (Maugin, [133]). From the statement of the existence of the inverse mapping, it follows that the deformation mapping is one-to-one. Thus, the deformation gradient $\mathbf{F}$ cannot be singular and its inverse exists:

$$\mathbf{F}^{-1} = \nabla_{\mathbf{x}}\boldsymbol{\chi}^{-1} = \frac{\partial \mathbf{X}}{\partial \mathbf{x}} \tag{1.8}$$

Naturally, this implies that $\det \mathbf{F} \neq \mathbf{0}$. The determinant of the deformation gradient is connected to the mapping between the infinitesimal current volume dv and the infinitesimal reference volumes dV. More precisely, given three infinitesimal line elements individuating an infinitesimal volume element, the latter can be computed by means of the scalar product between an infinitesimal line element and the cross product of the other two, for example $dv = (d\mathbf{x}_1 \times d\mathbf{x}_2) \cdot d\mathbf{x}_3$. The volume of this parallelepiped is algebraically the absolute value of the determinant of the matrix formed by the rows constructed from the vectors. As a consequence, by using equation (1.5), it is easy to verify that:

$$dv = (d\mathbf{x}_1 \times d\mathbf{x}_2) \cdot d\mathbf{x}_3 = \det \begin{bmatrix} d\mathbf{x}_1 \\ d\mathbf{x}_2 \\ d\mathbf{x}_3 \end{bmatrix} = \det \begin{bmatrix} \mathbf{F}\,d\mathbf{X}_1 \\ \mathbf{F}\,d\mathbf{X}_2 \\ \mathbf{F}\,d\mathbf{X}_3 \end{bmatrix} = \det \mathbf{F} \det \begin{bmatrix} d\mathbf{X}_1 \\ d\mathbf{X}_2 \\ d\mathbf{X}_3 \end{bmatrix} \tag{1.9}$$

Then it follows that

$$dv = J\,dV, \qquad J := \det \mathbf{F}\,(\mathbf{X}, t) = \frac{dv}{dV} \tag{1.10}$$

the local volumetric deformation measure J is known as *Jacobian* of the deformation gradient. Since both the infinitesimal volumes dv and dV are positive quantities, the Jacobian must also be positive,

$$J = \det \mathbf{F}\,(\mathbf{X}, t) > 0 \tag{1.11}$$

also implying that interpenetration of volume elements of body $\mathcal{B}$ is excluded. Coherently, volumetric dilatation and contraction occur when $J > 1$ and $J < 1$, respectively, while in case $J = 1$ the transformation is called *isochoric*. By now observing that a

generic spatial (as well as the material) infinitesimal area element $d\mathbf{a} = da\mathbf{n}$ –defined by means of its surface da and the normal outward vector $\mathbf{n}$– can be obtained from the cross product of two line elements, the infinitesimal volume can be rewritten as $dv = d\mathbf{a} \cdot d\mathbf{x}$. Analogously, $dV = d\mathbf{A} \cdot d\mathbf{X}$. Then, the use of equations (1.5) and (1.10) give [87]:

$$dv = d\mathbf{a} \cdot d\mathbf{x} = JdV$$
$$d\mathbf{a} \cdot \mathbf{F}d\mathbf{X} = Jd\mathbf{A} \cdot d\mathbf{X}$$
$$\left[d\mathbf{a} - J\mathbf{F}^{-\mathsf{T}}d\mathbf{A}\right] \cdot d\mathbf{X} = 0 \tag{1.12}$$

Since $d\mathbf{X}$ cannot vanish, equation (1.12) let to obtain the so called *Nanson's formula*

$$d\mathbf{a} = J\mathbf{F}^{-\mathsf{T}}d\mathbf{A} = \mathrm{Cof}\mathbf{F}\,d\mathbf{A} \tag{1.13}$$

which maps each infinitesimal material area $d\mathbf{A} = da\mathbf{N}$ into an infinitesimal spatial area element $d\mathbf{a} = da\mathbf{n}$ through the application of the $\mathrm{Cof}\mathbf{F}$. Equations (1.5), (1.10) and (1.13) give then the aforementioned transport theorems, schematically represented in Fig. 1.
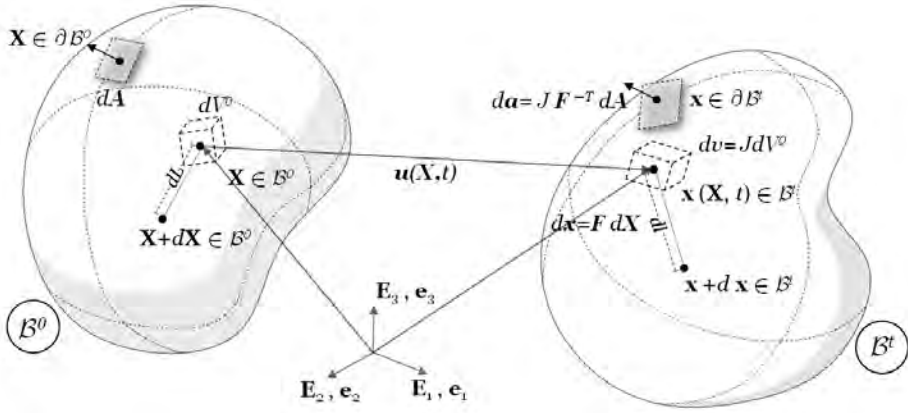
Figure 1: A hand-made sketch of the kinematics and deformation of material bodies

It can be shown that the deformation gradient $\mathbf{F}$ can be algebraically decomposed in two ways into a pure deformation and a pure rotation. This polar decomposition is multiplicative and reads as [46]

$$\mathbf{F} = \mathbf{RU} = \mathbf{VR} \tag{1.14}$$

where $\mathbf{R} \in \mathrm{Orth}^+$ is an orthogonal tensor (i.e. $\mathbf{R}^{\mathsf{T}}\mathbf{R} = \mathbf{R}\mathbf{R}^{\mathsf{T}} = \mathbf{I}$) representing the rotation and called the rotation tensor, while $\mathbf{U}$ and $\mathbf{V}$ are called the right and the left stretch tensors, respectively, and both represent the pure deformation contribution. The stretch tensors admit the following spectral decomposition:

$$\mathbf{U} = \lambda_1 \mathbf{N}_1 \otimes \mathbf{N}_1 + \lambda_2 \mathbf{N}_2 \otimes \mathbf{N}_2 + \lambda_3 \mathbf{N}_3 \otimes \mathbf{N}_3 \qquad (1.15)$$

$$\mathbf{V} = \lambda_1 \mathbf{n}_1 \otimes \mathbf{n}_1 + \lambda_2 \mathbf{n}_2 \otimes \mathbf{n}_2 + \lambda_3 \mathbf{n}_3 \otimes \mathbf{n}_3 \qquad (1.16)$$

where λ_k are the *principal stretches*, and $\mathbf{N}_k$ and $\mathbf{n}_k$ represent the material and current eigenvectors. Then, by adopting the first decomposition in (1.14), deformation occurs by first stretching material elements and then by applying a rigid rotation. The second decomposition of (1.14) provides a rotation before stretching fibres (still having material length) into their spatial length. Clearly, it emerges that $\mathbf{F}$ incorporates all the information for describing the deformation at a material point. However, it is not suitable for describing deformation seen as the change of shape of the body due to the presence of rigid body rotations. Also, $\mathbf{F}$ is not a symmetric tensor. To overcome these problems, the *right Cauchy Green tensor* $\mathbf{C}$ and the *left Cauchy Green tensor* $\mathbf{b}$ can be introduced:

$$\mathbf{C} = \mathbf{F}^\mathsf{T} \mathbf{F} = \mathbf{U}^\mathsf{T} \mathbf{R}^\mathsf{T} \mathbf{R} \mathbf{U} = \mathbf{U}^2, \qquad (1.17)$$

$$\mathbf{b} = \mathbf{F} \mathbf{F}^\mathsf{T} = \mathbf{V} \mathbf{R} \mathbf{R}^\mathsf{T} \mathbf{V}^\mathsf{T} = \mathbf{V}^2 \qquad (1.18)$$

They respectively connote as a material strain tensor and a spatial strain tensor. Moreover, they result symmetric and positive definite and do not account for rigid rotation, by definition.

Further several deformation measures can be adopted. If motion includes a deformational component, then the length $d\mathbf{x}$ will be different from the length $d\mathbf{X}$. To calculate this change in length the current square length $ds^2 = d\mathbf{x}^\mathsf{T} d\mathbf{x}$ and the material square length $dS^2 = d\mathbf{X}^\mathsf{T} d\mathbf{X}$ can be used. Then the half of the difference between the square lengths can be computed and, accounting for relationship (1.5) and (1.17)$_1$, one has [46]:

$$\frac{1}{2}(ds^2 - dS^2) = d\mathbf{X}^\mathsf{T} \frac{1}{2} \left[\mathbf{C} - \mathbf{I} \right] d\mathbf{X} \qquad (1.19)$$

The quantity in square brackets is called the *Green-Lagrange strain tensor*:

$$\mathbf{E} = \frac{1}{2} \left(\mathbf{C} - \mathbf{I} \right) \qquad (1.20)$$

An alternative representation of the Green-Lagrange tensor can be given in terms of the displacement vector $\mathbf{u}$, by recalling (1.6):

$$\mathbf{E} = \frac{1}{2} \left(\mathbf{F}^\mathsf{T} \mathbf{F} - \mathbf{I} \right) = \frac{1}{2} \left(\nabla_\mathbf{X} \otimes \mathbf{u} + \mathbf{u} \otimes \nabla_\mathbf{X} + (\nabla_\mathbf{X} \otimes \mathbf{u})(\mathbf{u} \otimes \nabla_\mathbf{X}) \right) \qquad (1.21)$$

This definition emphasizes the linear part and a geometrically nonlinear part. In the so called *small strain theory*, which implies the hypothesis $\partial u_i / \partial X_J \ll 1$, nonlinearties are not taken into account and the linear strain tensor is obtained as:

$$\boldsymbol{\epsilon} = \frac{1}{2} \left(\nabla_\mathbf{X} \otimes \mathbf{u} + \mathbf{u} \otimes \nabla_\mathbf{X} \right) = \mathrm{sym} \left(\mathbf{u} \otimes \nabla_\mathbf{X} \right) \qquad (1.22)$$

The eulerian counterpart of the Green-Lagrange tensor is given by the *Euler-Almansi strain tensor*, which reads as:

$$\mathbf{e} = \frac{1}{2} \left(\mathbf{I} - \mathbf{b}^{-1} \right) \qquad (1.23)$$

1.1.1   *Seth-Hill strain measures. The logarithmic (Hencky) strain*

It is clear that $\mathbf{U}$ or $\mathbf{V}$ provide a local measure of deformation because their principal components represent the stretch of the three orthogonal fibres aligned to the eigenvectors [22]. As said, the first represents a material measure of deformation since it transforms material quantities into material quantities, while the second exclusively acts on spatial quantities. The tensors $\mathbf{U}$ and $\mathbf{V}$, as well as $\mathbf{C}$ and $\mathbf{b}$ can be used to quantify the strain. However, strain measures are not limited to these choices. To quantify the strain, different measures can be adopted. More generally, the so-called *Seth-Hill* strain family can be defined:

$$
\mathbf{E}^{(m)} = \begin{cases} \frac{1}{m}\left(\mathbf{U}^m - \mathbf{I}\right), & m \neq 0 \\ \ln \mathbf{U}, & m = 0 \end{cases}, \qquad
\mathbf{e}^{(m)} = \begin{cases} \frac{1}{m}\left(\mathbf{V}^m - \mathbf{I}\right), & m \neq 0 \\ \ln \mathbf{V}, & m = 0 \end{cases}
\tag{1.24}
$$

defined for every integer m so that they vanish in absence of deformation. Note that, with attention on material definition, for example, the case $m = 1$ defines the engineering strains $\epsilon_i = \lambda_i - 1$, while the case $m = 2$ gives the definition of the Green-Lagrange tensor as defined in equation (1.21). The logarithmic strain tensor –or *Hencky strain*– can be defined by considering the logarithm of the eigenvalues in its spectral decomposition so that

$$
\mathbf{H} = \mathbf{E}^{(0)} = \ln \mathbf{U} = \ln \lambda_i \, \mathbf{N}_i \otimes \mathbf{N}_i
\tag{1.25}
$$

$$
\mathbf{h} = \mathbf{e}^{(0)} = \ln \mathbf{V} = \ln \lambda_i \, \mathbf{n}_i \otimes \mathbf{n}_i
\tag{1.26}
$$

The isotropy of the logarithmic tensor function implies that, since $\mathbf{V} = \mathbf{R}\mathbf{U}\mathbf{R}^{\mathsf{T}}$

$$
\mathbf{h} = \mathbf{R}\mathbf{H}\mathbf{R}^{\mathsf{T}}
\tag{1.27}
$$

In particular, the so-called logarithmic strain $\epsilon_H = \ln \lambda$ can be introduced by considering the incremental deformation of a fibre of initial length l_0 up to the final length l. An intermediate deformation between these two states is defined by a length l^*, in a way to define an incremental deformation $d\epsilon_H$ as

$$
d\epsilon_H = \frac{dl^*}{l^*}
\tag{1.28}
$$

The total deformation will be then given by the sum of the several incremental deformation:

$$
\epsilon_H = \int_0^{\epsilon_H} d\epsilon_H = \int_{l_0}^{l} \frac{dl^*}{l^*} = \ln \frac{l}{l_0}
\tag{1.29}
$$

where $\lambda = l/l_0$ represents the stretch of the fiber. Moreover, at small strain, the fiber engineering strain is readily obtained, i.e. $\epsilon_H \approx \lambda - 1$. Also, the advantage of adopting strain measure resides in the possibility of additively decomposing the stretches that are indeed multiplicatively combined. In the case of the fiber, for example, let the stretch λ be seen as the result of two combined stretches, say $\lambda_* = l/l_*$ and $\lambda_0 = l_*/l_0$,

where l_* depicts an intermediate configuration and the two stretches might be elastic or inelastic. Multiplicative decomposition is in fact widely adopted in finite thermoelasticity and plasticity. Naturally, in this simple case, it results $\lambda = \lambda_* \lambda_0$, and the Hencky strain will be given by:

$$\epsilon_H = \ln \frac{l}{l_0} = \ln \frac{l}{l_*} \frac{l_*}{l_0} = \ln \lambda_* + \ln \lambda_0 \tag{1.30}$$

This feature, opportunely generalized in order to take into account the configuration changes in combining deformations, can be useful for biomechanical problems, in which the multiplicative decomposition of the deformation gradient into its elastic and growth part is commonly employed.

1.1.2 *The multiplicative decomposition. The elasto-growth case*

In continuum mechanics of growing media, finite strain kinematics treats the total deformation by means of the aforementioned multiplicative decomposition. In particular, the deformation gradient $\mathbf{F}$ is assumed to be the result of a growth tensor $\mathbf{F}_g$ and a geometrically elastic tensor $\mathbf{F}_e$ that *de facto* combine in a multiplicative manner in order to give back the deformation gradient:

$$\mathbf{F} = \mathbf{F}_e \mathbf{F}_g \tag{1.31}$$

By following this representation, multiple configurations have to be taken into account. In fact, the body is first supposed to undergo a growth process that drives the latter towards a grown intermediate configuration, say $\mathcal{B}^g$. In this configuration, the material particles occupy the position $\mathbf{x}^g(\mathbf{X}, t) \in \mathcal{B}^g$ and their deformation can be described through an appropriate growth tensor $\mathbf{F}_g$, in a way that $d\mathbf{x}^g = \mathbf{F}_g \, d\mathbf{X}$. The polar decomposition of $\mathbf{F}_g$ reads:

$$\mathbf{U}_g = \lambda_{gi}(\mathbf{N}_i \otimes \mathbf{N}_i) \qquad \mathbf{F}_g = \mathbf{R}_g \mathbf{U}_g = \lambda_{gi}(\mathbf{N}_{gi} \otimes \mathbf{N}_i) \tag{1.32}$$

where λ_{gi} are the principal *growth stretches*, that are inelastic, $J_g = \det \mathbf{U}_g = dV_g/dV_0 = \lambda_{g1}\lambda_{g2}\lambda_{g3}$ being therefore the volumetric change with respect to the initial configuration due to growth, while $\mathbf{N}_{gi} = \mathbf{R}_g \mathbf{N}_i$ define the rotation on each eigenvector $\mathbf{N}_i$ in the configuration $\mathcal{B}^g$. During the growth process the body is also supposed to be unloaded, in this way the (inelastic) strain contribution being exclusively caused by the volumetric change induced by the growth itself. However, the introduction of this intermediate configuration also implies the need of discerning separately the contribution of volumetric growth and the densification that can combine together to furnish the growth seen as overall local mass addition/removal. However, as well-known, the growth strain alone does not completely describe the body motion since the growth deformation path has been deprived of external loads and it cannot generally ensure the geometric compatibility of the intermediate configuration. In fact, infinitesimal volume elements grow (or reasorb) independently from each other, as conceptually represented in Fig. 2, thus resulting in an overall incompatible configuration. For these reasons, the body experiences an elastic strain which permits to adapt the response to prescribed boundary conditions (i.e. the external mechanical loads and/or the given constraints) as well as to compatibilize the grown elements

by kindling suitable self-equilibrated (residual) stresses within the body. Then, the elastic strain $\mathbf{F}_e$ maps the points $\mathbf{x}^g \in \mathcal{B}^g$ onto the actual configuration $\mathbf{x} \in \mathcal{B}$, having the in-cascade transformation:

$$d\mathbf{x} = \mathbf{F}_e \, d\mathbf{x}^g = \mathbf{F}_e \mathbf{F}_g \, d\mathbf{X} \tag{1.33}$$

The polar decomposition of $\mathbf{F}_e$ gives:

$$\mathbf{U}_e = \lambda_{ei} \left(\mathbf{N}_{gi} \otimes \mathbf{N}_{gi} \right) \qquad \mathbf{F}_e = \mathbf{R}_e \mathbf{U}_e = \lambda_{ei} \left(\mathbf{n}_i \otimes \mathbf{N}_{gi} \right) \tag{1.34}$$

$\mathbf{U}_e$ then denoting the principal elastic stretch seen in the grown configuration. By combining the right stretch tensors introduced in (1.32) and (1.34), the total stretch tensor $\mathbf{U}$ can be determined by considering the right Cauchy-Green tensor and decomposition (1.31):

$$\mathbf{C} = \mathbf{F}^\mathsf{T}\mathbf{F} = \mathbf{U}^2 = \mathbf{U}_g^\mathsf{T} \left(\mathbf{R}_g^\mathsf{T}\mathbf{U}_e^\mathsf{T}\mathbf{U}_e\mathbf{R}_g \right) \mathbf{U}_g = \mathbf{U}_g^\mathsf{T}\overset{\circ}{\mathbf{U}}_e^{2}\mathbf{U}_g \tag{1.35}$$

with $\overset{\circ}{\mathbf{U}}_e^{2} = \mathbf{R}_g^\mathsf{T}\mathbf{U}_e^2\mathbf{R}_g$ thus representing the back rotated version of $\mathbf{U}_e$ reported to the reference configuration. This also let to write:

$$\mathbf{U} = \sqrt{\mathbf{U}_g^\mathsf{T}\overset{\circ}{\mathbf{U}}_e^{2}\mathbf{U}_g} \tag{1.36}$$

Also, the orthogonal rotation matrix $\mathbf{R}$ can be expressed as $\mathbf{R} = \mathbf{R}_e\mathbf{R}_g$.
A first Lagrangian type strain measure associated to the deformations $\mathbf{F}_e$ and $\mathbf{F}_g$ are:

$$\mathbf{E}_e = \frac{1}{2} \left(\mathbf{F}_e^\mathsf{T}\mathbf{F}_e - \mathbf{I} \right), \qquad \mathbf{E}_g = \frac{1}{2} \left(\mathbf{F}_g^\mathsf{T}\mathbf{F}_g - \mathbf{I} \right) \tag{1.37}$$

The total Green-Lagrange type strain can be expressed as a combination of these measure as

$$\mathbf{E} = \frac{1}{2} \left(\mathbf{F}^\mathsf{T}\mathbf{F} - \mathbf{I} \right) = \mathbf{E}_g + \mathbf{F}_g^\mathsf{T}\mathbf{E}_e\mathbf{F}_g \tag{1.38}$$

Clearly, since $\mathbf{E}_e$ and $\mathbf{E}_g$ are defined with respect to the reference configuration, it results $\mathbf{E} \neq \mathbf{E}_e + \mathbf{E}_g$. This additive decomposition becomes instead valid at small strains: in this case, geometrical small total strain imply that also growth strain keeps adequately small, in this way having

$$\boldsymbol{\epsilon} = \boldsymbol{\epsilon}_g + \boldsymbol{\epsilon}_e \tag{1.39}$$

Furthermore, with attention to the Hencky strain measure, by exploiting the logarithm properties together with (1.36), it is possible to write:

$$\mathbf{H} = \ln\mathbf{U} = \frac{1}{2}\ln\mathbf{U}_g^\mathsf{T}\overset{\circ}{\mathbf{U}}_e^{2}\mathbf{U}_g = \ln\mathbf{U}_g + \ln\overset{\circ}{\mathbf{U}}_e = \mathbf{H}_g + \overset{\circ}{\mathbf{H}}_e \tag{1.40}$$

where the back rotated tensor $\overset{\circ}{\mathbf{H}}_e$ to ensure the coaxiality of the summed Hencky strain tensors. Since logarithm is an isotropic function, the relationship $\overset{\circ}{\mathbf{H}}_e = \mathbf{R}_g^\mathsf{T}\mathbf{H}_e\mathbf{R}_g$ can be readily established. In the present work, this strategy will be particularized to describe the biomechanical problem of tumor spheroids growth.
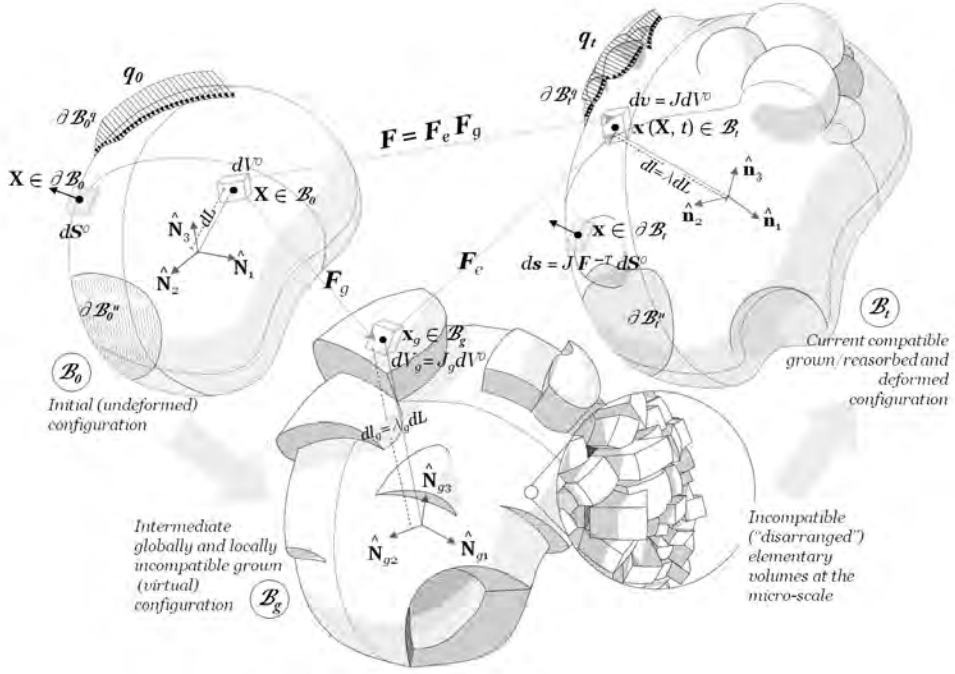
Figure 2: Schematic representation of the kinematics of growth. The body undergoes a growth process and reaches a grown, incompatible configuration in absence of external actions, and then experiences elastic adaptation and load-induced deformation.

It is worth to highlight that the Eulerian description of the deformation process can be argued in a completely analogous manner. In fact, by introducing the left stretch tensor $\mathbf{V} = \mathbf{R}\mathbf{U}\mathbf{R}^\mathsf{T}$, the left Cauchy-Green tensor, under the decomposition (1.31), can be written as:

$$\mathbf{b} = \mathbf{F}\mathbf{F}^\mathsf{T} = \mathbf{V}^2 = \mathbf{V}_e \mathbf{R}_e \mathbf{V}_g^2 \mathbf{R}_e^\mathsf{T} \mathbf{V}_e^\mathsf{T} = \mathbf{V}_e \check{\mathbf{V}}_g^2 \mathbf{V}_e^\mathsf{T}, \tag{1.41}$$

$$\mathbf{V} = \sqrt{\mathbf{V}_e \check{\mathbf{V}}_g^2 \mathbf{V}_e^\mathsf{T}} = \lambda_i \mathbf{n}_i \otimes \mathbf{n}_i \tag{1.42}$$

$\check{\mathbf{V}}_g$ denoting a push-forward operation of the growth left stretch throughout the current basis. Then the Eulerian Hencky strain is defined as

$$\mathbf{h} = \ln \mathbf{V} = \ln \mathbf{V}_e + \ln \check{\mathbf{V}}_g = \mathbf{h}_e + \check{\mathbf{h}}_g \tag{1.43}$$

1.1.3   *Material time derivative*

To fulfill the kinematic description, velocity vector fields have to be defined. A material time derivative is the derivative with respect to time holding $\mathbf{X}$ fixed, i.e.

$$\frac{DA}{Dt} = \frac{\partial A}{\partial t}\bigg|_{\mathbf{X}} \tag{1.44}$$

For a material field $\Phi = \Phi\left(\mathbf{X}, t\right)$ and a spatial field $\phi\left(\mathbf{x}\left(\mathbf{X}, t\right), t\right)$ the material time derivative reads

$$\frac{D\Phi}{Dt} = \dot{\Phi} = \frac{\partial \Phi\left(\mathbf{X}, t\right)}{\partial t} \tag{1.45}$$

$$\frac{D\phi}{Dt} = \frac{\partial \phi\left(\mathbf{x}\left(\mathbf{X}, t\right), t\right)}{\partial t}\bigg|_{\mathbf{X} = \boldsymbol{\chi}^{-1}(\mathbf{x}, t)} = \frac{\partial \phi\left(\mathbf{x}, t\right)}{\partial t} + \frac{\partial \phi\left(\mathbf{x}, t\right)}{\partial \mathbf{x}} \frac{\partial \mathbf{x}}{\partial t} \tag{1.46}$$

Then, in the second case, the material time derivative of a spatial field is performed by first pulling back the representation of ϕ to the material description, then a material derivative is taken and, finally, the resulting expression is again pushed forward to the spatial description. Therefore, one can introduce the *material* $\dot{\mathbf{x}}$ and *spatial* $\mathbf{v}$ descriptions of the velocity:

$$\dot{\mathbf{x}}\left(\mathbf{X}, t\right) = \frac{\partial \boldsymbol{\chi}\left(\mathbf{X}, t\right)}{\partial t} \quad \text{and} \quad \mathbf{v}\left(\mathbf{x}, t\right) = \dot{\mathbf{x}}\left(\boldsymbol{\chi}^{-1}\left(\mathbf{x}, t\right), t\right) \tag{1.47}$$

and the material $\ddot{\mathbf{x}}$ and spatial $\mathbf{a}$ acceleration fields

$$\ddot{\mathbf{x}}\left(\mathbf{X}, t\right) = \frac{\partial^2 \boldsymbol{\chi}\left(\mathbf{X}, t\right)}{\partial t^2} \tag{1.48}$$

$$\mathbf{a}\left(\mathbf{x}, t\right) = \ddot{\mathbf{x}}\left(\boldsymbol{\chi}^{-1}\left(\mathbf{x}, t\right), t\right) = \frac{\partial \mathbf{v}}{\partial t} + \mathbf{L}\frac{\partial \mathbf{x}}{\partial t} \tag{1.49}$$

where equation (1.49) is written according to definition (1.45). Also, in equation (1.49), the definition of the *spatial velocity gradient* has been employed:

$$\mathbf{L} = \frac{\partial \mathbf{v}\left(\mathbf{x}, t\right)}{\partial \mathbf{x}} = \mathbf{v} \otimes \nabla_{\mathbf{x}} \tag{1.50}$$

The *material velocity gradient* is instead given by:

$$\dot{\mathbf{F}} = \frac{\partial \dot{\mathbf{x}}\left(\mathbf{X}, t\right)}{\partial \mathbf{X}} = \dot{\lambda}_i\, \mathbf{n}_i \otimes \mathbf{N}_i + \lambda_i(\dot{\mathbf{n}}_i \otimes \mathbf{N}_i + \mathbf{n}_i \otimes \dot{\mathbf{N}}_i) \tag{1.51}$$

the summation over i being subtended. The relation between the spatial and the material velocity gradient can be derived through the chain rule differentiation:

$$\dot{\mathbf{F}} = \frac{\partial \dot{\mathbf{x}}\left(\mathbf{X}, t\right)}{\partial \mathbf{X}} = \frac{\partial \dot{\mathbf{x}}}{\partial \mathbf{x}} \frac{\partial \mathbf{x}}{\partial \mathbf{X}} = \mathbf{L}\mathbf{F}, \tag{1.52}$$

$$\mathbf{L} = \dot{\mathbf{F}}\mathbf{F}^{-1} = \frac{\dot{\lambda}_i}{\lambda_i}\mathbf{n}_i \otimes \mathbf{n}_i + \dot{\mathbf{n}}_i \otimes \mathbf{n}_i + \frac{\lambda_i}{\lambda_j}\bigg|_{i \neq j} \left(\dot{\mathbf{n}}_i \cdot \mathbf{n}_j\right) \mathbf{n}_i \otimes \mathbf{n}_j \tag{1.53}$$

Starting from (1.52), the back rotated rate of deformation can be defined as the symmetric part of the velocity gradient:

$$\mathbf{D} = \text{sym}(\mathbf{v} \otimes \nabla_{\mathbf{x}}) = \frac{1}{2} \left(\dot{\mathbf{U}} \mathbf{U}^{-1} + \mathbf{U}^{-1} \dot{\mathbf{U}} \right) =$$

$$= \begin{bmatrix} \frac{\dot{\lambda}_1}{\lambda_1} & \frac{\omega_3}{2} \left(\frac{\lambda_1}{\lambda_2} - \frac{\lambda_2}{\lambda_1} \right) & \frac{\omega_2}{2} \left(\frac{\lambda_3}{\lambda_1} - \frac{\lambda_1}{\lambda_3} \right) \\ & \frac{\dot{\lambda}_2}{\lambda_2} & \frac{\omega_1}{2} \left(\frac{\lambda_2}{\lambda_3} - \frac{\lambda_3}{\lambda_2} \right) \\ \text{sym} & & \frac{\dot{\lambda}_3}{\lambda_3} \end{bmatrix} \tag{1.54}$$

where ω_i are the components of the vector $\boldsymbol{\omega} = \text{axial}\left(\dot{\mathbf{R}}\mathbf{R}\right) = [\omega_3 \quad -\omega_2 \quad \omega_1]^{\mathsf{T}}$, which represents the rotation velocity of the principal axes $\mathbf{n}_i$, employing the relationship $\dot{\mathbf{n}}_i = \boldsymbol{\omega} \times \mathbf{n}_i$. The material time derivative of the Jacobian can be determined by means of the Jacobi formula and equation (1.52):

$$\dot{J} = \frac{\partial J}{\partial \mathbf{F}} : \dot{\mathbf{F}} = J\mathbf{F}^{-\mathsf{T}} : \mathbf{L}\mathbf{F} = J\mathbf{I} : \mathbf{L} = J\nabla_{\mathbf{x}} \cdot \mathbf{v} \tag{1.55}$$

In a completely analogous manner, one can define the rates of the Jacobian J_g and $J_e = \det \mathbf{U}_e$ in the case of multiplicative decomposition:

$$\mathbf{L}_g = \dot{\mathbf{F}}_g \mathbf{F}_g^{-1} \qquad \dot{J}_g = J_g \mathbf{I} : \mathbf{L}_g \mathbf{L}_e = \dot{\mathbf{F}}_e \mathbf{F}_e^{-1} \qquad \dot{J}_e = J_e \mathbf{I} : \mathbf{L}_e \tag{1.56}$$

and it readily follows that

$$\mathbf{L} = \mathbf{L}_e + \mathbf{F}_e \mathbf{L}_g \mathbf{F}_e \tag{1.57}$$

Also, through the identity $\dot{\mathbf{E}}_k = \mathbf{F}_k^{\mathsf{T}} \text{sym}(\mathbf{L}_k)\mathbf{F}_k$, the following rate expressions can be obtained:

$$\dot{\mathbf{E}} = \mathbf{F}_g^{\mathsf{T}} \text{sym}(\mathbf{L}_g)\mathbf{F}_g + 2\text{sym}(\mathbf{F}_g^{\mathsf{T}} \mathbf{E}_e \dot{\mathbf{F}}_g) + \mathbf{F}^{\mathsf{T}} \text{sym}(\mathbf{L}_e)\mathbf{F} \tag{1.58}$$

Finally, the rates of the Hencky strain introduced in (1.25) result

$$\dot{\mathbf{H}} = \frac{\dot{\lambda}_i}{\lambda_i}\mathbf{N}_i \otimes \mathbf{N}_i + \ln \lambda_i \left(\dot{\mathbf{N}}_i \otimes \mathbf{N}_i + \mathbf{N}_i \otimes \dot{\mathbf{N}}_i \right) \tag{1.59}$$

$$\dot{\mathbf{h}} = \frac{\dot{\lambda}_i}{\lambda_i}\mathbf{n}_i \otimes \mathbf{n}_i + \ln \lambda_i \left(\dot{\mathbf{n}}_i \otimes \mathbf{n}_i + \mathbf{n}_i \otimes \dot{\mathbf{n}}_i \right) \tag{1.60}$$

which admits, through similar considerations made for the symmetric part of the velocity gradient (1.54), the following representation:

$$\dot{\mathbf{H}} = \mathbf{R}^{\mathsf{T}} \dot{\mathbf{h}} \mathbf{R} =$$

$$= \begin{bmatrix} \frac{\dot{\lambda}_1}{\lambda_1} & \omega_3 \ln \left(\frac{\lambda_1}{\lambda_2} \right) & \omega_2 \ln \left(\frac{\lambda_3}{\lambda_1} \right) \\ & \frac{\dot{\lambda}_2}{\lambda_2} & \omega_1 \ln \left(\frac{\lambda_2}{\lambda_3} \right) \\ \text{sym} & & \frac{\dot{\lambda}_3}{\lambda_3} \end{bmatrix} \tag{1.61}$$

1.2 STRESS MEASURES

As a solid deforms, stresses are internally generated. For a deformable body on which external forces are applied (in an inertial system), the resulting field of internal reactive forces acting on infinitesimal surfaces within the body is connoted as stress. Therefore stress physically expresses the interactions among neighboring particles within the continuous material. While in small deformations stress is uniquely identified as the force per unit reference area, this implying that stress variations are exclusively due to forces changes, in large deformation the spatial infinitesimal area cannot be confused with the reference infinitesimal area and stress variation accounts also for the geometrical transformations. Therefore an actual measure of stress should be referred to the current area element. However, in many problems the current configuration is not known and alternative stress measures, referred to the reference configuration, might be employed. To define the true stress –or *Cauchy stress*– let us consider a cutting surface passing through a material point $P \in \mathcal{B}$. The body is subjected to a system of external forces $\mathbf{f}$, consisting of surface tractions and body forces and is supposed at equilibrium. When the body is cut by the surface, as a mechanical reaction to external loads, forces are then transmitted through the points of the cutting surfaces. Hence, each infinitesimal are da will experience a force aliquota $d\mathbf{f}$ so that, in the point P the Cauchy surface traction can be defined as the vector (see Fig. 3):

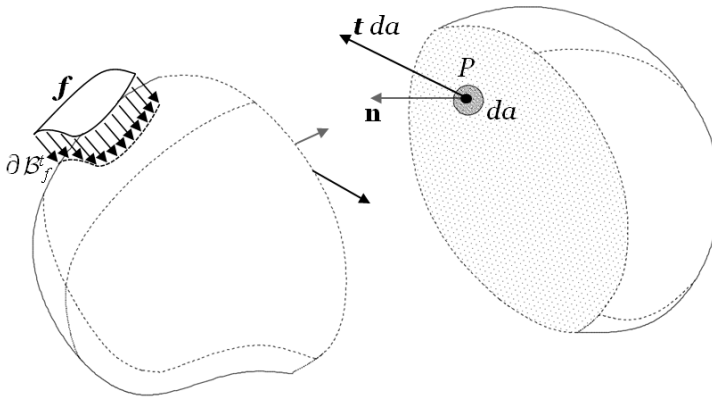$$\mathbf{t}\left(\mathbf{x}, t\right) = \frac{d\mathbf{f}}{da} \tag{1.62}$$

Figure 3: Definition of the Cauchy stress vector

According to Cauchy's postulate, the traction vector $\mathbf{t}$ persists for all surfaces passing through the point P and having the same normal vector $\mathbf{n}$ at P. The state of stress at a point in the body is then defined by all stress vectors $\mathbf{t}$ associated with all planes that pass through that point. According to *Cauchy's stress theorem*, there exists a second-order tensor $\boldsymbol{\sigma}\left(\mathbf{x}, t\right)$, such that $\mathbf{t}$ is a linear function of $\mathbf{n}$, i.e.

$$\mathbf{t}\left(\mathbf{x}, t, \mathbf{n}\right) = \boldsymbol{\sigma}\left(\mathbf{x}, t\right)\mathbf{n} \tag{1.63}$$

Mechanical equilibrium also implies that $\mathbf{t}\left(\mathbf{x}, t, \mathbf{n}\right) = -\mathbf{t}\left(\mathbf{x}, t, -\mathbf{n}\right)$ (Fig. 3). Therefore the stress elements of the Cauchy stress tensor will be the components of the traction vector at each material point P on that face. The Cauchy stress tensor is a pure Eulerian stress tensor, and can be represented as

$$\boldsymbol{\sigma}\left(\mathbf{x}, t\right) = \sigma_{ij}\mathbf{n}_i \otimes \mathbf{n}_j \tag{1.64}$$

Another useful stress measure is the *Kirchhoff stress*, which is given by the Cauchy stress $\boldsymbol{\sigma}$ multiplied by the Jacobian J:

$$\boldsymbol{\tau} = J\boldsymbol{\sigma} \tag{1.65}$$

The Lagrangian version of the Cauchy's stress theorem can be formulated as

$$\mathbf{T}\left(\mathbf{X}, t\right) = \mathbf{P}\left(\mathbf{X}, t\right)\mathbf{N} \tag{1.66}$$

in which $\mathbf{N}$ is the normal outward vector to the infinitesimal reference area element, and $\mathbf{T}$ is the corresponding traction. Then the following relation holds:

$$\mathbf{T}\left(\mathbf{X}, t\right)dA = \mathbf{t}\left(\mathbf{x}, t\right)da \tag{1.67}$$

Substituting into (1.67) the relations (1.66) and (1.63), and by taking into account the Nanson's formula (1.13), the so-called *Piola-Kirchhoff stress* is obtained as

$$\mathbf{P} = J\boldsymbol{\sigma}\mathbf{F}^{-\mathsf{T}} = \boldsymbol{\tau}\mathbf{F}^{-\mathsf{T}} \tag{1.68}$$

The Piola Kirchhoff tensor therefore relates the current force to the referential area element. It is obtained by means of a Piola transformation of the Cauchy stress $\boldsymbol{\sigma}$, and results to be a two-point tensor having representation[1]

$$\mathbf{P} = P_{ij}\mathbf{n}_i \otimes \mathbf{N}_j \tag{1.69}$$

It is worth noting that the Piola-Kirchhoff stress is not a symmetric tensor:

$$\mathbf{P}^{\mathsf{T}} = J\mathbf{F}^{-1}\boldsymbol{\sigma} \neq \mathbf{P} \tag{1.70}$$

In order to have a Lagrangian stress that is also symmetric, the *second Piola Kirchhoff stress* is introduced:

$$\mathbf{S} = \mathbf{F}^{-1}\mathbf{P} = \mathbf{F}^{-1}\boldsymbol{\tau}\mathbf{F}^{-\mathsf{T}}, \qquad \mathbf{S} = \mathbf{S}^{\mathsf{T}} \tag{1.71}$$

1.2.1 *The concept of residual stress in growing bodies*

Stress is the response of a deformable body to applied forces. However, a common feature of biological structures is the presence of nonzero stresses known as residual stresses. Such stresses reveal that kinematical growth takes place in an incompatible manner, meaning that the compatible total strain which is macroscopically observed is the result of an incompatible growth strain accompanied by an elastic adaptation (as previously discussed). The latter one is directly responsible of restoring tissue geometrical compatibility, this being guaranteed by imprisoned stresses. Therefore, residual

---

1 The stress tensor is not necessarily coaxial with the deformation tensor.

stresses are nonzero stresses detectable in a traction-free body (in a loaded configuration, a further superimosed elastic deformation might combine with the adaptive one). A simple example is represented by vessel structures: the growing overlapping layer of a vessel structure have to elastically stretch in the circumferential direction in order to respect geometrical compatibility. This feature implies that nonzero residual stress resides in vessel walls. In fact, Fung [69] showed that this stress can be revealed by observing the opening angle of the vessel when a cut is performed in longitudinal direction. However, the adjective "residual" might be ambiguous (or contradictory) because suggests that one can find residual stresses (also) after cutting a (grown) material, while - generally - when one ideally or practically cuts a material, it releases the imprisoned elastic energy so obtaining "stress-free" configurations. The term is however used to also denote the stresses accumulated in a (continuum model of a) tissue during growth to guarantee compatibility of the total deformation - that is, elastic and inelastic (growth-associated) strains - at each time, but the term "prestress" might suitably replace "residual stress" also in these cases. To qualitatively explain the nature of growth-induced stresses, let us consider a mechanically analogous deformation process in which, as in the growth, elastic and inelastic strains can appear combined to give the overall strain at each material point (and at any time), say a (linear) elementary thermo-elastic problem where, for instance, an one-dimensional bar is subjected to uniaxial stress/strain regime.

Then, one can distinguish two possible cases of interest.

- *Force-prescribed case:* the bar is subjected to a combined (compressive or tensile) axial load applied to its constraint-free ends and to a small uniform temperature increase; the body will homogeneously deform and at each point the total strain will be given by the sum of a purely inelastic (thermal) and a purely elastic (load-induced) strain. If an opposite in sign load is then applied (the load is removed to have homogeneous boundary conditions in term of forces), the beam will change its previous deformation state and a sole uniform inelastic strain will be exhibited by the bar, without any stress. As a consequence, by cutting at this stage the bar at an arbitrary section along its axis, neither (residual) stresses nor additional strains will be exhibited, but a residual strain (say a thermal strain analogous to the growth-induced strain) can be however observed by comparing the initial unladed and at room temperature bar length with the final one.

- *Displacement-prescribed case:* a complementary case can be constructed by assuming the same bar considered above, now subjected to an uniform temperature increase with the clamped (full constrained) ends. In this case, as well-known, no total strain can be observed at any bar point (at least until the material strength is reached), elastic strains locally equate inelastic (thermal or growth) strains and stresses (due to the reaction forces at the clamped ends) occur. The body already has homogeneous boundary conditions in terms of displacements (in case of non-zero displacements prescribed, to return to homogeneous boundary conditions one would have to apply an opposite-in-sign displacement at the ends) thus, by cutting at this stage in an arbitrary section the bar, the stored elastic energy is released and the beam will show a stress-free deformed configuration different from the initial one, characterized - as in the first case - by the sole inelastic *residual strain* and no *residual stresses.*

But how can we define residual strains and stresses? And what is then the difference between the two thermo-elastic cases presented above? A possible answer to the first question (the definition of residual stress and strain) is that the residual strain can be seen as the strain observed in an element when the material is returned to a stress-free condition, and the residual stress can be complementary interpreted as the self-equilibrated stress generated inside an element when it returns to a strain-free (zero total strain) condition (as also commonly done dealing with plasticity, for example). As a consequence, the definition given above allows to elucidate the difference between the two thermo-elastic cases. In both the situations, after the cutting, one actually has no residual stresses (both the bar final configurations are in fact stress-free) and, if the temperature increase was set to be the same, one also observes only inelastic (thermal, or growth) strains. The sole difference which one can recognize to distinguish between the two cases is given by the "energy release" after the cutting observed in the second situations and revealed to the observer by the change of configuration, which implicitly depends on the presence of a self-equilibrated stress field present into the bar *before the cutting.* The above described simple paradigm might be also exploited to interpret the wide use of the thermal stress. If in fact - after the cutting - one wanted to go back to the undeformed configuration (zero total strain at each point of the bar), one should ideally apply a stress field exactly equal to the *self-equilibrated stress state* present into the bar prior to cut the beam. This stress state would hence result to be associated to a zero-strain condition and, by virtue of the above given definitions of residual strains and stresses, should be thus thought as a *residual stress.*

Also, from the simple thermo-elastic paradigm utilized above in parallel with growth, two further aspects can be highlighted. Fist, *homogeneous* (spatially uniform) deformation states can determine residual stresses (the second case above described) and therefore the stresses can occur not only in "inhomogeneously grown" materials. Futhermore, as well-known, (in linear thermo-elasticity) if a linearly varying inelastic deformation field is imposed (e.g. a thermal strain field linearly varying with x, y and z of a Cartesian coordinate system in a generic three-dimensional domain of a not constrained and unloaded body with arbitrary shape) the inelastic strain does not generate stresses (because the compatibility equations $\nabla \times (\nabla \times \boldsymbol{\epsilon})^{\mathsf{T}} = \mathbf{0}$ are automatically satisfied and the total strain coincides with the inelastic one, thus producing vanishing stresses): thus, if inelastic thermal strains are replaced by inelastic growth strains, a tissue material can inhomogeneously (linearly in this case) grow without accumulating stresses.

1.3 CONSERVATION EQUATIONS

Conservation equations are material-independent principles. Due to their axiomatic character, they cannot be derived from other natural laws. In what follows, the main balance principles will consider continua with a growing mass and, therefore, multiplicative decomposition will be adopted. Also, some growth-specific and remodelling-specific terms will be introduced in order to appropriately provide mass supply/removal as well as remodelling-induced changes, by assuming a pure volumetric growth process.

1.3.1 *The mass conservation equation*

A substantial difference between the theory of open systems and the theory of closed systems resides in the formulation of the mass balance. Differently from the theory of closed systems, the mass of open systems is not constant. Then a *time rate of the mass growth* r_g has to be introduced (see e.g. Lubarda and Hoger [127]), and the mass balance can be written as

$$dm = dm^0 + dm^{gen}$$
$$\rho\,dv = \rho^0\,dV + \int_{t_i}^{t} r_g\,dvd\tau \tag{1.72}$$

where $\rho^{(k)} : \Omega^{(k)} \to \mathbb{R}$ denotes the mass density in the configuration (k), so that the mass of every $dv^{(k)}$-measurable subset of $\Omega^{(k)}$ is given by $dm^{(k)} = \rho^{(k)}\,dv^{(k)}$, in a way that also $\rho^{(k)} > 0, \quad \forall \mathbf{x}^{(k)} \in \Omega^{(k)}$. By deriving (1.72) with respect to time,

$$\frac{d}{dt}(\rho\,dv) = r_g dv \tag{1.73}$$

$$\frac{d\rho}{dt}\,dv + \rho\frac{d(dv)}{dt} = r_g dv \tag{1.74}$$

Dividing both members by the initial fixed volume dV and recalling equations (1.10) and (1.55), one obtains

$$\frac{d\rho}{dt} + \rho\nabla_{\mathbf{x}} \cdot \mathbf{v} = r_g \tag{1.75}$$

which is the current (Eulerian) local form of the mass balance. Also, a pull-back of variables in equation (1.73) gives the Lagrangian form of the mass balance:

$$\frac{d(J\left(\mathbf{X},t\right)\rho\left(\mathbf{x}\left(\mathbf{X},t\right),t\right))}{dt} = J\left(\mathbf{X},t\right)r_g\left(\mathbf{x}\left(\mathbf{X},t\right),t\right)$$
$$\text{or} \quad \frac{d\varrho}{dt} = \mathcal{R}_g \tag{1.76}$$

in which the position $\varrho = J\,\rho$ and $\mathcal{R}_g = J\,r_g$ have been introduced to denote material quantities.

1.3.2 *The momentum conservation equations*

1.3.2.1 *The Reynolds transport theorem*

It is convenient to briefly recall the *Reynolds transport theorem*, which generalizes the well-known Leibnitz integral rule. Considering a function $\mathcal{F}\left(\mathbf{x},t\right)$ (that can be tensor, vector or scalar valued), this theorem states that:

$$\frac{D}{Dt}\int_{\Omega}\mathcal{F}dv = \int_{\Omega}\frac{d\mathcal{F}}{dt} + \int_{\partial\Omega}(\mathbf{v}\cdot\mathbf{n})\mathcal{F}da \tag{1.77}$$

Also the well-known Gauss divergence theorem is recalled:

$$\int_\Omega \nabla_\mathbf{x} \cdot \mathbf{A} = \int_{\partial\Omega} \mathbf{A} \cdot \mathbf{n} da \tag{1.78}$$

1.3.2.2 *Conservation of linear momentum*

The first Euler's law of motion is here presented by introducing a specific growth term, representing the momentum rate associated with the growing mass [47]:

$$\frac{D}{Dt} \int_\Omega \rho \mathbf{v} dv = \int_{\partial\Omega} \mathbf{t} da + \int_\Omega \rho \mathbf{b} dv + \int_\Omega r_g \mathbf{v} dv \tag{1.79}$$

where $\mathbf{t}$ is the traction vector and $\mathbf{b}$ is the body force vector. By then applying the Reynolds transport theorem (1.77) to the first member of equation (1.79), and accounting for the balance of mass in (1.75), it results

$$\frac{D}{Dt} \int_\Omega \rho \mathbf{v} dv = \int_\Omega \rho \frac{d\mathbf{v}}{dt} + r_g \mathbf{v} \, dv \tag{1.80}$$

The direct substitution of the latter in equation (1.79), together with the application of the Cauchy's theorem (1.63) and the divergence theorem (1.78), leads to the local spatial form of the linear momentum conservation equation:

$$\nabla_\mathbf{x} \cdot \boldsymbol{\sigma} + \rho \mathbf{b} = \rho \frac{d\mathbf{v}}{dt} \qquad \forall \mathbf{x} \in \Omega \tag{1.81}$$

Also, a pull-back operation on members of balance (1.79) let to derive the material linear momentum equation, giving

$$\frac{D}{Dt} \int_{\Omega_0} \varrho \dot{\mathbf{x}} dV = \int_{\partial\Omega_0} \mathbf{T} dA + \int_{\Omega_0} \varrho \mathbf{B} dV + \int_{\Omega_0} \mathcal{R}_g \dot{\mathbf{x}} \, dV \tag{1.82}$$

Since Ω_0 is fixed, time differentiation on the left-side of equation (1.82) can be performed on the integrand

$$\frac{D}{Dt} \int_{\Omega_0} \varrho \dot{\mathbf{x}} dV = \int_{\Omega_0} \frac{d\varrho}{dt} \dot{\mathbf{x}} + \varrho \ddot{\mathbf{x}} \, dV = \int_{\Omega_0} \mathcal{R}_g \dot{\mathbf{x}} + \varrho \ddot{\mathbf{x}} \, dV, \tag{1.83}$$

and, by proceeding in an analogous manner through the account of the Cauchy's theorem (1.66) and of the mass balance in the form (1.76), one obtains:

$$\nabla_\mathbf{X} \cdot \mathbf{P} + \varrho \mathbf{B} = \varrho \ddot{\mathbf{x}} \qquad \forall \mathbf{X} \in \Omega_0 \tag{1.84}$$

where the pull-back evaluation of the acceleration has been considered (see equations (1.48)). Localized forms of equilibrium equations show therefore an intuitive representation of equilibrium: the body is entirely at equilibrium if each its element satisfies equilibrium requirements.

1.3.2.3 *Balance of angular momentum*

The second Euler's law of motion, written in its integral form, also presents a growth rate-dependent term and reads:

$$\frac{D}{Dt}\int_{\Omega}(\mathbf{x}\times\rho\mathbf{v})dv = \int_{\partial\Omega}(\mathbf{x}\times\mathbf{t})da + \int_{\Omega}(\mathbf{x}\times\rho\mathbf{b})dv + \int_{\Omega}r_g(\mathbf{x}\times\mathbf{v})dv \qquad (1.85)$$

From the application of the Reynolds transport theorem (1.77) (considering the field $\mathcal{F} = (\mathbf{x}\times\rho\mathbf{v})$), it results

$$\frac{D}{Dt}\int_{\Omega}(\mathbf{x}\times\rho\mathbf{v})dv = \int_{\Omega}\left[\rho\frac{d}{dt}(\mathbf{x}\times\mathbf{v}) + r_g(\mathbf{x}\times\mathbf{v})\right]dv =$$
$$= \int_{\Omega}\left[\rho(\mathbf{x}\times\frac{d}{dt}\mathbf{v}) + r_g(\mathbf{x}\times\mathbf{v})\right]dv \qquad (1.86)$$

in which the relation $\dot{\mathbf{x}}\left(\chi^{-1}(\mathbf{x},t),t\right)\times\mathbf{v}(\mathbf{x},t) = \mathbf{0}$ has been employed. Then, the substitution of equation (1.86) into equation (1.85), gives

$$\int_{\Omega}\rho(\mathbf{x}\times\frac{d\mathbf{v}}{dt})dv = \int_{\partial\Omega}(\mathbf{x}\times\mathbf{t})da + \int_{\Omega}(\mathbf{x}\times\rho\mathbf{b})dv \qquad (1.87)$$

By means of the Cauchy's theorem (1.63) and the Gauss theorem (1.78), the following identity can be obtained

$$\int_{\partial\Omega}(\mathbf{x}\times\mathbf{t})da = \int_{\partial\Omega}(\mathbf{x}\times\boldsymbol{\sigma}\mathbf{n})da = \int_{\Omega}\left[\mathbf{x}\times\nabla_{\mathbf{x}}\cdot\boldsymbol{\sigma} + \boldsymbol{\varepsilon}:\boldsymbol{\sigma}^{\mathsf{T}}\right]dv \qquad (1.88)$$

in which $\boldsymbol{\varepsilon}$ is the Levi-Civita permutation tensor. Therefore, substitution of (1.89) into (1.87), and imposing the conservation of linear momentum, the only remaining term is

$$\int_{\Omega}\mathbf{x}\times\left[\nabla_{\mathbf{x}}\cdot\boldsymbol{\sigma} + \rho\mathbf{b} - \rho\frac{d\mathbf{v}}{dt}\right] + \boldsymbol{\varepsilon}:\boldsymbol{\sigma}^{\mathsf{T}}dv = \mathbf{0},$$
$$\int_{\Omega}\boldsymbol{\varepsilon}:\boldsymbol{\sigma}^{\mathsf{T}}dv = \mathbf{0} \qquad (1.89)$$

By means of localization, the produced scalar equations are of the type $\sigma_{ij} - \sigma_{ji} = 0$, $i \neq j$, which imply the symmetry of the Cauchy stress, i.e.

$$\boldsymbol{\sigma} = \boldsymbol{\sigma}^{\mathsf{T}}, \qquad \forall\mathbf{x}\in\Omega \qquad (1.90)$$

The material form is formulated through a pull-back operation, and the result has already been reported in terms of second Piola-Kirchhoff stress tensor in equation (1.71).

1.3.2.4 *Energy conservation equation*

The first law of thermodynamics requires the balance of energy. It states that the rate of total energy, which is the sum of the internal energy $\mathcal{E}$ and the kinetic energy $\mathcal{K}$, equals the rate of mechanical work $\mathcal{W}$ plus the rate of non-mechanical work $\mathcal{Q}$:

$$\dot{\mathcal{E}} + \dot{\mathcal{K}} = \mathcal{W} + \mathcal{Q} \tag{1.91}$$

The rate at which external surface and body force do work on the current configuration is given by the expression [127]

$$\mathcal{P} = \int_{\partial\Omega} \mathbf{t} \cdot \mathbf{v}\, da + \int_{\Omega} \rho \mathbf{b} \cdot \mathbf{v}\, dv = \int_{\Omega} \left[\rho \frac{d}{dt}\left(\frac{1}{2}\mathbf{v} \cdot \mathbf{v} \right) + \boldsymbol{\sigma} : \mathbf{D} \right] dv \tag{1.92}$$

where $\mathbf{D} = \mathrm{sym}\mathbf{L}$. By considering the thermal power, an internal rate of heat source per unit mass w_h and heat flux vector $\mathbf{q}_h$ are introduced, so that

$$\mathcal{Q} = \int_{\Omega} \rho\, w_h\, dv - \int_{\partial\Omega} \mathbf{q}_h \cdot \mathbf{n}\, da = \int_{\Omega} (\rho\, w_h - \nabla_{\mathbf{x}} \cdot \mathbf{q}_h)\, dv \tag{1.93}$$

Therefore, the first law of thermodynamics in the form (1.91) can be written by considering the specific energy density per unit mass e and by further introducing two further related to growth (see [47, 127, 149]):

$$\frac{D}{Dt} \int_{\Omega} \rho e\, dv + \frac{D}{Dt} \int_{\Omega} \frac{1}{2} \rho \mathbf{v} \cdot \mathbf{v}\, dv = \mathcal{W} + \mathcal{Q} +$$
$$+ \int_{\Omega} \mathbf{k} \cdot \dot{\boldsymbol{\gamma}}\, dv + \int_{\Omega} r_g \left(\frac{1}{2} \mathbf{v} \cdot \mathbf{v} + e \right) dv + \int_{\Omega} \varepsilon_g\, \rho^{-1}\, r_g\, dv \tag{1.94}$$

The last three terms of equality (1.94) are kindled in association with the remodelling and growth processes. In particular, the microstructural changes due to remodelling can be described at a continuum scale through suitable remodelling variables, here represented by the vector $\boldsymbol{\gamma}$ and so $\mathbf{k}$ can be viewed as a thermodynamic driving force conjugated to the rate of remodelling variables. The second term represents the rate of kinetic energy and specific energy associated with the current mass generation and the last term takes into account a contribution to the growth enhanced by a specific metabolic energy supply per unit volume, say ε_g.

By then developing the first two terms of the energy balance (1.94) in the light of the Reynolds transport theorem (1.77), one has

$$\frac{D}{Dt} \int_{\Omega} \rho \left(\frac{1}{2}\mathbf{v} \cdot \mathbf{v} + e \right) dv = \int_{\Omega} \rho \frac{d}{dt}\left(\frac{1}{2}\mathbf{v} \cdot \mathbf{v} + e \right) dv + \int_{\Omega} r_g \left(\frac{1}{2}\mathbf{v} \cdot \mathbf{v} + e \right) dv \tag{1.95}$$

Inserting the latter into (1.94), the local form of the energy conservation equation is finally obtained:

$$\rho \frac{de}{dt} = \boldsymbol{\sigma} : \mathbf{D} + \rho\, w_h - \nabla_{\mathbf{x}} \cdot \mathbf{q}_h + \mathbf{k} \cdot \dot{\boldsymbol{\gamma}} + \varepsilon_g\, \rho^{-1}\, r_g \tag{1.96}$$

If the reference configuration is used to formulate the balance in a Lagrangian form, the mechanical work reads:

$$\mathcal{P} = \int_{\Omega_0} \left[\varrho \frac{d}{dt}\left(\frac{1}{2}\dot{\mathbf{x}} \cdot \dot{\mathbf{x}} \right) + \mathbf{P} : \dot{\mathbf{F}} \right] dV \tag{1.97}$$

in which the identity $J\boldsymbol{\sigma} : \dot{\mathbf{F}}\mathbf{F}^{-1} = \mathbf{P} : \dot{\mathbf{F}}$ has been used. Analogously, the pull-back on $\mathcal{Q}$ reads

$$\mathcal{Q} = \int_{\Omega_0} \left(\varrho W_h - \nabla_{\mathbf{X}} \cdot \mathbf{Q}_h \right) \tag{1.98}$$

in which $W_h = J w_h$ is the material heat source and $\mathbf{Q}_h = J \mathbf{q}_h \mathbf{F}^{-\mathsf{T}}$ is the nominal heat flux vector. The energy formulation reads

$$\frac{D}{Dt} \int_{\Omega_0} \varrho \left(\frac{1}{2} \dot{\mathbf{x}} \cdot \dot{\mathbf{x}} + e_0 \right) dV = \mathcal{W} + \mathcal{Q} +$$
$$+ \int_{\Omega_0} \mathbf{K} \cdot \dot{\boldsymbol{\gamma}}_0 \, dV + \int_{\Omega_0} \mathcal{R}_g \left(\frac{1}{2} \dot{\mathbf{x}} \cdot \dot{\mathbf{x}} + e_0 \right) dV + \int_{\Omega_0} \varepsilon_{g0} \, \varrho^{-1} \mathcal{R}_g \, dV \tag{1.99}$$

the subscript 0 denoting the corresponding material quantities, i.e. evaluated in $\mathbf{x}\left(\mathbf{X}, t\right)$. The differentiation of the left side of equation (1.100) together with mass balance (1.76), as well as of equations (1.97) and (1.98), gives

$$\varrho \frac{de_0}{dt} = \mathbf{P} : \dot{\mathbf{F}} + \varrho W_h - \nabla_{\mathbf{X}} \cdot \mathbf{Q}_h + \mathbf{K} \cdot \dot{\boldsymbol{\gamma}}_0 + \varepsilon_{g0} \, \varrho^{-1} \mathcal{R}_g \tag{1.100}$$

1.3.2.5 *Balance of Entropy*

The total internal dissipation per unit mass can be accounted by introducing two thermodynamic forces, say f_g and $\mathbf{f}_\gamma$ (per unit mass), respectively conjugated to the rates r_g and $\dot{\boldsymbol{\gamma}}$. In such a way, the total rate of dissipation, which is the product of the absolute temperature θ and is written down:

$$\theta \upsilon = \boldsymbol{f}_\gamma \cdot \dot{\boldsymbol{\gamma}} + f_g \rho^{-1} r_g \tag{1.101}$$

This term must be positive to be thermodynamically consistent. The second law of thermodynamics requires that the entropy production, defined as the difference between the rate of entropy and the entropy power has to be greater than zero. Thus, by indicating with s the entropy production per unit current mass, one has in the integral form that:

$$\frac{D}{Dt} \int_{\Omega} \rho s dv \geq \int_{\Omega} \rho \frac{w_h}{\theta} \, dv - \int_{\partial \Omega} \frac{1}{\theta} \mathbf{q}_h \cdot \mathbf{n} \, da + \int_{\Omega} r_g \, s \, dv + \int_{\Omega} \rho \upsilon \, dv \tag{1.102}$$

The application of the Reynolds transport theorem (1.77) to the left side of equation (1.102) and the exploitation of the mass balance (1.75) let to straightforwardly obtain:

$$\int_{\Omega} \rho \frac{ds}{dt} \, dv \geq \int_{\Omega} \rho \frac{w_h}{\theta} \, dv - \int_{\partial \Omega} \frac{1}{\theta} \mathbf{q}_h \cdot \mathbf{n} \, da + \int_{\Omega} \rho \upsilon \, dv \tag{1.103}$$

and, by means of the localization theorem, one has

$$\frac{ds}{dt} \geq -\frac{1}{\rho} \nabla_{\mathbf{X}} \cdot \left(\frac{\mathbf{q}_h}{\theta} \right) + \frac{1}{\theta} \left(w_h + \rho \, \boldsymbol{f}_\gamma \cdot \dot{\boldsymbol{\gamma}} + f_g \, r_g \right) \tag{1.104}$$

The corresponding material descriptions of (1.103) and (1.104) are respectively

$$\int_{\Omega_0} \varrho \frac{ds_0}{dt}\, dV \geq \int_{\Omega_0} \varrho \frac{W_h}{\theta}\, dV - \int_{\partial\Omega_0} \frac{1}{\theta} \mathbf{Q}_h \cdot \mathbf{N}\, dA + \int_{\Omega_0} \varrho v_0\, dV \tag{1.105}$$

$$\frac{ds_0}{dt} \geq -\frac{1}{\varrho}\nabla_\mathbf{X} \cdot \left(\frac{\mathbf{Q}_h}{\theta}\right) + \frac{1}{\theta}\left(W_h + \varrho\,\boldsymbol{F}_\gamma \cdot \dot{\boldsymbol{\Gamma}} + F_g\,\mathcal{R}_g\right) \tag{1.106}$$

in which s_0 is the entropy per unit reference mass, while $\boldsymbol{\Gamma} = J\boldsymbol{\gamma}$, $F_g = f_g\left(\mathbf{x}\left(\mathbf{X}, t\right), t\right)$ and $\boldsymbol{F}_\gamma = \boldsymbol{f}_\gamma\left(\mathbf{x}\left(\mathbf{X}, t\right), t\right)$.

1.3.2.6 *Combined energy and entropy equations*

It is convenient to express the local energy and entropy equations in a quasi-isothermal case:

$$\rho \frac{de}{dt} = \boldsymbol{\sigma} : \mathbf{D} + \rho\,w_h - \nabla_\mathbf{x} \cdot \mathbf{q}_h + \mathbf{k} \cdot \dot{\boldsymbol{\gamma}} + \varepsilon_g\,\rho^{-1}\,r_g \tag{1.107}$$

$$\rho\theta \frac{ds}{dt} \geq -\nabla_\mathbf{x} \cdot \mathbf{q}_h + \rho w_h + \rho\boldsymbol{f}_\gamma \cdot \dot{\boldsymbol{\gamma}} + f_g\,r_g \tag{1.108}$$

$$\varrho \frac{de_0}{dt} = \mathbf{P} : \dot{\mathbf{F}} + \varrho W_h - \nabla_\mathbf{X} \cdot \mathbf{Q}_h + \mathbf{K} \cdot \dot{\boldsymbol{\gamma}}_0 + \varepsilon_{g0}\,\varrho^{-1}\,\mathcal{R}_g \tag{1.109}$$

$$\varrho\theta \frac{ds_0}{dt} \geq -\nabla_\mathbf{X} \cdot \mathbf{Q}_h + \varrho W_h + \varrho\boldsymbol{F}_\gamma \cdot \dot{\boldsymbol{\Gamma}} + F_g\,\mathcal{R}_g \tag{1.110}$$

By now subtracting (1.108) from energy equation (1.107), it follows that

$$\rho\left(\frac{de}{dt} - \theta\frac{ds}{dt}\right) \leq \boldsymbol{\sigma} : \mathbf{D} + \left(\mathbf{k} - \rho\boldsymbol{f}_\gamma\right) \cdot \dot{\boldsymbol{\gamma}} + \left(\varepsilon_g - \rho\,f_g\right)r_g \tag{1.111}$$

Then, on the left side of equation (1.111), the Helmholtz free-energy per unit volume $\psi = \rho(e - \theta s)$ can be readily recognized, thus obtaining the Clausius-Duhem inequality

$$\frac{d\psi}{dt} \leq \boldsymbol{\sigma} : \mathbf{D} + \left(\mathbf{k} - \rho\boldsymbol{f}_\gamma\right) \cdot \dot{\boldsymbol{\gamma}} + \left(\varepsilon_g - \rho\,f_g\right)\rho^{-1}r_g \tag{1.112}$$

In an analogous manner, the material rate of free energy is obtained by combining (1.110) and (1.109):

$$\frac{d\psi_0}{dt} \leq \mathbf{P} : \dot{\mathbf{F}} + \left(\mathbf{K} - \varrho\boldsymbol{F}_\gamma\right) \cdot \dot{\boldsymbol{\Gamma}} + \left(\varepsilon_{g0} - \varrho\,F_g\right)\varrho^{-1}\mathcal{R}_g \tag{1.113}$$

Therefore, provided the set of the state variable on which the internal energy depends, suitable constitutive relations are obtained through direct comparison. Moreover, in what follows, isothermal processes will be conveniently assumed.

1.4 CONSTITUTIVE EQUATIONS

Constitutive relations are introduced to take into account the material-specific mechanical response. In order to deal with biomechanical problems, growth and remodelling terms are still considered and the kinematical multiplicative decomposition of the deformation gradient (1.31) can be employed. Then, in defining the *internal variables*, the free energy function will clearly depend upon the elastic part of the

deformation, as well as to other structural internal variables such as the remodelling ones. Besides the concept of internal variables, two further important principles for the construction of material equations are the *principle of material objectivity* and the *principle of material symmetry.*

The principle of material objectivity affirms that constitutive equations are invariant with respect to the observer. In other words, $\psi\left(\mathbf{QF}\right) = \psi\left(\mathbf{F}\right), \forall \mathbf{Q} \in \text{Orth}^+$. Observing that the Cauchy-Green tensor (as well as other purely Lagrangian and Eulerian strain measures) is free from rigid body motions, and so it might be reasonable to formulate constitutive equations in terms of this strain measure (or the others), this implying $\psi = \psi\left(\mathbf{C}\right)$ (or equivalently $\psi = \psi\left(\mathbf{b}\right)$).

The principle of material symmetry states that constitutive equations have to be invariant with respect to all transformations of the material coordinates, which belong to the symmetry group $\mathcal{G}_k$ of the underlying material. In other words, if one considers a material coordinate transformation, say $\mathbf{X}^* = \mathbf{QX}, \quad \forall \mathbf{Q} \in \mathcal{G}_k$, the corresponding deformation gradient and right Cauchy-Green tensor read as

$$\mathbf{F}^* = \frac{\partial \mathbf{x}}{\partial \mathbf{X}^*} = \mathbf{FQ} \qquad \mathbf{C}^* = (\mathbf{F}^*)^\mathsf{T} \mathbf{F}^* = \mathbf{Q}^\mathsf{T} \mathbf{C} \mathbf{Q} \tag{1.114}$$

Provided that the second Piola-Kirchhoff stress $\mathbf{S}$ is work-conjugate with $\mathbf{C}$, the material symmetry requires that

$$\psi\left(\mathbf{C}\right) = \psi\left(\mathbf{Q}^\mathsf{T} \mathbf{C} \mathbf{Q}\right) \quad \text{and} \quad \mathbf{S}\left(\mathbf{C}\right) = \mathbf{S}\left(\mathbf{Q}^\mathsf{T} \mathbf{C} \mathbf{Q}\right), \quad \forall \mathcal{G}_k \subseteq \text{Orth} \tag{1.115}$$

Consequently, *isotropic materials* is defined as the class of materials for which $\mathcal{G}_k = \text{Orth}$, and characterizes the materials whose response is the same in all directions.

If volumetric growth is now accounted, and by virtue of objectivity, it is convenient to consider the Helmoltz free energy ψ as a function of the elastic Cauchy-Green tensor $\mathbf{C}_e$ and of the remodelling parameters. In this case the tensor $\mathbf{C}_e$ is defined on the grown intermediate configuration, and thus it is not in its Lagrangian description. Then, the relationship $\overset{\circ}{\mathbf{C}}_e = \mathbf{R}_g^\mathsf{T} \mathbf{C}_e \mathbf{R}_g$ is utilized to describe $\mathbf{C}_e$ with respect to the initial configuration. Also, the following relation has to be considered in expressing the reference specific free energy:

$$\int_{\Omega_g} \psi\left(\mathbf{C}_e, \boldsymbol{\gamma}_g\right) dV^g = \int_{\Omega_0} J_g \psi(\overset{\circ}{\mathbf{C}}_e, \boldsymbol{\Gamma}) dV^0 \tag{1.116}$$

with $\boldsymbol{\gamma}_g = J_e \boldsymbol{\gamma}$. Therefore the relation $\psi_0 = J_g \psi$ (the overset symbol will be avoided in what follows for the sake of clarity). Also, by taking into account the identity $\dot{\mathbf{E}} = \frac{1}{2}\dot{\mathbf{C}} = \mathbf{F}^\mathsf{T} \mathbf{dF}$ one can write

$$\frac{1}{2}\mathbf{S} : \dot{\mathbf{C}} = \boldsymbol{\tau} : \mathbf{d} = \mathbf{P} : \dot{\mathbf{F}} \tag{1.117}$$

The latter relation, together with (1.116), are inserted into (1.113) in a way to have

$$J_g \dot{\psi} + \psi \dot{J}_g \leq \frac{1}{2}\mathbf{S} : \dot{\mathbf{C}} + (\mathbf{K} - \varrho \boldsymbol{F}_\gamma) \cdot \dot{\boldsymbol{\Gamma}} + (\varepsilon_{g0} - \varrho F_g) \varrho^{-1} \mathcal{R}_g \tag{1.118}$$

by also taking into account the multiplicative decomposition of the deformation gradient (1.31), it is possible to write $\mathbf{C} = \mathbf{F}_g^{\mathsf{T}}\mathbf{C}_e\mathbf{F}_g$ in a way that

$$J_g\frac{\partial\psi}{\partial\mathbf{C}_e} : \dot{\mathbf{C}}_e + J_g\frac{\partial\psi}{\partial\mathbf{\Gamma}} : \dot{\mathbf{\Gamma}} + J_g\psi\mathbf{I} : \mathbf{L}_g \leq \frac{1}{2}\mathbf{S} : \left(\dot{\mathbf{F}}_g^{\mathsf{T}}\mathbf{C}_e\mathbf{F}_g + \mathbf{F}_g^{\mathsf{T}}\mathbf{C}_e\dot{\mathbf{F}}_g + \mathbf{F}_g^{\mathsf{T}}\dot{\mathbf{C}}_e\mathbf{F}_g\right) +$$
$$+ (\mathbf{K} - \varrho\mathbf{F}_\gamma)\cdot\dot{\mathbf{\Gamma}} + (\varepsilon_{g0} - \varrho\,F_g)\,\varrho^{-1}\mathcal{R}_g \quad (1.119)$$

or, since the symmetry of the second Piola-Kirchhoff tensor,

$$J_g\frac{\partial\psi}{\partial\mathbf{C}_e} : \dot{\mathbf{C}}_e + J_g\frac{\partial\psi}{\partial\mathbf{\Gamma}} : \dot{\mathbf{\Gamma}} + J_g\psi\mathbf{I} : \mathbf{L}_g \leq \mathbf{S} : \mathbf{F}_g^{\mathsf{T}}\mathbf{C}_e\dot{\mathbf{F}}_g + \frac{1}{2}\mathbf{S} : \mathbf{F}_g^{\mathsf{T}}\dot{\mathbf{C}}_e\mathbf{F}_g +$$
$$+ (\mathbf{K} - \varrho\mathbf{F}_\gamma)\cdot\dot{\mathbf{\Gamma}} + (\varepsilon_{g0} - \varrho\,F_g)\,\varrho^{-1}\mathcal{R}_g \quad (1.120)$$

Now, focusing on the last term of (1.120), two considerations can be introduced. By first observing that the adaptation (elastic) path of the deformation is mass preserving (i.e. there is no growth/resorption during elastic deformation), the hypothesis

$$dm = dm^g, \qquad J\rho = J_g\rho_g \quad (1.121)$$

can be introduced, with ρ_g being the body true density in the grown configuration, and mass balance (1.72) can be rewritten as

$$\rho_g\,J_g = \rho^0 + \int_{t_i}^{t} \mathcal{R}_g\,d\tau \quad (1.122)$$

It is reasonable now to assume that density does not change during mass growth (meaning that growth is purely volumetric), implying that $\rho_g = \rho^0$. It follows that, by differentiating with respect to time

$$J_g = 1 + \frac{1}{\rho^0}\int_{t_i}^{t}\mathcal{R}_g\,d\tau, \quad \dot{J}_g = \frac{1}{\rho^0}\mathcal{R}_g, \quad J_g\mathbf{I} : \mathbf{L}_g = \frac{1}{\rho^0}\mathcal{R}_g \quad (1.123)$$

in which the relation $\dot{J}_g = J_g\,tr(\mathbf{L}_g)$ has been used. Also, from the mass balance (1.76), in the light of the present substitutions one has

$$\frac{d(J\rho)}{dt} = \rho^0\dot{J}_g, \qquad \dot{\rho} + \rho\,tr(\mathbf{L}_e) = 0, \quad \text{or} \quad \frac{\dot{\rho}}{\rho} = -\frac{\dot{J}_e}{J_e} \quad (1.124)$$

which coherently describes the change of density throughout the elastic adaptation path of the whole deformation, implying that a direct relationship between elastic expansion and density rarefaction (and contrarily, elastic compression implies local densification).
Substitution of (1.123) into (1.120) let to collect the various terms

$$\left(\frac{1}{2}\mathbf{F}_g\mathbf{S}\mathbf{F}_g^{\mathsf{T}} - J_g\frac{\partial\psi}{\partial\mathbf{C}_e}\right) : \dot{\mathbf{C}}_e + \left(\mathbf{K} - J_g\frac{\partial\psi}{\partial\mathbf{\Gamma}} - \varrho\mathbf{F}_\gamma\right)\cdot\dot{\mathbf{\Gamma}} +$$
$$+ \left(J_g\left(\frac{\rho^0}{\varrho}\varepsilon_{g0} - \psi\right)\mathbf{I} + \mathbf{F}_g\mathbf{S}\mathbf{F}_g^{\mathsf{T}}\mathbf{C}_e - J_g\,\rho^0\,F_g\mathbf{I}\right) : \mathbf{L}_g \geq 0 \quad (1.125)$$

This method, also known as Coleman's method (see), let to derive through direct comparison the elastic stress response for the present case, as well as an expression for the thermodynamic forces above postulated. More precisely, for the first two brackets:

$$\mathbf{S} = 2J_g\mathbf{F}_g^{-1}\frac{\partial\psi}{\partial\mathbf{C}_e}\mathbf{F}_g^{-\mathsf{T}} = J_g\mathbf{F}_g^{-1}\mathbf{S}_e\mathbf{F}_g^{-\mathsf{T}} = 2\frac{\partial\psi_0}{\partial\mathbf{C}} \tag{1.126}$$

$$\tilde{\boldsymbol{F}}_\gamma = \mathbf{K} - J_g\frac{\partial\psi}{\partial\boldsymbol{\Gamma}} \tag{1.127}$$

the tilde indicating the quantity expressed per unit volume. It is clear that the stress emerges, as known, as a response of the material to a deformation process which induces a change of the *strain energy density*. The thermodynamic force $\tilde{\boldsymbol{F}}_\gamma$ can be interpreted as a driving force guiding the remodeling process and takes into account the effect of a referential force $\mathbf{K}$ with respect to which a certain aliquota of energy is spent for kindling the remodelling process. With attention on the thermodynamic force associated to growth, the substitution of (1.126) into the last term of equation (1.125) let to derive:

$$\boldsymbol{\mathcal{F}}_g = \mathbf{S}_e\mathbf{C}_e + \left(\frac{\rho^0}{\varrho}\varepsilon_{g0} - \psi\right)\mathbf{I} \tag{1.128}$$

with the position $\boldsymbol{\mathcal{F}}_g = \rho^0\,F_g\mathbf{I}$. It follows that the thermodynamic force associated to growth, i.e. thermodynamically conjugated to the growth deformation gradient velocity $\mathbf{L}_g$, are inevitably associated to the *change of configuration*. The physical quantity underlying this change of natural configuration is called *configurational stress* and can be expressed in terms of an Eshelby-like stress tensor $\boldsymbol{\Sigma}$, as defined by Cgurtin [79], for example. A suitable definition for the configurational stress, responsible in this case of the domain variations induced by the volumetric growth, has been given by Maugin [133] and it is in this case related to $\boldsymbol{\mathcal{F}}_g$ through

$$\boldsymbol{\Sigma} = -\boldsymbol{\mathcal{F}}_g = \left(\psi - \frac{\rho^0}{\varrho}\varepsilon_{g0}\right)\mathbf{I} - \mathbf{S}_e\mathbf{C}_e \tag{1.129}$$

Remarks

The expression for the first Piola Kirchhoff stress tensor can be obtained by considering relation (1.71) in conjunction with (1.126). The other stress measures are:

$$\mathbf{P} = \mathbf{FS} = 2J_g\mathbf{F}_e\frac{\partial\psi}{\partial\mathbf{C}_e}\mathbf{F}_g^{-\mathsf{T}} = J_g\frac{\partial\psi}{\partial\mathbf{F}_e}\mathbf{F}_g^{-\mathsf{T}} \tag{1.130}$$

$$\boldsymbol{\tau} = \mathbf{P}\mathbf{F}^\mathsf{T} = J_g\frac{\partial\psi}{\partial\mathbf{F}_e}\mathbf{F}_e^\mathsf{T} \tag{1.131}$$

$$\boldsymbol{\sigma} = J^{-1}\boldsymbol{\tau} = J_e^{-1}\frac{\partial\psi}{\partial\mathbf{F}_e}\mathbf{F}_e^\mathsf{T} \tag{1.132}$$

Furthermore, standard stress-strain relations can be obtained by opportunely depriving balances (1.107)–(1.110) of the growth- and remodelling-related terms, or by

vanishing growth deformation form equations (1.126), (1.130)–(1.132) (i.e. by imposing $\mathbf{F}_g = \mathbf{I}$):

$$\mathbf{S} = 2\frac{\partial\psi}{\partial\mathbf{C}} = \frac{\partial\psi}{\partial\mathbf{E}} \tag{1.133}$$

$$\mathbf{P} = \mathbf{F}\mathbf{S} = \frac{\partial\psi}{\partial\mathbf{F}} \tag{1.134}$$

$$\boldsymbol{\tau} = \mathbf{P}\mathbf{F}^\mathsf{T} = \frac{\partial\psi}{\partial\mathbf{F}}\mathbf{F}^\mathsf{T} \tag{1.135}$$

$$\boldsymbol{\sigma} = J^{-1}\boldsymbol{\tau} \tag{1.136}$$

All these stress measures are in accord with the Hill's [84] general definition:

$$\boldsymbol{\tau} : \mathbf{d} = \mathbf{S}^{(m)} : \mathbf{E}^{(m)} \tag{1.137}$$

where $\mathbf{E}^{(m)}$ is the Hill strain family (1.24). Therefore the first Piola-Kirchhoff tensor is work-conjugate with $\mathbf{F}$ (they are both two-point tensors), the second Piola-Kirchhoff stress $\mathbf{S}$ is work-conjugate with $\mathbf{E}^{(2)}$, and each stress has a *unique* counterpart. For the sake of completeness, it is here then reported the expression of the stress tensor $\mathbf{T}$ conjugate to the Hencky strain ([86]):

$$\mathbf{T}^{(0)} = \mathbb{A}^{-1} : (\mathbf{R}^\mathsf{T}\boldsymbol{\tau}\mathbf{R}) \tag{1.138}$$

where $\mathbb{A}$ is a fourth-order structure tensor defined such as:

$$\mathbb{A} = \sum_{i=1}^{3}\mathbf{M}_i \otimes \mathbf{M}_i + \sum_{\substack{i,j=1 \\ i \neq j}}^{3}\frac{2\lambda_i\lambda_j\ln(\frac{\lambda_i}{\lambda_j})}{\lambda_i^2 - \lambda_j^2}\mathbf{M}_i \otimes \mathbf{M}_j, \tag{1.139}$$

with the second order tensors $\mathbf{M}_i$, $i = \{1,2,3\}$ being defined through the eigenvectors $\mathbf{N}_i$, in a way that $\mathbf{M}_i\mathbf{M}_j = \delta_{ij}\mathbf{M}_i$ and $\sum_{i=1}^{3}\mathbf{M}_i = \mathbf{I}$. Relationship (1.138) can be easily established starting from equality (1.137) and observing that, through direct comparison, the rate matrices $\mathbf{D}$ in (1.54) and $\dot{\mathbf{H}}$ in (1.61) can be related each other by the matrix $\mathbb{A}$, i.e. $\dot{\mathbf{H}} = \mathbb{A} : \mathbf{D}$ (for a more detailed derivation see also Hoger [86] and Itskov [100]). In case the stress $\mathbf{T}^{(0)}$ and $\mathbf{U}$ (thus $\mathbf{H}$) are coaxial, $\mathbf{T}^{(0)}$ admits the following representation

$$\mathbf{T}^{(0)} = T_i\mathbf{N}_i \otimes \mathbf{N}_i \tag{1.140}$$

where T_i denote the principal stresses. In this case only the first term of (1.139) actually is needed and follows that

$$\mathbf{T}^{(0)} = (\mathbf{R}^\mathsf{T}\boldsymbol{\tau}\mathbf{R}) \tag{1.141}$$

Furthermore, if deformation is homothetic and no rotations occur, one has the Hencky strain actually conjugated with the Kirchhoff stress:

$$\mathbf{T}^{(0)} = \frac{\partial\psi}{\partial\mathbf{H}} = \boldsymbol{\tau} \tag{1.142}$$

By finally recalling (1.27), the following relations hold

$$\boldsymbol{\tau}^{(0)} = \mathbf{R}\mathbf{T}^{(0)}\mathbf{R}^\mathsf{T} = \mathbb{A}\boldsymbol{\tau} = \frac{\partial\psi}{\partial\mathbf{h}}, \tag{1.143}$$

$$\boldsymbol{\tau}^{(0)} = \boldsymbol{\tau} \tag{1.144}$$

the second relation being obtained in case that $\mathbf{V}$ and $\boldsymbol{\tau}^{(0)}$ share the same eigenvectors.

1.5   SPECIAL CONSTITUTIVE MODELS FOR ISOTROPIC HYPERELASTICITY

Some of the most frequently used hyperelastic models are briefly recalled below. As a direct consequence of the frame indifference, the strain energy functions will exclusively depend on the invariants of the strain measure adopted.

1.5.1   *St. Venant-Kirchhoff model*

The St. Venant-Kirchhoff model represents one of the simplest hyperelastic material model involving two sole material constants, here given in terms of terms of Lamé moduli Λ and μ:

$$\psi = \frac{1}{2}\mathbf{E} : \mathbb{C} : \mathbf{E} = \frac{\Lambda}{2}\left(tr(\mathbf{E})\right)^2 + \mu\, tr(\mathbf{E}^2) \tag{1.145}$$

The fourth-order tensor $\mathbb{C} = 2\mu\mathbb{I} + \Lambda\,\mathbf{I}\otimes\mathbf{I}$ denotes the *stiffness tensor*. It follows that

$$\mathbf{S} = \frac{\partial\psi}{\partial\mathbf{E}} = 2\mu\,\mathbf{E} + \Lambda\,tr(\mathbf{E})\mathbf{I} \tag{1.146}$$

Under the assumption of small strains this model gives the well-known generalized Hooke's law

$$\boldsymbol{\sigma} = 2\mu\,\boldsymbol{\epsilon} + \Lambda\,tr(\boldsymbol{\epsilon})\mathbf{I} \tag{1.147}$$

1.5.2   *Ogden incompressible materials. Mooney-Rivlin and Neo-Hookean models*

In the context of rubber-like materials, for which a substantial incompressibility occur, i.e. $J = \lambda_1\lambda_2\lambda_3 = 1$, Ogden [87, 148] postulated the following phenomenological strain energy function, given in terms of the principal stretches:

$$\psi = \psi\left(\lambda_1, \lambda_2, \lambda_3\right) = \sum_{p=1}^{N} \frac{\mu_p}{\alpha_p}\left(\lambda_1^{\alpha_p} + \lambda_2^{\alpha_p}\right) + \lambda_3^{\alpha_p} - 3 \tag{1.148}$$

On comparison with linear elastic material coefficients, the Ogden model parameters have to satisfy to the consistency conditions:

$$\sum_{p=1}^{N} \mu_p\alpha_p = 2\mu, \qquad \mu_p\alpha_p > 0, \qquad p = 1, ..., N \tag{1.149}$$

By setting $N = 1$, $\alpha_1 = 2$ the so called Neo-Hookean material is found

$$\psi = \frac{\mu_1}{2}\left(\lambda_1^2 + \lambda_2^2 + \lambda_3^2 - 3\right) = c_1\left(I_1(\mathbf{C}) - 3\right) \tag{1.150}$$

while, for $N = 2$, $\alpha_1 = 2$ and $\alpha_2 = -2$, the Mooney-Rivlin model is obtained:

$$\psi = \frac{\mu_1}{2}\left(\lambda_1^2 + \lambda_2^2 + \lambda_3^2 - 3\right) - \frac{\mu_2}{2}\left(\lambda_1^{-2} + \lambda_2^{-2} + \lambda_3^{-2} - 3\right) =$$
$$= c_1\left(I_1(\mathbf{C}) - 3\right) + c_2\left(I_2(\mathbf{C}) - 3\right) \tag{1.151}$$

1.5.3 *Fung model*

In relation to the modelling of biological soft materials, which typically exhibit an exponential like stress-strain response, Fung successfully proposed [46, 69] the following strain energy function, constituted of a bilinear standard term and an exponential term:

$$\psi = \frac{1}{2}\mathbf{E} : \mathbb{A} : \mathbf{E} + \frac{c}{2}\left[\exp\left(\mathbf{E} : \mathbb{B} : \mathbf{E}\right) - 1\right] \tag{1.152}$$

The stresses are calculated from the strain energy function as

$$\mathbf{S} = \frac{\partial \psi}{\partial \mathbf{E}} = \mathbb{A} : \mathbf{E} + c(\mathbb{B} : \mathbf{E})\,e^{(\mathbf{E}:\mathbb{B}:\mathbf{E})} \tag{1.153}$$

The Fung-model, under the simplified isotropic hypothesis, can be written in terms the principal stretches as:

$$\psi = \frac{1}{2}a\left(\lambda_1^2 + \lambda_2^2 + \lambda_3^2 - 3\right) + \frac{c}{2}\left[\exp\left(b\left(\lambda_1^2 + \lambda_2^2 + \lambda_3^2 - 3\right)\right) - 1\right] \tag{1.154}$$

in the sole material constants a,b and c.

APPENDIX

Invariants and their tensor-derivatives:

Given generic second-order tensor $\mathbf{A}$, its *invariants* are defined as:

$$I_1\left(\mathbf{A}\right) = \operatorname{tr}\left(\mathbf{A}\right) = \mathbf{A} : \mathbf{I}$$

$$I_2\left(\mathbf{A}\right) = \frac{1}{2}\left[\left(\operatorname{tr}\left(\mathbf{A}\right)\right)^2 - \operatorname{tr}\left(\mathbf{A}^2\right)\right]$$

$$I_3\left(\mathbf{A}\right) = \det\left(\mathbf{A}\right)$$

and the derivatives of these invariants with respect to $\mathbf{A}$ are

$$\frac{\partial\, I_1}{\partial \mathbf{A}} = \mathbf{I}$$

$$\frac{\partial\, I_2}{\partial \mathbf{A}} = I_1\mathbf{I} - \mathbf{A}^{\mathsf{T}}$$

$$\frac{\partial\, I_3}{\partial \mathbf{A}} = \det\left(\mathbf{A}\right)\mathbf{A}^{-\mathsf{T}}$$

SPECIES GROWTH AND VOLTERRA-LOTKA SYSTEMS

Turning point of the study of population dynamics in the early 20th can be *sine dubio* attributed to A.J. Lotka, an American byophisicist and a statistician, and V. Volterra, one of the most important Italian mathematicians.

Volterra and Lotka had physics as a reference, but did not consider *only* mechanics: they both took also into account the energetic approach of thermodynamics, and in fact, considered evolution as the expression of the second law of thermodynamics [98]. In the following, some global properties of Volterra-Lotka approach and its extensions are briefly treated in order to then transpose this exact logic to the modelling of tissues constituents.

2.1 INTRODUCTION

Elements of Physical Biology (1925, [115]) by Lotka is actually the first book on mathematical biology. In its pages, Lotka described his view of nature as a complex system plentiful of "energy transformers", in which natural selection was the result of the struggle among living organisms to ensure themselves the available energy: species that survive and prosper are those that maximize both the rate at which resources are procured and the effectiveness with which this resources are used and converted into gain (offspring). In particular, among other considerations, the book presented a mathematical model regarding the interaction of two animal species, one of which was the parasite of the other, inspired to chemical reaction systems. Lotka then extended his energetic framework to human society, in demographic studies and economics. In the same period, and in a completely independent manner, Volterra published his first result on variations and fluctuations of animal species living together (*Variazioni e fluttuazioni del numero d'individui in specie animali conviventi* [206]). He was requested to investigate the possible reasons concealing behind the increase in fish population of Selachians and other predators in the Adriatic Sea during World War 1 as compared with the preceding and following periods, as well as the decrease in their prey, which feed on vegetables or invertebrates. Differently from Lotka, Volterra intuition exclusively arose from biological considerations related to the observation of the biosystem. However, the *rationale* on which Volterra founded his view of nature is completely analogous. In the essay *Una teoria matematica sulla lotta per l'esistenza*[204], he explains that biocenosis, i.e. the community inhabiting the ecosystem, is constituted of more species interacting together. Ordinarily, individuals of a certain species fight for the same amount of food or some species live at the expense of other species of which they feed. Of course, some species can also cooperate and benefit each other. The combination of these factors resides in what Volterra calls *the fight for life*, and it quantitatively manifests in fluctuations of species individuals, as well as, under different conditions, in the extinction or uncontrolled growth (*Mathematical Theory of Struggle for Existence*[205]). This analysis represented to Volterra the mathematical form to Darwin's intuition of phenomena of vital competition. The result is the model

which is nowadays known as Volterra-Lotka (VL) equations, treated in the following, and a particular well-known case in the *predator-prey model*. This model provides a generalization of the Verhulst logistic model by accounting for the effects that the "encounters" among species individuals produce, following the hypothesis that predation is directly proportional to the rate of encountering between two different species individuals. The early model was then refined and sophisticated by Volterra, also in correspondence with Lotka, in collaboration with other scientists such as U. D'Ancona (zoologist, Volterra's collaborator and future son-in-law). It is worth noting that the intuition and the logic on which the VL equations found represent *de facto* the progenitor of the modern Evolutionary Game Theory (EGT) introduced by J.M. Smith and the renowned Nash *equilibria games*. In fact, EGT extended the classical game theory between two or more players to study the behavior of large populations that repeatedly engage in strategic interactions, on which the survivor of a population depend. The most of interaction is based on the idea that the current state of a player depends on the presence of the other players. In brief, in classical games (single round or repetitive) each player is *rational* as he considers the opponents strategies in making appropriate choices for maximizing *utilities*. In EGT, it is only required player to have a strategy (sometimes unwillingly, depending on its natural attitude). This strategy is known as *fitness function* and often depends on other players in the game. In case of natural selection, another hypothesis players (animals) do not choose their strategy or have the ability to change it, they are born with a strategy and their offspring will inherit that same identical strategy. As a result, the organism with the best interaction strategy can have the highest fitness and increase their ability to reproduce.

2.2 SIMPLE-SPECIES GROWTH

In particular, Volterra himself remarked that the model of unbounded growth of a population N with proliferation rate $\varepsilon > 0$

$$\frac{dN}{dt} = \varepsilon\, N, \qquad N(t) = N_0 e^{\varepsilon\, t} \tag{2.1}$$

was "unacceptable for biologists" [98] and mathematically unstable (the case $\varepsilon < 0$ is instead related to the so-called exponential decay). A first simple development of this model can be introduced by considering the (negative) influence of the number of individuals through another characteristic coefficient λ

$$\frac{dN}{dt} = (\varepsilon - \lambda N)\, N, \qquad N(t) = \frac{\varepsilon N_0 e^{\varepsilon\, t}}{\varepsilon + \lambda\, N_0\, (e^{\varepsilon\, t} - 1)} \tag{2.2}$$

where N_0 is the initial number of individuals, this solution highlighting a species in a given environment develop more realistically until its density distribution approaches values that modify the conditions of life. The maximum number of individuals potentially sustainable by the environment is $\lim_{t\to\infty} N(t) = \varepsilon/\lambda$; in the VL sense, the coefficient λ can be also viewed as the weight of the influence that individuals of a species exert on their similar. In a general case of more species, the extension of the idea of the simple species logistic behavior lies on the fundamental hypothesis of the existence of a certain interaction bond between two or more of them, or, as Volterra

says using a mechanical analogy, *a growth under "friction" among individuals of every single species.*

2.3 MULTIPLE SPECIES SYSTEMS

A dynamical system can be in general written in the form

$$\dot{\mathbf{x}} = \mathbf{x} \boldsymbol{f}(\mathbf{x}), \qquad \dot{x}_i = f_i(x_1, ..., x_n) \tag{2.3}$$

where $i = 1, .., n$ and $f_i : \mathbb{R}^n \to \mathbb{R}^n$ is $\mathcal{C}^1$. It can be demonstrated that populations that start from non-negative values remain non-negative. Volterra-Lotka system are of the type $\boldsymbol{f} = \mathbf{b} + \mathbf{A}\mathbf{x}$, where $\mathbf{b}$ is a $n-$dimensional vector collecting the intrinsic rates of each species x_i, while $\mathbf{A}$ is a $n \times n$ matrix collecting the inter-species weight coefficient, such that

$$\dot{\mathbf{x}} = \mathbf{x} \left(\mathbf{b} + \mathbf{A}\mathbf{x} \right), \qquad \dot{x}_i = b_i \, x_i + \sum_{j=1}^{n} \alpha_{ij} \, x_j, x_i \tag{2.4}$$

In this form, if $\alpha_{ij} < 0$ systems are known as *competitive systems* and each species competes with all others including itself; contrarily, if $\alpha_{ij} \geq 0, \, i \neq j$ the system is denoted as a *cooperative system* in the sense that each species enhance the other species growth. The terms α_{ii} represent competition between members of the same population and are known as *intraspecific* terms. The main interesting properties of VL systems can be discussed by literally constructing the more general case (2.6) starting from the simplest *two species model* up to the more sophisticated models.

2.3.1 *The predator-prey model*

The simplest VL model, which is the one originally presented by both the scientists, is the so-called *predator-prey model*. It is constituted of a couple of ordinary and non-linear differential equations. In his work [206], Volterra denoted by x the density of preys and by y that of predators. He assumed that, in absence of predators, preys tend to grow with a certain positive rate $a > 0$ and the influence parameter (intro-duced above with respect to a single species in (2.2)) –say b– is in this case related to the encounter of the predator y, whose presence then acts negatively on the prolif-eration of the species x. With regard to the predators, it is assumed that they decay exponentially with rate c when preys run out, while their growth will be weighted by the encounters with the preys through an opportune predation rate d. The following system of differential equations is then obtained:

$$\begin{cases} \dot{x} = x \, (a - b \, y) \\ \dot{y} = y \, (-c + d \, x) \end{cases} \quad , \qquad \mathbf{b} = \begin{bmatrix} a \\ -c \end{bmatrix}, \quad \mathbf{A} = \begin{bmatrix} 0 & -b \\ d & 0 \end{bmatrix} \tag{2.5}$$

The phase space consistent with the physics of the problem is represented by the first Cartesian orthant, i.e. $\mathbb{R}_+^2 = \{\{x, y\} | x \geq 0, \, y \geq 0\}$. Three solutions can be immediately obtained. If $x(0) = y(0) = 0$, the dynamics is not kindled at all and $x(t) = y(t) = 0, \qquad \forall \, t > 0$. If only $x(0) = 0$ then $y(t) = y_0 \, e^{-ct}$, while if $y(0) = 0$

then $x(t) = x_0 \, e^{a\,t}$. The case $x(0) > 0$ and $y(0) > 0$ remains to be discussed. It can be seen from (2.16) that, for the particular values $x^* = c/d$ and $y^* = a/b$, species rates vanish and the density of predators and preys do not vary. The point $\{x^*, y^*\}$ is known as *stationary point* or *equilibrium point*. A system with this initial condition will remain in this state for all $t > 0$. Also, system (2.16) can be rewritten as

$$\begin{cases} \dot{x} = b\,x\,(y^* - y) \\ \dot{y} = -d\,y\,(x^* - x) \end{cases} \tag{2.6}$$

Hence, the signs of the rates $\dot{x}$ and $\dot{y}$ will depend on whether x and y are larger or smaller than x^* and y^* respectively. More precisely, the couple $\{x^*, y^*\}$ divides the phase space into four regions, and the sign pattern $\{\dot{x}, \dot{y}\}$ can be determined in each quarter through (2.6) (see Fig. 4). This operation shows that orbits $\{x(t), y(t)\}$ counter-clockwise in the phase space around the point $\{x^*, y^*\}$. Such a behavior denotes a *orbiting motion* or *periodic*, i.e. the two species have periodic solutions and oscillate around the equilibrium point. This feature can also be revealed by analyzing the stability of the equilibrium point (stability analysis will be introduced in the following; however this case can be simply illustrated). In other words, the linearized system can be obtained by means of the Jacobi Matrix. By defining also with $\mathbf{x} = \{x(t), y(t)\}$, the system (2.16) can be written in the form $\dot{\mathbf{x}} = \boldsymbol{f}(\mathbf{x})$. The linearization of the orbits around a generic state $\mathbf{x}_p$ then is described by the following linear system

$$\dot{\mathbf{x}} = \boldsymbol{J}(\mathbf{x}_p)(\mathbf{x} - \mathbf{x}_p), \qquad \boldsymbol{J}(\mathbf{x}_p) = \left.\frac{\partial \boldsymbol{f}}{\partial \mathbf{x}}\right|_{\mathbf{x}=\mathbf{x}_p} \tag{2.7}$$

where $\boldsymbol{J}(\mathbf{x}_p)$ is also known as *community matrix*. In the present case, in correspondence of $\mathbf{x}_p = \mathbf{x}^*$:

$$\boldsymbol{J}(\mathbf{x}^*) = \left.\frac{\partial \boldsymbol{f}}{\partial \mathbf{x}}\right|_{\mathbf{x}=\mathbf{x}^*} = \begin{bmatrix} a - b\,y & -b\,x \\ d\,y & d\,x - c \end{bmatrix}_{\{x=\frac{c}{d}, y=\frac{a}{b}\}} = \begin{bmatrix} 0 & -\frac{b\,c}{d} \\ \frac{d\,a}{b} & 0 \end{bmatrix} \tag{2.8}$$

By exploiting the spectral decomposition theorem, one finds that $\boldsymbol{J}(\mathbf{x}^*) = \mathbf{V}^H \boldsymbol{\Lambda} \mathbf{V}$, where $\boldsymbol{\Lambda} = \text{Diag}\{\lambda_1, \lambda_2\}$ is the matrix of the eigenvalues and $\mathbf{V}$ the corresponding eigenvectors matrix (the H denoting the hermitian matrix). In correspondence of the state $\mathbf{x}^*$, eigenvalues result imaginary and opposite in phase:

$$\lambda_1 = i\sqrt{a\,c} \qquad \lambda_2 = -i\sqrt{a\,c} \tag{2.9}$$

Since system (2.7) is linear, by performing the substitution $\mathbf{y} = \mathbf{V}(\mathbf{x} - \mathbf{x}^*)$ and by then exploiting the fundamental theorem for linear systems [150], local solution can be given in the

$$\begin{cases} \dot{\mathbf{y}} = \boldsymbol{\Lambda}\mathbf{y} \\ \mathbf{y}(0) = \mathbf{y}_0 \end{cases} \quad , \qquad \mathbf{y}(t) = e^{\boldsymbol{\Lambda}}\mathbf{y}_0 \tag{2.10}$$

which in this case gives

$$\mathbf{y}(t) = \begin{bmatrix} \cos(\sqrt{a\,c}\,t) & -\sin(\sqrt{a\,c}\,t) \\ \sin(\sqrt{a\,c}\,t) & \cos(\sqrt{a\,c}\,t) \end{bmatrix} \begin{bmatrix} y_{01} \\ y_{02} \end{bmatrix} \tag{2.11}$$

which represents a *cyclic oscillation* with no decaying (since the real part of the eigen-values (2.9) are zero), and amplitude equal to $|\mathbf{y}_0| = |\mathbf{x}_0 - \mathbf{x}^*|$. This also explains why the system is stationary if initial conditions approach the equilibrium point, as said before. Another remarkable property of this system can be derived from the direct observation of the eigenvalues (2.9): in fact, it can be noticed that $tr(\boldsymbol{J}(\mathbf{x}^*)) = 0$. This means that the *dilatation/shrinkage* of the phase space is null. Then, since dynamics preserves the phase space volume, the system under discussion is *conservative*. By definition, with reference to system (2.6), a dynamical system is conservative if there exists a matrix $\mathbf{D} > 0$ such that $\mathbf{AD}$ is skew-symmetric. In the case of (2.16), it simply results $\mathbf{D} = \text{Diag}\{d^{-1}, b^{-1}\}$, this implying the already discussed consequences.

Furthermore, analogous considerations can be made by observing that the system (2.16) is *Hamiltonian*, with $\mathcal{H}$ taken to be the Hamiltonian function. In fact the system can be written in Hamiltonian canonical form by performing the substitution $p = \log x$ and $q = \log y$. In this case one has:

$$\begin{cases} \dot{p} = \frac{\dot{x}}{x} = a - b\,e^q = \frac{\partial \mathcal{H}}{\partial q} \\ \dot{q} = \frac{\dot{y}}{y} = -c + c\,e^p = -\frac{\partial \mathcal{H}}{\partial p} \end{cases} \tag{2.12}$$

that, integrated, readily gives

$$\mathcal{H}(p, q) = a\,q - b\,e^q + d\,p - c\,e^p, \qquad \text{or} \tag{2.13}$$

$$\mathcal{H}(x, y) = d\,(x - x^* \log x) + b\,(y - y^* \log y) \tag{2.14}$$

This function remains constant along the orbit, since it is easy to verify by exploiting equations (2.6) that $\mathfrak{H}$ provides the *constant of motion*, since

$$\dot{\mathcal{H}} = d\,(x - x^*)\frac{\dot{x}}{x} + b\,(y - y^*)\frac{\dot{y}}{y} = 0 \tag{2.15}$$

This means that, since H is independent of time, the energy conserves at each time, i.e. the energy of each state $\{x(t), y(t)\}$ has the same energy at each point of the orbit, and, since orbit is closed a curve and species densities are constrained by energy to remain on this curve, it follows that *solution are periodic*.

2.3.1.1   *Dissipative associations*

Now, a first modification that can be taken into account is to relax the ideal hypothesis according to which preys growth exponentially in absence of predators. Therefore, by essentially following reasons discussed in section 2.2, luet us suppose that preys have a limited growth. This can be done by opportunely introducing a intraspecific logistic term (modeling the competition between preys for the available resources), analogously to equation (2.2). The system becomes

$$\begin{cases} \dot{x} = x\,(a - b\,y - e\,x) \\ \dot{y} = y\,(-c + d\,x) \end{cases} \tag{2.16}$$

Equilibrium points are the origin, the predators extinction and the coexistence scenario:
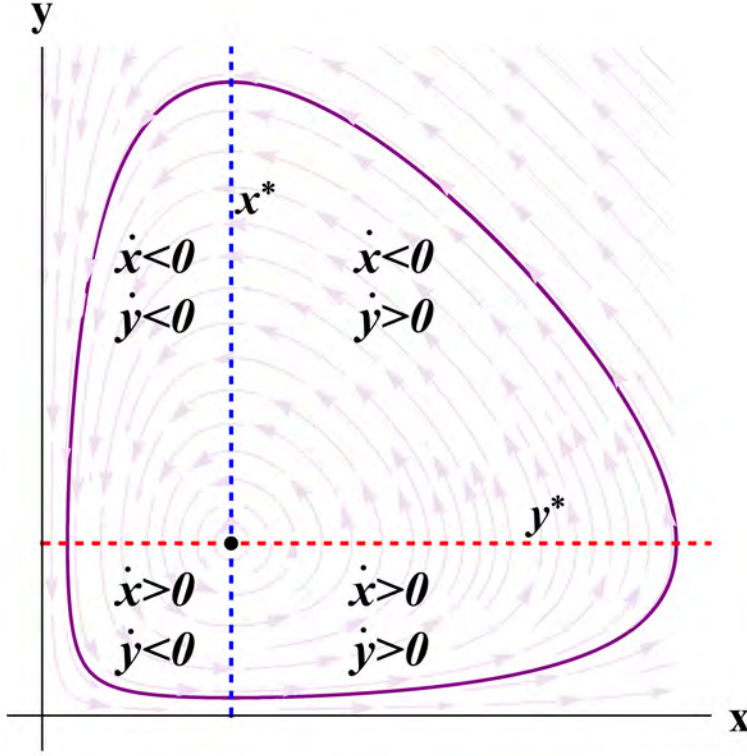
Figure 4: Phase portrait of a predator prey model.

$$P_0 = \{0,0\}, \quad P_1 = \{\frac{a}{e},0\}, \quad P_2 = \{\frac{c}{d}, \frac{a\,d - c\,e}{b\,d}\} \tag{2.17}$$

Then the community matrix will be modified by the presence of the self competition term as follows

$$\mathcal{J}(\mathbf{x}) = \begin{bmatrix} a - 2ex - by & -bx \\ dy & dx - c \end{bmatrix} \tag{2.18}$$

and the eigenvalues matrices corresponding to the rest points are in this case

$$\mathbf{\Lambda}(P_0) = \mathrm{Diag}\,\{a,\,-c\} \tag{2.19}$$

$$\mathbf{\Lambda}(P_1) = \mathrm{Diag}\left\{\frac{a\,d - e\,c}{e},\,-a\right\} \tag{2.20}$$

$$\mathbf{\Lambda}(P_2) = \mathrm{Diag}\left\{-\frac{c\,e}{2d} \pm \frac{\sqrt{\Delta}}{2d}\right\}, \tag{2.21}$$

$$\Delta = c\left(c\,e(4d + e) - 4a\,d^2\right);$$

In the light of linearized solution (2.10), we can see that the origin is unstable since possessing an unstable and a stable eigenvector: this behavior, that is analogous
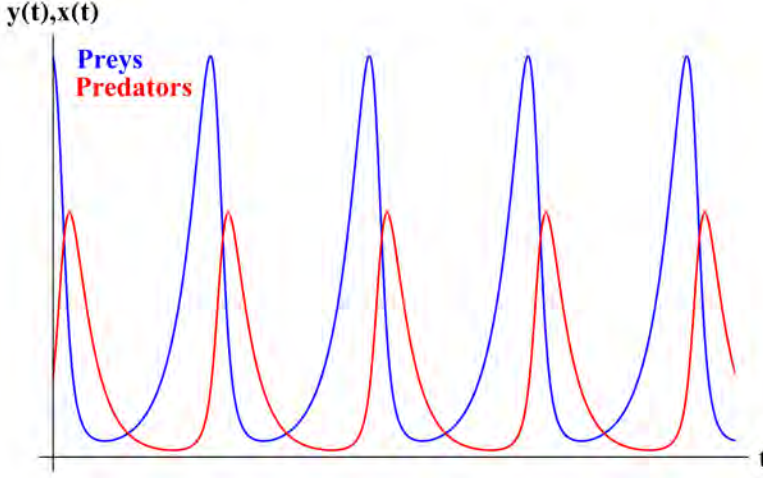
Figure 5: Periodic solutions of the predator prey model. It can be qualitatively appreci-
ated the chaining established between preys and predators, in the sense that
preys abundance calls predators, and the peak of the latter ones induces preys
plumbing.

to that one of the pure predator-prey model connotes the well known *saddle point*.
With an analogous reasoning, the prey dominance point can present a stable manifold.
This situation will occur if prcisely if $c > d(a/e)$, i.e. the predators death rate will be
greater than the predation rate, opportunely weighted by a coefficient indicating the
probability at which live preys can be encountered. Also the third point can be stable.
In particular, if $\Delta > 0$, one may have a stable coexistence if $ce > \sqrt{\Delta}$ (otherwise, a
stable and an unstable eigenvector will occur). If $\Delta < 0$ is verified, complex conjugate
eigenvalue will occur and solution of (2.10) will be

$$\mathbf{y}(t) = e^{-\frac{ce}{2d}} \begin{bmatrix} \cos(\frac{\sqrt{\Delta}}{2d}\,t) & -\sin(\frac{\sqrt{\Delta}}{2d}\,t) \\ \sin(\frac{\sqrt{\Delta}}{2d}\,t) & \cos(\frac{\sqrt{\Delta}}{2d}\,t) \end{bmatrix} \begin{bmatrix} y_{01} \\ y_{02} \end{bmatrix} \tag{2.22}$$

Hence we have an oscillating behavior, but this time, damped by a *dissipative
coefficient* equal to $tr(\Lambda(P_2)) = -ce/d$. The presence of term tells us that dynamics
do not conserve energy due to damping, and, therefore, no close orbits will occur.
Moreover, as near the state $\{x(t), y(t)\}$ is to the point P_2, the less will be its energy.
In this case the point P_2 is *asymptotically stable*.

2.3.1.2   *Volterra-Lotka competitive case*

Let us now consider, in the light of the biologically consistent considerations according
to which species growing in a confined environment fight for the same resources, the
case in which two species have similar nature and are in competition, i.e. suppose that
also the second species can generate offspring independently from the other species
and that interspecific terms are negative and indicated with c_1 and c_2. In this case
species are competitive. Also, let us introduce intraspecific coefficients, that can be
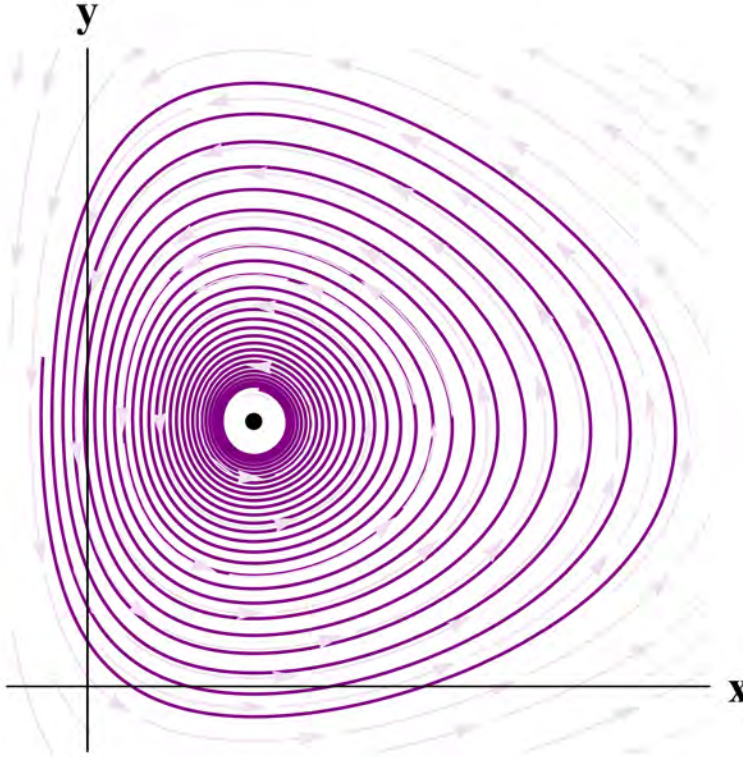
Figure 6: Phase portrait of a non-conservative orbit.

expressed in terms of the species *environmental carrying capacities*, say K_1 and K_2, which indicate the maximum density that species can achieve. Let us then express the system (2.4) in the form:

$$\begin{cases} \dot{x}_1 = b_1\, x_1 \left(1 - \frac{x_1}{K_1} - c_1\, x_2\right) \\ \dot{x}_2 = b_2\, x_2 \left(1 - c_2\, x_1 - \frac{x_2}{K_2}\right) \end{cases} \tag{2.23}$$

To simplify calculations, the substitutions $x = x_1/K_1$ and $y = x_2/K_2$, indicating with $a_{12} = c_1\, K_2$ and $a_{21} = c_2\, K_1$. Also time can be rescaled by setting $t = b_1\, t$ and $b = b_2/b_1$. This considerably reduces the number of parameters, without affecting the topology of solutions:

$$\begin{cases} \dot{x} = x\,(1 - x - a_{12}\, y) \\ \dot{y} = b\, y\,(1 - a_{21}\, x - y) \end{cases} \tag{2.24}$$

Equilibrium points can be found by vanishing rates, i.e. by imposing:

$$\begin{cases} x = 0 \\ y = 0 \end{cases} \qquad \begin{cases} r_1 : (1 - x - a_{12}\, y) = 0 \\ r_2 : (1 - a_{21}\, x - y) = 0 \end{cases} \tag{2.25}$$
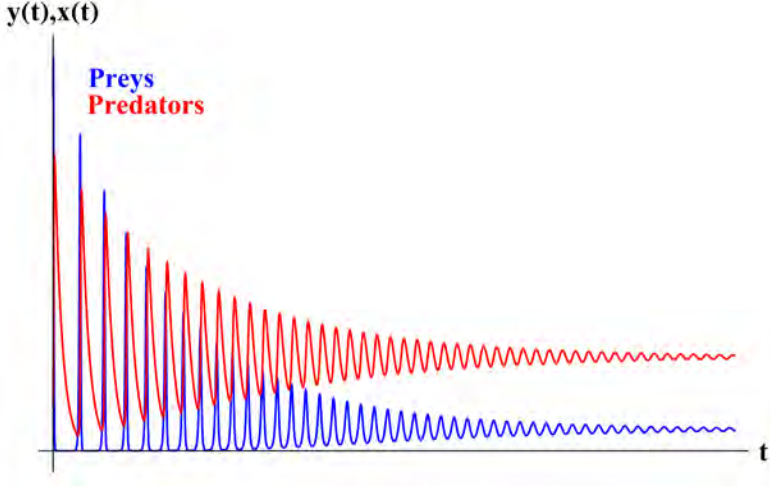
Figure 7: Oscillating solutions of the predator prey with dissipative associations. The damping effect is clearly visible. $a = 2.4$, $b = 0.45$, $c = 0.18$, $a = 0.15$, $e = 0.015$,

the lines r_1 and r_2 being denoted as *nullclines*. From (2.25) the following state $\{x^*, y^*\} \in \mathbb{R}^2_{\geq 0}$ can be individuated:

$$P_0 = \{0, 0\} \quad P_1 = \{1, 0\} \quad P_2 = \{0, 1\} \quad P_3 = \left\{ \frac{1 - a_{12}}{1 - a_{12}a_{21}}, \frac{1 - a_{21}}{1 - a_{12}a_{21}} \right\} \quad (2.26)$$

Since populations are non-negative, the existence of the last point occurs when either $a_{12} > 1$ and $a_{21} > 1$ or $a_{12} < 1$ and $a_{21} < 1$. We can then write the community matrix:

$$\mathbf{J} = \begin{bmatrix} 1 - 2x - a_{12}y & -a_{12}x \\ -a_{21}y & 1 - a_{21}x - 2y \end{bmatrix}, \quad (2.27)$$

and find that

$$\mathbf{J}(P_0) = \{1, 1\}, \quad \mathbf{J}(P_1) = \{-1, 1 - a_{21}\}, \quad \mathbf{J}(P_2) = \{-1, 1 - a_{12}\},$$
$$\mathbf{J}(P_3) = \left\{ -\frac{(1 - a_{12})(1 - a_{21})}{1 - a_{12}a_{21}}, -1 \right\}, \quad (2.28)$$

and, by studying the linearized behavior through the observartion of the eigenvalues, the system near equilibrium will behave as $\mathbf{y} = e^{\mathbf{\Lambda}}\mathbf{y}_0$ with the sole difference that $\mathbf{\Lambda} \in \mathbb{R}$ and so trajectories will either converge towards the rest point or diverge from it, depending on the sign of the eigenvalues. These considerations let to discriminate four cases of interest, also shown in Fig. 8:

1. Case $a_{12} < 1$ and $a_{21} < 1$. This is the case of weak interaction. In this case the point P_3 exists and constitutes an *attractor*, while the other 3 points are *unstable*, i.e. candidate equilibria that will not occur and energetically diverging.

2. Case $a_{12} > 1$ and $a_{21} > 1$. In this case there is aggressive competition and ultimately one population wins, while the other is driven to extinction. Then coexistence P_3 is now unstable together with the origin (unstable node), while P_1 and P_2 are stable nodes. It can be shown that the prevalence of one of these points with respect to the others depends on the initial conditions of the problem. In other words, The winner depends upon which has the starting advantage.

3. Case $a_{12} < 1$ and $a_{21} > 1$. In this case P_4 does not exist. Equivalently, this conditions says that in the phase space $r_1 > r_2$, where r_1 and r_2 have been defined in (2.25). This imply that species x has a better strategy, in the sense that for every y his rate prevail, and so the first species will in time drive the second to the extinction. In other words, x is *dominant* and P_1 is a stable node.

4. Case $a_{12} > 1$ and $a_{21} < 1$. In this case situation is inverted, since $r_2 > r_1$ and y is dominant; thus, only P_2 will constitute a stable node.

Also, it can be demonstrated that this system does not admit isolated periodic orbits.

2.4   STABILITY

In the previous section we have checked the stability of the system by analyzing only neighborhood stability against small perturbations away from equilibrium points. In the following the definition of stability and the Lyapunov criteria will be resumed. Let us consider the system (2.4)

$$\dot{\mathbf{x}} = \mathbf{x}\left(\mathbf{b} + \mathbf{A}\mathbf{x}\right), \qquad \dot{x}_i = b_i\,x_i + \sum_{j=1}^{n} a_{ij}\,x_j, x_i \tag{2.29}$$

and let the equilibrium values of the ecosystem be known, i.e.

$$\mathbf{b} = -\mathbf{A}\mathbf{x}^*, \qquad b_i = -\sum_j a_{ij}x_j^* \tag{2.30}$$

The system is said to be *Lyapunov stable* [129], if

$$\forall\,\epsilon > 0 \quad \exists\,\delta > 0 \quad : \quad ||\mathbf{x}(0) - \mathbf{x}^*|| < \delta \Rightarrow ||\mathbf{x}(t) - \mathbf{x}^*|| < \epsilon \tag{2.31}$$

This means that trajectories starting close enough to the equilibrium point (within a certain distance δ) remain close enough to the equilibrium point (within a certain distance ϵ), in case of stable system (see Fig. 10).

The equilibrium of the system (2.29) is also *asymptotically stable* if it is Lyapunov stable and

$$\exists\,\delta > 0 \quad : \quad ||\mathbf{x}(0) - \mathbf{x}^*|| < \delta \Rightarrow \lim_{t \to \infty} ||\mathbf{x}(t) - \mathbf{x}^*|| = 0 \tag{2.32}$$

this definition indicating that trajectories (starting near the equilibrium points) converge to equilibrium point. A stronger condition is the *exponential stability*, which occur when the equilibrium is asymptotically stable and $\exists\,\alpha > 0$, $\beta, \delta > 0$ such that

$$||\mathbf{x}(0) - \mathbf{x}^*|| < \delta \Rightarrow ||\mathbf{x}(t) - \mathbf{x}^*|| \leq \alpha||\mathbf{x}(t) - \mathbf{x}^*||\,e^{-\beta t}, \tag{2.33}$$
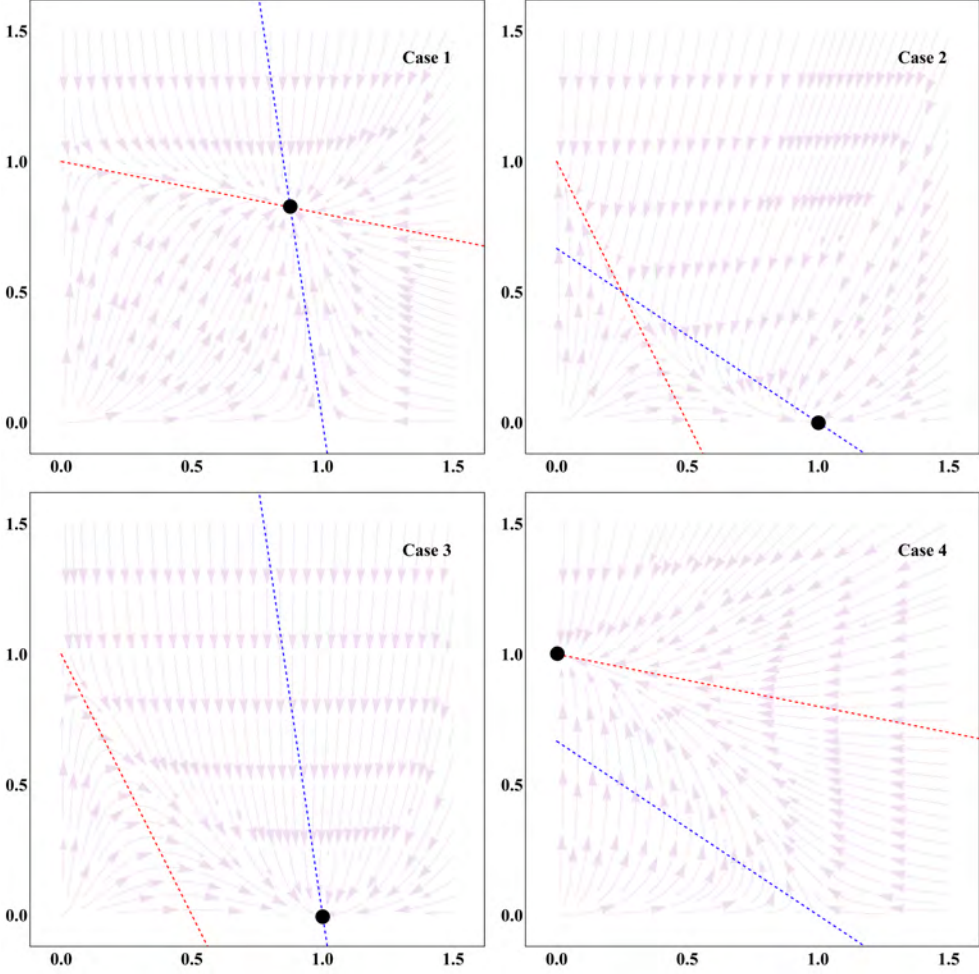
Figure 8: Phase planes for 2 species VL equations in the different discussed cases. Stable nodes are highlighted in each case, and the nullclines r_1 and r_2 are respectively in blue and red. Case 1. $a_{12} = 0.15$ and $a_{21} = 0.2$, Case 2. $a_{12} = 1.5$ and $a_{21} = 2$, Case 3. $a_{12} = 0.15$ and $a_{21} = 2$, Case 4. $a_{12} = 1.5$ and $a_{21} = 0.2$

$\forall t \geq 0$. This then requires that the rate of asymptotic convergence, for solutions starting close enough to the rest point, remains always bounded by a particular known rate $\alpha ||\mathbf{x}(t) - \mathbf{x}^*|| e^{-\beta t}$. In the previous section we have investigated local stability by linearizing the system in the neighborhood of the equilibrium point, in order to establish if the latter one constituted a *stable node* (i.e. a point in which trajectories converge) or an *unstable node* (i.e. a point that can become a source of trajectories). The *basin of attraction* of $\mathbf{x}^*$ is defined by the set of points $\mathbf{x}(0)$ satisfying $\mathbf{x}(t) \to \mathbf{x}^*$ as $t \to \infty$. It is standard argument to construct the stability Hurwitz matrix (which in this case is the Jacobian) and determine the stable directions by studying the sign of its eigenvalues, recalling that an equilibrium point is asymptotically stable if the stability matrix eigenvalues have *all* negative real part. The *first theorem of Lyapunov*
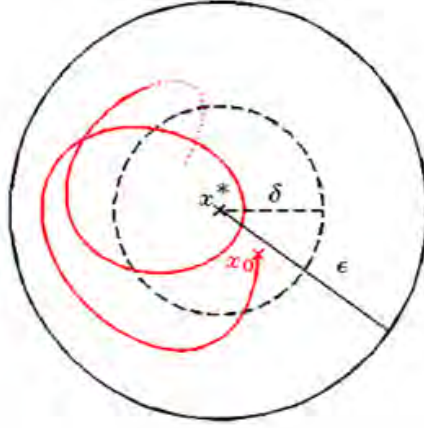
Figure 9: Lyapunov stability definition

(Lyapunov theorem for linear systems) also implies that the matrix $\mathcal{J}$ with elements $\{a_{ij}x_j^*\}$ is stable if and only if there exists a positive matrix $\mathbf{Q}$ such that $\mathbf{Q}\mathcal{J} + \mathcal{J}^{\mathsf{T}}\mathbf{Q}$ is *definite negative*.

Furthermore the presence of one or more eigenvalues with positive real part gives unstable solutions, while the existence of zero eigenvalues (i.e. no corresponding eigenvectors) constitutes a so-called *center manifold* and the behavior of this point can be analyzed through the center-manifold theory, for example (see e.g. [107]).

The second method exploits the *Lyapunov stability theorem* and makes use of *Lyapunov function*. Considering a system $\dot{\mathbf{y}} = \mathbf{f}(\mathbf{y})$ with $\mathbf{f}(\mathbf{0}) = \mathbf{0}$ (this condition can be fulfilled through the substitution $y_i = x_i - x_i^*$), a function $V : \mathbb{R}^n \to \mathbb{R}$ is defined such that:

$$V(\mathbf{0}) = 0$$
$$V(\mathbf{y}) \geq 0, \ \mathbf{y} \neq \mathbf{0}$$
$$\dot{V} = \frac{\partial V}{\partial \mathbf{y}} \mathbf{f}(\mathbf{y}) \leq 0 \tag{2.34}$$

Then, if the system admits a Lyapunov function, then solution is asymptotically stable. Moreover, if V is radially unbounded, solution is globally stable. The main advantage of Lyapunov criterion is that stability can be proven without requiring knowledge of the true physical energy, provided a Lyapunov function can be found to satisfy the above constraints.

Due to $(2.34)_1$ and $(2.34)_2$ the Lyapunov function presents a strict minimum in $\mathbf{y} = 0$. Now, let the set K_c be defined as:

$$K_c = \{\mathbf{y} : V(\mathbf{y}) \leq c \quad \text{and} \quad ||\mathbf{y}|| \leq \epsilon_0\} \tag{2.35}$$

Then for any $c > 0$, there exists a $\delta(c) > 0$ such that

$$\{||\mathbf{y}||\} \subset K_c, \tag{2.36}$$

and for every $0 < \epsilon < \epsilon_0$ there is a $c(\epsilon)$ such that

$$K_c \subset \{||\mathbf{y}|| < \epsilon\} \quad \text{for } c \leq c(\epsilon) \tag{2.37}$$
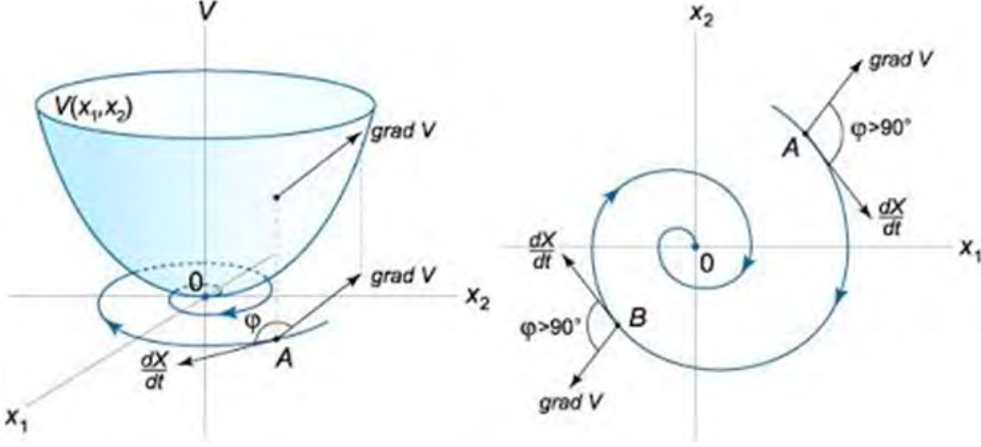
Figure 10: Illustration of the geometrical interpretation of the Lyapunov stability theorem.

Statement (2.36) follows immediately from the continuity of V at $\mathbf{y} = 0$. For (2.37) note that $\{\epsilon < ||\mathbf{y}|| < \epsilon_0\}$ is compact and V is therein positive. Therefore $\min_{||\mathbf{y}||\in(\epsilon,\epsilon_0)} V(\mathbf{y}) = c(\epsilon)$ and, chosen $c < c(\epsilon)$ the set K_c satisfies (2.37). Therefore, given $0 < \epsilon < \epsilon_0$ and $c < c(\epsilon)$, one has $K_c \subset \{||\mathbf{y}|| < \epsilon\}$. Since for hypothesis

$$\dot{V} = \frac{\partial V}{\partial \mathbf{y}} \mathbf{f}(\mathbf{y}) \le 0$$

$V(\mathbf{y})$ cannot increase. So, if $\mathbf{y}(0) \in K_c$, $\mathbf{y}(t)$ is in K_c for all t in its forward interval of existence. By condition (2.36) we can ensure that $\mathbf{y}(0) \in K_c$ by taking $||\mathbf{y}(0)|| \le \delta(c)$, which is the delta requested for stability theorem. In fact, if this is guaranteed, $\mathbf{y}(t) \in K_c \quad \forall t > 0$.
A typical Lyapunov function for general LV can be taken in the form

$$V(\mathbf{x}) = \sum_i q_i \left[(x_i - x_i^*) + x_i^* \ln \frac{x_i}{x_i^*} \right] \tag{2.38}$$

where q_i are the elements of $\mathbf{Q}^{-1}$. In particular, this well-known form of the Lyapunov function recalls the Boltzmann-type entropy production of statistical mechanics, which therefore implies a substantial equivalence between dynamical system stability and entropic, i.e. thermodynamic, stability (see for example the work by Chakrabarti and Ghosh [36]). This important result *de facto* confirms what both Volterra and Lotka had postulated and gives insights in the thermodynamic analysis of mechanical systems coupled with interspecific dynamics that will be presented in the following. To this aim, finally, another remarkable result deriving from theses two theorems has been shown by Tuljapurkar and Semura ([193]). The particular structure of the general Volterra-Lotka systems let in fact to demonstrate that *local stability ensures global stability* in absence of center manifolds.

In the light of the arguments presented, the Volterra-Lotka logic, as well as more modern EGT framework, can be transposed from the animal species context to the

scale of biological tissues and in particular, to describe the interactions between cells, both in ordinary physiological processes and disease. It can be in fact assumed that in an organism, cells act in an evolving environment (the extra-cellular space) and share the same spaces, thus inevitably compete for the same resources. If cells growth were kindled "ignorantly", probably any biological structure would be originated with the existing functionality and hierarchy. In a physiological context, this is guaranteed by an orchestrated by an orchestrated cascade of biophysical, chemical and mechanical stimuli, which likely determine the tissue development. In disease, some of these balances as well as some cells gene expressions might be altered and disordered mechanisms occur, and also mutations might be present. In particular, in the following chapters, we will assume cancer and healthy cells as populations in evolutionary games, with fitness functions designed using Volterra-Lotka type functions in order to see tumor development as cancer (mutated) cells ousting normal cells population and host environment.

Part II

UNCOUPLED MODELLING

Growth and mechanical variables can be studied by essentially starting from elemental uncoupled models in which either the one or the other is treated as a free-parameter of the problem. This essential approaches result highly effective and have the advantage to exploit well-known analytical solutions and simplified approaches in order to dwell on the implications that the variation of growth and remodelling parameters have on the phenomenological aspects in foreground

UNCOUPLED MODELS EXPLORING BIOMECHANICAL ISSUES

Theory of elasticity provides the possibility of taking into account macroscopic body growth as an inelastic deformation that combines with elastic effects in order both to find the stresses harboring within the tissue environment and to understand how these stresses affect the leading physiological processes. In principle, biomechanical models might constitute a synthesis of all these aspects, endeavoring to describe how they interlace each other by determining a complex machinery in which mechanical-driven feedback and growth and remodelling-induced structural changes are comprehensively taken into account. However, to better the understand the causes and the consequences of this crosstalk and to gain insights into the way in which these processes can be opportunely modeled, some simplified cases can be first introduced. The exploitation of small strains hypothesis as a first analysis gives in fact the advantage of getting key information about the knowledge of the reciprocal influence between the mechanical environment and the tissue growth and remodelling attitudes, through a well-established mathematical setting. In this sense, some important theoretical insights about the consequences that the alterations of the "healthy" mechanical environment can have on tissue development –seen as the fate of a growth and remodelling process– can be readily evidenced. To this purpose, experimental observations then give a fundamental feedback and allow the development and the optimization of the mechanically-based hypotheses of some growth phenomena. Therefore, simple *uncoupled* problems can be treated, in which growth is additively combined with geometrical deformation and is supposed known on the basis of experimental data. Uncoupled modelling then aims to achieve valuable information on tissue properties and evolutionary tissue response by treating the mechanical problem and the growth-related dynamics in a relatively separate way, i.e. trying not to explicitly include in the biomechanical model all the feedback mechanisms describing the crosstalk between mechanical variables and tissue constituents. Thus, the assumption is that these effects can be in some fashion reported on a side by supposing known the way in which macroscopic growth affects the mechanical problem, and, on the other side, by analyzing tissue evolutionary dynamics in the attempt to describe mechanically-driven alterations at the constituents scale in the simplest way possible.

In the following sections, some elemental models dealing with different physiological and abnormal situations will be presented, and the focus will be on some qualitative information that these models let to put in evidence despite the aforementioned assumptions. In particular, some adverse consequences of the maladaptation of pulmonary arteries reinforced with synthetic and transposed in aortic position will be investigated by exploiting well known analytical solutions (see for example [60]); also, the problem of the formation of fibrotic capsula around breast implants will be analyzed by means of a simple biomechanical model. Finally, the last section is dedicated to the modelling of the BMU (Basic Multicellular Unit) activity involved in bone

remodelling process through a straightforward application of the Volterra-Lotka logic presented in Chapter 2.

3.1 REPRESENTATIVE EXAMPLES

3.1.1 *Compliance mismatch and compressive wall stresses give clues for explaining anomalous remodelling of pulmonary arteries with Dacron synthetic grafts*

Synthetic grafts are often satisfactory employed in cardiac and vascular surgery, including expanded poly(ethylene terephthalate) or expanded poly(tetrafluoroethylene). However, accumulating evidences suggest the emergence of worrisome issues concerning the long-term fate of prosthetic grafts as large vessel replacement. Disadvantages related to the use of synthetic grafts can be traced in their inability of mimicking the elasto-mechanical characteristics of the native vascular tissue, local suture overstress leading to several prosthesis-related complications and retrograde deleterious effects on valve competence, cardiac function and perfusion. Motivated by this, in this section it is analyzed –by means of both elemental biomechanical paradigms and more accurate *in silico* Finite Element simulations– the physical interactions among aorta, autograft and widely adopted synthetic (Dacron) prostheses utilized in transposition of pulmonary artery, highlighting the crucial role played by somehow unexpected stress fields kindled in the vessel walls and around suture regions, which could be traced as prodromal to the triggering of anomalous remodeling processes and alterations of needed surgical outcomes. Theoretical results are finally compared with histological and surgical data related to a significant experimental animal campaign conducted by performing pulmonary artery transpositions in 30 two-month old growing lambs, followed up during growth for six months. The *in vivo* observations demonstrate the effectiveness of the proposed biomechanical hypothesis and open the way for possible engineering-guided strategies to support and optimize surgical procedures.

The evidence supporting the large availability and ease of synthetic grafts, including expanded poly(ethylene terephthalate) (Dacron®) or Valsalva Dacron, has allowed an extensive application of these conduits in a wide spectrum of vascular pathologies ([40, 162]). To the best of our present knowledge, the advantage of synthetic conduits, especially Valsalva Dacron, has encouraged the development of aortic valve sparring operation in surgery of aortic disease ([51, 52, 180]) and recently it has been proposed as external reinforcement to prevent dilatation of the pulmonary autograft in the Ross Operation ([33, 34, 141, 190]). Nevertheless, the evidence supporting an implementation of synthetic graft has not erased the complications related to his employment. The unresolved issue are represented by degradation for threadbare, impairment of the electromechanical properties of the vascular wall and elicit the inconvenient issue of windkessel phenomenon. ([17, 21, 95, 96, 110, 130, 139]). Among persons receiving polyethylene terephthalate grafts implant, this complication is related to an initial increasing diameter vs. the package size range to 26% ([42, 209]), leaving unanswered the problem about the morphological impairment of the native aorta and biomechanics future of synthetic grafts ([14, 20, 152, 163]). To re-create the same dynamic stress, we set out to study in a large experimental growing ovine model the interaction between stress shielding, strain and growth in the synthetic coating and in the native vascular structure. The rapid growth and systemic blood pressure are used in

the animal model as a catalyst to induce the dynamic stress. A mathematical model was developed to quantify these stress distributions and to obtain insights about the growth and remodeling capability of the pulmonary artery transposed in aortic position from a biomechanical point of view, as well as to investigate the physical causes underlying the above mentioned adverse phenomena.

The experimentation on growing ovine animal model provided the execution of pulmonary trunk transposition from right ventricular outflow tract and transposed into the descending aorta. Growth, remodelling and stress shielding of this unitary tubular structure was studied between two groups of animals receiving an external reinforcement with expanded poly (ethylene terephthalate), or Dacron®, and animals subjected to PA transposition alone. The measurement were reported at day one, three and six months by angiography and echocardiography. Biological processes were evaluated with the histochemistry. In what follows, a biomechanical model describing the mechanical conditions of the native aorta and pulmonary artery with synthetic graft is developed, in order to discuss the relationship between the *in vivo* model observations and the mechanics of these systems. We studied the implications that the mechanical properties of the different constituents can have in determining long-term non-physiological alterations.

3.1.1.1 *Qualitative insights into stress fields and remodelling from elemental elastic schemes*

One of the most relevant aspects for expecting successful outcomes in a clinical intervention –such as the pulmonary autograft transposition reinforced with Dacron graft– lies in the possibility of restoring ordinary physiological conditions through an adequate process of remodeling within the transplanted tissue. From a biomechanical standpoint, it is well known that tissue grows and remodels in response to an altered mechanical environment ([89]). These adaptations are then inevitably associated with the (local and average) state of stress, or strain, within the tissue induced by both the external loads and constraints. Nevertheless, the effectiveness of the remodeling process may result unfaithful if such stress-induced stimuli and their alterations are not compatible with certain physiological ranges, which let the soft vessel tissue undergo a progressive natural remodeling over characteristic timescales (weeks to months, [135]), needed to reorganize its microstructure and to accommodate its mechanical properties to the new environment, in this way reaching a homeostatic configuration. By focusing on the vascular remodeling, for instance, Fung and Liu ([70]) experimentally induced morphological and structural alterations of the pulmonary artery in rats by gradually increasing systemic pressure from 15 mmHg up to 30 mmHg in a month, the tunica media and adventitia opportunely adapting and thickening over this period. From a mechanical point of view, it is widely suggested ([43, 82, 216]) that the circumferential stress assumes a primary role in influencing the process of vessels remodeling. For these reasons, with the purpose of analyzing the post-operative remodeling potential of a pulmonary artery vessel tract transposed in aortic position, subjected to arterial pressure and reinforced with a Dacron graft, a simple mechanical model has been here proposed to analyze the stresses distribution prodromal to vascular remodeling. More specifically, three significant scenarios are taken into account: the *healthy aorta* (A), the *healthy pulmonary artery* (PA) and the *reinforced pulmonary artery* (PA+D)

transposed in aortic position. The first two cases represent physiological situations, thus respectively subjected to arterial and venous pressures, while the last case of interest is simulated by considering a vessel exhibiting venous-like material properties when subjected to both arterial blood pressure and external confinement due to the presence of the non-resorbable Dacron mesh, mechanically represented by an additional outer layer with elastic properties related to its actual material and fabric structure.

3.1.1.2 *Balance equations and closed-form solutions to model vessels structure*

Within the above mentioned perspective of determining the essential form and the order of magnitude of the stress fields in the blood vessels under the cardiac cycle-induced internal pressure for the three above mentioned scenarios of interest, a first analysis can be conducted in the realm of linear elasticity ([15, 68]): relevant qualitative information can be in this way gained by exploiting analytical solutions, available by invoking classical results presented in the literature also with reference to composite hollow cylinders under different load conditions ([60]), including anisotropic ([61]) and inhomogeneous ([63]) elasticity. By following this line of reasoning, the cases of healthy aorta and pulmonary artery are therefore modeled as isotropic homogeneous hollow cylinders, with arterial and venous pressures p_A and p_{PA} respectively exerted at their internal walls. In a similar way, the case of PA reinforced with Dacron (PAD) is then simulated by considering a two-phase composite hollow cylinder where the inner layer represents the vessel wall and the surrounding layer replicates the non-resorbable coating, whose overall mechanical properties are homogenized to take into account the penalization of the *bulky* material stiffness due to the low volume fraction offered by the structure to the effective elastic confinement of the graft. Formally, the three vessels are thus geometrically described by the cylindrical regions as follows (see Fig. 11):

$$\text{A and PA}: \quad r_i \leq r \leq r_i + h, \quad 0 \leq \theta \leq 2\pi, \quad 0 \leq z \leq l, \qquad (3.1)$$

$$\text{PA+D}: \quad r_i \leq r \leq r_i + h \vee r_i + h \leq r \leq r_i + h + h_D,$$
$$0 \leq \theta \leq 2\pi, \quad 0 \leq z \leq l \qquad (3.2)$$

where r_i is the internal lumen radius, h and l are the vessel thicknesses and heights, respectively, while h_D is the thickness of the Dacron prosthesis. Also, being the aorta and the pulmonary artery significantly different in terms of intrinsic material parameters, corresponding elastic moduli E_A and E_{PA} were adopted, while a common Poisson's coefficient ν was instead assumed. With reference to the homogenized Dacron layer, an effective elasticity modulus E_D was assigned to taking into account the non-linear dependence of the overall stiffness with respect to mesh volumetric fraction and a different Poisson's coefficient ν_D was also selected. By further introducing the hypothesis of axisymmetric of the problem, the stress vector (in the so-called Voigt notation) can be written as $\boldsymbol{\sigma}^k = \{\sigma_{rr}^k, \sigma_{\theta\theta}^k, \sigma_{zz}^k\}$, where σ_{rr}^k, $\sigma_{\theta\theta}^k$ and σ_{zz}^k denote the radial, circumferential and longitudinal stress components, respectively (Fig. 11), while the superscript $k = \{A, PA, D\}$ specifies the stress components (and the related moduli) of the material to be considered. In duality with the stress, the deformation vector, $\boldsymbol{\epsilon}^k = \{\epsilon_{rr}^k, \epsilon_{\theta\theta}^k, \epsilon_{zz}^k\}$, is defined, where ϵ_{rr}^k measures the radial strain, $\epsilon_{\theta\theta}^k$ the
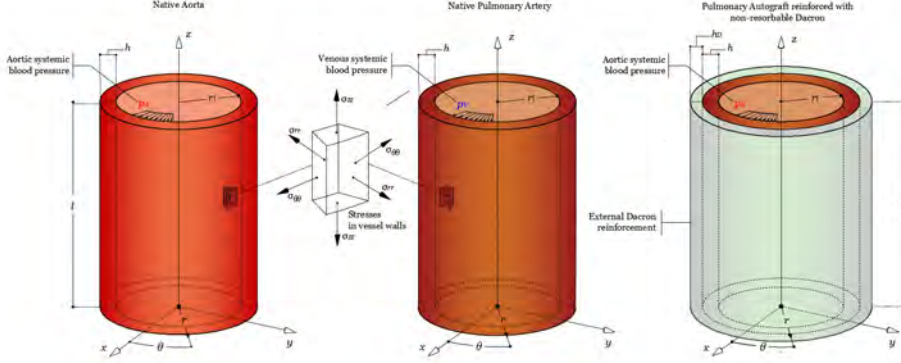
Figure 11: A hand-made sketch illustrating the geometry and the mechanical features of the native aorta (on the left), the native pulmonary artery (in the midlle) and the pulmonary autograft (on the right).

circumferential strain and ϵ_{zz}^k the longitudinal (along the z–axis) elongation/contraction. For the problem at hand, without loss of generality, a plane state of deformation can be additionally postulated, $\epsilon_{zz}^k = 0$ being therefore assumed for all the cases. By making reference to the above recalled elastic moduli and invoking the generalized Hooke's law, stresses can be linearly associated to the strains and, under the hypothesis of cylindrical symmetry, the equilibrium equations reduce to the sole one in the radial direction, that is

$$\frac{d\sigma_{rr}^k}{dr} + \frac{1}{r}(\sigma_{rr}^k - \sigma_{\theta\theta}^k) = 0 \tag{3.3}$$

In particular, symmetry gives the displacements as

$$u_r^k = u^k(r), \qquad u_\theta = 0, \qquad u_z^k = w^k = \epsilon_0^k z \tag{3.4}$$

to which are associated the strains in the simplified form

$$\epsilon_{rr}^k = \frac{du_r^k}{dr}, \qquad \epsilon_{\theta\theta}^k = \frac{u_r^k}{r}, \qquad \epsilon_{zz}^k = \epsilon_0^k \tag{3.5}$$

Linear isotropic elasticity allows to therefore write

$$\sigma_{rr}^k = 2\mu^k \epsilon_{rr}^k + \lambda^k \epsilon^k, \tag{3.6}$$

$$\sigma_{\theta\theta}^k = 2\mu^k \epsilon_{\theta\theta}^k + \lambda^k \epsilon^k, \tag{3.7}$$

$$\sigma_{zz}^k = 2\mu^k \epsilon_{zz}^k + \lambda^k \epsilon^k \tag{3.8}$$

where $\sigma_{\theta\theta}^k = 2\mu^k \epsilon_{\theta\theta}^k + \lambda^k \epsilon^k$ is the linear dilation (the trace of the strain tensor), $2\mu^k = \frac{E^k}{(1+\nu^k)}$, $\lambda^k = \frac{\nu^k E^k}{(1+\nu^k)(1-2\nu^k)}$, and E^k and ν^k are the Young modulus and the Poisson ratio of the $k-th$ phase, respectively.

By substituting (3.5) in (3.6) and finally in (3.3), the classical Navier-Cauchy differential equation in terms of displacements is finally obtained as

$$r^2 \frac{d^2 u^k}{dr^2} + r \frac{du^k}{dr} - u^k = 0 \qquad (3.9)$$

For the three scenarios and the related boundary conditions, the solutions in terms of the displacements can be easily found in closed-form as $u_r^k = C_1^k r + C_2^k r^{-1}$, with the constants C_1^k and C_2^k being particularized for each case. In particular, to obtain the explicit the solutions, for the case of the aorta (A) the equation (3.9) is integrated between r_i and $r_i + h$ by imposing the boundary conditions $\sigma_{rr}^A(r_i) = -p_A$ and $\sigma_{rr}^A(r_i + h) = 0$, whereas in the PA case the equation (3.9) is integrated over the vessel thickness with conditions $\sigma_{rr}^{PA}(r_i) = -p_{PA}$ and $\sigma_{rr}^{PA}(r_i + h) = 0$. Differently, the problem of reinforced PA in aortic sight requires to solve equation (3.9) of equilibrium for each layer, by both assuming the radial stress to balance the arterial pressure at the internal radius, i.e. $\sigma_{rr}^{PA}(r_i) = -p_A$ and to vanish outside of the Dacron layer, i.e. $\sigma_{rr}^D(r_i + h + h_D) = 0$; also, continuity of radial stresses at the vessel-prosthesis interface, that is $\sigma_{rr}^{PA}(r_i + h) = \sigma_{rr}^D(r_i + h)$, as well as compatibility of radial displacements have to be ensured. Once each displacements function is defined, stresses can be readily calculated through compatibility equations (3.5) and constitutive relations (3.6). The discussion of the each vessel's environmental stress will be analyzed in order to understand how the reinforced PA and the communicating healthy aorta interchange forces in correspondence of the interface and predict the vessels remodelling capabilities. In fact, in the suture ring zone, a more complex stress distribution occur, which provides the emergence of non-zero shear stresses $\sigma_{\theta z}$. This shear stress can be in fact likely related to the problematic splitting-like phenomena of the pulmonary autograft. Finally, it is worth to notice that long term effects of growth and remodelling have not been taken into account in this linear model, since the latter ones would require a more detailed description involving a nonlinear theoretical approach (see for example [143]).

Integration constants for displacements deriving from (3.9)

- *Reference Aorta:*

$$C_1^A = -\frac{2\nu^2 p_A r_i^2}{E_A \left(r_i^2 - (h + r_i)^2 \right)} - \frac{\nu p_A r_i^2}{E_A \left(r_i^2 - (h + r_i)^2 \right)} + \frac{p_A r_i^2}{E_A \left(r_i^2 - (h + r_i)^2 \right)}$$

$$C_2^A = \frac{\nu p_A r_i^2 (h + r_i)^2}{E_A \left(r_i^2 - (h + r_i)^2 \right)} + \frac{p_A r_i^2 (h + r_i)^2}{E_A \left(r_i^2 - (h + r_i)^2 \right)}$$

- *Reference Pulmonary Artery:*

$$C_1^P = -\frac{2\nu^2 r_i^2 p_P}{E_P \left(r_i^2 - (h + r_i)^2 \right)} - \frac{\nu r_i^2 p_P}{E_P \left(r_i^2 - (h + r_i)^2 \right)} + \frac{r_i^2 p_P}{E_P \left(r_i^2 - (h + r_i)^2 \right)}$$

$$C_2^P = \frac{\nu r_i^2 p_P (h + r_i)^2}{E_P \left(r_i^2 - (h + r_i)^2 \right)} + \frac{r_i^2 p_P (h + r_i)^2}{E_P \left(r_i^2 - (h + r_i)^2 \right)}$$

- *Pulmonary Artery transposed in aortic sight and reinforced with the external Dacron layer:*

$$
\begin{aligned}
C_1^{PA} = {}& [(\nu+1)(1-2\nu)p_A r_i^2 E_{PA}(\nu_D+1)(2\,(\nu_D-1)\,(h+r_i)^2 - 2h_D\,(h+r_i) - h_D^2) + \\
& + (\nu+1)^2(1-2\nu)p_A E_D h_D r_i^2(h_D + 2(h+r_i))] \Big/ \\
& E_{PA}[(\nu+1)E_D h_D\,(h_D + 2\,(h+r_i))\left((1-2\nu)\,(h+r_i)^2 + r_i^2\right) + \\
& - h\,(\nu_D+1)\,E_{PA}\,(h+2r_i)\left(2\,(\nu_D-1)\,(h+r_i)^2 - 2h_D\,(h+r_i) - h_D^2\right)]
\end{aligned}
$$

$$
\begin{aligned}
C_2^{PA} = {}& -(\nu+1)p_A r_i^2\,(h+r_i)^2\,[2h_D\,(h+r_i)\left(\left(2\nu^2+\nu-1\right)E_D - (\nu_D+1)\,E_{PA}\right) + \\
& + 2\left(\nu_D^2-1\right)E_{PA}\,(h+r_i)^2 + h_D^2\left(\left(2\nu^2+\nu-1\right)E_D - (\nu_D+1)\,E_{PA}\right)] \Big/ \\
& E_{PA}[h_D^2\left((\nu+1)E_D\left(h^2(2\nu-1) + 2h(2\nu-1)r_i + 2(\nu-1)r_i^2\right) - h\,(\nu_D+1)\,E_{PA}\,(h+2r_i)\right) + \\
& + 2h_D\,(h+r_i)\,((\nu+1)E_D\left(h^2(2\nu-1) + 2h(2\nu-1)r_i + 2(\nu-1)r_i^2\right) - h\,(\nu_D+1)\,E_{PA}\,(h+2r_i)) + \\
& + 2h\left(\nu_D^2-1\right)E_{PA}\,(h+r_i)^2\,(h+2r_i)]
\end{aligned}
$$

$$
\begin{aligned}
C_1^{D} = {}& [2\left(\nu^2-1\right)p_A\left(2\nu_D^2+\nu_D-1\right)r_i^2\,(h+r_i)^2] \Big/ \\
& [h_D^2\left((\nu+1)E_D\left(h^2(2\nu-1) + 2h(2\nu-1)r_i + 2(\nu-1)r_i^2\right) - h\,(\nu_D+1)\,E_{PA}\,(h+2r_i)\right) + \\
& + 2h_D\,(h+r_i)\left((\nu+1)E_D\left(h^2(2\nu-1) + 2h(2\nu-1)r_i + 2(\nu-1)r_i^2\right) - h\,(\nu_D+1)\,E_{PA}\,(h+2r_i)\right) \\
& + 2h\left(\nu_D^2-1\right)E_{PA}\,(h+r_i)^2\,(h+2r_i)]
\end{aligned}
$$

$$
\begin{aligned}
C_2^{D} = {}& -[2\left(\nu^2-1\right)p_A\,(\nu_D+1)\,r_i^2\,(h+r_i)^2\,(h_D+h+r_i)^2] \Big/ [h_D^2(-h\,(\nu_D+1)\,E_{PA}\,(h+2r_i) + \\
& \left((\nu+1)E_D(h^2(2\nu-1) + 2h(2\nu-1)r_i + 2(\nu-1)r_i^2)\right) + \\
& + 2h_D\,(h+r_i)\,((\nu+1)E_D\left(h^2(2\nu-1) + 2h(2\nu-1)r_i + 2(\nu-1)r_i^2\right) + \\
& - h\,(\nu_D+1)\,E_{PA}\,(h+2r_i)) + 2h\left(\nu_D^2-1\right)E_{PA}\,(h+r_i)^2\,(h+2r_i)]
\end{aligned}
$$

3.1.1.3 *Finite Element Modeling of the pulmonary artery*

To analyze in more detail the mechanical effects of Dacron net-reinforcement on the response of the overall vascular system (the artery integrated with the reinforced pulmonary autograft), a numerical analysis has been performed by means of the Finite Element Method (FEM). The simulation has been conducted with the aid of the commercial FEM-based code ANSYS©([1]). The FEM model let to examine the anastomosis zone in a more faithful way by constructing a geometry constituted of the reinforced PA directly communicating with aorta tract, and internally subjected to arterial pressure. Each tract was externally provided of the mechanical conditions already described for the analytical solutions: the artery was externally unloaded, while the Dacron synthetic graft has been positioned outside the PA tract (Fig. 12). Coherently with the analytical model, the numerical analyses have been performed under the hypothesis of linear elasticity and small deformations referring to the material properties reported in Table 1. To this aim, an *ad hoc* custom made Ansys procedure, written in APDL parametric language, has been developed to reconstruct the FE vessels model by considering the geometrical parameters in the Table 1. The woven structure of the Dacron graft has been built parametrically on the external surface of the PA tract by fixing a fine mesh net of about $1\,mm^2$.

Table 1: Synoptic table of geometrical and material parameters

Symbol [Unit]	r_i [mm]	h_k [mm]	E_k [kPa]	ν_k [-]
Aorta (A)	10	1.5	400	0.49
Pulmonary Artery (PA)	10	1.5	20	0.49
Dacron (D)	-	0.5	7500	0.4

The Dacron Young modulus here reported accounts for the mesh volume fraction of 5%.

The geometrical models of both PA and aorta have been meshed by means of about 121 000 standard hexahedral elements and almost 152 000 nodes with three degrees of freedom for each node, while the synthetic structure of the graft has been meshed by means of about 10 000 classical beam elements –based on Timoshenko beam theory– and 9 500 nodes. The magnitude of the applied load was about 16 kPa (representing a typical mean value of the arterial pressure), which acts in radial direction on the internal vessel walls; in addition, symmetrical boundary conditions have been considered on the bottom and top circular surface of the structures. This refined model therefore permits to investigate the stress state generated on the arteries walls and to evaluate the "cage-effect" of the stiffer Dacron structure on the integrated system, by then highlighting the perturbations of the analytical solutions when aorta, PA and the Dacron mesh are working together.

3.1.1.4   *The animal model*

Preparation of the animals. Thirty two-month (8-10 weeks) old growing lambs weighting about 18±3 kg underwent transposition of pulmonary artery autograft in aortic position under cardiopulmonary bypass. Technical and anatomical issues imposed reimplantation of the PA in the descending aorta while the right ventricle outflow tract was reconstructed with a fresh homograft from another lamb of the same age and weight. We observed the progression of autograft diameter during the period of fastest growth such us the biomechanical futures and histological modification.

Non-Resorbable Materials. Meshes used in this study were cut into a rectangle measuring 20 mm in height matching with the height of autograft, rolled out on a metallic candle, and then reassured by a suture to create a cylinder with an internal diameter of 10 mm (20 mm in height in 10 mm diameter directly adherent to the PA). In addition to animals subjected to PA transposition (control group, n=15), the experimental design included a group (n=15) in which the PA was reinforced with an external synthetic non-absorbable grid of Polyester and group (n=15). The autograft was then inserted into the fibrillar cylinder and was anastomosed suturing both its margins and those of the prosthetic structure to the pulmonary autograft trunk.

Implantation. Lambs were premedicated with ketamine (25 mg/kg IM) and anesthesia was guaranteed by the injection of sodium thiopentothal (6, 8 mg /kg) via the internal jugular. Animal received 100mg of lidocaine intravenously as prophylaxis against rhythm disturbance. After endotracheal intubation, ventilation was provided up to animal awakening and the anaesthesia was maintained with inhalation isoflurane (1% to 2, 5%). The electrocardiogram was monitored. Chest was prepped and shaved. The heart was approached via left thoracotomy. After opening the pericardium, the
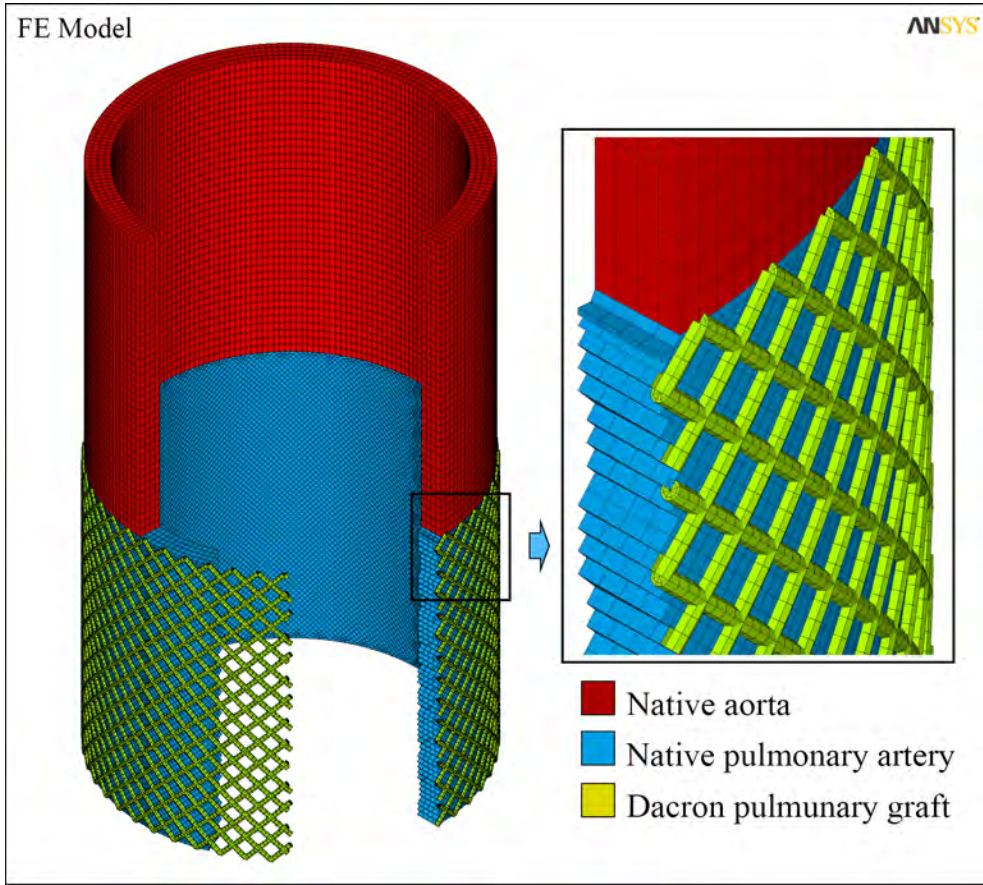
Figure 12: Geometry of the FE model, with a detail showing the communication of the native aorta (in red) with the pulmonary artery tract (blue), integrated with the external Dacron structure.

right atrium was exposed for cannulation and the trunk of the pulmonary artery was dissected free from its right ventricular origin up to its bifurcation in the pulmonary arteries. The same was done for the descending thoracic aorta and a region distal to the portion of choice for the PA transposition was cannulated. Approximately 8 cm of the descending thoracic aorta was left for clamp positioning and to perform the anastomosis with the pulmonary artery trunk under optimal conditions. Three mg/kg of heparin was given intravenously, and cardiopulmonary bypass was started between right atrium and descending aorta. The cerebral circulation of the animal was guaranteed on a beating heart. Tree cm of the pulmonary artery trunk was transposed into the descending aorta with an end-to-end anastomosis in 5-0 prolene. A fresh pulmonary artery homograft, explanted from animals sacrificed on the same day for another experimental study, was inserted to reconstruct the right outflow tract, with a proximal and distal end-to-end anastomosis in 5-0 prolene. Left thoracotomy was closed and aspiration drainage left in place. All experiments have been performed in respect of guidelines for animal care and handling. The protocol was approved by the

institutional animal care committee.

3.1.1.5 *Pulmonary Catheterization, Angiographic and Echocardiographic study.*

The angiography was assessed injecting contrast medium by means of direct puncture of pulmonary trunk, and its diameter in situ was measured. In addition, a catheter was positioned for injection in to the ascending aorta and the basal diameter was determined (BV Pulsera Philips). Animals were humanely sacrificed and tissue harvested for histopathological analysis. Measurement of the ascending aorta, descending aorta proximally and distally to the autograft were made in order to obtain a reference to be compared to the diameter of the PA. A weight curve for each animal during the growing period was parallely processed. A serial of standard 2D and Doppler transthoracique echocardiography examination with colour flow mapping were used in all animal before and after operation and every two-week during follow-up to correctly evaluate the unfolding of the experiment (commercially available GE Medical System, Vivid 7, Milwaukee, Win). Colour flow imaging was performed to determine the permeability of pulmonary autograft and the presence or absence of any blood clots.

3.1.1.6 *Theoretical outcomes from analytical solutions and FE models.*

Analytical results, obtained by using the computational software MATHEMATICA® [210], for all the scenarios and independently from the vessel type, the maximum absolute value of the principal stresses can be recognized in the circumferential (hoop) one, whose peaks are in fact strictly greater than both the radial and longitudinal stresses. In particular, with reference to Fig. 13, the hoop stress $\sigma_{\theta\theta}$ in the reference aorta is about 120 kPa (compatibly with the most of homeostatic values furnished in literature, [89]), this value being correlated to both the higher blood pressure regimes and to the higher degree of distensibility, as well as to the aorta major stiffness and thickness with respect to the other vessel walls. The circumferential stress in the reference pulmonary artery is instead visibly smaller, provided that the venous pressure p_{PA} is about 2 kPa (15 mmHg) and also stretches are sustained. However, a first relevant difference between these two described situations and the case of the reinforced PA in aortic position emerges from Fig. 13: it can be in fact noticed that, while in the two previous physiological conditions tensile hoop stresses occur in the vessel walls, the reinforced pulmonary artery results instead to be compressed in circumferential direction. This somehow unexpected compressive stress state, as shown in Fig. 13 is the result of the confining action of the stiffer Dacron outer mesh, which *de facto* absorbs the most part of the extensional mechanical energy induced by the arterial pressure p_A during the entire lifetime (differently from PDS, Dacron is a not resorbable material [143]), by thus approaching tensions close to the those registered in the reference aorta and so providing an almost complete shielding effect on the PA. As a consequence, the partition of the stresses among reinforced PA and Dacron regions is altered by the significant stiffness mismatch between the biological and synthetic materials: the stress state experienced by the constrained PA walls becomes compressive and therefore opposite-in-sign with respect to the tensile one needed to stimulate a tissue PA remodeling towards an arterialization process. As highlighted

in Fig.13, this creates a distance of the *in situ* stress from the mechanical signaling range which would ensure the starting of a favorable and gradual adaptation of the PA structure to the aortic pressure, the amplitude of this range having been determined on the basis of experimental findings present in the literature [69]. In addition, it is worth to notice that also radial stresses (see Fig. 14) are essentially uniform and compressive in the reinforced PA due to the cooperation of the aortic pressure and the confining reaction of the polymer graft, with an average value of -16 kPa, that practically equals the aortic pressure p_A. The latter value is very different from the healty PA radial compression, while the mean radial stress of the native aorta over the vessel thickness is found to be about -7 kPa. These stress fields allows to infer that, at long-term, the exceeding mechanical constraints realized by the stiff scaffold can determine a persistent static compression that in turn stimulate an increased ratio of the collagen/elastin expression in the extra-cellular matrix synthesized by the cells during growth ([39, 41]). Moreover, in response to the interventional procedure, the natural reparative process enhances vascular smooth cells (VCMs) proliferation leading to neointima development and causing hyperplasic intimal remodeling and stenosis, with an accentuation of hypertension ([135]). This effect can be also aggravated when combined with the external mechanical constriction, that prevents the elastic stretching of the vessel, and can in turn increase the process of cells migration over the successive weeks towards the intimal layer, where proliferation in a compressed environment may provoke thicker wrinkled surfaces. Finally, the inability to adequately sense elastic stretch due to confinement and localized inflammation might start fibrotic processes. Furthermore, VCMs being so more prone to apoptosis under hypertension ([135]). In this sense, a prolonged wall compressive stress might represent an enhancer for starting these physiological processes.

   A further interesting results from analytical solutions is that longitudinal stresses σ_{zz} are also compressive in the reinforced PA (15), differently from the tensile regimes in the same direction occurring in the Dacron as well as in the reference aorta and pulmunary artery under corresponding physiological pressures. This forces the overall stress state inside the prosthesized PA towards a hydrostatic compression –which further suggest a possible compromised arterialization process– in turn generating an anomalous changing in sign of the stress at hand across the PA-aorta junction.

   In particular, it can be predicted that the discrepancy between the stress states in the PA-tract and native aorta determines the spurious shear σ_{rz} across the suture section to ensure the longitudinal equilibrium on, say, a ring of vessel material with height h_s, that represents the segment out of which both the regime aorta and PA stress states are restored as uniform (see Fig. 16). Despite this more complex local stress state constitutes a detail behind those caught by the analytical solutions of the elemental models under analysis, a rough estimation of the averaged value of this shear stress can however obtained by considering that it must be proportional to the gap between the aorta and the reinforced PA longitudinal stresses, i.e. $\overline{\sigma}_{rz} \simeq (\overline{\sigma}_{zz}^A - \overline{\sigma}_{zz}^{PA})r_m/h_s$, where r_m is the average radius of the vessels. From the biomechanical standpoint, this implies that the more the PA is compressed, the more the anastomotic region might become stenotic, this effect being amplified for larger vessels and reduced heights h_s, thus producing strong localized stress gradients. Since local symmetry of the stress tensor and global rotational equilibrium on the ring zone give $\overline{\sigma}_{rz} = \overline{\sigma}_{zr}$, tangential stresses also arise perpendicularly to the lines of suture
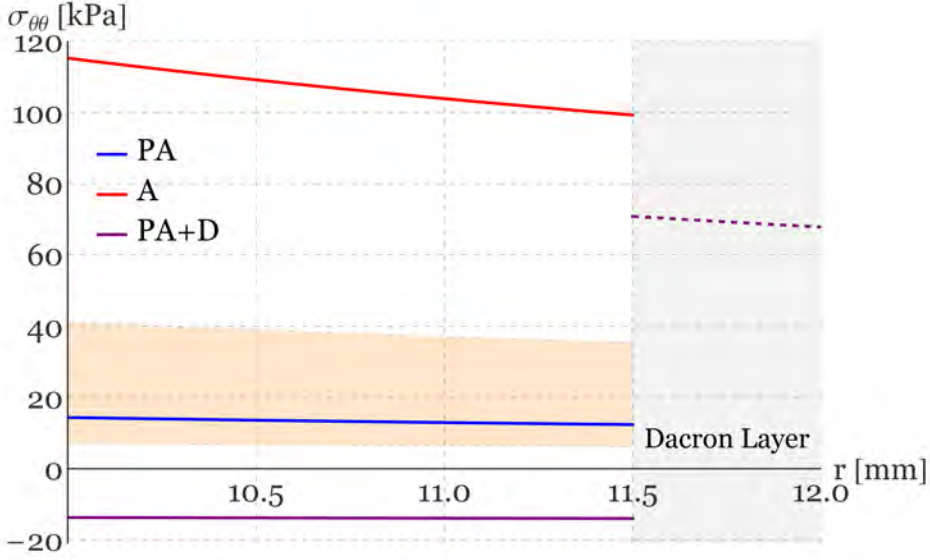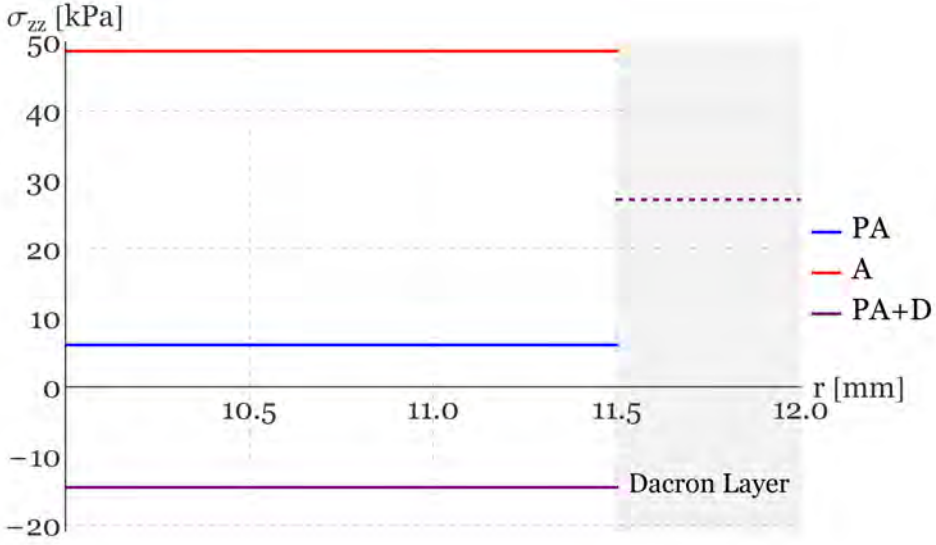
Figure 13: Distribution of the circumferential stresses over the vessel thickness. (A-red line) Reference Aorta. (PA-blue line) Reference Pulmonary Artery. (PAD-purple full line) Pulmonary artery reinforced with non-resorbable Dacron mesh. (PAD-Purple dashed line) Stresses in the region occupied by the Dacron region (in gray). The active remodeling window compatible with PA initial material properties is highlighted in orange.

(the z-axis, in the model at hand), and the corresponding forces can thus provoke local pull out distortions correlated to anastomotic disruption phenomena.

To analyze in more detail the influence of these spurious stresses on the localization of strain prodromal to possible anomalous biomechanical responses of the tissues, a numerical simulation has been performed by means of the finite element method (FEM) code ANSYS®. The FE model let to include the anastomosis zone by constructing a geometry constituted of the reinforced PA integrated with the aorta tract, which were internally subjected to arterial pressure. Each tract was externally provided of the mechanical conditions already described for the analytical solutions: the artery was externally unloaded, while Dacron synthetic graft was added to the PA region. Artery, PA and Dacron were then given the material properties already introduced (reported in Table 1) and a linear constitutive behavior was assigned to them. Results of the numerical simulations confirmed the values of the circumferential and longitudinal stresses obtained from the analytical model in the two vessels separately, as reported in Fig. 17.

In addition, the FEM results revealed the theoretically hypothesized shear stresses concentrations (see Fig. 18), with peaks of about 75 kPa, within a narrow transition zone in the suture region whose height is comparable to the vessel thickness. This means that a steep gradient of stress concentrates in a small height, causing geometrical anastomotic deformation which can affect the generation of local disruptions.
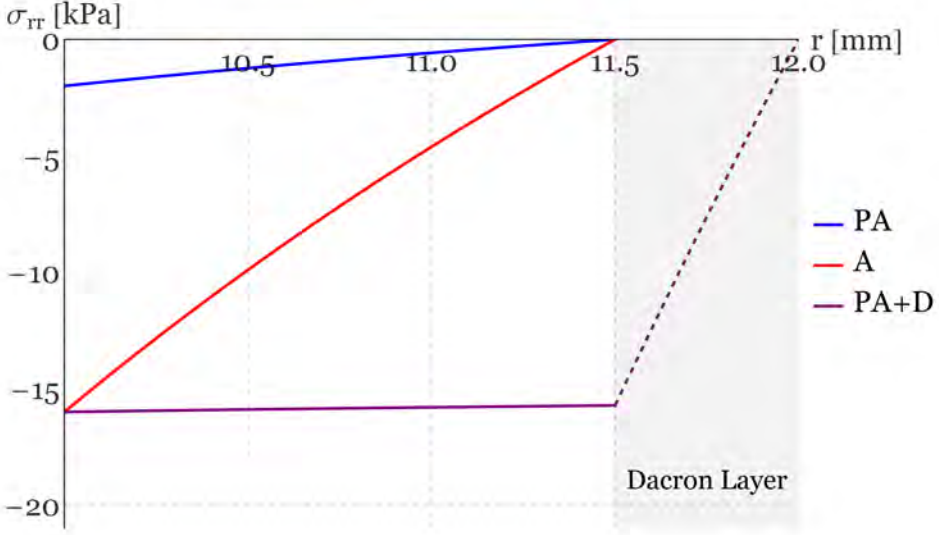
Figure 14: Distribution of the radial stresses over the vessel thickness. (A-Red line) Reference Aorta. (PA-Blue line) Reference Pulmonary Artery. (PAD-Purple full line) Pulmonary artery reinforced with non-resorbable Dacron mesh. (PAD-Purple dashed line) Stresses in the region occupied by the Dacron region (in gray).

In addition, localized equivalent stresses prone to yielding conditions can potentially occur in the suture region and can be at the basis of the pseudoaneurysmal degeneration observed in such zone, where the PA wall effectively experiences higher levels of strains (Fig. 19).

Finally, in order to have a direct comparison with the experimental results of the control group (the one subjected to not-reinforced PA transplantation), the analytical procedures have been also applied to the case of not-reinforced PA, by means of the equation (3.3). Aortic pressure have been imposed on a pulmonary artery material cylinder, with free stress conditions at the external boundary. The results showed that, in absence of longitudinal deformation, say $\epsilon_{zz} = 0$), the circumferential stress in the PA was essentially analogous to the aorta one. However, provided the greater compliance of the PA venous-like structure with respect to the stiffer aorta, such stress results excessive to be adequately sustained by the PA walls, and inevitably the mechanical integrity of the vessel would be compromised. In accord with these considerations, the not-reinforced PA circumferential stretch $\lambda_{\theta\theta}^{nrPA}$ –which measures the increase of dilation– results to be about four times greater than the aorta circumferential stretch $\lambda_{\theta\theta}^{A}$, thus tending to an overall aneurysmal diametral expansion. In addition, if one relaxes the hypothesis of plane deformations, the difference between the respective circumferential stresses $\sigma_{\theta\theta}^{nrPA}$ and $\sigma_{\theta\theta}^{A}$ is proportional both to the difference between the Young moduli and the longitudinal strain, i.e. $\sigma_{\theta\theta}^{nrPA} - \sigma_{\theta\theta}^{A} \propto (E_A - E_P)\epsilon_{zz}$ (see Fig. 20).

As a consequence, the combined presence of elevated aortic pressure and longitudinal *in situ* elastic stretch of the vessels can cause a severe increase of the non-reinforced

Figure 15: Distribution of the longitudinal stresses over the vessel thickness. (A-Red line) Reference Aorta. (PA-Blue line) Reference Pulmonary Artery. (PAD-Purple full line) Pulmonary artery reinforced with non-resorbable Dacron mesh. (PAD-Purple dashed line) Stresses in the region occupied by the Dacron region (in gray).

PA stress, approaching theoretical values from 200 kPa up to 700 kPa, already at strains $\epsilon_{zz} < 10\%$. These significantly high magnitudes are close to the aortic stress thresholds (von Mises stress) reported in some literature works ([88, 178]), and can be for this reason directly connected to mechanical critical states that invite yielding processes, irreversible deformations and, therefore, aneurysmal degeneration.

3.1.1.7 *Surgical and Histopathological findings*

Clinical outcomes obtained from the histological analyses and the animal model overall confirm the occurrence of some expected pathological events that have been theoretically predicted by the biomechanical results. The immediate outcome –at day 0 (D0)– of the surgical implant of both reinforced and not reinforced group is shown in Fig. 21A. The not reinforced PA clearly already exhibits an over distension (25±3 mm) with respect to the more stable reinforced implant (16±2 mm).

The abnormal dilation of the non reinforced PA with respect to the dimensions of the surrounding native aorta then progressively increases up to approximately 40 mm, as the opened structure in Fig. 21C distinctly shows. On the other side, the long-term histological changes observed in the group polyester, documented by signs of inflammatory reaction to a foreign body, are the end results of the abnormal phenomena of transmural and endoluminal migration of the mesh cutting the PA wall, highlighted in Fig. 21D, where the knitted Dacron structure can be clearly identified within the PA wall. This fact can be related to a sort of mechanically induced "cage-effect", which
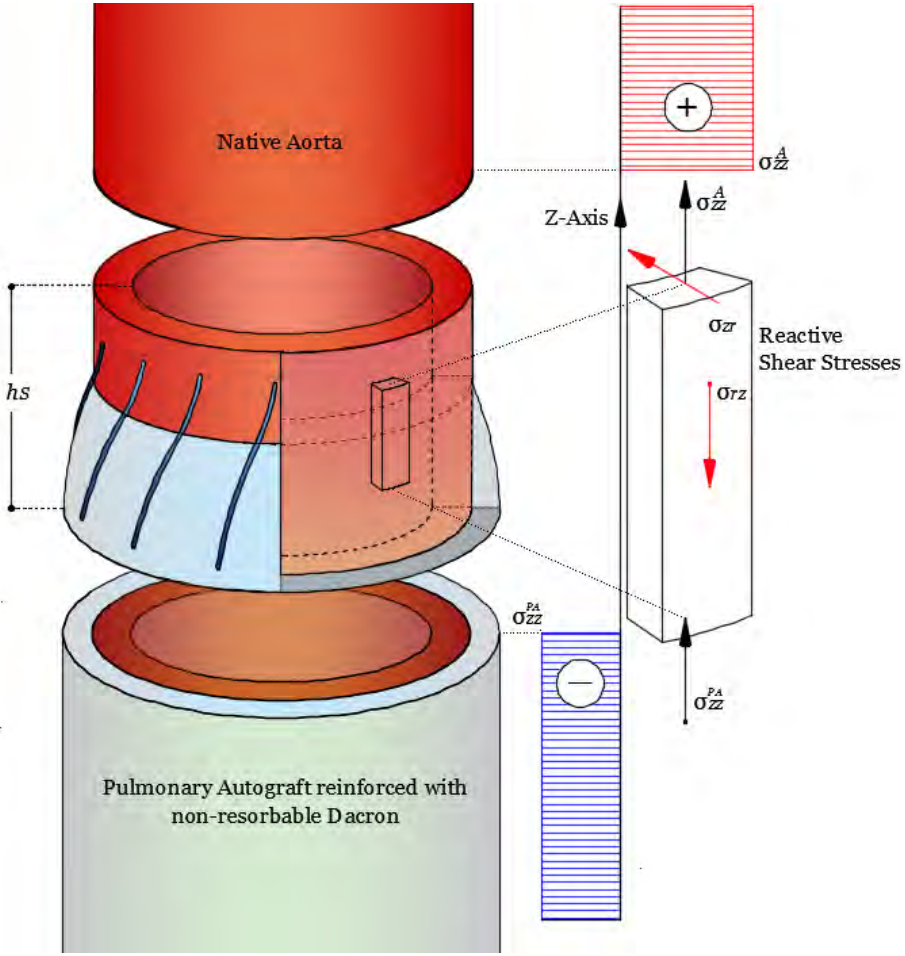
Figure 16: Illustration of the spurious stress state emerging in the anastomosis region, along the suture line.

produces the particular vessel wall configuration also shown in Fig. 18). As a matter of fact, the vessel tissue –which already suffers from the anomalous compressive hoop stresses due to the excessive confinement that degrades its mechanical properties– is locally over-stressed by the pressure exerted by the Dacron wires: the PA material is therefore damaged and thus resorbs, allowing the polyester fibers to penetrate across the wall thickness, finally leading to a gradual embedding of the Dacron structure, as illustrated in Fig. 22B.

Histological pathways was a conspicuous inflammatory infiltrate and fewer smooth muscle cells and more interstitial connective tissue could be seen with respect to control. Abnormal processing of the extracellular matrix protein fibrillin 1 by vascular smooth-muscle cells initiates detachment of vascular smooth-muscle cells from the extracellular matrix, leading to the release of matrix metalloproteinases (MMPs) together with their tissue inhibitors. The resulting matrix disruption, elastin and lamellar fragmentation lead to increased apoptosis of vascular smooth-muscle cells
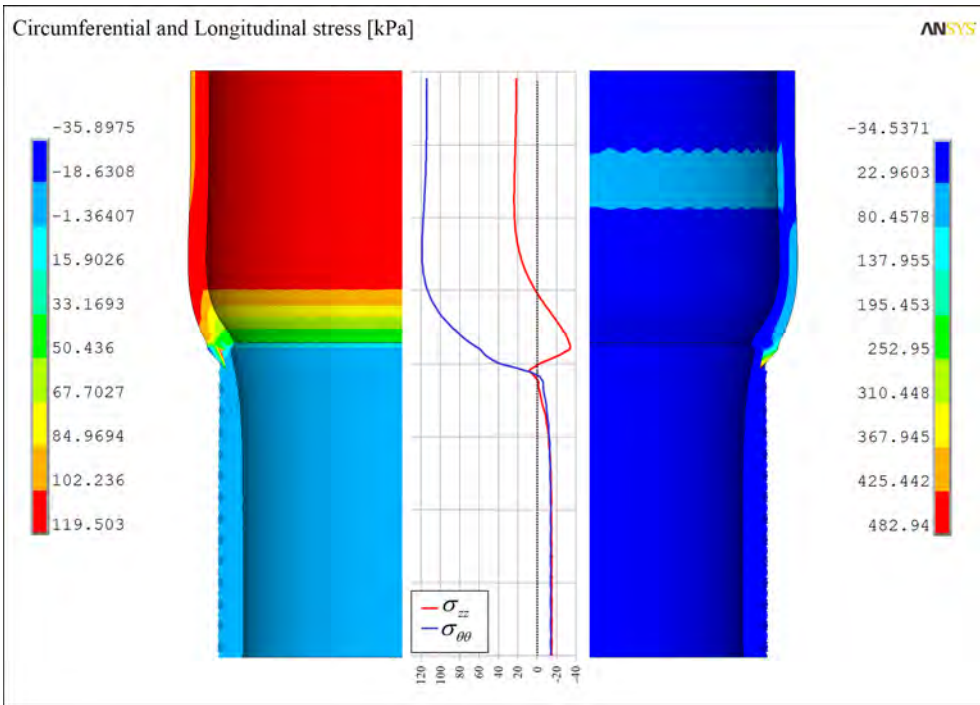
Figure 17: Numerical simulation provides the quantitative estimation of shear stresses at the reinforced PA-aorta interface.

and disruption of the media layer (see Fig.22A), adversely affecting the structural integrity and flexibility of the autograft reinforced with polyester mesh.

In the control, intima denudation and media disruptions were observed (Fig. 22B). In the tunica media, smooth muscle cells were present, but had irregular profiles and no discernible alignment; moreover, cells were widely spaced with intervening collagen fibers, grouped in thick and dense bundles. Deeper in the media, scant elastic fibers formed irregular fascicles. Adventitia was formed by dense connective tissue.

All the qualitative considerations derived from the biomechanical analysis of the vessel walls stresses have been then traced in the histological observations. The histological study of the polyester group actually revealed a pathological structure of the vessel section constituents, presenting noticeable intimal hyperplasia, inflammatory reaction and adventitial fibrosis at 10 weeks (see Fig. 22C). Moreover, experimental observations found that the intensification of these adverse phenomena can bring in a six-month period to an accentuation of reactive fibrosis and to the formation of localized calcifications in the *tunica media*, as reported in Fig. 22E. Also, the *ex vivo* examination revealed that the unfaithful remodeling circumstances predicted by the theoretical models can bring to the formation of macroscopic lesions, as well as to pathological thinning of the composite layers. The difference with the native grown and remodeled aorta clearly appears at six months, as shown in Fig. 22F.

Echocardiographic and angiographic measurements were taken by two independent observers blinded in regard to the treatment group. An interrater reliability analysis using the Kappa statistic was performed to determine consistency among raters.
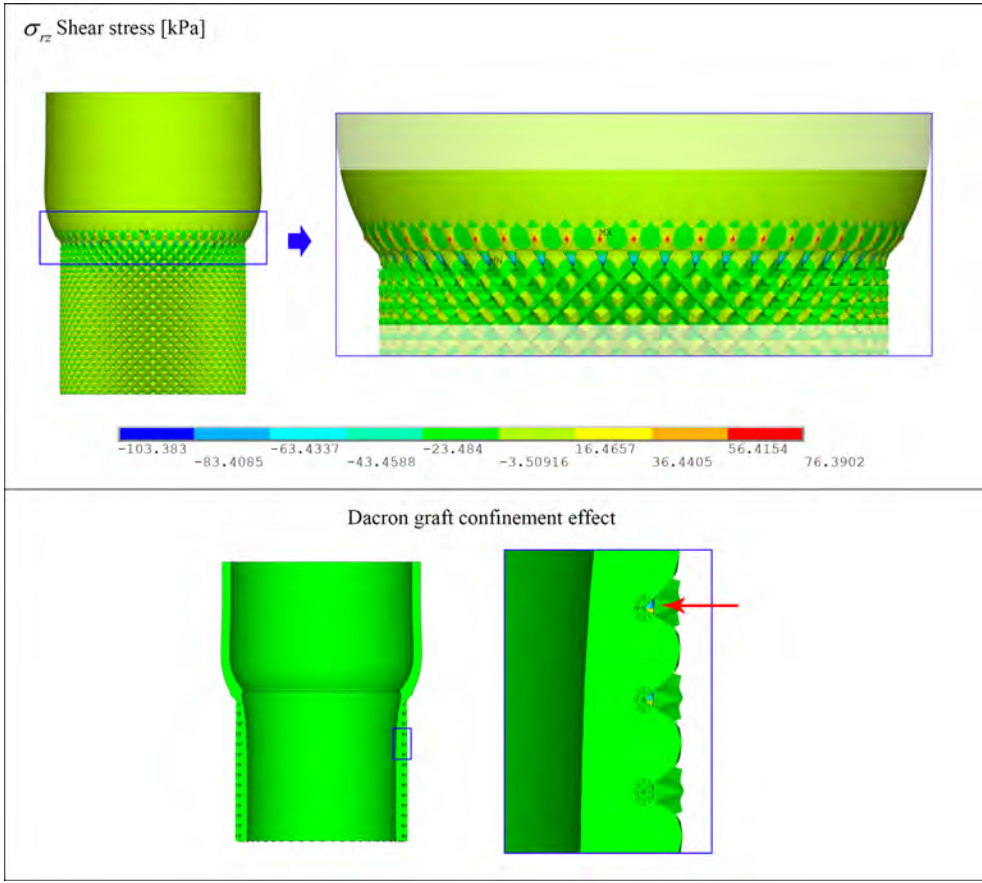
Figure 18: Illustration of the spurious shear stresses in the suture zone (Top), and of the Dacron structure confinement acting on the PA pressurized vessel (Bottom).

K coefficient was 0.82 indicating adequate agreement. Echocardiographic and angiographic time points were assessed at day 0 (D0) and 6 months (M6) postoperatively. Two main criteria guided the selection of the time span. The finally weight of animal fixed at 54±12 kg which might reliably reflect the body mass of the average human patients normally undergoing Ross operations. Also, this time period was assumed sufficient to observe a likely definitive growth and thus mature remodelling outcomes. In the PA alone group, an instantaneous distension of implanted trunk (25±3 mm) was noted, followed by development of one case of intraluminal thrombosis at ten weeks (39±3 mm, P<0.001, see Fig. 22G-H). A 56% diameter increase was revealed with respect to D0 (Fig. 23) and indexed ratio of 2.5 with respect to reference. In the synthetic reinforcement group, the graft diameter increased initially to 16±2 mm, but remained stable at M6 (20±1 mm, indexed ratio 1.05; overall increase 5%, P=0.4).

Advances in biomechanical features, histological and molecular assessments should be used to get a better understanding of the mechanisms underlying the improved use of prosthesis Dacron graft in cardiovascular surgery. The unresolved issue are represented by evidence of the discrepancy between the elastomechanical properties of
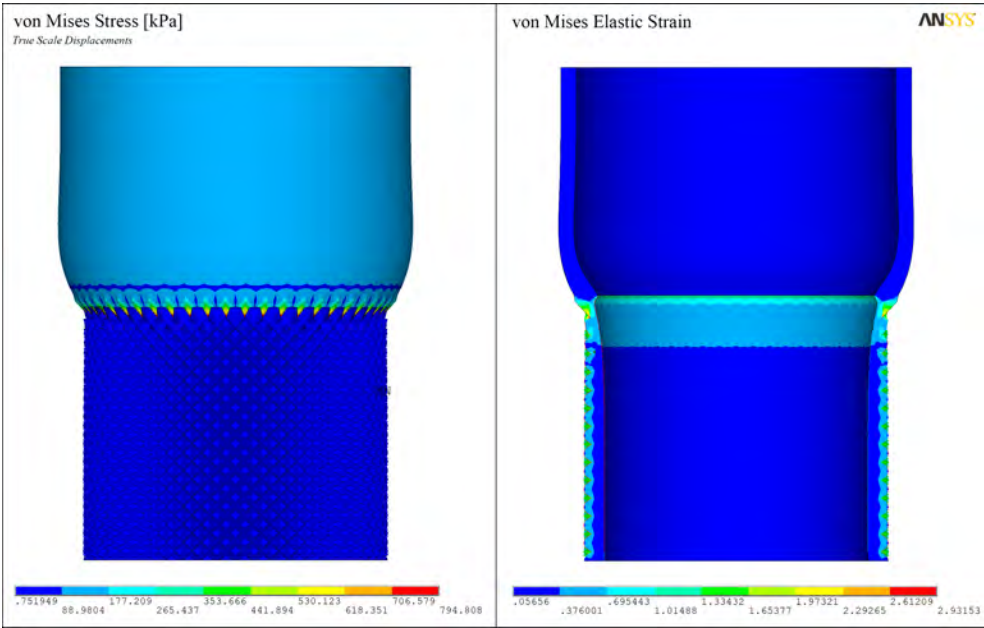
Figure 19: Von Mises equivalent stress concentrations (on the left) and equivalent strain (on the right).
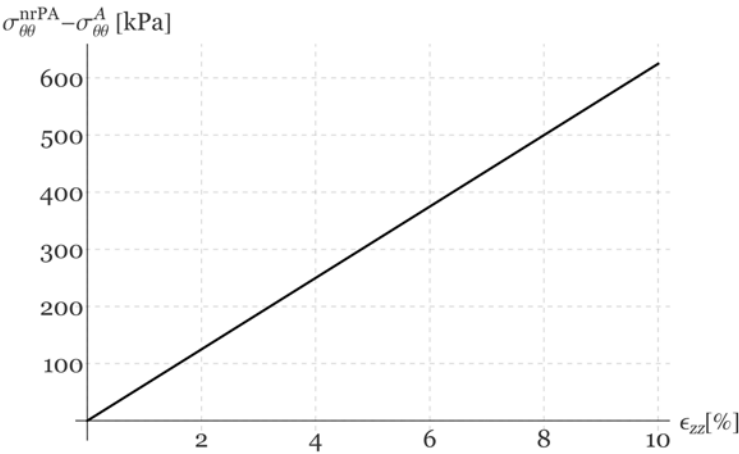
Figure 20: Circumferential stress increase in the non reinforced PA with respect to circumferential stress in the reference aorta, as a function of the longitudinal strain.

the grafts and of the native vessel favoring the worrisome sequelae both locally, at the anastomotic site, and, retrogradely, in terms of valve dysfunction and ventricular workload. In this realm, the results of the present study revealed the following findings: 1) the definition of a "compliance mismatch" phenomenon is appearing as a potentially important concern in cardiac surgery and might be responsible of daunting issues, especially in the long-term follow up of patients; 2) the mismatch between prosthetic
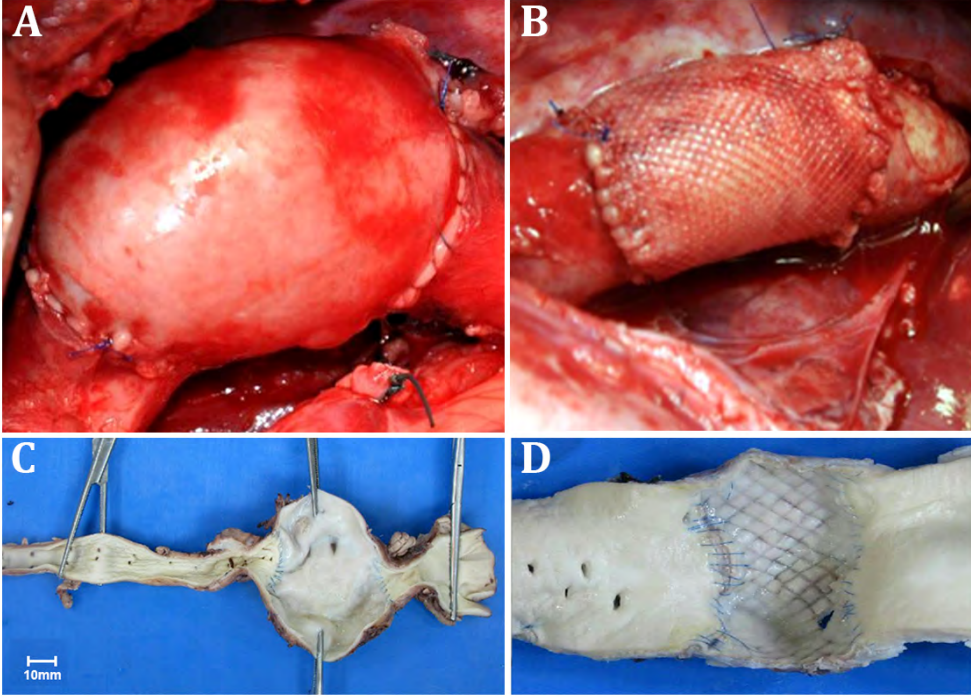
Figure 21: A. Not-reinforced PA at D0; **B**. The PA reinforcd with Dacron implant at D0; **C**. Not-reinforced PA trunk with aneurismal formation (analysis after the break at 3 months); **D**. The Dacron reinforcement cut through vessel wall at six months (M6);

material and native vessel biomechanical properties results in a considerable disadvantage determining "tissue incompatibility" that can exert detrimental effects on the normal efficiency of the pulmonary autograft; 3) the compliance loss induced by the interposition of an inextensible grafting at the level of the neoaortic root may impart excessive stresses on the suture line, leading to dangerous anastomotic aneurysm. In perspective, starting from this study and by enhancing the modeling by including at long-term mathematical descriptions of the biomechanical interaction among vessel growth and remodeling and syntetic grafts, it is felt that mechanically-oriented strategies can be envisaged and helpfully employed to find alternatives to the Dacron polymer structure in the PA transposition through the design optimization of new polymer-based composed prostheses systems.
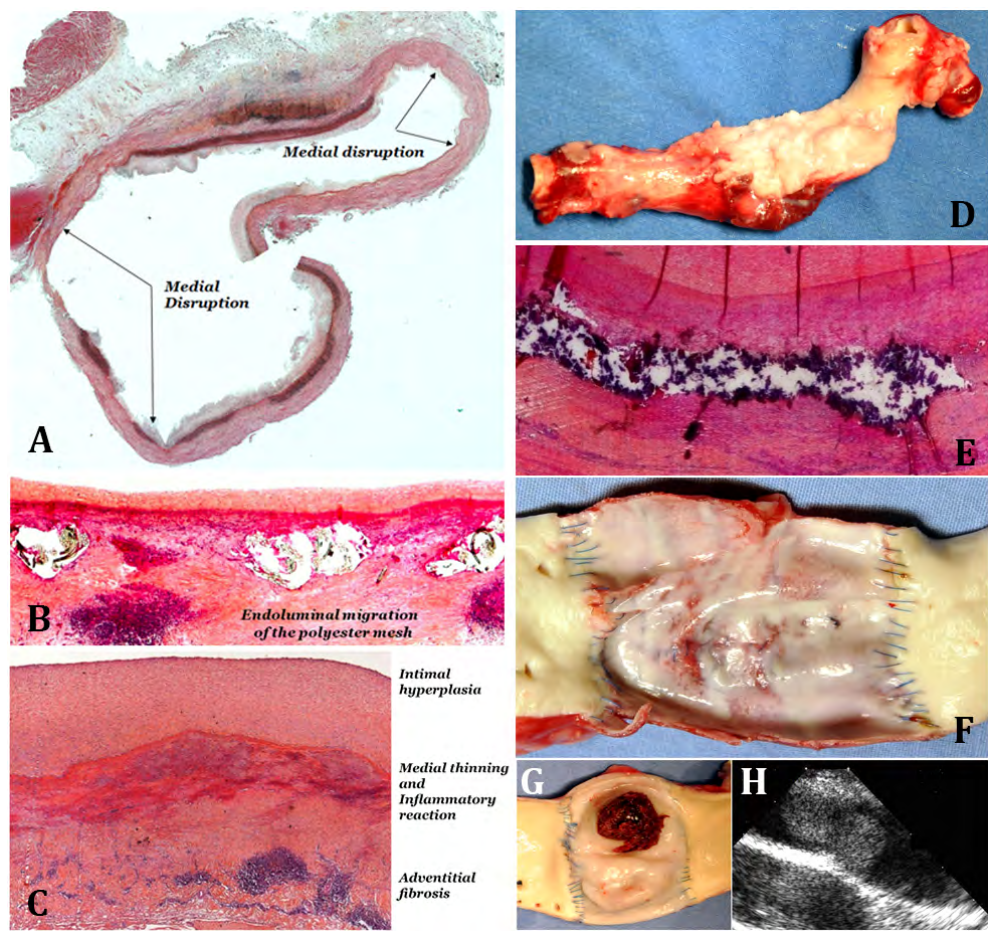
Figure 22: A. Medial disruption phenomena occurred at six months; **B**. Endoluminal migration of the polyester mesh at six months; **C**. Histological analysis of the Dacron reinforced pulmonary artery at 10 weeks; **D**. Reactive fibrosis of the external wall after removed of the reinforcement at six months; **E**. Localized calcification of the media at six months; **F**. Syntetic reinforcement macroscopic lesion at six months; **G**. Thrombus attached to the wall. Macroscopic lesion in PA alone explanted at 10 weeks; **H**. Echocardiographic control of the implant with throumbus.
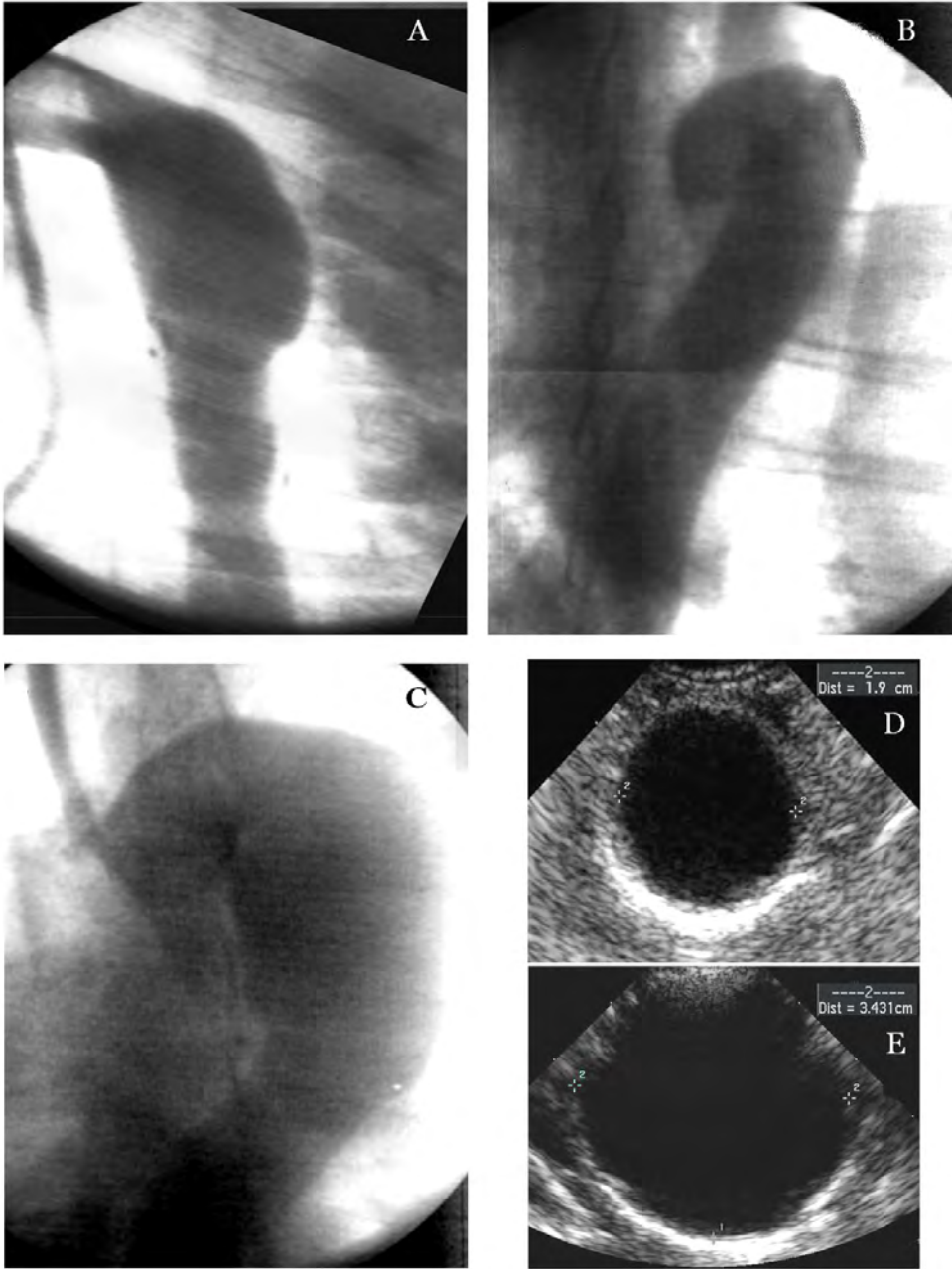
Figure 23: Angiographic controls: **A**. Non-reinforced group, at D0. **B**. Reinforced group, at D0. **C**. Non-reinforced group, at M6. Ecochardiographic controls at M6: **D**. Reinforced group. **E**. Non-reinforced group.

3.1.2   *The role of biomechanics in breast implants capsular contracture*

Breast Capsular Contracture (BCC) is one of the adverse complications occurring with greater incidence in breast augmentation surgical procedure. Its formation (see Fig. 24) can be interpreted as the conclusive phase of the physiological process known as response to a foreign body. By starting from a biochemical standpoint, the formation of the peri-prosthesic capsule is certainly a multifactorial process and many hypotheses concerning its etiology have been developed, as well as a number of pharmacological protocols have been suggested in Literature. However, the majority of the proposed theories seems to be only partially supported by clinical data. On the other hand, clinical follow-up and observed morphological microstructure of capsules with respect to the overall size of breast implants address the hypothesis that biomechanical interactions between prosthesis and host tissue may play a crucial role in the biological processes governing the phenomenon.
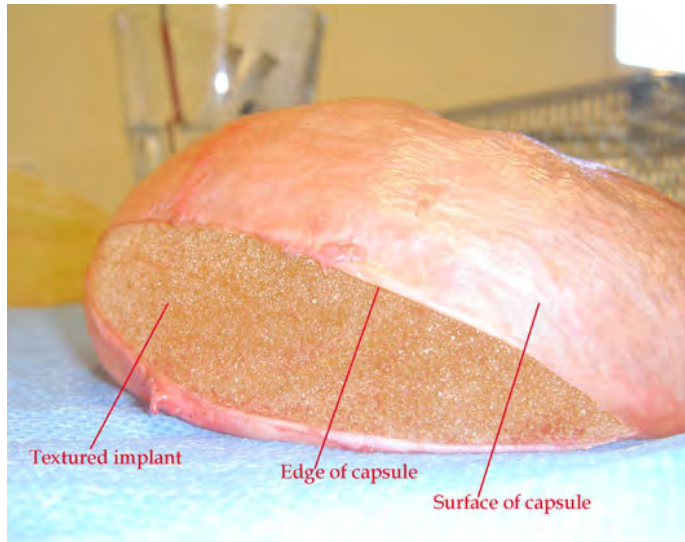
Figure 24: Silicon implant with a peri-prosthesic capsule.

Silicone breast implants have been widely used in both reconstructive and aesthetic surgery and breast augmentation has become, nowadays, one of the most frequently performed operations in plastic surgery: it is estimated, e.g., that more than 1% of the female population in the only USA has undergone this kind of operation ([134]). After breast augmentation, many complications may occur, such as double-bubble deformity, mal-position, breast ptosis, wrinkling and rippling, as well as hyperanimation deformity, hematoma and seroma. Anyway, the most common postoperative complication in breast reconstruction and augmentation is certainly the capsular contracture; as well known, this phenomenon is the formation of a fibrotic capsule around the breast implant as the conclusive phase of the physiological process known as response to a foreign body. Although this peri-prosthetic capsule is useful to the primary stabilization of the implant keeping it in its proper position in the breast, it frequently contracts around the prosthesis, generating on its surface an anomalous pressure increase. This process causes deformity and hardening of the breast, with consequent

pain for the patient; it may appear since the early post-operative period until some years after the breast augmentation ([218]) and it's also the primary reason for revision in breast implant studies, ranging from 15% to 30%, with up to 50.000 patients treated yearly ([19, 188]). Such far-ranging statistical data have urged Literature to investigate capsular contracture etiology suggesting different pharmacological protocols in order to minimize its incidence and consequences. By starting from a biochemical standpoint, many hypotheses concerning capsular contracture etiology have been developed, but the majority of the proposed theories seems to be only partially supported by clinical data. Capsular contracture can be regarded as the net result of the interaction among different factors –such as, e.g., bacteria contamination, tissue trauma, surgical technique, implant geometry– that ultimately result in a pathologic state ([2, 154]), but it's not clear, at the moment, how and how much each factor has influence on the origin and the development of this pathology. Many studies regarding the effectiveness of different drugs in the treatment or prevention of capsular contracture have been carried out in the last years, but further controlled experiments in humans are required ([18, 71, 175, 218]). The most applied practiced pharmacological protocol to prevent this complication is the prophylactic administering of antimicrobial agents. Indeed, breast pocket irrigation has been universally recommended for many years; but, since multiple bacteria seem to be implicated in the pathogenesis of capsular contracture, many of the irrigations used by surgeons have been inadequate to give broad-spectrum coverage against these bacteria ([2]). The remarkable decrease in capsular contracture achieved with the polyurethane foam-covered implants and the contemporary questions about the safety of these kind of devices related to their no longer manufacture drove to turn out mammary implants with textured surfaces with the aim of achieving the same favorable outcomes ([59, 134, 211]). What is currently sure is that any capsular contracture benefit of polyurethane devices was due to biochemical effects on the capsule and not to the surface texture ([2]); however there is still a lack of definitive data to support a real benefit of texturization in regard to capsular contracture ([59, 153]). At the moment, the gold standard for the treatment of this pathology is a total capsulectomy, which consists of a removal of the entire affected capsule and implant. When treating a contracted capsule, it is advisable to use a new implant in the affected breast, other than considering a site change or, in extreme cases, moving the implant to a fresh pocket ([2]). The will to avoid this kind of complication with so high economic and clinical impact suggested researchers to explore the mechanisms at the basis of this pathology, but, up to the present, none of the proposed studies concern the merely mechanical aspect of the problem. Clinical follow-up and observed morphological microstructure of capsule, with respect to the overall size of breast implants, address the hypothesis that biomechanical interactions between prosthesis and host tissue may play a crucial role in the biological processes governing the phenomenon. To encounter these phenomenological aspect from a mechanical point of view, an analytical biomechanical model of the fibrotic capsule growing around the prosthesis has been developed, with the aim both of analyzing the mechanical interactions of the two bodies –by evaluating mutual forces exerted across their surfaces– and of interpreting the role of these forces in terms of the negative outcomes characterizing the capsular contracture phenomenon. This is pursued by analyzing by modeling the growth of an elastic homogeneous mass lying on a spherical substrate, an approach frequently encountered in literature and formu-

lated by means both of a non-linear and a linear case (see e.g. the works by Defalias [50] as well as by Araujo and McElwain [12]). The linear approach furnishes from a side a considerable mathematical simplification and somehow neglects the complexity of the soft tissue constitutive behavior, but, on the other hand, it may find particularly helpful in order to interpret from a mechanical standpoint the phenomenona underlying the adverse outcomes related to the formation of the periprosthesic fibrotic capsule.

3.1.3 *Basic Equations of a linear elastic continuum with growth associated deformation*

The observed microscopic anatomy of the tissue growing around the mammary implants ([56, 157, 168]) addressed us to model the fibrotic capsule like a hollow sphere made of isotropic material growing around the prosthesis, whose geometry has been considered spherical. In order to define the suitable boundary value problem, the formal analogy between the thermo-elasticity equations and the ones ruling biological tissues growth mechanics has been used ([127]), the latter providing a parallel between thermal and growth-associated inelastic strain. In particular, the growth of a homogeneous elastic biological material around a spherical substrate, which is the mammary prosthesis, has been simulated in order to study the mechanical influence of this fibrotic layer in terms of exchanged forces, both at the (lower) capsule-prosthesis and at the (upper) capsule-breast interfaces. The kinematics of elastic mass growth has been addressed in continuum mechanics on the basis of the well-established multiplicative decomposition of the deformation gradient $\mathbf{F} = \mathbf{F}_e\mathbf{F}_g$, where $\mathbf{F}_e$ is the elastic component and $\mathbf{F}_g$ the growth one ([48, 164]), both of them singularly not representing a true gradient. Given the symmetry of the spherical problem at hand and a linearly elastic and isotropic constitutive behavior, the classical linear isotropic elasticity law involving a Green-Lagrange strain measure will be first employed for describing the effects of small strains. Under this assumption, the above mentioned decomposition of the deformation gradient can be reformulated in a way to have an additive decomposition of the linearized strain tensor into the sum of an elastic and a pure growth aliquots, in complete agreement with a classical thermo-elastic analogy, i.e.

$$\mathbf{E} = \mathbf{E}_e + \mathbf{E}_g = \mathbb{S} : \boldsymbol{\sigma} + g\,\boldsymbol{\Gamma},$$
$$\mathbf{E} = \operatorname{sym}\left(\mathbf{u} \otimes \nabla\right) \tag{3.10}$$

where $\mathbf{u} \in C^2\left(\Omega\right)$ is the displacement vector function defined on a closed subset $\Omega \subset \mathbb{R}^3$, $g\,\boldsymbol{\Gamma}$ is a growth strain tensor, with $g \in \mathbb{R}$ being a pure volumetric growth strain function and the matrix $\boldsymbol{\Gamma} = \operatorname{Diag}\{\gamma_k\}$ containing the anisotropic multipliers for each principal direction so that $tr\left(\boldsymbol{\Gamma}\right) = \sum_k \gamma_k = 1$, whereas $\boldsymbol{\sigma} = \{\sigma_{ij}\}$ is the Cauchy stress tensor and $\mathbb{S}$ represents the compliance fourth rank tensor. By deriving the stress tensor $\boldsymbol{\sigma}$ from equation $(3.10)_1$ and by introducing the elastic stiffness tensor $\mathbb{C} = \mathbb{S}^{-1} = 2\mu\mathbb{I} + \Lambda\mathbf{I} \odot \mathbf{I}$ (here given in terms of the Lamé moduli μ and Λ, while $\mathbb{I}$ and $\mathbf{I}$ are respectively the fourth order and the second order identity tensors), the

constitutive relation and the quasi-static equations of motions in three dimensions read as

$$\boldsymbol{\sigma} = \mathbb{C} : (\mathbf{E} - \boldsymbol{\Gamma}\, g)$$
$$\nabla \cdot \boldsymbol{\sigma} = -\mathbf{b}, \tag{3.11}$$
$$\boldsymbol{\sigma} = \boldsymbol{\sigma}^{\mathsf{T}}$$

in which the superscript T denotes the transpose, $\mathbf{b}$ the body force vector and $\nabla \cdot (\cdot)$ is the divergence operator. The Cauchy stress is then directly connected to the pure elastic strain and, more precisely, it is usually derived from the well known de Saint Venant-Kirchhoff strain energy density:

$$W\left(\mathbf{E}_e\right) = \mu\, tr\left(\mathbf{E}_e^2\right) + \frac{\Lambda}{2} tr\left(\mathbf{E}_e\right)^2 \tag{3.12}$$

under the further hypothesis of small strain, with the stress tensor then resulting $\boldsymbol{\sigma} = \partial W/\partial \mathbf{E}_e$. The direct coupling of compatibility equations $(3.10)_2$ with both constitutive law $(3.11)_1$ and equilibrium equation $(3.11)_2$ gives the Navier-Cauchy equations:

$$\mu \nabla \cdot (\mathbf{u} \otimes \nabla) + \mu \nabla \cdot (\nabla \otimes \mathbf{u}) + \Lambda \nabla (\nabla \cdot \mathbf{u}) +$$
$$- 2\mu \left(\nabla \cdot \boldsymbol{\Gamma}\, g + \boldsymbol{\Gamma} \cdot \nabla g\right) - \Lambda \nabla g = \mathbf{0} \tag{3.13}$$

in which body forces have been neglected. The statement of the boundary value problem (BVP) also provides the prescription of suitable boundary conditions, either by imposing known displacements $\overline{u}$ in correspondence of the subset points $\partial\Omega_u \subseteq \Omega$ subjected to constraints acting along the direction $\mathbf{n}_u$ (i.e. $\mathbf{u} \cdot \mathbf{n}_u = \overline{u}$), or by assigning traction $\mathbf{t}$ on the loaded surface $\partial\Omega_t \subseteq \Omega$ –identified by the normal vector $\mathbf{n}_t$– through the widely known Cauchy's theorem $\boldsymbol{\sigma} \cdot \mathbf{n}_t = \mathbf{t}$.

3.1.4 *Capsule-Breast system as a double-layered hollow sphere: analytic solution and clinical clues*

By focusing on a spherically symmetric and quasi-static case, a spherical frame of coordinates $\{r, \theta, \phi\}$ has been adopted, so that a bilayer composite hollow sphere has been used to describe the periprosthetic capsule-breast gland system. More precisely, the entire body volume Ω can be simply viewed by the union of the capsule region $\Omega^{(c)} = \{r \in \mathbb{R}^+/\{0\} : R_1 \leq r \leq R_2\}$ and the breast tissue region $\Omega^{(b)} = \{r \in \mathbb{R}^+/\{0\} : R_2 \leq r \leq R_3\}$, where the superscripts c and b indicate the capsule and the breast, respectively, while R_1 is the prosthetic capsule internal radius (coinciding with the implant radius), R_2 is the interface radius that accounts for the capsule thickness and R_3 is the external breast radius (see Fig. 25).

For each hollow spherical layer, the deformation tensor $(3.10)_2$ becomes $\mathbf{E}^{(i)} = \text{Diag}\left\{du^{(i)}/dr,\ u^{(i)}/r,\ u^{(i)}/r\right\}$ –the radial displacements $u^{(i)}$ being function of the sole radial coordinate r– and the the anisotropy coefficients matrix is written as $\boldsymbol{\Gamma}^{(i)} = \text{Diag}\left\{\gamma_r^{(i)},\ (1 - \gamma_r^{(i)})/2,\ (1 - \gamma_r^{(i)})/2\right\}$. In order to readily find analytic solutions in
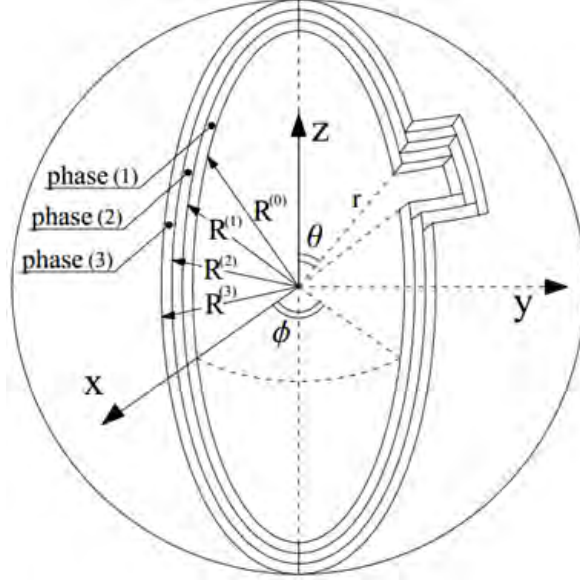
Figure 25: The multi-layer hollow sphere model

the most straightforward manner, one can introduce incompressibility relations for both the bodies. This imply a modification of the classical Kirchhoff potential (3.12) by introducing a pressure, say $q^{(i)}$ for each body, which represents a Lagrangean multiplier for ensuring the constant elastic volume constraint, then obtaining:

$$W^{(i)}\left(\mathbf{E}_e^{(i)}\right) = \mu^{(i)} tr\left((\mathbf{E}_e^{(i)})^2\right) + \frac{\Lambda^{(i)}}{2} tr\left(\mathbf{E}_e^{(i)}\right)^2 - q^{(i)} tr\left(\mathbf{E}_e^{(i)}\right) \qquad (3.14)$$

the two pressures then representing classical Lagrange multipliers. As a consequence, by deriving with respect to the deformation, the Cauchy stresses in a spherical eigenspace read:

$$\sigma_r^{(i)} = k^{(i)}\left(\left(1-\nu^{(i)}\right)\frac{du^{(i)}}{dr} + 2\nu^{(i)}\frac{u^{(i)}}{r} - \left(\nu^{(i)} + \left(1-2\nu^{(i)}\right)\gamma_r^{(i)}\right)g^{(i)}\right) - q^{(i)} \qquad (3.15)$$

$$\sigma_\theta^{(i)} = \sigma_\phi^{(i)} = k^{(i)}\left(\frac{u^{(i)}}{r} + \nu^{(i)}\frac{du^{(i)}}{dr} - \frac{1}{2}\left(1 - \left(1-2\nu^{(i)}\right)\gamma_r^{(i)}\right)g^{(i)}\right) - q^{(i)} \qquad (3.16)$$

where $k^{(i)} = E^{(i)}/((1+\nu^{(i)})(1-2\nu^{(i)}))$, $E^{(i)}$ and $\nu^{(i)}$ are the Young modulus and the Poisson ratio of each material, respectively. By invoking symmetry, a sole non-trivial equilibrium equation $d\sigma_r^{(i)}/dr + 2r^{-1}(\sigma_r^{(i)} - \sigma_\theta^{(i)}) = 0$ emerges from (3.11)$_2$. Further simplifications can be introduced by assuming both that the fibrotic capsule undergoes homogeneous growth, also the anisotropy multiplier $\gamma_r^{(c)}$ being taken constant, and that the surrounding breast tissue is in a not growing homeostatic state, i.e. the bulk net growth function $g^{(b)}$ is null. To close the problem, the method of Lagrange multipliers is applied, so that the two radial equilibrium equations (above mentioned) result coupled with the constant volume constraints. In this way an ODE system of four equations is obtained, the four unknowns being the two displacements

and the Lagrangean pressures. In addition, the BVP also provides the continuity of displacements and radial tensions are imposed at the interface, while the other boundary conditions are given by prescribing zero radial stress at the external radius $r = R_3$ and null displacement at $r = R_1$, in this way assuming the silicon prosthesis as a rigid substrate (due to the fluid incompressibility). Under these considerations, after few calculations one obtains:

$$
\begin{cases}
\frac{d}{dr}\left(\frac{1}{r^2}\frac{d}{dr}\left(r^2 u^{(c)}\right)\right) = \frac{1-2\nu^{(c)}}{1-\nu^{(c)}}\left(3\gamma_r^{(c)} - 1\right)\frac{g^{(c)}}{r} + \frac{\left(1-2\nu^{(c)}\right)\left(1+\nu^{(c)}\right)}{E^{(c)}\left(1-\nu^{(c)}\right)}\frac{dq^{(c)}}{dr} \\[2ex]
\frac{d}{dr}\left(\frac{1}{r^2}\frac{d}{dr}\left(r^2 u^{(b)}\right)\right) = \frac{\left(1-2\nu^{(b)}\right)\left(1+\nu^{(b)}\right)}{E^{(b)}\left(1-\nu^{(b)}\right)}\frac{dq^{(b)}}{dr} \\[2ex]
\frac{1}{r^2}\frac{d}{dr}\left(r^2 u^{(c)}\right) = g^{(c)} \\[2ex]
\frac{1}{r^2}\frac{d}{dr}\left(r^2 u^{(b)}\right) = 0 \\[2ex]
u^{(c)}|_{r=R_1} = 0 \\[2ex]
u^{(c)}|_{r=R_2} = u^{(b)}|_{r=R_2} \\[2ex]
\sigma_r^{(c)}|_{r=R_2} = \sigma_r^{(b)}|_{r=R_2} \\[2ex]
\sigma_r^{(b)}|_{r=R_3} = 0
\end{cases}
\tag{3.17}
$$

System (3.17) is in this form *de facto* uncoupled, so that it can be readily solved analytically in a cascade manner. Solutions were performed by using the commercial computational software *Mathematica*®([210]). Displacements are obtained from (3.17)$_{3,4}$ together with conditions (3.17)$_{5,6}$:

$$
u^{(c)} = \frac{g^{(c)}r}{3}\left(1 - \frac{R_1^3}{r^3}\right) \qquad \text{and} \qquad u^{(b)} = \frac{g^{(c)}\left(R_2^3 - R_1^3\right)}{3r^2}
\tag{3.18}
$$

The direct substitution of (3.18) in the first two equations of (3.17) let the pressures $q^{(c)}$ and $q^{(b)}$ be derived through a direct integration. It immediately follows that:

$$
q^{(c)} = Q^{(c)} + 2\mu^{(c)}g^{(c)}(1 - 3\gamma_r^{(c)})\log\left(\frac{r}{R_2}\right) \qquad \text{and} \qquad q^{(b)} = Q^{(b)}
\tag{3.19}
$$

In this way, the stresses within the capsule layer read:

$$
\sigma_r^{(c)} = 2\mu^{(c)}\frac{g^{(c)}}{3}\left((1 - 3\gamma_r^{(c)}) + 2\frac{R_1^3}{r^3}\right) - 2\mu^{(c)}g^{(c)}(1 - 3\gamma_r^{(c)})\log\left(\frac{r}{R_2}\right) - Q^{(c)}
\tag{3.20}
$$

$$
\sigma_\theta^{(c)} = -\mu^{(c)}\frac{g^{(c)}}{3}\left((1 - 3\gamma_r^{(c)}) + 2\frac{R_1^3}{r^3}\right) - 2\mu^{(c)}g^{(c)}(1 - 3\gamma_r^{(c)})\log\left(\frac{r}{R_2}\right) - Q^{(c)}
\tag{3.21}
$$

and, in the breast external shell, one has

$$\sigma_r^{(b)} = -4\mu^{(b)} \frac{g^{(c)} \left(R_2^3 - R_1^3\right)}{3r^3} - Q^{(b)}$$
$$\sigma_\theta^{(b)} = 2\mu^{(c)} \frac{g^{(c)} \left(R_2^3 - R_1^3\right)}{3r^3} - Q^{(b)}$$

(3.22)

where, in (3.19), (3.22) and (3.20), $Q^{(c)}$ and $Q^{(b)}$ are integration constants given by:

$$Q^{(b)} = -\frac{4g^{(c)}\mu^{(b)} \left(R_2^3 - R_1^3\right)}{3R_3^3}$$

(3.23)

$$Q^{(c)} = \frac{4g^{(c)}}{3} \left(\mu^{(c)} \left(\left(\frac{R_1}{R_2}\right)^3 + \frac{1}{2}\left(1 - 3\gamma_r^{(c)}\right)\right) + \mu^{(b)} \left(\frac{1}{R_2^3} - \frac{1}{R_3^3}\right)\left(R_2^3 - R_1^3\right)\right)$$

(3.24)

The linear analysis carried out shows how the growth of the fibrotic periprosthetic capsule –modeled in terms of an inelastic strain $g^{(c)}$– implies the accumulation of a self-equilibrated (residual) stress which can give some important suggestions for analyzing the biomechanical reasons underlying the clinically observed adverse phenomena of the capsular contracture. The deformations obtainable from the displacement functions (3.18), in the light of the linear analysis proposed, suggests a good reliability of the solutions up to a 10 % of growth strain, this value being then effectively adopted for the present results. A capsule thickness of 3 mm has been assumed, coherently with the most of the experimental observations. Regarding the material parameters, an almost incompressible Poisson's ratio has been used, equal to 0.495 coherently with the majority of the literature works concerning the study of the breast tissue mechanical properties, as well as the Young modulus that was set to $E^{(c)} = 28$ MPa in accord with the averaged values proposed in literature ([157]). By observing the stress distributions over the capsule thickness, reported in Fig. 26, it clearly emerges that the radial stresses arising in the capsule generate a state of compression in the surrounding breast tissue, which can effectively justify the clinical evidence of painful sensations. The circumferential stresses –relevant in magnitude with respect to the radial ones in the capsule– can be directly connected to the hardening of the capsule. Indeed the phenomenon of contraction is explained in the clinical practice as a circumferential tightening which acts as a "wrap", making the implant feel hard and loose mobility. Also, the combined actions of radial tractions and negative hoop stresses can be involved in the detachment phenomena observed at the capsule-prosthesis interface, and this particular conformation can likely concur in determining the wrinkling of the prosthesis surface, detectable by means of a nonlinear analysis.

The high circumferential compression are substantially independent from the implant sizes and the capsule thickness (see Fig. 27). Radial stresses instead exhibit a direct proportionality with the capsule thickness, *de facto* demonstrating the positive correlation between capsular thickness and Baker clinical score ([155]). Conversely, an inverse proportionality with the prosthesis size suggesting a higher incidence of capsular contracture in the case of smaller implants.

3.1.4.1 *Finite Element-based computational model*

Standard round smooth silicone gel-filled breast implants have been considered. Numerical simulations, implemented by means of the code ANSYS®([1]), have been car-
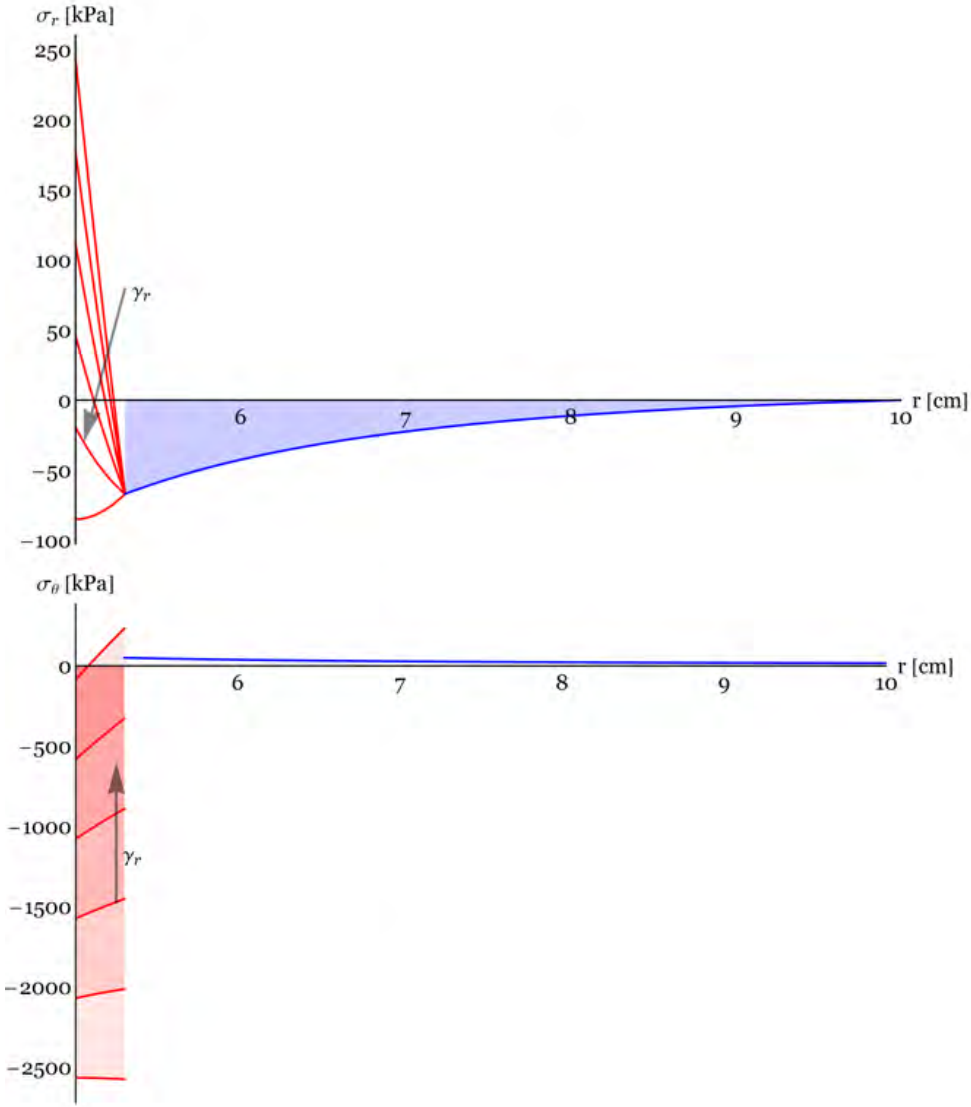
Figure 26: Stresses in the capsula-breast system. The stresses within the capsula generate a state of compression in the overlying breast tissue (top). The negative circumferential stress is instead responsible of the capsule hardening. Stresses in the capsula are plotted by varying the anisotropy coefficient γ_r.

ried out by referring to breast implant sizes ranging from 100 cc to 400 cc, values suggested by surgical follow-up. In order to create a 3-D model to be used in a FEM context, a parametric reconstruction algorithm has been defined. We referred to a standard round gel-filled prosthesis, which has been regarded as a solid of revolution, obtained by rotating the surface S, shown in Fig. 28, around axis y. As shown in Fig. 28, surface S has been described in a parametric way, where:
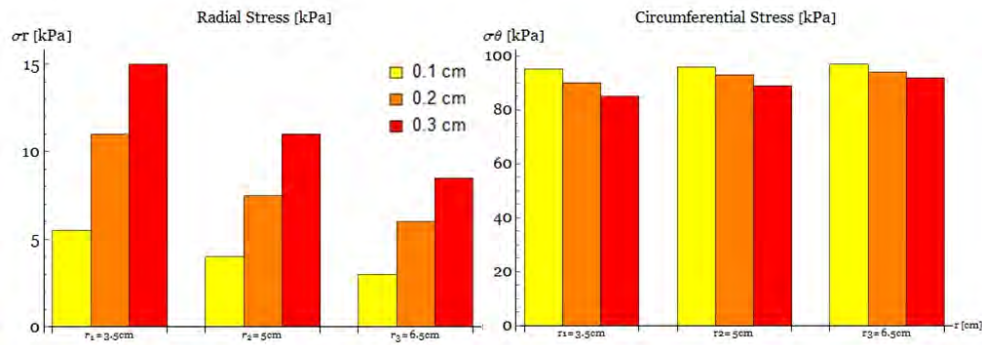
Figure 27: Correlation between stress, prosthesis size (ideal spherical model) and capsular thickness.
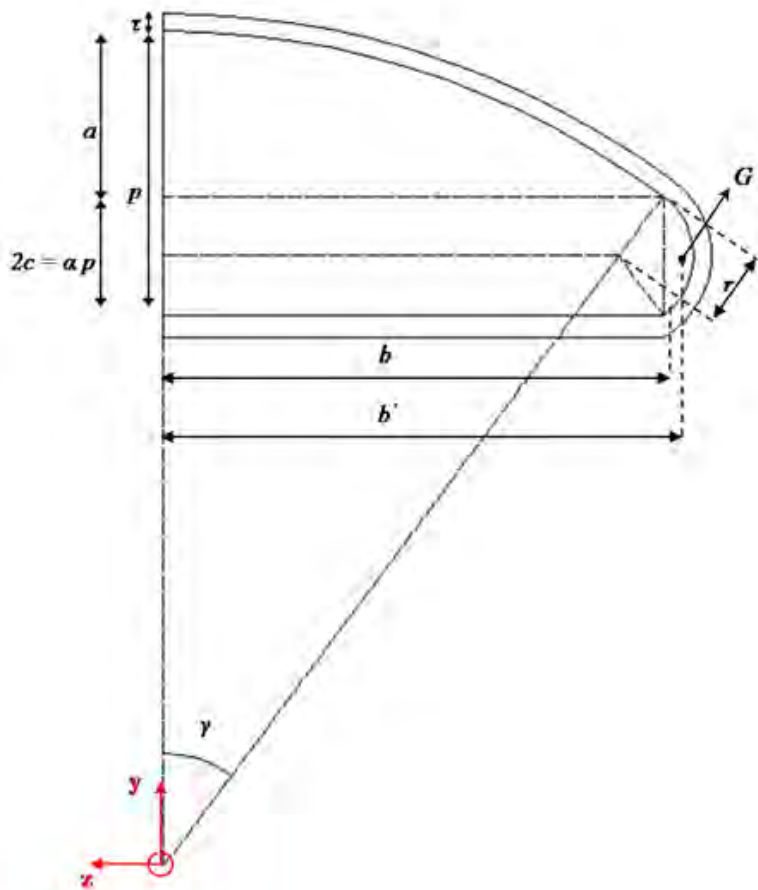
Figure 28: Geometrical features of the breast implant reconstruction.

$$a = (1 - \alpha)p \tag{3.25}$$

$$b = D/2 \tag{3.26}$$

$$c = p/2 \tag{3.27}$$

$$R = (a^2 + b^2)/2a \tag{3.28}$$

$$r = c(a^2 + b^2)/(b^2 - a^2) \tag{3.29}$$

$$\gamma = \arctan[b/(R - a)] \tag{3.30}$$

$$\sin \gamma = b/R \tag{3.31}$$

$$\cos \gamma = (R - a)/R \tag{3.32}$$

Notation is different from that used in the analytical model: p is prosthesis projection, b is half diameter, τ is the pathologic capsular thickness, b' is the x-axis of the center of gravity of circular segment with basis $2c = \alpha p$ and radius r. As previously, we assumed $\tau = 3$mm, that is the average value of the pathologic capsular thickness found in literature. The geometric symmetry of the problem and the mechanical conditions let us carry out perform FEM analysis on a volume V, equal to a quarter of the entire prosthesis, calculated as $V = V_1 + V_2$, where:

$$V_1 = \frac{\pi a^2}{4} \left(R - \frac{a}{3} \right) \tag{3.33}$$

$$V_2 = \frac{\pi}{2} \left(\frac{b}{2} S_1 + b' S_2 \right), \tag{3.34}$$

$$b' = b + r \left[\frac{\cos^3 \gamma}{\left(\frac{\pi}{2} - \gamma \right) - \sin \gamma \cos \gamma} - \sin \gamma \right] \tag{3.35}$$

where S_1 is the surface of the rectangle with basis b and height $2c$ and S_2 is the surface of the circular segment with basis $2c = \alpha p$ and radius r. This custom-made algorithm let us to obtain the specific geometric model for any size of the prosthesis, inputting only the projection p and the diameter D, values simply available from manufactures web sites. The element type chosen to mesh the volumes is 8 nodes hexahedral whit 3 degrees of freedom and linear shape functions for each node. A very fine mesh (about 100.000 elements) let us to minimize geometric distortions and structural error energy. Figure 29 shows 250cc half prosthesis-capsular mesh.

Both the silicone and the capsular tissue have been considered homogeneous, isotropic and linear elastic materials. We set $E^{(c)} = 28$MPa as the average value found in Literature for pathologic status ([157]) and $E^{(s)} = 3$MPa ([46]); both silicone and capsule have been considered near to be incompressible. The formal analogy between equations ruling growth and thermo-elasticity has been used again, so linear quasi-static thermo-elastic analyses have been carried out. We set a thermal load $|\Delta T| = 10°C$ and the thermal dilation coefficient was set to $\beta_T = 0.01[T^{-1}]$, in order to obtain a volumetric contraction of the capsular tissue of about 10%. Capsule thickness was still equal to 3 mm. In particular, the inverse proportionality of the interface average stress with the prosthesis size has been confirmed also by looking at the numerical results (Fig. 30), which let to obtain a more faithful geometrical description.
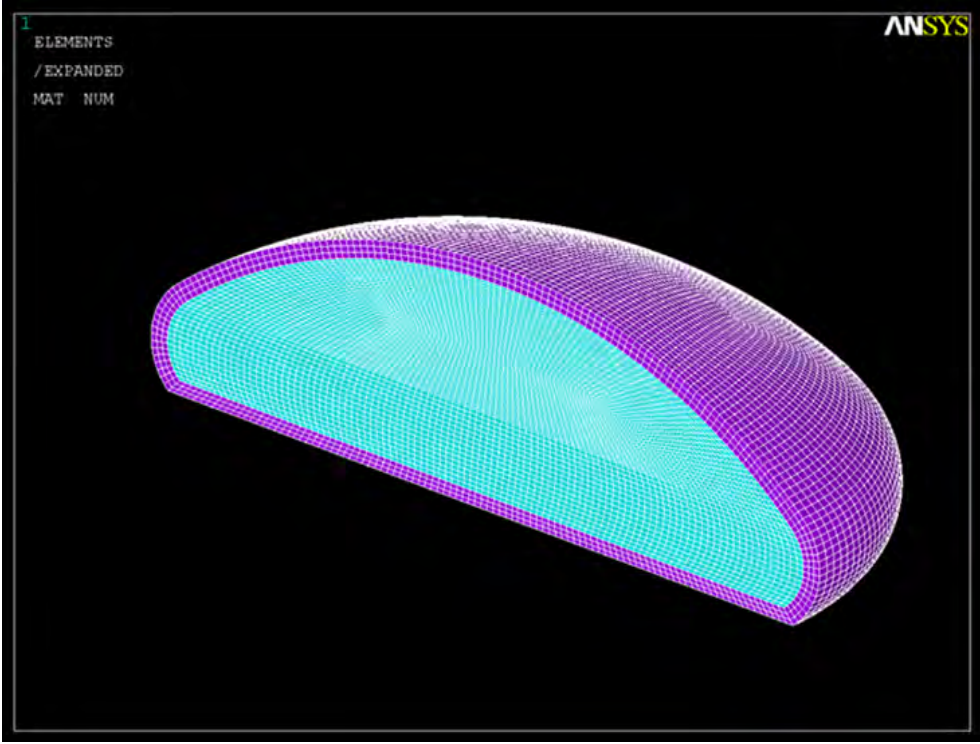
Figure 29: A half 250 cc prosthesis-capsular mesh

Thermo-growth analogy

It is here briefly reported (for a spherically symmetric case) the direct comparison between the thermoelastic constitutive equations and the stress-strain relationship including a growth-associated term, in order to highlight the substantial analogy between thermal and growth induced deformations, i.e. $\mathbf{A}\vartheta \leftrightarrow \mathbf{\Gamma}g$, with ϑ and $\mathbf{A}$ respectively denoting the temperature scalar field and the thermal dilatation coefficient matrix:

$$\begin{cases} \sigma_r = \frac{E}{(1+\nu)(1-2\nu)} \left[(1-\nu)\,\varepsilon_r + 2\nu\,\varepsilon_\theta - (1+\nu)\,\alpha_r\,\Delta\vartheta \right] \\ \sigma_\theta = \frac{E}{(1+\nu)(1-2\nu)} \left[\varepsilon_\theta + \nu\,\varepsilon_r - (1+\nu)\,\alpha_\theta\,\Delta\vartheta \right] \\ \frac{\rho\,c}{k_\vartheta}\frac{\partial\vartheta}{\partial t} + \frac{\vartheta'\,\beta}{k_\vartheta}\frac{\partial(\varepsilon_r+2\varepsilon_\theta)}{\partial t} = \frac{1}{r^2}\frac{\partial\left(r^2\vartheta\right)}{\partial r} + Q_\vartheta \end{cases} \quad (3.36)$$

$$\begin{cases} \sigma_r = \frac{E}{(1+\nu)(1-2\nu)} \left[(1-\nu)\,\varepsilon_r + 2\nu\,\varepsilon_\theta - \gamma_r g \right] \\ \sigma_\theta = \frac{E}{(1+\nu)(1-2\nu)} \left[\varepsilon_\theta + \nu\,\varepsilon_r - \gamma_\theta g \right] \\ \frac{\partial g}{\partial t} = \mathcal{G}\left(g,\sigma\right) \end{cases} \quad (3.37)$$

It is worth noting that the full analogy provides also the introduction of a evolutionary growth counterpart of the well-known Fourier's heat equation $(3.36)_3$. Equation $(3.37)_3$ then represents a scalar equation (or a system) coupled with the mechanical problem in order to determine the evolution of the growth term g.
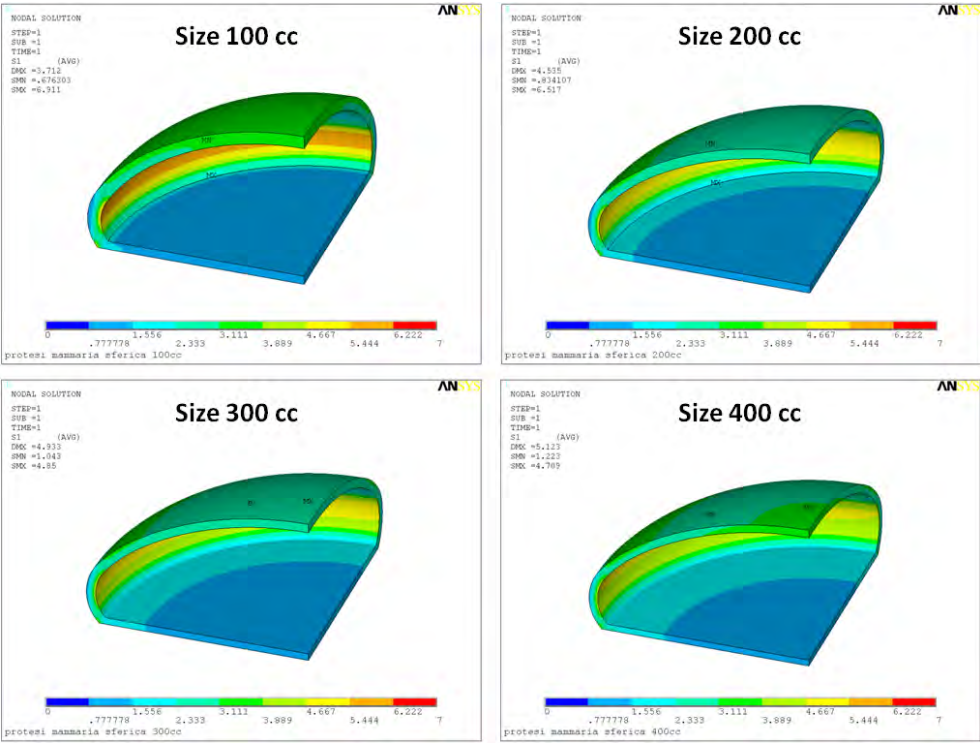
Figure 30: Medium capsular pressure versus size

3.1.5 *Volterra-Lotka equations to predict BMU remodelling*

Bone is a complex tissue that, as the most of living tissues, is being dynamically subjected to repair and synthesis processes throughout an individual's life [219]. These processes of continuous rebuilt and repair are known to affect bone tissue mechanical response. For example, among the several theories focusing on bone mechanics, Cowin and Hegedus's *theory of adaptive elasticity* [47] provides that bone tissue elastic constants are weighted by the volume fractions, which accounts for the tissue porosity and also enters as a key variable into bone-implants optimization procedures (see for example Fraldi et al. [62]). The macroscopic mechanical properties of bone tissue are determined, at the cell scale, by the continuous activity of different type of cells, responsible of resorbing and synthesizing new bone matrix constituents, also in response to mechanical signaling, such as local microstrain [81], stress concentrations and microdamage [73].

The process by which bone adapts its internal microstructure and subsequently changes its mechanical properties in relation to the specific mechanical and physiological environment is denoted as *bone remodelling cycle.* As anticipated, bone remodeling consists of two leading sub-processes: the resorption of old bone and the formation of new bone. At the cellular level, the former is performed by *osteoclasts* (OCLs), multinuclear cells of hematopoietic origin, while the latter is carried out by *osteoblasts* (OBLs), which are mononuclear cells of mesenchymal origin ([219]).

Therefore bone remodelling can be interpreted as the result of the *interaction* of different cellular species forming the BMUs ("Basic Multicellular Units"). The whole process is regulated by the opposite actions of the two aforementioned cell species. Osteoclasts excavate a resorption space that is subsequently filled with new bone tissue by osteoblasts. In cortical bone osteoclasts dig tunnels through solid bone while in trabecular bone they dig trenches across the trabecular surface, while osteoblasts fill these resorption cavities creating osteons and hemi-osteons respectively, which are aligned to the dominant loading isostatics. As a result bone tissue is continuously broken down by osteoclasts and rebuilt by osteoblasts and a well-known macroscopic evidence is that bone tissue fibres are oriented in the meaning loading directions (Wolff's laws); so, it can be hypothesized that mechanical signaling regulating bone macroscopic properties *de facto* directly orients cellular activity. The biochemical coupling factor between osteoclast resorption and osteoblast remodelling is then assumed to have a mechanical origin, and recent studies showed that metabolic process is controlled by *osteocytes* (OCYs), that are the most abundant species in bone tissue with respect to the *transient* recruitment of OCLs and OBLs. Osteocytes are mature and differentiated osteoblasts that have been embedded within the bone matrix after the bone formation phase. These cells present develop cytoplasmic processes which run through the *canaliculi* and form a communication network that can convert mechanical signals into biochemical signals ([77]), so playing a fundamental role. In fact, Han et al. ([81]) have shown from a mechanical standpoint that the role of osteocyte mechanotrasduction overcomes a precedent paradox according to which bone tissue microstrain was too small to initiate cellular response, since the osteocytes tethering elements excitation amplifies the locomotion strain signal and allows to achieve an adequate signaling threshold to kindle the BMU remodelling cascade. From a biochemical viewpoint, mechaotrasduction induce osteocytes to secrete growth factors

that stimulates bone tissue synthesis, as well as the inhibitory factors able to stop the latter activity. Consequently, osteoblasts are enhanced by these signals and bone formation occurs in the loaded directions, while osteoclast resorption is triggered by the lack of them, due to disuse or microcracks in the canicular networks. The result is that packets of bone are removed where demand is low and new bone is formed where mechanical strains/stresses are sufficiently detected. This also permits the restoration of micro-damages caused by fatigue and shocks.

3.1.5.1 *The phases of BMU remodelling*

In bone remodeling, bone formation succeeds the osteoclastic bone resorption, so that resorbed *lacunae* are alternately filled with new bone matrix ([132]). In this sense bone remodelling connotes as a cyclic physiological process, orchestrated by the complex interplay of the three cell types previously presented. BMU communication occurs by means of opportune autocrine signaling (i.e. communication among cells of the same type) and paracrine signaling (communication among cells of different types). More precisely, this "cycle" consists of activation, resorption, reversal, and formation phases ([132]). In brief, the development of a single BMU in the bone can be summarized as follows ([169]):

- *Initiation and Resorption.* Initially, from 10 to 20 osteoclasts are recruited to the initiation site and resorb the old bone tissue. This phenomenologically occurs in response to different stimuli, such as underload (due to disuse), microcracks generation, low calcium levels and other hormonal alterations. At the single-cell level, early OCLs hematopoietic progenitors differentiate to osteoclasts when receive opportune signals from stromal support cells, that belong to the osteoblast lineage [103]. These stromal cells express macrophage-colony stimulating factor (M-CSF) and RANKL, which act via their respective receptors (c-fms and RANK) on osteoclast progenitors to promote their differentiation. Stromal cells also secrete osteoprotegerin (OPG) which binds to RANKL and thus inhibits osteoclasts by lowering the RANK/RANKL binding formation. OPG would thus act to promote osteoclast death, and active osteoclasts have a life span of about ten days ([169]). During the whole resorption phase, OCLs aggregate into a well-confined zone, called *cutting cone*. Dead cells are continually replaced by new ones so that the population size remains approximately constant.

- *Transition or reversal.* Bone formation takes place exclusively in sites when bone resorption had previously occurred [103]. The recruitment of OBLs is then attributed to the release of *coupling factors* from the bone matrix during resorption disarrangement. Therefore, the presence of OCLs stimulates osteoblast precursors to differentiate into active OBLs. Activation of OBLs down-regulates OCls via OPG/RANKL pathways, and so OCLs undergo apoptosis in Bim/caspase-3 manner. *Formation and mineralization.* Up to 1000-2000 OBLs ([169]) are responsible of filling resorbed trench with new bone (*closing cone*). Furthermore, osteoblasts are much less efficient than osteoclasts, and the bone formation takes roughly 10 times longer than the resorption. Finally, the new formed bone matrix mineralizes and OBLs either undergo apoptosis or differentiate into osteocytes. Approximately, BMU activity can take from 100 to 200 days ([58]).

After activation (approximately 8 days), osteoclastic resorption is completed 9-34 days. Reversal and coupling period takes about two weeks, while less efficient osteoblasts fill the caniculi in a period between 60 and 130 days ([16]).

All these considerations let to describe the biological phenomenon of bone remodelling by introducing competitive Volterra-Lotka model, in which bone cells and bone matrix are identified with the "populations" taking part into the system at hand, and the corresponding rates model the BMU activity. In particular, the focus is on the modelling of OCLs, OBLs and bone matrix. Each equation will present coupling terms, which are positive or negative according to the biology of the process. In fact, following the present analogy, resorbing osteoclasts can be seen as "predators" of the bone matrix and are simultaneously inhibited by the OBLs during the transition phase (and thus negatively coupled with them). On the other side, OBLs rate are positively affected by the previously described communication with OCLs, but OBLs cells are also progressively preyed by the bone tissue, since some of them are embedded within the deposed matrix. Naturally, mass does not have an intrinsic activation coefficient and its rate will be given by the balance between OCLs resorption activity and OBLs formation.

Furthermore, in order to directly take into account the strain-dependent behavior of the remodeling rate, suitable coefficients have been introduced to simulate the activation process of both OBLs and OCLs driven by the osteocytes mechanical signaling. It has been in fact experimentally observed that mechanical stimulation outside a certain physiological window, i.e. under disuse and overloading, affects the apoptosis of osteocytes, which exhibit a "U-shaped" survival response to mechanical loading ([207]). More precisely, it was observed that osteocytes apoptosis was significantly high before $1000\,\mu\varepsilon$ and over $5000\,\mu\varepsilon$, and very low within this range ([146]). In our elemental model, this characteristic can be used to reproduce the BMU cells activation, in this way regulating their action on bone matrix on the basis of the tissue resident strain (that is supposed assigned). This is done by means of two suitable strain dependent functions which act in order to maximize OBLs recruitment in the central window, as well as to enhance OCLs resorption in the non-physiological loading windows. The system in its general form then reads:

$$\dot{\mathbf{x}} = \mathfrak{F}\left(\varepsilon, \varepsilon_1, \varepsilon_2, \mathbf{x}\right) \tag{3.38}$$

where the vector $\mathbf{x}$ collects the species and the way they interact, while mechanical-driven recruitment is taken into account through cells activation coefficients and is a function of the levels of the deformation experienced at the the cell level [81], and is based on the threshold behavior analyzed by [207], with ε_1 and ε_2 denoting such micro-strain thresholds. Furthermore, each species x_i represents the species density opportunely normalized with respect to a reference value, i.e. $x_i = \rho_i/\rho_i^*$. In the light of the interactions described, the explicit system actually results:

$$\begin{cases} \dot{x}_{obl}\left(t\right) = \left(r_1\left(\varepsilon, \varepsilon_1, \varepsilon_2\right) - a_{11}x_{obl}\left(t\right) + a_{12}x_{ocl}\left(t\right) - a_{13}x_b\left(t\right)\right)x_{obl}\left(t\right) \\ \dot{x}_{ocl}\left(t\right) = \left(r_2\left(\varepsilon, \varepsilon_1, \varepsilon_2\right) - a_{21}x_{obl}\left(t\right) - a_{22}x_{ocl}\left(t\right) + a_{23}x_b\left(t\right)\right)x_{ocl}\left(t\right) \\ \dot{x}_b\left(t\right) = \left(a_{31}x_{obl}\left(t\right) - a_{32}x_{ocl}\left(t\right) - a_{33}x_b\left(t\right)\right)x_b\left(t\right) \end{cases} \tag{3.39}$$

with the activation rate r_1 and r_2 respectively being modeled as

$$r_1 = r_{10} \left((1 + e^{-\mu_1(\varepsilon - \varepsilon_1)})^{-1} - (1 + e^{-\mu_2(\varepsilon - \varepsilon_2)})^{-1} \right) \tag{3.40}$$

$$r_2 = r_{20} \left(1 - \delta \left((1 + e^{-\mu_1(\varepsilon - \varepsilon_1)})^{-1} - (1 + e^{-\mu_2(\varepsilon - \varepsilon_2)})^{-1} \right) \right) \tag{3.41}$$

where r_{10} and r_{20} denote the differentiation rate of OBLs and OCLs precursors, respectively. The solutions of the proposed system gives information about the cooperation of the cells activity during the remodelling process, in terms of development of bone density which is formed or resorbed, as well as the time sequencing related to the alternation of the several phases of the BMU cycle, as shown in Fig. 31. In particular, at low microstrain OCLs are recruited in order to resorb the unloaded material, as well as at excessively high microstrain prone to damages. In these two situations, the stable equibblirium for the system is represented by the state which provides the bone matrix extinction see Fig.32. For a physiological value of microstrain, in correspondence of which BMU cycle is activated for promoting bone tissue remodelling, the BMU cycle phases can be clearly recognized (Fig. 31) by noticing the alternation of the OCLs resorption period with the (longer) OBLs formation period, until the process tends to quiescence with an increased bone matrix density. Of course, this solution provides the coexistence of the three species, and therefore the stability of the solution will be guaranteed in correspondence of the respective equilibrium point (Fig.32).

Naturally, bone remodelling might strictly depend upon the spatial distribution of the strain within the bone tissue. However, this simple example let to highlight the dynamics underlying the BMU cycle itself in order to propose a way to couple adaptive elasticity-based algorithm (that focus on a higher scale) with a suitable remodelling rate, which can be determined on the basis of the knowledge of inner the cells dynamics. This let to have resorption in hypo-loaded regions as well as bone matrix production in densely loaded regions and obtain a synthetic index of bone mass fraction.
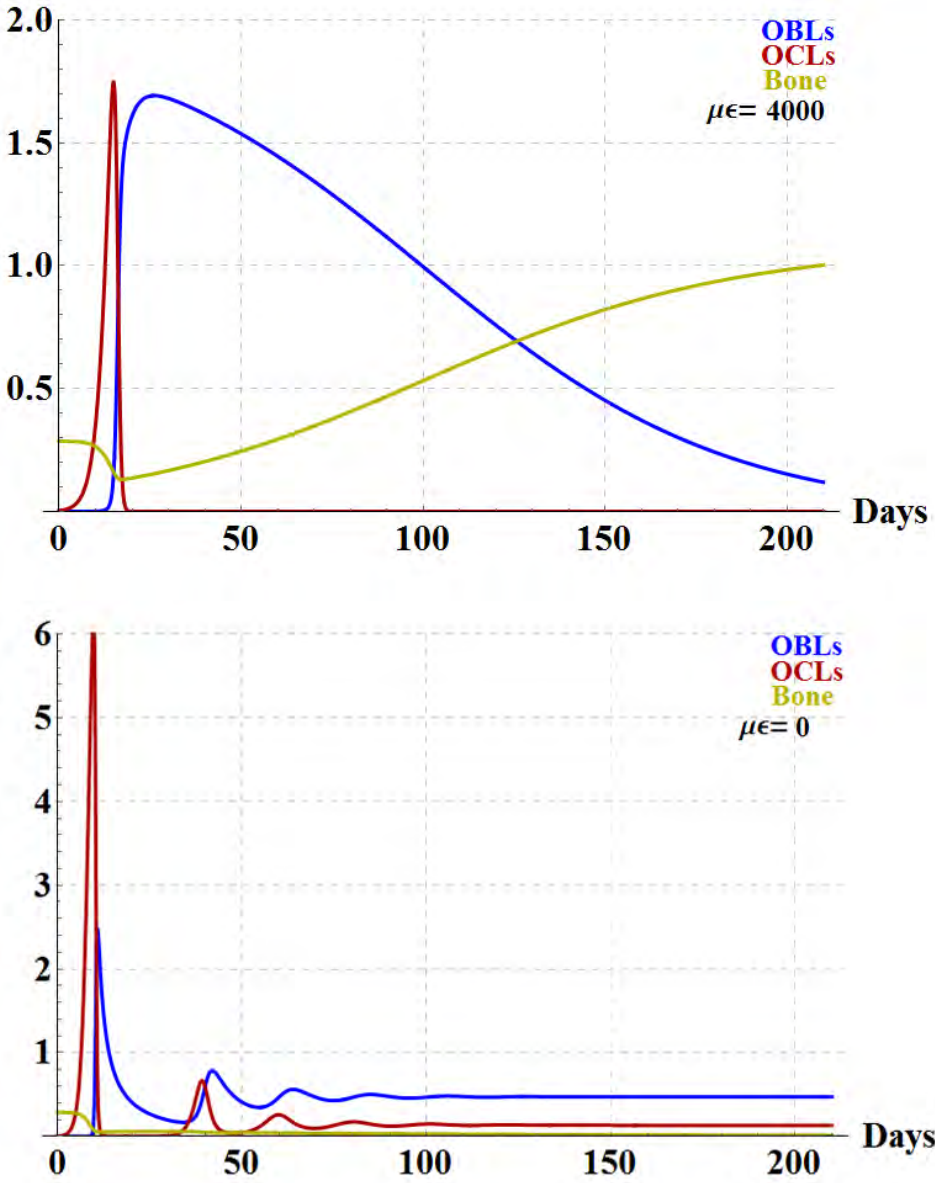
Figure 31: Bone remodelling dynamics obtained from the numerical simulations. Cells number and bone density have been scaled; $r_{10} = 0.4\,d^{-1}$, $r_{20} = 0.9$[122, 207], $a_{11} = 0.02\,d^{-1}$[28], $a_{12} = 0.075\,d^{-1}$, $a_{21} = 0.19\,d^{-1}$[219], $a_{22} = 0.01\,d^{-1}$[169], $a_{31} = 0.0012\,d^{-1}$, $a_{32} = 0.01\,d^{-1}$[169, 170], $a_{33} = 0.00025\,d^{-1}$, $\rho_b^* = 1.75\,g/cm^3$[123], $\rho_{ocl}^* = 400\,\text{cells}/mm^3$, $\rho_{obl}^* = 20000\,\text{cells}/mm^3$[97].
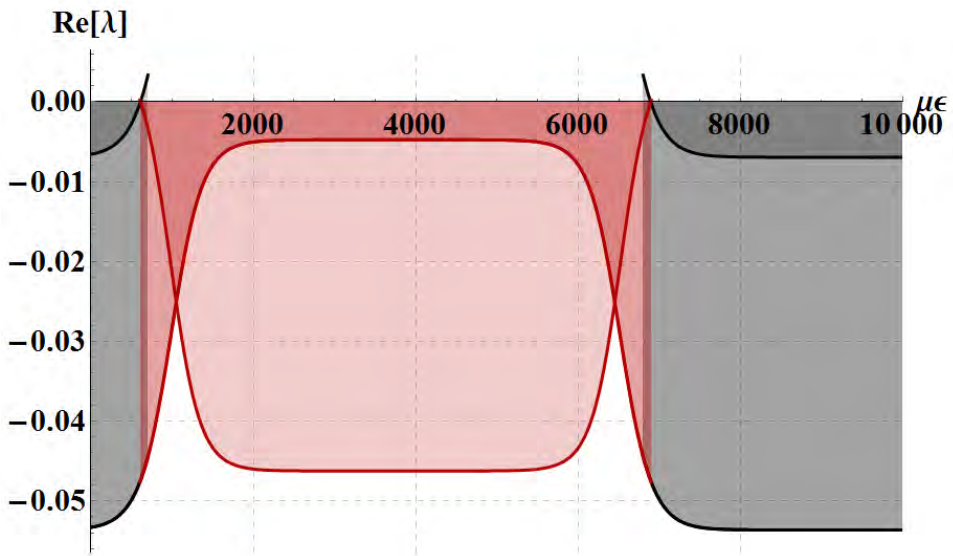
Figure 32: Analysis of the local stability of solutions in correspondence of the equilibrium points related to non-physiological (black) and physiological (red) stimuli.

Part III

COUPLED MODELLING

This part is dedicated to the analysis of biomechanical problems in which growth and remodelling phenomenological equations are in direct coupling with solid mechanics. In this way, all the interactions describing the influence of the mechanical environment on cells activities and, *vice versa*, the effects of growth and remodelling on the mechanical response of the biological material are simultaneously taken into account through a full coupled strategy.

THE "WEAK" COUPLING

The so-called *weak coupling* is referred to the modelling of biomechanical problems in which growth and remodelling are explicitly included with the aim of analyzing growth-induced stresses and deformations, by opportunely deriving *ad hoc* constitutive assumptions. This is often done by means of kinematical equations describing the two processes in a phenomenological way, for example by adopting specific evolution models whose parameters are calibrated on the basis of experimental observations. The following sections are dedicated to the application of this modelling strategy to the problem of effects of growth and remodelling of vessel structures in vascular diseases and surgical practice, demonstrating that they can be strictly correlated to the mechanical alterations in a non-physiological environment. This is done by means of a hyperelastic material model in which both growth, remodelling and their mechanical counterpart have simultaneously been taken into account, this interactions also opening to further considerations about the role that the the communication between mechanical and physiological events has in determining positive (or either adverse) outcomes, as well as in driving the cooperation between biological and synthetic prosthesis materials.

4.1 BIOMECHANICS MEETS ROSS OPERATION IN CARDIOVASCULAR DISEASES

Ross operation, i.e. the use of autologous pulmonary artery to replace diseased aortic valve, has been recently at the center of a vivid debate regarding its unjust underuse in the surgical practice. Keystone of the procedure regards the use of an autologous biologically available graft which would preserve the anticoagulative and tissue homeostatic functions normally exerted by the native leaflets and would harmoniously integrate in the vascular system, allowing for progressive somatic growth of aortic structures.

Since the introduction in 1967 of Ross Operation in the cardiac surgery scenario, the PA represented a valuable substitute for both congenital and acquired disease of the left ventricular outflow tract in children and young adult [167, 189, 196]. Accumulating evidences suggest that the advantages of the PA are related to the ability to match the somatic growth of cardiovascular structures in pediatric surgery and to the avoidance of life-long anticoagulation [141, 142]. Conversely, the reported incidence of PA dilatation without loss of integrity of the leaflets among patients undergone to Ross Operation ranges from 20 to 40%. The consequence is PA regurgitation that might lead to severe left ventricular dysfunction in the long-term follow-up of persons who had surgery for congenital and acquired heart disease [53]. In order to overcome these issues and design an *ad hoc* system capable of both allowing somatic growth and providing mechanical sustain to the PA-vessel, a composite reinforcement constituted of a resorbable scaffold ([145, 187]) and a e-PTFE armor has been introduced
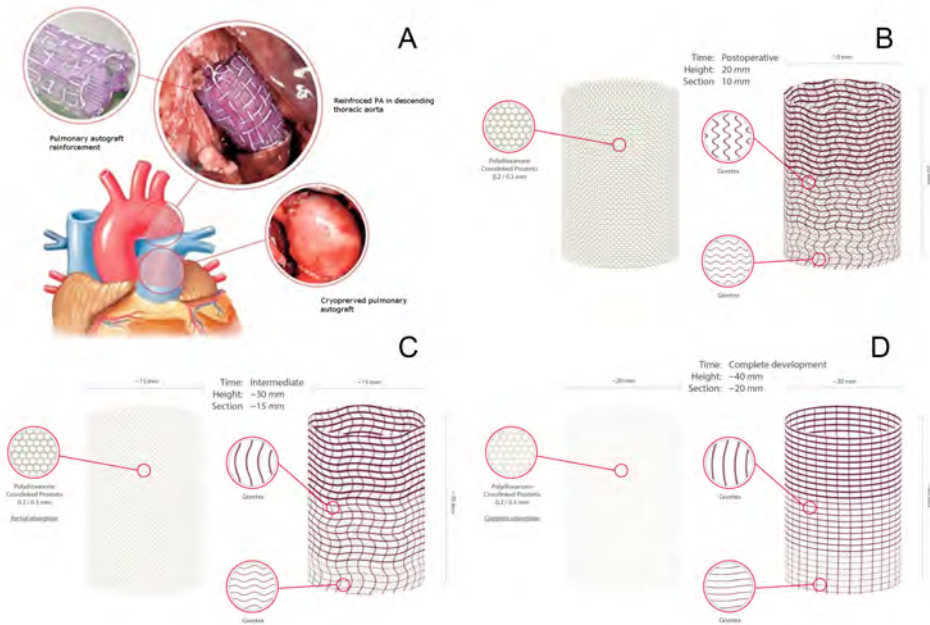
Figure 33: A. Scheme of the implantation of a cryopreserved pulmonary artery homograft into the discending aorta. **B**,**C**,**D**. Concept and design of composite semiresorbable armored bioprosthesis. The specific design of the GORE-TEX auxetic armor will allow multidirectional growth and resistance to abnormal dilatation (**B**: Initial implantation, **C**: Intermediate phase, **D**: Complete development).

in Ross procedure (see Fig. 33). In order to reproduce the clinical scenario in which this procedure might be applied and allow the development and testing of different devices or techniques aimed to improve the pulmonary autograft (PA) performance, a large animal model was successfully pioneered, by performing Ross Operation in a statistically significant court of growing lambs.

Therefore, to support and supplement the *in vivo* animal experimentation and to investigate the impact of this new device on mechanisms of growth, remodelling and stress shielding of the reinforced PA, a mathematical model has been developed, simulating the biomechanical changes of pulmonary artery subjected to systemic pressure load and reinforced with a combination of resorbable and auxetic synthetic materials. The positive biological effects on vessel wall remodeling, the regional somatic growth phenomena and prevention of dilatative degeneration have been analyzed. The theoretical outcomes show that a virtuous biomechanical cooperation between biological and synthetic materials takes place, stress-shielding guiding the physiological arterialization of vessel walls, consequently determining the overall success of the autograft system.

The application of principles of tissue engineering through the use of bioresorbable materials is increasingly considered an attractive and valid alternative for cardiovascular structures replacement ([184]). Specific studies have been also focused on the development of drug-releasing vascular bioresorbable prosthesis able to ameliorate and accelerate processes of endothelialization and vascular regeneration using manu-
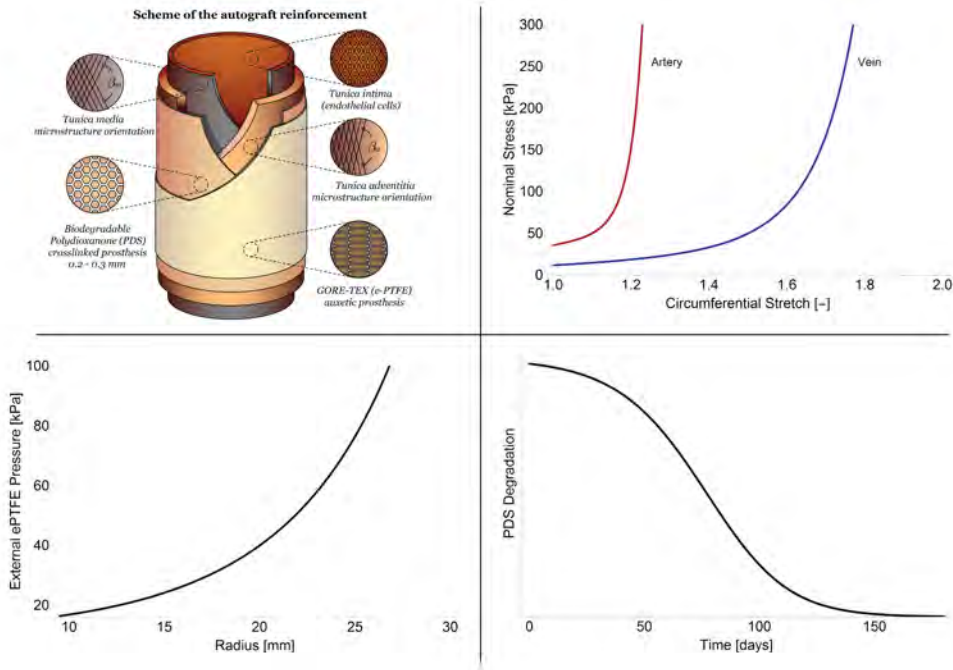
Figure 34: Left (top): Sketch of the main biomechanically relevant features of the pulmonary autograft and the reinforcement. Right (top): Nominal (first Piola-Kirchhoff) hoop stress versus circumferential stretch in artery and vein-like materials. Left (bottom): elastic reaction pressure against external vessel radius dilation exhibited by GORE-TEX auxetic reinforcement during pulmonary autograft growth and deformation. Right (bottom): in-time mass degradation of bioresorbable polydioxanone (PDS) structure.

facturing techniques which allow for both a permissive action on the biology of the vessel ([185]) and the realization of graft able to bear significant hemodynamic loads ([35]).

In particular, the PA composite reinforcement enveloping the arterial walls (*intima*, *media* and *adventitia*) is constituted by a biodegradable scaffold made of polydioxanone (PDS), integrated with an external GORE-TEX weave (expanded polytetrafluoroethylene, e-PTFE) whose structure is characterized by a negative Poisson's ratio (see Figure 34). In particular, it might reliably speculate that the temporary interaction between the bioresorbable reinforcement and the PA might have orchestrated a complex process of vascular remodelling based on a balance between inflammation and extracellular matrix production resulting, after biomaterial resorption, in an arterial-like vessel still biologically alive and capable of growth ([187]). Indeed, the biomaterial on a side accompanied and accelerated the naturally occurring pressure-load adaptation phenomena attenuating the pressure load exerted on the pulmonary artery and compensating the tendency to dilation preventing aneurysmal degeneration, but on the other, still permitted and respected somatic growth of vascular structure over time ([145]). The observations discussed by ([92]) concerning the differential poten-

tial of dilation at the various segments of the aorta, i.e. annulus, Valsalva sinuses (0.5 mm/year) and sinutubular junction (increase of 0.7-0.9 mm/year), outlined the need to study the biomechanical changes of pulmonary artery reinforcements in their different parts. This induced to reconsider their design with the aim to better adapt to the normal physiology of the aortic root improving the resistance of the zones, which are meant to majorly suffer from dilatative degeneration. The mechanical stress associated to progressive overstrain of the pulmonary artery under systemic pressure might in fact affect PA integrity and the endothelialization process ([186]); therefore, in this context, prevention of the graft stretching is crucial.

The biomechanical response is then studied to validate the *in vivo* results and overcome some unresolved surgical issues of growth and remodelling of pulmonary arteries subjected to systemic pressure, and to thus analyze the effects of an innovative prosthesis system realized by combining resorbable and auxetic synthetic materials. The proposed biomechanical model seems to provide the positive effects of the synergy of these two synthetic materials, that accommodate mechanical loads guaranteeing graft integrity, controlling the progressive graft dilation, allowing regional somatic growth and preventing dilatative degeneration ([126, 159]).

4.2 DETAILS OF THE EXPERIMENTAL ANIMAL MODEL

The experimental model of transposition of the pulmonary trunk as autograft in aortic position has been developed and performed under cardiopulmonary bypass in 20 growing lambs ([141, 142, 144]). Technical and anatomical issues imposed reimplantation of the PA in the descending aorta, with the pulmonary trunk being replaced by a homograft from another lamb of the same age and weight. The age of the animals at the moment of the implant was 2 month (8-10 weeks) and baseline mean weight was about 21±3 kg, allowing to observe the progression of the autograft diameter during the period of fastest growth. Morphometric and cardiovascular parameters were comparable preoperatively among animals. There were no difference in haemoglobin levels and ventricular function. The group of 20 lambs was divided into two subgroups: a control group (n=10), subjected to ordinary PA transposition, and a group of 10 animals in which the PA was reinforced with an external synthetic semiresorbable armored scaffold (prosthetic). All animal experiments have been performed in respect of the guidelines for animal care and handling and the protocol was approved by the institutional animal care committee.

Semiresorbable copolymer scaffold. The experimental design of the device consisted of an internal bio-resorbable scaffold made with Polydioxanone (PDS), arranged in a frame of hexagonal cells, externally coupled with a non-resorbable layer of e-PTFE, having an auxetic behavior. The mesh structure and arrangement were specifically designed in order to constrain the excessive enlargement of the vascular graft diameter by also absorbing wall mechanical stress, while accommodating its natural longitudinal growth by embracing the root of the aorta. For this purpose, the unit cells of the PDS and e-PTFE plies have been respectively positioned as sketched in Figure 35.

Surgical Model. Lambs were premedicated with ketamine (25mg/kg via intramuscular injection) and anesthesia was guaranteed by the injection of sodium thiopentothal

(6-8mg/kg) via the internal jugular. Animal received 100mg of lidocaine intravenously as prophylaxis against rhythm disturbance. After endotracheal intubation, ventilation was provided up to animal awakening and the anesthesia was maintained with inhalation isoflurane (1% to 2.5%). The electrocardiogram was monitored and chest was prepped and shaved. The heart was approached via left thoracotomy. After opening the pericardium, the right atrium was exposed for cannulation and the trunk of the pulmonary artery was dissected free from its right ventricular origin up to its bifurcation in the pulmonary arteries. The same was done for the descending thoracic aorta and a region distal to the portion of choice for the PA transposition was cannulated. Approximately 8cm of the descending thoracic aorta was left for clamp positioning and to perform the anastomosis with the pulmonary artery trunk under optimal conditions. Heparin (3mg/kg) was administered intravenously, and cardiopulmonary bypass was started between right atrium and descending aorta. The cerebral circulation of the animal was guaranteed on a beating heart. A 3cm tract of pulmonary artery trunk was transposed into the descending aorta with an end-to-end anastomosis in 5-0 prolene. A fresh pulmonary artery homograft, explanted from animals sacrificed on the same day for another experimental study, was inserted to reconstruct the right outflow tract, with a proximal and distal end-to-end anastomosis in 5-0 prolene, as in the Ross operation. Left thoracotomy was closed and aspiration drainage left in place. Before implantation, in the experimental group the PA has been reinforced with PDS and e-PTFE meshes according to the study design. The resorbable mesh was prepared at the operative table (time 10±2 min). Meshes used in this study were cut into a rectangle measuring 20mm in height matching with the height of autograft and rolled out on a metallic candle and then reassured by a suture to create a cylinder with an internal diameter of 10mm (20mm in height in 10mm diameter directly adherent to the PA). The autograft was then inserted into the fibrillar cylinder and was anastomosed suturing both its margins and those of the prosthetic structure to the pulmonary autograft trunk. The mesh was oriented to allow maximal extensibility in the longitudinal direction and minimal transverse extensibility. The principal stages of the implant *in situ* deployment are reported in Fig. 33B,C,D. All animals survived to the procedure and did not experience surgical complications. A case of PA initial rupture and thrombosis occurred at 6 months follow-up in the control group, without causing animal decease. Procedure did not pose particular technical challenges. At 6 months the lambs weight was doubled (21±3kg at day 0 and 55±10kg at 6 months) suggesting a normal growth process. The animal model was mainly focused on the development of an effective and reproducible model of pulmonary autograft transposition into arterial system with the aim to study the behavior of the autograft and develop suitable strategies to prevent its future dilation, which represents one of the major drawback of this operation.

4.3 MATHEMATICAL MODELLING

4.3.1 *Nonlinear mechanics and growth of blood vessels*

In the last decades, biomechanical behavior and mechanobiology of cells, tissues and organs have been intensively investigated, with the aim of discovering key feedback mechanisms governing the ways in which cascades of chemical signals are transmitted

within the hierarchically organized living structures and interplay with physical events at different scale levels ([66]). Continuum Mechanics has deeply contributed to develop this research area and to meet related challenges, by mainly creating the physically and mathematically consistent ground on which large deformation, stresses, evolving constitutive laws, growth, remodeling and morphogenesis do interact ([10],[46],[89]). Within this framework, by essentially starting from an approach proposed by [90] and [91] in some recent milestone works on biomechanics of arterial walls, it is here constructed an *ad hoc* non-linear mathematical model for PA, by incorporating tissue growth, remodeling, large deformations and hyperelasticity.

Going *in medias res*, let us consider the body $\mathcal{B}^{(0,0)}$ in its reference stress-free configuration, with dV_0 indicating its volume elements and $\mathbf{X}$ the position of each material point. The evolution of the elastic body can be entirely described by the motion vector $\mathbf{x} = \mathbf{x}(\mathbf{X}, t)$ that maps the material points $\mathbf{X} \in \mathcal{B}^{(0,0)}$ onto spatial points $\mathbf{x}$ at any time t through the definition of the deformation gradient $\mathbf{F}$ defining an application between the two tangent spaces. This deformation gradient can be written by also accounting compatibility with the body particles displacement field $\mathbf{u}(\mathbf{X}, t) \in C^2(\mathcal{B}^{(0,0)})$ as:

$$\mathbf{F} = \nabla_{\mathbf{X}} \mathbf{x}(\mathbf{X}, t) = \mathbf{I} + \mathbf{u}(\mathbf{X}, t) \otimes \nabla_{\mathbf{X}} \qquad (4.1)$$

where ∇ is the *nabla* operator (the subscript indicating the space to which it is referred), while $\otimes$ is the dyadic product. It is standard argument to consider the deformation gradient as composed by different aliquots, respectively responsible of growth, elastic load-induced deformations and residual stress-associated stretches. The most common structure adopted to describe these contributions is a multiplicative decomposition in a way that $\mathbf{F} = \mathbf{F}_e \mathbf{F}_g$ (see e.g. [164]): herein $\mathbf{F}_g$ represents a volumetric growth tensor and $\mathbf{F}_e$ the elastic tensor ensuring compatibility and taking into account both elastic load-induced deformation and residual stresses[1].

As a matter of fact, the presence of self-equilibrated stresses can be traced if, after cutting out a ring from a blood vessel tract, it contracts (or dilates) along the cylinder generator to release the elastic energy associated to axial stresses and/or if a nonzero opening angle α is measured after cutting the cylindrical ring along its generator to relax hoop stresses ([69, 91]). Material points $\mathbf{X}$ are then mapped through the reference configuration towards first non-compatible grown intermediate configuration $\mathcal{B}_g^t$ in which they occupy position $\mathbf{x}_g(\mathbf{X}, t) \in \mathcal{B}_g^t$ and then onto the current loaded configuration $\mathcal{B}^{(t,s)}$, being here denoted by the position vectors $\mathbf{x}(\mathbf{X}, t)$ (see Figure 35).

In this configuration, t denotes the ordinary long timescale that follows the growth process (which is of the order of days or months), whereas s indicates the short timescale at which typically mechanical equilibrium is reached. Also, volume elements

---

1 From a rigorous mechanical point of view, the term "residual stress" –although widely used in the Literature– is often incorrectly adopted: in fact, in absence of applied loads, *before* to ideally (and suitably) cut a grown material, the stress kindled within the tissue as a result of the inhomogeneous growth is "self-equilibrated" rather than "residual" ("remaining"), while –*after* cutting an inhomogeneously grown material– a "stress-free" (deformed) configuration is recovered rather than a "residual stress." The adjective "residual" is hence erroneous in the first case and ambiguous in the second, because suggests that one can find residual stresses after cutting a (grown) material, while on the contrary a "stress-free" deformed configuration characterized by "residual (inelastic) strain" is actually found. This is the reason for which, in the present work, the terms "residual strain", "self-equilibrated (residual) stress" and/or "stress-free deformed state" have been preferred.

Biomechanical model of autograft arterialization
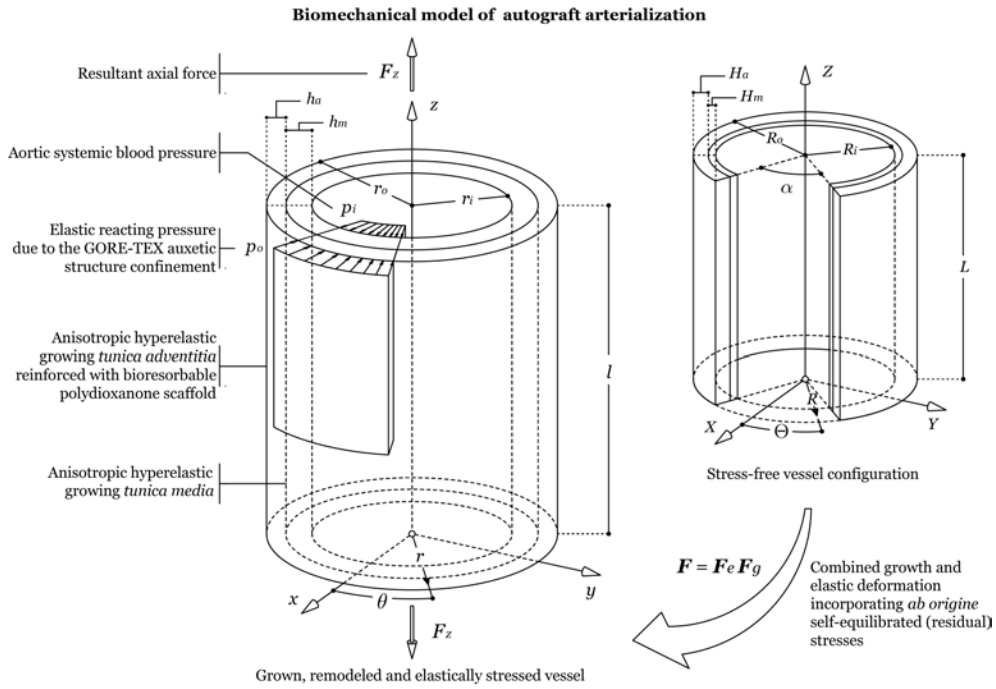
Figure 35: Sketch of the biomechanical model of reinforced pulmonary autograft under aortic systemic pressure including *ab origine* self-equilibrated (residual) stresses, growth, remodeling and elastic deformation.

in these configurations are $dV_g = J_g dV_0$ and $dv = J_e dV_g = J dV_0$, with $J_g = \det \mathbf{F}_g$, $J_e = \det \mathbf{F}_e$ and $J = \det \mathbf{F} = J_g J_e$, respectively. Coherently with experimental observations, the body is assumed to be elastically incompressible, so that $J_e = 1$ and $dv = dV^g$ or $J = J_g$; this also implies that density ρ does not change, growth being purely volumetric ([127]). The evolution growth equation then represents a kinematic relation for the body elementary growing volume; in particular, by introducing a growth volumetric source (and sink) term r_g, under the assumptions of no mass fluxes and constant density ρ (which implies a pure volumetric growth), the mass conservation for the elastically incompressible body (i.e. $J_e = 1$) can be expressed by:

$$\frac{d}{dt}(dm) = r_g dv \tag{4.2}$$

In order to describe the growth behavior of the experimental animal models and reproduce the effects of the physiological growth on the stresses in vessel walls, a logistic rate form will be assigned to the source (or sink) term r_g. Mass fluxes have been neglected, and the hypothesis of constant density leads to:

$$\dot{J}_g = \frac{1}{\rho} J_g r_g, \quad \text{or} \quad \mathbf{F}_g^{-1} : \dot{\mathbf{F}}_g = \bar{r}_g \tag{4.3}$$

where dot denotes the material time derivative and $\bar{r}_g = \rho^{-1} r_g$ accounts for the mass supply/removal due to the growth process which describes how the body evolves. In general, the growth may depend on different factors, such as the availability of metabolic energy needed for activating the biological process ([69, 201]) and other internal conditions, defining the type of interaction among biomaterial constituents and *in situ* stresses, that is known to inhibit (or eventually enhance) selected cellular processes at the basis of the growth mechanisms ([6]). In addition, due to axis-symmetry of geometry and loads of the problem at hand, the growth is also expected to be symmetrical and the growth tensor can be thus taken in diagonal form:

$$\mathbf{F}_g = Diag\left\{ J_g^{\frac{1-\zeta}{2}}, J_g^{\frac{1-\zeta}{2}}, J_g^{\zeta} \right\} \tag{4.4}$$

ζ being a coefficient deputed to catch possible tissue growth anisotropies along the longitudinal direction and in the vessel cross-section plane.
By neglecting inertia terms, balance of linear momentum can be written by making reference to both unstressed and current (grown and elastically deformed) configurations as follows (see e.g. [46])

$$\nabla_{\mathbf{X}} \cdot \mathbf{P} = -\hat{\mathbf{b}}, \qquad \qquad \forall\, \mathbf{X} \in \mathcal{B}^{(0,0)} \tag{4.5}$$

$$\mathbf{P} \cdot \mathbf{N} = \hat{\mathbf{t}}, \qquad \qquad \forall\, \mathbf{X} \in \partial\mathcal{B}^{(0,0)} \tag{4.6}$$

or

$$\nabla_{\mathbf{x}} \cdot \boldsymbol{\sigma} = -\mathbf{b}, \qquad \qquad \forall\, \mathbf{x} \in \mathcal{B}^{(t,s)} \tag{4.7}$$

$$\boldsymbol{\sigma} \cdot \mathbf{n} = \mathbf{t}, \qquad \qquad \forall\, \mathbf{x} \in \partial\mathcal{B}^{(t,s)} \tag{4.8}$$

where $\mathbf{b}$ and $\hat{\mathbf{b}}$ respectively represent the body force vector in the current config-uration and its *pulled-back* version, analogous arguments being applied, by recalling the Nanson's formula, for geometrically interpreting tractions $\mathbf{t}$ and $\hat{\mathbf{t}}$, as well as the outward normal vectors $\mathbf{N}$ and $\mathbf{n}$ to the body surfaces, in the reference and current configurations. In (4.7) $\boldsymbol{\sigma}\left(\mathbf{x}, t\right)$ represents the Cauchy stress, while $\mathbf{P}\left(\mathbf{X}, t\right)$ is the first Piola-Kirchhoff (or nominal) stress, these two second order tensors –which coincides under small deformations– being related to each other through the Piola transform:

$$\mathbf{P} = J\boldsymbol{\sigma}\mathbf{F}^{-T} \tag{4.9}$$

Furthermore, in order to faithfully reconstruct the biomechanical constitutive be-havior of the vessel, the strain energy density ψ is here considered as a function of the elastic deformation tensor $\mathbf{F}_e$ and of a vector $\boldsymbol{\gamma}$ containing n_γ remodeling parameters describing the average microstructural changes occurring at the material particles as a consequence of growth and deformation processes. Hence, by following the approach proposed in [149], the total elastic energy referred to the initial configuration takes the form:

$$\Psi = \int_{\mathcal{V}_0} J_g\psi\left(\mathbf{F}_e, \boldsymbol{\gamma}\right)dV_0 \tag{4.10}$$

with $\mathcal{V}_0 = measure(\mathcal{B}^{(0,0)})$.

To obtain the specific constitutive laws involving the Piola-Kirchhoff stress and the growth and remodelling conjugate forces, the dissipation principle has been written down by essentially following the approach by [127] and [149]. In particular, under the hypothesis of isothermal process, the balance of energy can be written by taking into account a contribution to the growth which represents a metabolic energy supply per unit mass, say ε_g, and a vector of driving forces $\mathbf{k}$ responsible of the remodeling-associated microstructural changes. In this way one finally obtains:

$$\frac{d}{dt}\int_{\mathcal{V}} \rho\left(\frac{1}{2}\mathbf{v}\cdot\mathbf{v} + u\right)dv = \int_{\mathcal{V}}\left(\rho\frac{d}{dt}\left(\frac{1}{2}\mathbf{v}\cdot\mathbf{v}\right) + \boldsymbol{\sigma}:\mathbf{d} + \mathbf{k}\cdot\dot{\boldsymbol{\gamma}}\right)dv +$$
$$+ \int_{\mathcal{V}} r_g\left(\frac{1}{2}\mathbf{v}\cdot\mathbf{v} + u\right)dv + \int_{\mathcal{V}} \varepsilon_g\, r_g\, dv \tag{4.11}$$

u and $\mathcal{V}$ being the internal energy per unit current mass and the current volume measure, respectively. Also, $\mathbf{v}$ is the velocity vector and $\mathbf{d} = sym(\dot{\mathbf{F}}\mathbf{F}^{-1})$ is the symmetrical velocity gradient, the other quantities $\boldsymbol{\sigma}$ and $\dot{\boldsymbol{\gamma}}$ defining the Cauchy stress tensor and the rate of the remodeling parameters vector, as also specified in the main text. By using (4.2), the balance of energy (4.11) reduces to:

$$\int_{\mathcal{V}} \rho\frac{du}{dt}\, dv = \int_{\mathcal{V}}\left(\boldsymbol{\sigma}:\mathbf{d} + \mathbf{k}\cdot\dot{\boldsymbol{\gamma}}\right)dv + \int_{\mathcal{V}} \varepsilon_g\, r_g\, dv \tag{4.12}$$

The total internal dissipation per unit initial mass can be instead accounted by introducing two thermodynamic forces f_g and $\boldsymbol{f}_\gamma$, respectively conjugated to the rates r_g and $\dot{\boldsymbol{\gamma}}$: in such a way the rate of dissipation is written down:

$$\int_{\mathcal{V}} \theta \frac{ds}{dt} \rho \, dv = \int_{\mathcal{V}} \left(f_g \, \rho^{-1} r_g + \boldsymbol{f}_\gamma \cdot \dot{\boldsymbol{\gamma}} \right) \, dv \tag{4.13}$$

where s is the entropy per unit current mass and θ is the absolute temperature. The second law of thermodynamics requires the right side of (4.13) to be non negative. By combining the energy equation (4.12) and the entropy equation (4.13), the free energy per unit volume $\psi = \rho \left(u - \theta \, s \right)$ can be thus obtained as a function upon the elastic deformation $\mathbf{F}_e$ and the remodeling parameters $\boldsymbol{\gamma}$, as also established in (4.10). At the end, it results:

$$\frac{d}{dt} \int_{\mathcal{V}} \psi \, dv = \tag{4.14}$$
$$= \int_{\mathcal{V}} \left(\boldsymbol{\sigma} : \mathbf{d} + \left(\mathbf{k} - \boldsymbol{f}_\gamma \right) \cdot \dot{\boldsymbol{\gamma}} + \left(\rho \varepsilon_g - f_g \right) \rho^{-1} r_g \right) \, dv$$

or

$$\frac{d}{dt} \int_{\mathcal{V}^0} J_g \psi \, dV^0 = \tag{4.15}$$
$$= \int_{\mathcal{V}^0} \left(\mathbf{P} : \dot{\mathbf{F}} + J_g \left(\mathbf{k} - \boldsymbol{f}_\gamma \right) \cdot \dot{\boldsymbol{\gamma}} + \left(\rho \varepsilon_g - f_g \right) \dot{J}_g \right) dV^0$$

$\mathcal{V}^0$ denoting the referential volume. By means of the localization theorem and exploiting the deformation multiplicative decomposition $\mathbf{F} = \mathbf{F}_e \mathbf{F}_g$ one has:

$$J_g \frac{\partial \psi}{\partial \mathbf{F}_e} : \dot{\mathbf{F}}_e + J_g \frac{\partial \psi}{\partial \boldsymbol{\gamma}} \cdot \dot{\boldsymbol{\gamma}} + \psi \dot{J}_g = \tag{4.16}$$
$$= \mathbf{P} \mathbf{F}_g^T : \dot{\mathbf{F}}_e + \mathbf{F}_e^T \mathbf{P} : \dot{\mathbf{F}}_g + J_g \left(\mathbf{k} - \boldsymbol{f}_\gamma \right) \cdot \dot{\boldsymbol{\gamma}} + \left(\rho \varepsilon_g - f_g \right) \dot{J}_g$$

A direct comparison of the terms at both sides of (4.16) leads to:

$$\mathbf{P} = J_g \frac{\partial \psi}{\partial \mathbf{F}_e} \mathbf{F}_g^{-T}$$
$$\boldsymbol{f}_\gamma = \mathbf{k} - \frac{\partial \psi}{\partial \boldsymbol{\gamma}} \tag{4.17}$$
$$f_g = \rho \varepsilon_g + \Sigma$$

from which it follows that the growth-conjugate force is the result of the interplay of metabolic (e.g. biochemical) and mechanical factors, with $\Sigma = \boldsymbol{\Sigma} : \mathbf{I}$ being the trace of the Eshelby-like stress tensor related to the change of domain variations induced by the volumetric growth $\boldsymbol{\Sigma} = \mathbf{F}_e^T \partial \psi / \partial \mathbf{F}_e - \psi \mathbf{I}$, as obtained for example by [7] and [149]. As a consequence, the dissipation inequality, derivable by imposing the second member of (4.13) to be non negative, can be split into two independent contributions:

$$\int_{\mathcal{V}^0} \left(\mathbf{K} - J_g \frac{\partial \psi}{\partial \boldsymbol{\gamma}} \right) \cdot \dot{\boldsymbol{\gamma}} \, dV^0 \geq 0 \tag{4.18}$$

$$\int_{\mathcal{V}^0} \left(\rho \varepsilon_g + \Sigma \right) \dot{J}_g \, dV^0 \geq 0 \tag{4.19}$$

The respect of the first of the reduced dissipation inequalities $(4.18)_1$ allows to write the remodeling evolution equation in the following form:

$$\dot{\gamma} = c_\gamma \left(\mathbf{K} - J_g \frac{\partial \psi}{\partial \gamma} \right), \qquad c_\gamma \geq 0 \qquad (4.20)$$

c_γ being a non-negative term (either constant or not) accounting for the characteristic remodeling time, and $\mathbf{K} = J_g \mathbf{k}$ representing a proper referential (or drag) force which drives the remodeling process ([149]). The second inequality is a pressure-volume relationship (vanishing in the pure remodeling case, $\dot{J}_g = 0$). Its validity implies that the growth case $\dot{J}_g > 0$ is characterized by the presence of a pressure responsible of the domain expansion and by an adequate amount of metabolic energy, convertible into mass growth, that is assumed to be indefinitely available; *vice versa*, the resorption case $\dot{J}_g < 0$ can be associated to the lack of energy supply and to the presence of stresses contracting the volume domain.

Finally, by then recalling constitutive relation (4.17) and the Nanson's formula (4.9), the Piola-Kirchhoff and Cauchy stress tensors can be expressed as follows:

$$\mathbf{P} = J_g \frac{\partial \psi}{\partial \mathbf{F}_e} \mathbf{F}_g^{-T} \quad \text{and} \quad \boldsymbol{\sigma} = \frac{\partial \psi}{\partial \mathbf{F}_e} \mathbf{F}_e^T \qquad (4.21)$$

4.3.2 *Inflation and growth-associated stresses in vessel walls*

From a geometric viewpoint, a blood vessel can be seen as a thick-walled hollow (composite) cylinder, each layer exhibiting elastic anisotropy as a result of the tissue microstructure (see Figure 34). From the mechanical standpoint, several works can be found in literature where the problem of determining the elastic response of composite cylinders under different load conditions is approached and analytically solved ([60]), also in case of anisotropy ([61]) and for general inhomogeneous media ([63]). However, pressure regimes and growth generally induce large deformations in the blood vessels and therefore non-linear models are required (see for instance [91] and [41]). Within the non-linear theory of elasticity, and by making reference to the geometrical symmetries, the unstressed reference configuration $\mathcal{B}^{(0,0)}$ can be then described in terms of cylindrical coordinates by the region:

$$\begin{aligned} R_i \leq &R \leq R_o, \\ 0 \leq &\Theta \leq (2\pi - \alpha), \\ 0 \leq &Z \leq L \end{aligned} \qquad (4.22)$$

where R_i and R_o indicate the inner and the outer radii of a relaxed and excised configurations, L is the vessel trunk length and α is the opening angle, a measure of the elastic energy imprisoned within the material before ideally cutting the vessel to go back to a virtual stress-free reference configuration and due to *ab origine* self-equilibrated (residual) stress (see Figure 35). Analogously to the pure inflation problem, under the hypotheses of axis-symmetry of both loads (i.e. the systemic aor-

tic blood pressure) and growth, the deformed *in situ* configuration can be instead described by the region:

$$
\begin{aligned}
r_i \leq r \leq r_o, \\
0 \leq \theta \leq 2\pi, \\
0 \leq z \leq l
\end{aligned}
\tag{4.23}
$$

with $\theta = h\Theta$ and $h = 2\pi / (2\pi - \alpha)$. This also implies that the deformation gradient can be helpfully written in terms of principal stretches, i.e. $\mathbf{F} = \lambda_{rR}\mathbf{e}_r \otimes \mathbf{e}_R + \lambda_{\theta\Theta}\mathbf{e}_\theta \otimes \mathbf{e}_\Theta + \lambda_{zZ}\mathbf{e}_z \otimes \mathbf{e}_Z$. By taking into account the residual stress-induced opening angle, growth and elastic deformations, the total stretches are univocally determined by starting from the relation $dv = J_g dV_0$ accounting the elastic incompressibility, thus obtaining:

$$
\begin{aligned}
\lambda_{rR} &= \frac{\partial r}{\partial R} = J_g^{1-\zeta}\frac{R}{rh\lambda_{ezZ}} \\
\lambda_{\theta\Theta} &= h\frac{r}{R} \\
\lambda_{zZ} &= \frac{l}{L} = J_g^{\zeta}\lambda_{ezZ}
\end{aligned}
\tag{4.24}
$$

where the axial stretch time-history λ_{zZ} may be assumed to be prescribed, for example deriving it from experimental observations ([141]). In particular, by considering that *in situ* vessels exhibit residual axial strains which allometrically increase as the overall body grows, a possible form of the stretch λ_{zZ} can be faithfully described by means of the following evolution function:

$$
\begin{aligned}
\lambda_{zZ}(t) =& \frac{\lambda_{zZ}^f + \lambda_{zZ}^i}{2} + \\
&+ \frac{\lambda_{zZ}^f - \lambda_{zZ}^i}{2}\tanh\left(\omega_z\left(t - t_z\right)\right)
\end{aligned}
\tag{4.25}
$$

where λ_{zZ}^i and λ_{zZ}^f represent the initial and the final observed stretch ratios, while t_z and ω_z are a characteristic time and a suitable frequency constant, respectively. Furthermore, by virtue of the elastic incompressibility constraint, the following relation for the radius r at the current time can be derived:

$$
\begin{aligned}
r &= \sqrt{\frac{2}{h\lambda_{ezZ}}\int_{R_i}^{R} J_g^{1-\zeta}\left(\overline{R}\right)\overline{R}d\overline{R} + r_i^2} = \\
&= \sqrt{J_g^{1-\zeta}\frac{R^2 - R_i^2}{h\lambda_{ezZ}} + r_i^2}
\end{aligned}
\tag{4.26}
$$

in which the assumption of uniform growth tensor has been introduced, according to recent literature works ([160, 202]).

By following the work by [91], arteries can be mechanically modeled by considering a two-layer hollow cylinder, the inner and the outer layers representing the *tunica media* and the *tunica adventitia*, respectively, the mechanical contribution of the *tunica intima* being negligible. Both of them can be constitutively characterized by a strain

energy function made of an isotropic part and an anisotropic contribution which accounts for the fibers orientation. Hence, by also introducing a suitable Lagrange multiplier q^ξ to take into account the elastic incompressibility constraint, the strain energy functions reads as:

$$
\begin{aligned}
\psi^\xi = & \psi_{iso}^\xi\left(I_1\right) + \psi_{aniso}^\xi\left(I_4, I_6\right) = \\
= & \frac{k_0^\xi}{2}\left(I_1 - 3\right) + \frac{k_1^\xi}{2k_2^\xi} \sum_{i=4,6}\left(e^{k_2^\xi\left(I_i^\xi - 1\right)^2} - 1\right) + \\
& - q^\xi\left(J_e - 1\right)
\end{aligned}
\tag{4.27}
$$

where ψ_{iso}^ξ and $\psi_{aniso}^\xi\left(I_4, I_6\right)$ respectively characterize the mechanical response of the volumetric part and the response of the vessel (elastic and collagen) fibers; the superscript $\xi = \{m, a\}$ denotes *media* and *adventitia*, while $k_{0,1,2}^\xi$ are suitable material constants, being k_0^ξ related to the volumetric response. The above introduced energy densities are then written as a function of the invariants ([91]):

$$
\begin{aligned}
I_1 &= \operatorname{tr} \mathbf{C}_e \\
I_4^\xi &= \mathbf{C}_e : \left(\mathbf{a}_+^\xi \otimes \mathbf{a}_+^\xi\right) \\
I_6^\xi &= \mathbf{C}_e : \left(\mathbf{a}_-^\xi \otimes \mathbf{a}_-^\xi\right)
\end{aligned}
\tag{4.28}
$$

where $\mathbf{C}_e = \mathbf{F}_e^T \mathbf{F}_e$ is the left Cauchy-Green tensor and $\mathbf{a}_{+,-}^\xi = \cos\beta\mathbf{e}_\Theta \pm \sin\beta\mathbf{e}_Z$ represent the fibers directors lying within the *media* and the *adventitia*. The application of the Piola transform $(4.21)_2$ returns the expression for the Cauchy stress tensor, connected to (4.27) by the relationship:

$$
\boldsymbol{\sigma}^\xi = J_g^{-1}\mathbf{P}^\xi\mathbf{F}^T = \frac{\partial\psi^\xi}{\partial\mathbf{F}_e}\mathbf{F}_e^T - q^\xi\mathbf{I}
\tag{4.29}
$$

Then, by rewriting $(4.7)_1$ in absence of body forces and in the current configuration as $\nabla_{\mathbf{x}} \cdot \boldsymbol{\sigma}^\xi = \mathbf{0}$, the sole non-trivial equilibrium equation to be satisfied is:

$$
\frac{d\sigma_{rr}^\xi}{dr} + \frac{\sigma_{rr}^\xi - \sigma_{\theta\theta}^\xi}{r} = 0
\tag{4.30}
$$

Direct integration of this equation –separately written for both *media* and *adventitia*– combined with the condition describing the inner deformed radius once the tractions on the walls are prescribed, gives:

$$
\begin{aligned}
\sigma_{rr}^a\left(r_o\right) - \sigma_{rr}^m\left(r_i\right) = &\, \Delta p = \\
= \sum_\xi \int_{\mathfrak{I}^\xi} J_g^{\frac{\zeta-1}{2}}\left(h\frac{r}{R}\frac{\partial\psi^\xi}{\partial\lambda_{\theta\Theta}} - \frac{\partial r}{\partial R}\frac{\partial\psi^\xi}{\partial\lambda_{rR}}\right)\frac{\partial r}{\partial R}\frac{dR}{r} &
\end{aligned}
\tag{4.31}
$$

with $\mathfrak{I}^m = [R_i, R_i + H_m]$ and $\mathfrak{I}^a = [R_i + H_m, R_o]$, H_m denoting the thickness of the *tunica media*. By prescribing continuity of radial stresses and of displacements at

the vessel layers interface, the corresponding interface radius in the deformed configuration can be determined through the relation $r_H = \sqrt{r_i^2 + J_g^{1-\zeta} h^{-1} \lambda_{ezZ}^{-1} H_m \left(H_m + 2R_i \right)}$. The pressures $\sigma_{rr}^a \left(r_o \right)$ and $\sigma_{rr}^m \left(r_i \right)$ are instead related to the external loading condition through the Cauchy's theorem $(4.7)_2$ or $\boldsymbol{\sigma}^\xi \cdot \mathbf{n}^\xi = \mathbf{t}^\xi$, $\forall \mathbf{x} \in \partial \mathcal{B}^\xi$.

From the computational standpoint, it is worth to highlight that, once the loading conditions have been assigned, the equilibrium relation (4.31) can be analytically solved for each finite time step during which growth can be assumed constant, in this way reducing to the sole unknown r_i and thus obtaining the deformed configuration through (4.26).

4.3.3 *Biomechanics of reinforced pulmonary artery transposed into aortic position*

As already said, by testing an *ad hoc* designed prosthesis system made of a combined bioresorbable scaffold and an auxetic reinforcement, a large animal model of transposition of pulmonary artery in systemic pressure load. This experimental *in vivo* study, aimed to replicate actual clinical scenarios, has enabled to observe a physiological arterialization of the reinforced pulmonary vessels transposed into aortic position ([141, 145, 187]), resulting in PA medial thickening and matrix rearrangement (see Figure 36).

To biomechanically explain these *in vivo* experimental findings and gain insights into possible enhancements of PA reinforcements design criteria, a mathematical model is built up by incorporating vessel growth, remodeling and large elastic deformations of both biological and synthetic materials.

Three theoretical simulations of experimental interest have been then performed:

- *Reference Aorta*, regarding the modeling of a benchmark aortic tract subjected to internal systemic pressure, say p_i, of 120 mmHg (16 kPa, assumed constant). This case establishes for the reference aorta selected benchmark quantities, say the physiological growth over a six-month period (represented by the evolution of both diameter and thickness of the vessel layers) and the wall mechanical stresses.

- *No Reinforcement*, analyzing the case of a not reinforced pulmonary artery transposed into aortic position at the pressure p_i and subjected to growth and remodeling processes. Results of this simulation are directly compared with the outcomes from the control group of the animal model.

- *Composite Reinforcement*, concerning the mechanical analysis of the reinforced PA system undergoing growth and remodeling. The presence of the prosthesis is simulated by integrating the mechanical properties of the *adventitia* with those of the PDS biodegradable structure, by thus additionally providing an external variable pressure p_o, accounting for the e-PTFE armor elastic confinement whose value depends on the armor constitutive properties and evolves as a function of the pulmonary artery dilatation and growth.

With reference to the theory presented in the previous Sections, some additional key features have been introduced to faithfully describe the above mentioned cases. First of all, the effect of the blood vessel structural remodeling on the tissues elasticity
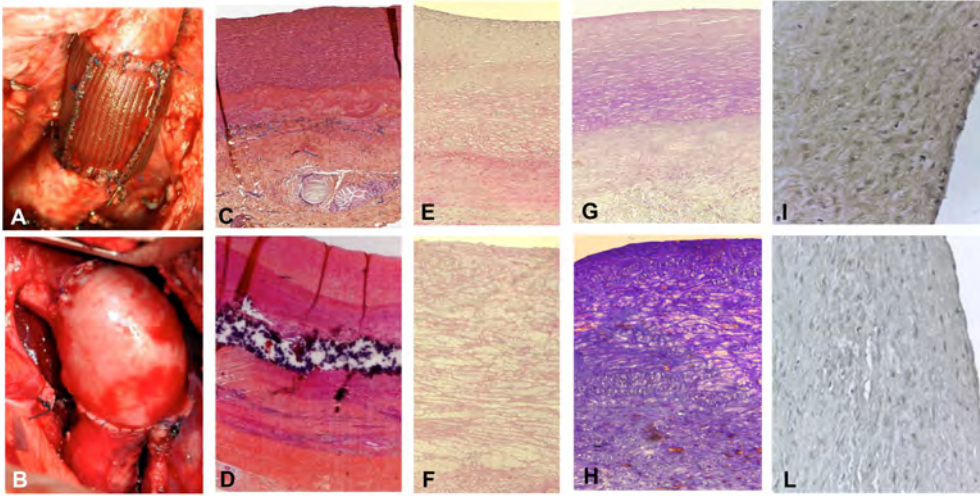
Figure 36: A-B) Surgical implant. **A**. Bioresorbable reinforcement; **B**. Control. **C-D**) Hematoxylineosin staining. **C**. Bioresorbable reinforcement. Note remnants of PDS. **D**. Control. Note medial disruption and inflammatory infilitrates; **E-F**) PicroSirius red staining. **E**. Bioresorbable reinforcement compact collagen organization: the "elastic zone" of the vessel and less pronounced cellular infiltrate. **F**. Control. Dispersed collagen fibers; **G-H**) Mallory staining; **G**. Bioresorbable reinforcement. Elastin deposition (pink). **H**. Control. Presence of collagen (blue); **I-L**) MMP-9 immunohistochemistry. **I**. Bioresorbable reinforcement. Note MMP-9 overexpression in the PDS group indicating active matrix remodeling phenomena. **L**. Control.

has been analyzed and thus mathematically described in terms of change of mechanical properties. To make this, suitable remodeling parameters γ^m and γ^a have been introduced to guide the evolution of bulk moduli k_0^m and k_0^a of *media* and *adventitia*, respectively. As a result, the tunics energy densities become explicitly dependent on them, i.e. $\psi_{iso}^\xi = \psi_{iso}^\xi \left(I_1, \gamma^\xi \right)$, so mimicking the temporal elastic properties changes also experimentally observed by [101]. Also, with reference to (4.20), the role of the remodeling enhancers **K** is assumed to be played by the average levels of energy densities occurring in the aortic layers in a physiological situation, in this manner interpreting the remodeling as an energy-driven process which dynamically responds to energy supplies with tissue structural changes –over selected timescales– to accommodate stress and strain and in turn minimize energy, a logic to which many biomaterials seem to obey if subjected to remodeling ([46]).

For the sake of simplicity, the parameters γ^ξ have been here considered as volume averaged values, so that the equation (4.20) can be written in the following scalar form:

$$\dot{\gamma}^\xi = c_\gamma J_g \left(\overline{\psi}_{A,iso}^\xi - \frac{\partial \overline{\psi}_V^\xi}{\partial \gamma^\xi} \right) \tag{4.32}$$

where $c_\gamma \geq 0$ is a dimensional constant which takes into account the characteristic long-term timescale of remodeling (ranging from about 4000 h to 40000 h, as reported by [216]), whereas ψ_A^ξ and ψ_V^ξ respectively denote the energy functions specialized for the aorta and the PA trunk subjected to a volume averaging process (see the synoptic Table 3 for the adopted material parameters):

$$\overline{\psi}_{A,V}^\xi = \frac{1}{\mathcal{V}_0} \int_{\mathcal{V}_0} \psi_{A,V}^\xi dV_0 \tag{4.33}$$

Furthermore, to accurately model the reinforced PA case, how degrading polydioxanone (PDS) mesh and e-PTFE external armor do cooperate and in-time support the vessel walls must be additionally mathematically described. With reference to the PDS structure, this is indirectly done by mechanically *enriching* the *adventitia* with an augmented time-dependent bulk modulus decreasing in time according to a selected experimentally based degradation law. In this way, the updated *adventitia* bulk modulus, say κ_0^a, takes the form:

$$\kappa_0^a = \gamma^a \left(t \right) k_0^a + \left(\phi \left(t \right) \right)^\nu k_0^s \tag{4.34}$$

where k_0^s constitutes the PDS contribution to the overall (reinforced) *adventitia* bulk modulus, $\phi \left(t \right)$ is a degradation law which describes the scaffold volume fraction pauperization[2] (according to the actual PDS mass bioresorption program in a six-months period, see e.g. [147]), here chosen as (see Figure 34, right-bottom graphic):

$$\phi \left(t \right) = \frac{\phi_0}{1 + \omega_1 e^{\omega_2 (t - t_s)}} \tag{4.35}$$

---

2 There is thus a direct effect of the PDS pauperization on the growth, remodeling and in turn on the overall elastic properties of the *adventitia*, but not vice versa, that is growth and remodeling do not affect (or perturb) the PDS degradation law.

where ϕ_0 is a constant representing the initial PDS volume fraction which accounts for the porosity of the scaffold ([24]) while ν is a dimensionless, strictly positive (typically between 1 and 3) penalization power, employed to have as a result the well-known less than proportional stiffness increase with the material volume fraction of a porous representative volume element ([46, 116]). Also, in (4.35), t_s accounts for a characteristic inflection time and ω_1 and ω_2 represent constants to be set in order to fit the experimental PDS degradation curve ([171], [24], [136]). In this way, the model accurately catches the role exerted by the PDS scaffold in terms of vessel wall stiffening, at the early stages of growth the PDS mesh supporting the pulmonary artery to resist to higher systemic blood pressures –so avoiding excessive strain in turn provoking high stress and finally aneurysms– then progressively degrading and slowly accompanying the autograft toward possible remodeling and arterialization-like processes. On the other hand, the role played by the e-PTFE auxetic structure –that is somewhat complementary to that of PDS– has been modeled to reproduce an initial auxetic-induced relatively low contribution to vessel elastic resistance against load pressure, becoming the confinement effect increasing as tissue grows up, moving outward the external PA radius. From the mathematical point of view, this is translated into an elastic *reactive* pressure transmitted at the PA outer cylindrical surface as the external radius expands (see Figure 34, left-bottom graphic). Therefore, by imaging the e-PTFE net as an external layer simply described by an exponential strain energy potential whose structure is similar to that in (4.10), and assuming that no external pressure is applied on this layer, the following relationship can be established ([90]):

$$\sigma_{rr}^n (r_o) = - \int_{\lambda_e}^{\lambda_o} \frac{1}{\lambda_T^2 \lambda_Z - 1} \frac{\partial \psi^n}{\partial \lambda_T} d\lambda_T, \tag{4.36}$$

$$\psi^n = \frac{k_1^n}{k_2^n} \left(e^{k_2^n (I_4^n - 1)} - 1 \right) \tag{4.37}$$

given that $I_4^n = I_6^n = \lambda_T^2 \cos^2 \eta_n + \lambda_Z^2 \sin^2 \eta_n$, η_n being the mesh half-angle. In equation (4.36) λ_T and λ_Z denote the azimuthal and the longitudinal stretches which completely describe the deformation of the auxetic net, whose associated deformation gradient is thus

$$\mathbf{F}^n = Diag \left\{ \frac{RL_n}{r_n l_n}, \frac{r_n}{R}, \frac{l_n}{L_n} \right\} \tag{4.38}$$

By taking $\lambda_Z = l_n / L_n$ to be constant, the condition at the interface $r_o = r(R_o)$ immediately gives $\lambda_Z = J_g^\zeta \lambda_{ezZ}$ and the e-PTFE structure motion r_n can be described similarly to (4.26) and related to the vessel outer radius as written down:

$$r_n = \sqrt{\frac{R^2 - R_o^2}{\lambda_Z} + r_o^2} = \sqrt{J_g^{-\zeta} \frac{R^2 - R_o^2}{\lambda_{ezZ}} + r_o^2}, \tag{4.39}$$

where

$$r_o = \sqrt{J_g^{1-\zeta} \frac{R_o^2 - R_i^2}{h \lambda_{ezZ}} + r_i^2} \tag{4.40}$$

Hence, the equations (4.26) and (4.39) allow to derive the square stretches at the the boundary as a function of r_i:

$$\lambda_o^2 = \frac{r_o^2}{R_o^2} = \frac{1}{R_o^2}\left(J_g^{1-\zeta}\frac{R_o^2 - R_i^2}{h\lambda_{ezZ}} + r_i^2\right) \tag{4.41}$$

$$\lambda_e^2 = \frac{r_e^2}{(R_o + H_n)^2} = \frac{1}{(R_o + H_n)^2}\left(J_g^{-\zeta}\frac{H_n\,(2R_o + H_n)}{\lambda_{ezZ}} + r_o^2\right)$$

where H_n is the initial auxetic armor thickness. The equilibrium equation $\sigma_{rr}^n\,(r_o) = \sigma_{rr}^a\,(r_o)$ to be satisfied at the interface r_o then gives the possibility of finding, by integrating (4.36), the actual pressure that the armor applies on the *adventitia* by elastically reacting to the vessel deformation and growth. In particular, by performing the substitution $x = k_2^n\,(I_4^n - 1)$, it is possible to compactly write:

$$\sigma_{rr}^a\,(r_o) = -p_o = \frac{k_1^n e^{-Q}\cos^2\eta_n}{\lambda_Z}\int_{x_o}^{x_e}\frac{e^{x+Q}}{x+Q}dx =$$

$$= \frac{k_1^n e^{-Q}\cos^2\eta_n}{\lambda_Z}\left(\mathrm{Ei}\,(x_e + Q) - \mathrm{Ei}\,(x_o + Q)\right) \tag{4.42}$$

with $Q = 1 - k_2^n\lambda_Z^2\sin^2\eta_n - k_2^n\lambda_Z^{-1}\cos^2\eta_n$ and $\mathrm{Ei}\,(x)$ representing the exponential integral function, while $x_e = x\,(\lambda_e^2)$ and $x_o = x\,(\lambda_o^2)$ are both functions of the updated vessel outer radius r_o (or equivalently r_i) through (4.41)$_1$ and (4.41)$_2$, that is:

$$x_e + Q = k_2^n\cos^2\eta_n\,(\lambda_e^2 - \lambda_Z^{-1})$$

$$x_o + Q = k_2^n\cos^2\eta_n\,(\lambda_o^2 - \lambda_Z^{-1}) \tag{4.43}$$

Lastly, all the *in silico* simulations (in detail discussed below) are conducted by assuming the growth to obey a typical logistic profile, a law largely encountered in the literature to describe many different growth dynamics of living systems, at different scale levels, and hence widely adopted among biologists to fit related experimental data ([105]); as a consequence, in order to consider the direct effect of the experimentally observed growth of the lambs discussed in [141] on the mechanical analysis of the vessels alone and the reinforced PA system, it is here proposed to transpose the logistic growth assumption also to the tissue scale, as a first step also hypothesizing a stress-uncoupled growth as a simplifying rationale to mimic the physiological growth curve. Thus, the equation (4.3) can be explicitly given in the form:

$$\dot{J}_g = c_g J_g\left(1 - \frac{J_g}{J_g^{max}}\right) \tag{4.44}$$

where J_g^{max} represents a prescribed upper bound reference value, in the present case evaluated on the basis of the (allometrically scaled) body size achieved by the adult animal model with respect to the initial size ([141, 142, 144]), while $c_g \geq 0$ is a proper growth rate (see e.g. [80]).

With respect to the case of reference artery, only physiological growth during a six-month period with no internal remodeling has been assumed: also, for both the cases of reference artery and not reinforced PA, the analyses have been conducted by considering the presence of the sole systemic aortic pressure, thus prescribing to the

biomechanical models zero external loads at the outer radius and internal pressure p_i –typically of the order of 100-120 mmHg– assumed to be constant during the time step of the analyses. As a result, the equation (4.31) becomes:

$$p_i = \sum_{\xi \in \{m,a\}} \int_{\mathfrak{I}^\xi} J_g^{\frac{\zeta-1}{2}} \left(h \frac{r}{R} \frac{\partial \psi_{A,V}^\xi}{\partial \lambda_{\theta\Theta}} - \frac{\partial r}{\partial R} \frac{\partial \psi_{A,V}^\xi}{\partial \lambda_{rR}} \right) \frac{\partial r}{\partial R} \frac{dR}{r}$$

with which the two above mentioned cases can be distinguished and separately treated by specializing the strain energy functions through proper assignments of different intrinsic parameters, so that ψ_A^ξ and ψ_V^ξ can be recognized as representative of aorta and pulmonary artery (vein-like) materials, respectively.

On the other side, by making reference to the above proposed theoretical strategy for describing how the bioresorbable scaffold and the auxetic structure do cooperate to reinforce the pulmonary autograft, the balance equation (4.31) reads as:

$$p_i - p_o = \sum_{\xi \in \{m,a\}} \int_{\mathfrak{I}^\xi} J_g^{\frac{\zeta-1}{2}} \left(h \frac{r}{R} \frac{\partial \psi_V^\xi}{\partial \lambda_{\theta\Theta}} - \frac{\partial r}{\partial R} \frac{\partial \psi_V^\xi}{\partial \lambda_{rR}} \right) \frac{\partial r}{\partial R} \frac{dR}{r}$$

Finally, the equations (4.44) and (4.45) constitute the system to be solved for analyzing the reference aorta, in which the sole unknowns are the growth term J_g and the inner radius r_i; the same equations have to be coupled with (4.32) to model the not reinforced PA biomechanical response. Analogously, to simulate the biomechanical behavior of the reinforced PA, the equations (4.45), (4.44) and (4.32), which incorporate the remodeling parameters γ^a and γ^m responsible for arterialization phenomena, have to be instead used.

From the numerical standpoint, the simulations to be conducted for reference artery, pulmonary artery and reinforced autograft, require suitable material and geometric parameters, in detail reported in Table 3. For the sake of clarity, the parameters have been divided in different sections regarding the different model constituents: both aortic and pulmonary artery constitutive parameters have been deduced from [32, 91, 149, 203], the opening angle value being instead referred to the range proposed by [4]. The geometric parameters have been extrapolated by the *ex vivo* data obtained throughout the experimental observations. Lastly, the material parameters concerning both the PDS and the e-PTFE volumetric response have been determined from the inflation compliance data reported in literature ([24, 109, 172, 179, 183, 195]).

4.4   THE RELAY RACE EFFECT OF PDS SCAFFOLD AND E-PTFE ARMOR

The analyses have been performed by implementing the above detailed biomechanical models in the computational software program MATHEMATICA® ([210]). Here, the partial differential equations governing the problems have been solved analytically in space, for each time step, and hence the complete solution found by numerically integrating over the whole six-month observation period related to the animal model ([141]).

The obtained results highlight that, although the PA tracts were initially the same from a physiological and a constitutive point of view, under the systemic blood pressure their behavior significantly diverges in the two cases, i.e. reinforced and not

reinforced vessels. In fact, results show that the cooperation between bioresorbable PDS scaffold and permanent e-PTFE auxetic structure plays a crucial role in preventing a fateful yielding of the vessel, wall intrinsic mechanical properties in absence of reinforcement being absolutely inadequate to both respond to the new imposed aortic pressure regimes and limit large deformations prodromal to aneurismal complications. In particular, theoretical outcomes, illustrated in Figure 39, clearly show a marked difference among reference aorta, PA alone and PA with prosthesis, in terms of pressure-induced initial burst dilatation and final associated vessels diameters, a fact also quantitatively confirmed by experimental observations ([141]) and summarized in Table 2. Theoretical predictions are indeed in very good agreement if compared with experimental data, except for a slight underestimation of not reinforced PA sizes, mainly related to the fact that, in absence of prosthesis, actual strains are not purely due to combined elastic deformation and growth, additional inelastic strains being kindled by locally occurring irreversible (i.e. visco-elastic-plastic and damaging) phenomena, as can be seen by direct observations (Figure 37).
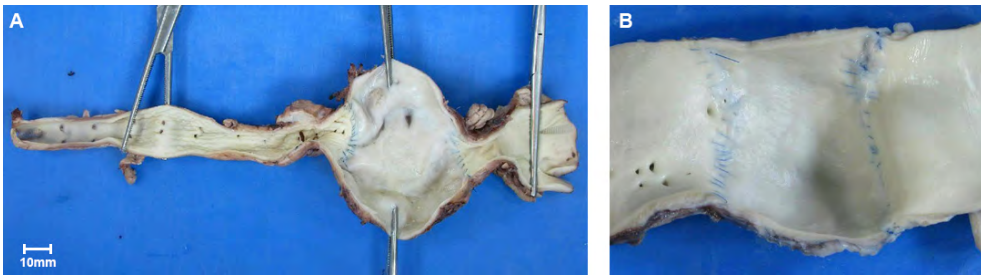
Figure 37: A. Not reinforced PA trunk with aneurismal formation (analysis after the break at 3 months); **B**. PA reinforced with knitted polydioxanone resorbable copolymer scaffold (explanted at 6 months): note the homogeneous vessel profile denoting the success of the implant.

The analytical curves also underline a specific non-linear trend, in terms of vessel diameters time-history, which shows a sort of asymptotic behavior that furnishes an upper bound to vessel growth in proximity of body adulthood, a phenomenon otherwise unforeseeable on the basis of the sole initial (at one day) and final (at six months) observations and qualitatively crucial to envisage a successful prognosis of the PA reinforcement also when this surgical protocol is applied to young human patients. As a matter of fact, the not reinforced PA excessively dilates during the time window considered, passing from an initial diameter of about 29.5 mm –measured in the first days– to a diameter of about 38.1 mm, after six months. Moreover, the actual deformation profiles of the not reinforced PA go off the vessel from the tube-like shape, by losing the axis-symmetry of the response assumed in the present theoretical model, as can be observed from the angiographic measures (Figure 38), as well as from *in situ* (Figure 36) and explanted *ex vivo* vessel trunks (Figure 37).

On the contrary, in the doubly reinforced PA, the mathematical model demonstrates that the prosthesis system overall works as a sort of "relay race", by guaranteeing the handover of the bearing structure functions from the PDS scaffold (at the early stages of tissue growth and remodeling) to the e-PTFE armor, initially "dormant" as a consequence of the typically low stiffness exhibited by stress-free auxetic structures
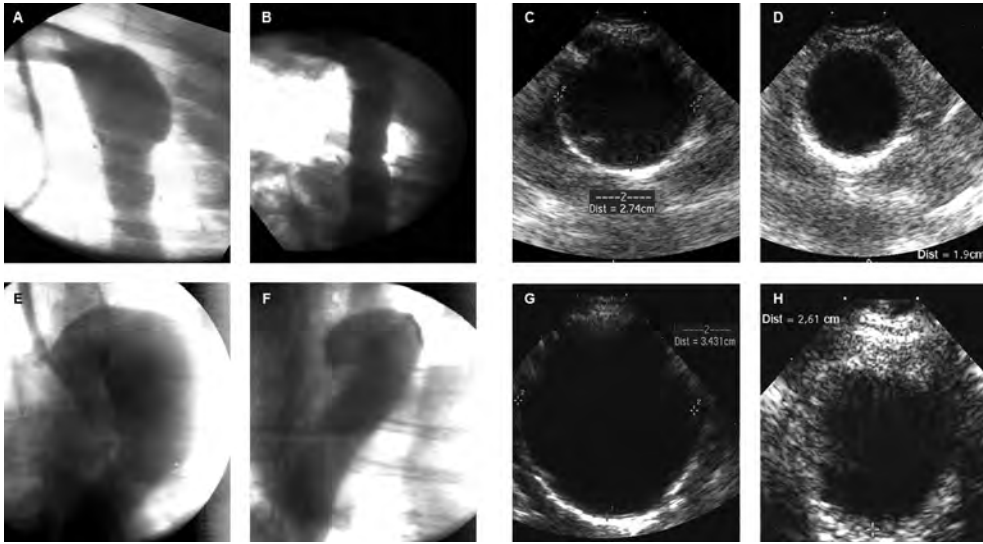
Figure 38: **A**,**B**,**E**,**F**) Angiographic images. **A**. Not reinforced PA at day 1; **E**. Not reinforced PA at day 180; **B**. Reinforced PA at day 1; **F**. Reinforced PA at day 180. Note the uniformity of the vessel profile in case of reinforcement (**B**,**F**) and loss of physiological shape, prone to aneurismal complication (**A**,**E**). **C**,**D**,**G**,**H**) Ecographic images (vessel cross sections). **C**. Not reinforced PA at day 1; **G**. Not reinforced PA at day 180; **D**. Reinforced PA at day 1; **H**. Reinforced PA at day 180. Note the severe diameter dilation in the not reinforced case (**C**,**G**).

at small strains. In this way, the mechanical shielding of the lapse vessel confines the radial expansion and simultaneously allows to the pulmonary artery to remodel its tunics for attaining an adequate level of mechanical properties (e.g. elastic bulk moduli, see Figure 41). Finally, once the bioresorbable scaffold has completed its degradation program and the strengthened vessel walls can actively respond to the systolic pressure, the e-PTFE structure accompanies PA *media* and *adventitia* toward their progressive aortic somatic growth, by stretching its weave to gain stiffness and effectively confine further vessel expansion, so avoiding tissue prolapse and aneurismal degenerative phenomena.

Table 2: Comparison of the external diameters (expressed in mm) - experimental observations vs analytical predictions

	Day 1		Day 180	
	Experimental	Analytical	Experimental	Analytical
Reference Aorta	13.0–16.4	13.1	17.0–21.0	21.0
Composite Reinforcement	14.0–20.0	16.3	25.0–33.0	27.2
No Reinforcement	25.0–33.0	24.2	34.3–42.0	36.1

Furthermore, Figure 39 also shows that the mathematical model predicts a "gain" of the reinforced grown PA to be measured in terms of wall thickness occurring when the PA tracts are ideally excised and relaxed, as well as when the vessels are sub-
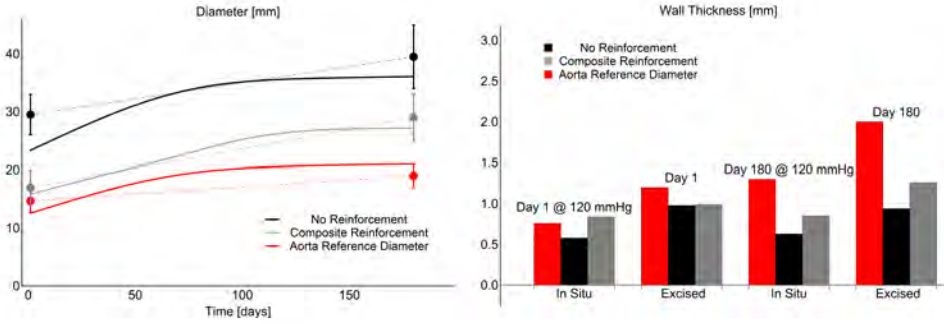
Figure 39: Left: Evolution of the outer diameters (continuous lines represent theroetical outcomes while markers are experimental measures). Right: Vessels thicknesses provided by the simulations at day 1 and at day 180 when the vessels are either in position or excised.

jected to the *in situ* inflation pressure, so highlighting an effective thickening of the reinforced graft after the observation period that can be directly related to actual PA arterialization. It is worth to notice that the estimated Cauchy (actual) stresses, predicted by the mathematical model at 180 days and illustrated in Figure 40, bring to light further aspects that may help to better understand the actual effects of both PDS scaffold and e-PTFE armor in reinforced PA on growth and elastic response of the vessel to systemic pressure. In fact, from the stress profiles illustrated in Figure 40, it can be inferred (and somewhat quantified) the mechanical role of the prosthesis system and, in particular, of the GORE-TEX structure. The effective pressure difference between the internal systolic push and the external armor confinement *de facto* determines a "stress shielding" phenomenon which maintains the stress distribution over the PA thickness sufficiently uniform, by also forcing the stress level in the *tunica media* to be moderate with respect to the physiological one in the (ticker and stiffer) reference aorta, in this way creating a safe state of stress settling at about 100 kPa. On the contrary, from theoretical outcomes, the not reinforced PA exhibits equivalent (von Mises) and circumferential (hoop) stresses in the *tunica media* with peaks of about 800 kPa, a value sufficiently high and close to tissue stress threshold to determine mechanically critical states and invite yielding processes potentially undergoing aneurismal degeneration. Also, Figure 40 shows the non-linear pressure-diameter curves one would virtually measure in the three cases examined (reference aorta, reinforced and not-reinforced PA) at 180 days, if an *ex vivo* inflation test were performed. It can be there noticed how the not reinforced PA experiences strong dilatation in a low range of inflation pressures –below 50 mmHg– with the external diameter achieving pathological dimensions before the curve exhibits a theoretical hardening. The behaviors of reference and reinforced pulmonary arteries are instead different, and, in both the cases, the diameters dilation at systemic pressure is in good agreement with the experimental observations in the animal model ([141]).

In particular, by comparing pressure-diameter curves for reinforced and not reinforced PA, it emerges from the results a significantly and qualitatively different mechanical response in the two cases, the former exhibiting much smaller variations of the outer diameter than the latter, within the same pressure interval, say in the
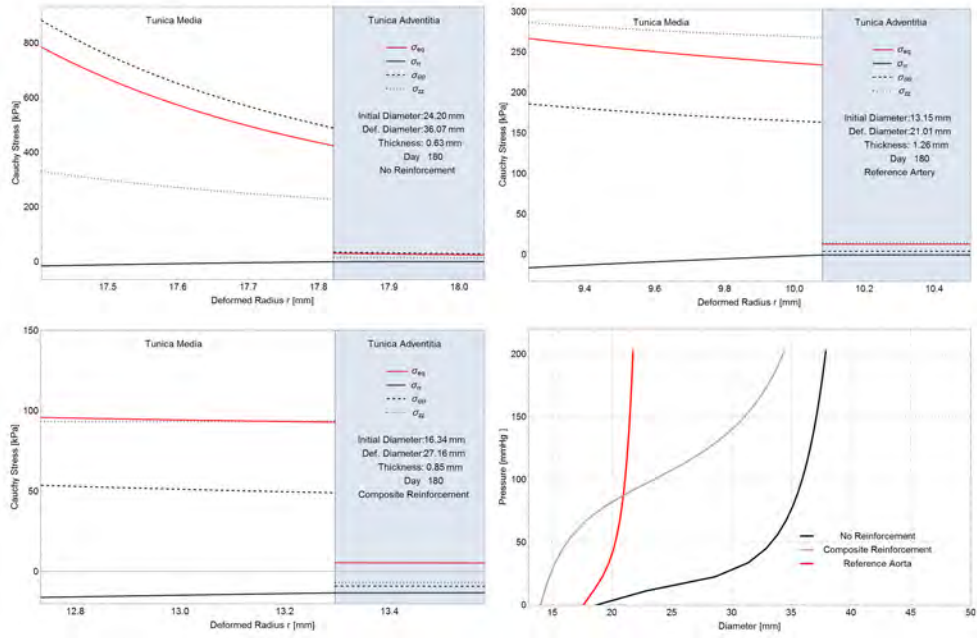
Figure 40: Cauchy stress profiles along the wall thicknesses in reference aorta (top-right), reinforced (bottom-left) and not reinforced (top-left) Pulmonary Autografts, with related pressure-diameter curves at 180 days for the grown vessels (bottom-right).

order of tens kPa. In the reinforced PA, this initial stiff behavior can be attributed to the balancing between the internal push and the e-PTFE external pressure due to the GORE-TEX elastic reaction to the vessel expansion. After that, a region of approximately proportional dilatation is observed, followed by an elastic hardening at higher pressures due to the combined effect of the intrinsic hardening of the vessel walls related to stress levels and reorientation of elastic fibers and the increasing stiffness of the auxetic material induced by severely dilated armor elements.

It is finally worth to notice that, albeit the stiffer behavior of reinforced PA exhibited in Figure 40 in terms of pressure-diameter is theoretical derived at 180 days –thus in absence of PDS– the effect of the bioresorbable scaffold is implicitly taken into account by the model through the (at six months registered) PA arterialization, a result biomechanically due to the stress shielding, initially ensured by the biodegradable PDS and finally stabilized by the confining action of the GORE-TEX structure. The concrete consequence of this interplay can be explicitly traced in the proposed mathematical model by analyzing the results in terms of in-time remodeling of average wall bulk moduli k_0. In Figure 41 the comparison between reinforced and not reinforced PA intrinsic stiffness variation during the six-month is for this purpose shown.
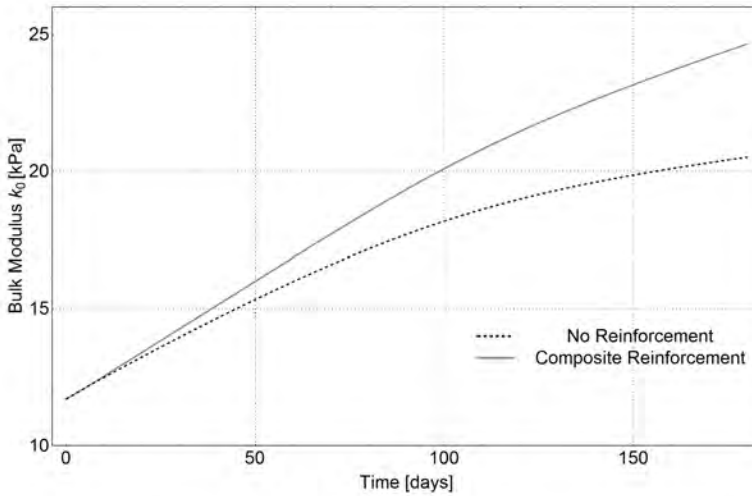
Figure 41: Evaluation of the bulk moduli remodeling in reinforced and not reinforced PA.

The theoretical outcomes, related to the modeling of the structural changes of reinforced pulmonary artery grafts under systemic pressure regimes, have shown that a virtuous biomechanical cooperation between biological and synthetic materials takes place, "stress-shielding" guiding the physiological arterialization of the vessel walls, consequently determining the overall success of the autograft system. The modeling has in fact theoretically demonstrated that in doubly reinforced PA, the prosthesis system *de facto* works as a sort of "relay race", by guaranteeing the handover of the bearing structure functions from the PDS scaffold (at the early stages of tissue growth and remodeling) to the e-PTFE armor, initially "dormant" as a consequence of the typically low stiffness exhibited by stress-free auxetic structures at small strains. In this way, the mechanical shielding of the lapse vessel contains the radial expansion and

simultaneously allows to the pulmonary artery to remodel its tunics for attaining an adequate level of mechanical properties. Once the bioresorbable scaffold has completed its degradation program and the strengthened vessel walls can actively respond to the systolic pressure, the e-PTFE structure accompanies PA *media* and *adventitia* toward their progressive aortic somatic growth, by stretching its weave to gain stiffness and to effectively confine further vessel expansion, so avoiding tissue prolapse and aneurismal degenerative phenomena. From the engineering point of view, all the results have essentially shown a very good agreement when compared with experimental data, also quantitatively, thus encouraging the use of the mathematical model for better understanding the specific biomechanical dynamics and designing possible new criteria and strategies for optimizing PA prostheses and successfully applying the surgical protocols to human patients.

Table 3: Synoptic table of data and employed parameters

References: 1. [149] ; 2. [203] ; 3. [32] ; 4. [91] ; 5. [4] ; 6. [5] ; 7. [179] ; 8. [116] ; 9. [24] ; 10. [171] ; 11. [109] ; 12. [195] ; 13. [172] ; 14. [183] ; 15. [217] ; 16. [142] ; 17. [144] ; 18. [141] ; 19. [94] ; 20. [80] ; 21. [216]. E. O. - Experimentally Observed Parameters. F./A. P. - Fitting/Assumed Parameters

Symbol	Unit	Value				References
		Aorta		**PA**		
		Media	**Adventitia**	**Media**	**Adventitia**	
Material Parameters						
k_0	[kPa]	51.1	5.1	16.7	1.67	[1, 2, 3]
k_1	[kPa]	18.6	1.86	4.9	0.49	[1, 2, 3]
k_2	[-]	17.4	1.74	0.839	0.711	[1, 4]
β	[°]	29	62	29	62	[4]
Geometrical Parameters						
H	[mm]	0.8	0.4	0.667	0.333	E. O.
R_i	[mm]	7.8		9.5		E. O.
α	[°]	91		120		[5]
λ_{zZ}^i	[-]	1.7		1		[4, E. O.]
λ_{zZ}^f	[-]	2		2		[6, E. O.]
PDS Parameters						
k_0^s	[kPa]	267				[7]
ν	[-]	1.34				[8]
ϕ_0	[-]	0.25				[9]
ω_1	[-]	0.07				F./A. P.
ω_2	[-]	0.05				F./A. P.
t_s	[day]	30				[10]
ePTFE Parameters						
k_1^n	[kPa]	1000				[7, 11, 12, 13, 14]
k_2^n	[-]	0.4				F./A. P.
H_n	[mm]	0.2				[15]
η_n	[°]	26				F./A. P.
Growth-Remodeling data						
J_g^{max}	[-]	3.375				[16, 17, 18]
ζ	[-]	0.133				F./A. P.
c_g	[day^{-1}]	0.025				[19, 20]
c_γ	[kPa^{-1} day^{-1}]	8.64×10^{-5}				[21]
ω_z	[day^{-1}]	0.02				F./A. P.
t_z	[day]	90				F./A. P.

5

POROELASTICITY COUPLED WITH VOLTERRA-LOTKA DYNAMICS IN SOLID TUMOR GROWTH

The full connection between dynamical systems used as predictive models in computational biology and the biomechanical theory of growth and remodelling represents the key activity described in the following. The continuum modeling of growing bodies draws from time upon the well-known finite strain formulation widely adopted also in elastoplasticity and thermoelasticity, see e.g. the renowned works by Rodriguez, Cowin and Lubarda, for example([164], [48], [128]). The mechanics of growth and remodelling opened a scientific thread which is up to now currently investigated more and more avidly because of both the increasing interest aroused and the enormous number of applications, which might have a remarkable resonance on medical treatments and surgical procedures. As mentioned in the previous chapters, a growing soft biomaterial can be realistically associated with a heterogenous multi-component and eventually multiphasic body, whose consituents are changing in mass. For this reason, a growing body can be likely thought as an open system in which growth itself is the overall result of the complex interactions between constituents inhabiting the body and what enters/leaves the system. Consequently, although the main role in the growth process is played by the solid constituents, the further coupling with the fluid counterpart seems necessary, since the latter one plays the role of nutrient carrier and enhance the growth process by filtrating through the solid compartments and letting the exchange of biochemicals at the cellular level. In order to faithfully describe solid-fluid interplays connected with growth, the mechanical problem is described by means of the Biot's poroelasticity theory, in which the mechanical field variables account for the presence of a fluid phase and a heterogeneous solid phase that coexist and interact by experiencing reciprocal forces and exchanging mass. In this way solid mass generation can be directly connected to growth, and the deriving solid stresses and interstitial fluid pressure are separately recognizable, the two stresses having a different physiological interpretation: fluid pressure is in fact connected with the interstitial fluxes that drive macromolecules walkways through the tissue *interstitium* previously mentioned, while solid skeleton stress translates the physical forces exerted by the solid constituents during the growth process. This growth-induced stress might be therefore expressly determined from the knowledge of the dynamics of such living constituents within the tissue "ecosystem" (i.e. from the description of the interactions between cells and extra-cellular environments), searching for a suitable way of determining an expression for the growth-induced strain and related eigenstresses.

With reference to the subsequent applications, this strategy will let to comprehensively present a model of tumor growth, and the focus will be on a byosystem whose solid part is composed by tumor and healthy cells and extracellular matrix, namely the ECM, the variations of which are translated in terms of their volumetric fractions

at the tissue scale[1]. A fully coupled system of PDEs is derived and the effort of enriching the mechanical problem with these dynamics lies into the fact that growth is not treated as a system parameter or a canonical *a priori* prescribed function, as often encountered in the most of Literature, but as a variable itself of the problem, i.e. the growth will be a direct consequence of the way in which the interactions between the species inhabiting the living tissue will be modeled. In this sense, the population dynamics and the games theory offer a powerful tool allowing the possibility of describing the interaction among biological entities in the same way as individuals of an ecosystem. In this context, the Volterra-Lotka equations –adopted for the tumor model under discussion– have commonly been used for describing the oscillations of the number of animals in a restricted ecosystem. For example, they have been recently adopted to describe the migration and the interations of herbivorouse angulate species (*Cervus elaphus, Capreolus capreolus, Sus scrofa*) in "Parco Nazionale dell'Abruzzo" (see e.g. [31]). With an analogous imaginative effort, this way of establishing inter-specific interactions has been transposed to the scale of the cells and the other elementary biological constituents, with the difference that the corresponding ecosystem is largely more complicated than its macroscopic ecologic counterpart and actively affects the behaviour of the species, in this way representing an explicit unknown. By combining the population dynamics with the mechanical problem, the result is a heterogeneous poroelastic model, where the interaction between soft matrix and interstitial fluid flow is coupled with inelastic effects *ad hoc* introduced to simulate the macroscopic volumetric growth determined by cells division, cells growth and extracellular matrix changes occurring at the micro-scale level. The continuum modeling framework embracing the poroelastic approach has been preferred since it seems to overcome some limitations associated to other alternative approaches based on mass balances in multiphase systems because the crucial role played by residual stresses accompanying growth, and nutrient walkway (solidarily to fluid flow) is preserved. However, when these strategies have applied to analyze growth in solid tumors (see e.g. [166, 192]), some important cell-cell dynamics governing mass evolution, remodelling and invasion rates of cancer cells are inevitably lost. For this reason, the enhanced poroelastic model with inelastic growth has been developed through a full-coupling strategy, where the net growth induced deformation and the rise of internal pressures result from the competitive dynamics between healthy and cancer cell species, modeled by Volterra/Lotka-like equations. In this way the following system of non-linear fully-coupled PDEs has been derived to describe the complex mechanism of mutual influences among the cell species competition that is due to available common resources, stress gradients, interstitial fluid flows and inhomogeneous growth are all taken into account. The description of the activities related to this argument can be approximately divided into three parts: the linear formulation, the non linear formulation and the experimental setups (with comparisons). Despite the mathematical description, the complex interactions constituting the problem actually provide that the tumor and healthy cells compete within the extracellular space for the common resources, in this way determining a growth strain which is directly responsible of the rise of inelastic stresses in confined environments. The stress state within the tissue is then straightly responsible to activate and regulate mechano-sensing processes

---

[1] Cells interaction could be also treated by adopting a discrete approach, for example by modelling populations in terms of the cells number.

driving changes in cells cycles, proliferation and migration capabilities. In particular, hydrostatic stress can affect proliferation and impair cell mitosis, in this way determining a complete coupling between the mechanical and the dynamical physiological events. The complex machinery deriving from these interactions, in the case of the MultiCellular Tumor Spheroid –MCTS– growth, can be summarized in the "logical" scheme proposed in Fig. 42.
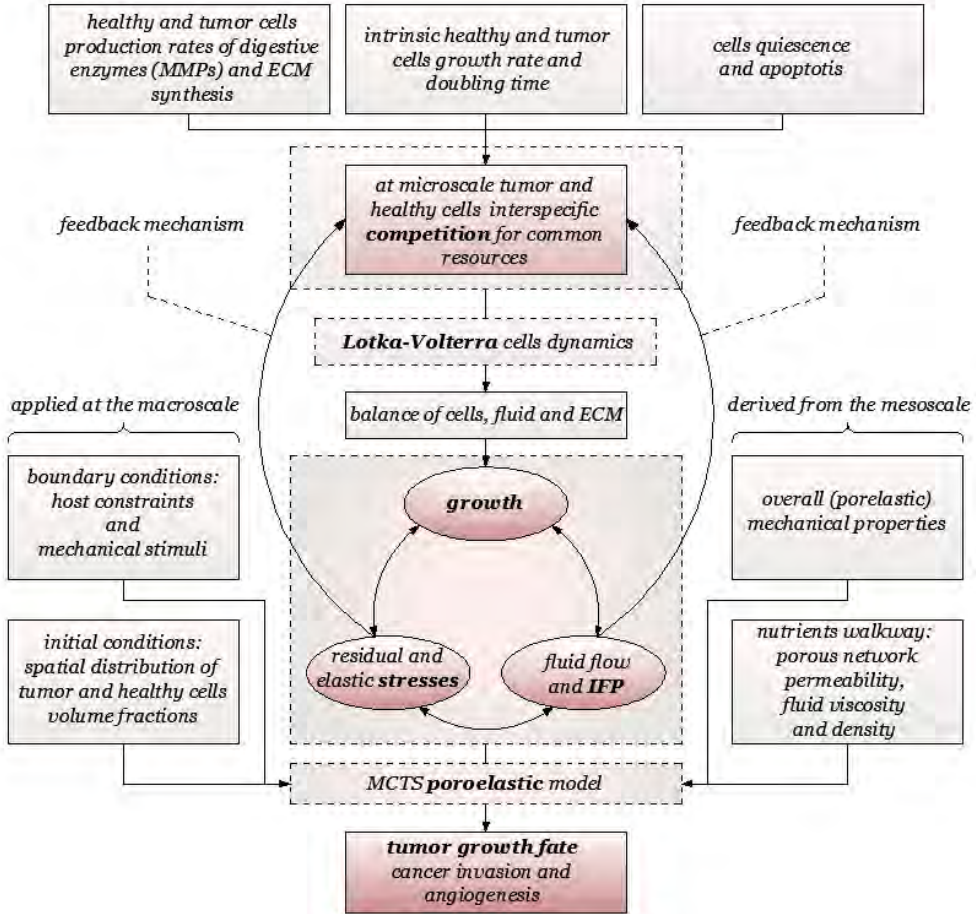
Figure 42: Logical connections highlighting the interaction network coinceved for the MCTS model.

5.1   INTRODUCTION

The rapidly growing advances of the research in tissue engineering continuously redraw new scenarios for applications in medicine, leading to the design of innovative drug delivery systems and biomaterials ([140, 181], [131]). A multiphysics vision in analysing the complex behavior of the living matter has in particular consolidated Tissue Mechanics (TM) theoretical approaches and modeling strategies ([46]) which

are currently recognized as helpful and indispensable tools for explaining experimental evidences as well as for supporting the design of prostheses for both soft ([143]) and hard ([62]) tissues. In this framework, an increasing interest has been in particular registered in literature for the mechanical properties of living cells –and for the understanding of the dynamics to which they obey at different scale levels– also motivated by some recent discoveries which seem to allow to envisage new horizons for therapy and diagnosis of human diseases like cancer, by for example exploiting the different in-frequency response of single healthy and tumor cells stimulated by utrasound ([64]).

The challenge to give a unified description of what tumor is, by providing a comprehensive model that would include the overall complexity of its physiology, is still hard to deal with, both because tumors have different natures and characteristics and since there are several causes that can be associated to their generation and development, and each physiological process is actually the integration of a considerable number of sub-processes occurring at different spatial (and temporal) scales. However, at the macroscopic scale –say at the tissue level– the feedback mechanisms and the cascade of bio-chemical and physical signals characterizing the complex interaction of dynamics occurring at different scales significantly complicates the biomechanical response of, say, tumor masses, thus requiring enriched models which encorporate the mechanobiology of solid tumor growth ([3]).

Cancer diseases occur when in a healthy tissue the cell-cell and cells-ECM (the Extra-Cellular Matrix) interactions are altered, and hyperplasia is generated as effect of sudden and often unforeseeable genetic modifications followed by a cascade of bio-chemical events leading to abnormal cell growth, lost of apoptosis, back-differentiation and metastasis. In this framework, the determination of models capable to describe how tumor masses behave and evolve in living tissues has been object of several studies which, by starting from different standpoints, have been aimed to predict tissue growth –and selected biochemical and physical phenomena– by invoking heuristic, diffusion-based, multiphase-reactive or purely mechanical models. This variety in theoretical approaches also reflects the difficulties related to harmonize experimental evidences and theoretical outcomes within an unifying fence, where the complexity of the mechanobiology at the basis of the tumor development might be better understood. As a matter of fact, how tumor invasion dynamics determined by cell-cell and cells-environment, elastic and residual stresses, do interact seems to be crucial for deeply tracing actual mechanisms occurring in complex heterogeneous materials like tumor masses during growth ([13]).

From the mechanical point of view, the behavior of heterogeneous bodies is modeled in the literature by means of different approaches. In particular, to follow different solid and fluid constituents in a tissue, the Biot poromechanical theory certainly represents a well-recognized strategy for describing the coupling between fluid and solid phases ([49]), some specific features of living bodies being caught through thermodynamic models of open systems ([117] and [127]). With reference to the biomechanics of growing tumors, linearly elastic ([12] and poroelastic ([173]) models, as well as non-linear hyperelasticity in which the multiplicative decomposition of the deformation gradient into a growth and an adaptive strain is helpfully adopted ([128], [164], [194]) have been widely used. The two main approaches employed to model the mechanical behavior and the growth of solid tumors are based on the theory of mixtures ([30, 156])

and on theory of linear poroelasticity ([166]), also in light of the fact that many soft tissues behave obeying the linear consolidation theory by Terzaghi ([65]). The dualism between mixture's theory and theory of porous media has been often summoned in dealing with the characterization of biological tissue, see for example the work by Garikipati ([74]). The two approaches provide complementary information. In fact, on a side, multiphase models mainly focus on the microscopic interactions among the phases of a continuous medium whose solid part is inhomogeneous at the micro- and the macro-scale levels, as well as the effects that the diffusion of particles (like nutrients, enzymes etc.) can have on its constituents. On the other side, heterogeneous poroelastic models, in this case associated with inelastic growth functions, permit to characterize of the effective growing stresses harboring in tumor tissues due to the inner mass expansion into the surrounding medium, to which some stiffness and permeability features are attributed. In particular, if one adopts poroelastic models, the effective stress is partitioned into solid stress and interstitial fluid pressure –in principle capable to strain alone the porous matrix– to which a growth-associated stress is added. In this approach, the observer varies solidarily to the solid phase and the fluid phase diffuses with respect to the latter one (while nutrient and chemicals can diffuse with respect to the fluid). The fluid walkway in the porous medium is driven by interstitial fluid pressure gradients engendered by spatially inhomogeneous pore volumetric dilation associated with resident stress fields. Nevertheless, some coupled key dynamics occurring at different scale levels and characterizing tumor growth are generally not taken into account simultaneously. In particular, to the best authors knowledge, how the cell populations actually interact at the microscale within the ECM and determine stresses, strain and nutrients walkway at the macroscopic level, in turn driving growth and invasion, has been not yet described explicitly ([76]). In fact, the vast majority of the models dealing with the analysis of growth-induced stresses introduces an *a priori* prescribed growth function –generally with a Gompertzian profile ([192])– in the form of a volumetric strain contribution that appears into the momentum equation ([8]). This implies that the growth-associated strains influence the stress but not *vice versa*, because of the absence of both the modeling of the interactions among cell species and ECM –from which macroscopic mass growth results– and the coupling between growth and stress. As a consequence, the growth dynamics is strongly affected by these simplified assumptions and thus the final tumor mass (e.g. multi-cellular spheroid) growth profiles somehow slavishly copies the growth function given in input, in this way *de facto* reducing the growth from an unknown to a data.

Actually, the cell-cell and cells-ECM dynamics –which occur at micro-scale level– continuously give/receive feedback to/from stress and strain events at the macroscale, this affecting the growth process, residual stresses and tumor fate as well.

At the microscale level, mechanical interactions between cells and ECM have been described in some recent works by simulating the mutual effects in terms of exchanged forces ([156, 177]) or, by making use of single-cell models based on the tensegrity structure paradigm by Ingber ([93]), to explain some experimentally observed evidences related to reorganization of cell cytoskeleton, cell migration, adhesion and evolution of cell stiffness properties mediated by polymerization-depolymerization phenomena of the protein filaments.

At the micro/mesoscale level, say the level at which cell populations collectively inter-

act and can be seen as aggregates, the competition between healthy and tumor cell species has been very recently presented in the light of the Game Theory - GT ([99, 108, 124, 125, 212]), highlighting the effectiveness of this peculiar standpoint. Overall tumor growth can be in fact seen as the result of the indirect interaction (interspecific competition) between tumor and healthy species, both oriented towards the biological environment to grab resources, the abnormal cells playing the role of a mutant cell line attacking and compromising the homeostasis of the healthy tissue development. In the framework of GT, with reference to interspecific competition, Volterra-Lotka (VL) models certainly represent accredited candidates to describe the above mentioned biological dynamics, for example by identifying tumor and healthy populations as introduced by [75] and more recently proposed by ([208]). However, when these strategies are applied to analyze growth in solid tumors, some key coupled effects relating mechanics and cell-cell dynamics governing mass evolution and invasion rates of cancer cells are inevitably lost.

In fact, in dealing with tumor growth, there is the need of inevitably interlacing the ordinary VL structure with non-constant terms accounting for the mutual –and "inter-scale"– influence of metabolic and mechanical factors, an example being the influence of macroscopic solid stresses on the alteration of the resulting duplication rate of the cell species.

In order to overcome the modeling obstacles above mentioned and to catch the effective bio-mechanical coupling in solid tumor growth, it here is proposed an enhanced multiscale poroelastic model with inelastic growth where the net growth terms result from the internal Volterra/Lotka-like competition between healthy and cancer cells occurring at the micro-scale level. In this way, a system of fully-coupled non-linear PDEs is derived to describe the complex machine in which the mutual influences of the competition among cell species due to available common resources, stress gradients, interstitial fluid flows, nutrient provision and inhomogeneous growth are all simultaneously taken into account, as schematically summarized with reserence to a solid tumor (the multi-cellular tumor spheroid (MCTS)) in Fig.42.

In the hereinafter discussed system, the mechanics of tumor growth is constructed by considering a multi-constituent solid tissue in which each species (cells, ECM and fluid) is represented by its volumetric fraction ϕ_γ, where the subscript γ will be adopted to indicate the set $\mathcal{S}$ of the solid species, i.e. the tumor (T), the healthy (H) and the apoptotic (A) cells volume fractions, the ECM and fluid volume fractions being denoted by the the subscripts (M) and (F), respectively. Hereinafter, the cascade of events related to the growth of these species will be described by means of a simpler linear poroelastic model coupled with inelastic growth and then by introducing a more detailed nonlinear poromechanical model based on the logarithmic Hencky strain together with a Fung-like hyperelastic constitutive law, to which the coupling with the interspecific evolution equations is associated through the construction of an appropriate species-derived growth strain tensor.

5.2   AN ENHANCED INTERSPECIFIC POROELASTIC MODEL OF TUMOR GROWTH

Cancer can be viewed as a disease involving irreversible genomic alterations affecting intrinsic cellular cycles. These genomic alterations act in combination with the

modification of the environmental conditions defined by immune response, matrix metabolism and stiffness, mechanical and biochemical gradients ([8]). The growth of solid tumors can be treated physically as a mechanical process according to which a heterogeneous tissue expands within a surrounding medium. Tumor expansion is controlled by some internal driving stresses, which are counterbalanced by mechanical resistance provided by the surrounding environment. Internal stresses are mostly generated by cells proliferation dynamics, which is influenced by the diffusion of nutrients within the tumor. This implies that the physical forces pushing the tumor ahead do not involve the sole surface tension and the pressure of the surrounding medium, but also the explicit active cellular forces deputy in the momentum balance that, in turn, retrospectively activate mechanosensitive cellular processes. With the aim to gain some new insights into the basic understanding of the complex machine of the host-tumor interaction in growing solid tumors, we present a heterogeneous poroelastic model of a tumor spheroid subjected to different prescribed boundary conditions, in which the mechanically activated stress fields, fluid pressure and nutrient walkway are coupled with spatially inhomogeneous and time-varying bulk growth. This growth is induced by competitive dynamics occurring at the microscopic scale level among healthy cells, cancer cells and ECM, macroscopically modeled by introducing ad hoc non-linear Lotka/Volterra-like equations. The basic idea is that cancer and healthy cell species do not compete directly, as it would happen in a pure predator-prey logic, but fight to contend the common resources occupying the shared environment. The common resources are here constituted by the available fluid content supposed to be saturated of nutrients, the environment being simply represented by the space that cells can inhabit at a certain time during growth and proliferation processes. The introduction of this transitive effect, that permeates through the system and enriches previously proposed poroelastic models ([173]), well mimics the actual competition among cell species by reproducing the experimentally observed coupled dynamics in which the presence of one species tends to somehow limit the development of the other, and here described as a behavioral phenomenon occurring in the cells community. This mutual inhibition in turn modifies the intrinsic growth rates of the cell populations and leads to spatially inhomogeneous elastic and residual stresses as well as non-uniform IFP distributions within the tumor spheroid. In the present treatment, however, in order to limpidly elucidate the key aspects of the dynamics at hand, further elements that would imply a direct competition between cancer and healthy cells depending on additional factors, such as the anti-oncogenic potentials of some immune cells or the aggressiveness of pre-malignant cells which become malignant as a result of mutation processes, will be neglected.

5.3 THE LINEAR MCTS MODEL

5.3.1 *Poroelasticity equations coupled with the model to tumor spheroids*

By recalling the constitutive equations of linear poroelasticity ([46]), the strain tensor $\mathbf{E}$, defined on a closed subset $\Omega \subset \mathbb{R}^3$ in presence of volumetric growth, can be written as follows

$$\mathbf{E} = \mathbf{S} : \boldsymbol{\sigma}^{eff} + \boldsymbol{\gamma}\, g,$$
$$\mathbf{E} = sym\left(\mathbf{u} \otimes \nabla\right), \tag{5.1}$$
$$\boldsymbol{\sigma}^{eff} = \boldsymbol{\sigma} + \mathbf{A}\, p.$$

where $\mathbf{u} \in C^2\left(\Omega\right)$ is the displacement vector, $\boldsymbol{\gamma}\, g$ is a growth strain tensor, with $g \in \mathbb{R}$ being a pure volumetric growth strain function and the matrix $\boldsymbol{\gamma} = diag\left\{\gamma_k\right\}$ containing the anisotropic multipliers for each principal direction so that $tr\left(\boldsymbol{\gamma}\right) = \sum_k \gamma_k = 1$ (already defined in Chapter 3), whereas $\mathbf{S}$ represents the *drained* compliance fourth rank elasticity tensor (the apex (d) will be avoided not to burden the notation) and $\boldsymbol{\sigma}^{eff}$ is the effective stress tensor. Its definition includes the Cauchy stress tensor $\boldsymbol{\sigma}$ and the interstitial fluid pressure p (IFP), $\mathbf{A}$ denoting the so-called *Biot effective stress coefficient symmetric tensor*, equal to $\mathbf{A} = \left(\mathbb{I} - \mathbb{C} \cdot \mathbf{S}^{(m)}\right) \cdot \mathbf{I}$, in which $\mathbb{C} = \mathbf{S}^{-1}$ is the drained stiffness tensor and $\mathbf{S}^{(m)}$ is the matrix-associated compliance fourth order tensor, while $\mathbb{I}$ and $\mathbf{I}$ respectively indicate the fourth-rank identity tensor and the second-rank identity vector (in Voigt notation). By deriving the stress tensor $\boldsymbol{\sigma}$ from equations (5.1) and in absence of body forces and neglecting inertia terms, the stress equations of motions in three dimensions read as

$$\boldsymbol{\sigma} = \mathbb{C} : \mathbf{E}_e - \left(\mathbb{I} - \mathbb{C} \cdot \mathbf{S}^{(m)}\right) \cdot \mathbf{I}\, p$$
$$\nabla \cdot \boldsymbol{\sigma} = \mathbf{0}, \qquad \boldsymbol{\sigma} = \boldsymbol{\sigma}^\mathsf{T} \tag{5.2}$$

in which $\mathbf{E}_e = \left(\mathbf{E} - \boldsymbol{\gamma}\, g\right)$ represents the elastic part of the deformation, by assuming an additive decomposition following the hypothesis of small deformations (see Chapter 1). By combining $(5.2)_2$ with compatibility equations $(5.1)_2$, together with the hypothesis of considering an elastic isotropic material (also implying that $\mathbf{A} = A\mathbf{I}$), the quasi-static balance of linear momentum can be expressed as:

$$\mu\nabla \cdot \left(\nabla \otimes \mathbf{u}\right)^\mathsf{T} + \left(\mu + \lambda\right)\nabla\left(\nabla \cdot \mathbf{u}\right) - 2\mu\left(\nabla \cdot \boldsymbol{\gamma}\, g + \boldsymbol{\gamma} \cdot \nabla g\right) - \lambda\nabla g - A\nabla p = \mathbf{0} \tag{5.3}$$

with $A = \left(1 - K/K^{(m)}\right)$, K and $K^{(m)}$ being the drained and matrix bulk moduli, while $\mu = E/2\left(1 + \nu\right)$ and $\lambda = E/\left(1 + \nu\right)\left(1 - 2\nu\right)$ are the Lamé moduli.

Also, the other basic field variable of poroelasticity is the dimensionless (under the hypothesis of constant density) variation in fluid content, named ζ, linearly related to the elastic strain and the pore pressure field through the relationship [46]:

$$\zeta = \phi_F - \phi_{F0} = \mathbf{A} : \mathbf{S} : \boldsymbol{\sigma} + C^{eff}\, p = \mathbf{A} : \left(\mathbf{E} - \boldsymbol{\gamma}\, g\right) + M^{-1}\, p,$$
$$C^{eff} = \mathbf{I} : \left(\mathbf{S} - \mathbf{S}^{(m)}\right) : \mathbf{I} - \varphi\left(1/K^{(F)} - \mathbf{I} : \mathbf{S}^{(m)} : \mathbf{I}\right), \tag{5.4}$$

This constitutive assumption let the fluid mass conservation equation–by assuming constant fluid density–be rewritten as:

$$\frac{\partial\zeta}{\partial t} + \nabla \cdot \mathbf{q}_F = \Gamma_F, \quad \Gamma_F = \kappa_v\left(p_v - p - \varpi\left(\pi_v - \pi_\iota\right)\right) - \kappa_l\left(p - p_l\right) \tag{5.5}$$

in the balance above $\mathbf{q}_F$ representing the vector flux that is supposed to obey Darcy's law, so that $\mathbf{q}_F = -1/\upsilon_F \mathbf{K} \nabla p$, with υ_F denoting the fluid viscosity and $\mathbf{K}$ the intrinsic permeability symmetric tensor, whereas Γ_F is a source/sink term (fluid mass supply per unit volume) introduced as a measure of fluid interchange from the leaky capillaries to the absorbing lymphatic vessels within the interstitial space at the microcirculation level, modeled according to the Starling's theory. In the definition of Γ_F, it is taken into account that the difference between the capillary and the interstitial pressures $(p_v - p)$ is the principal driving force regulating IFP as suggested by [25] affecting the movement of fluid within the microvascular beds, the latter being contrasted by the difference between the capillary and interstitial osmotic pressures $(\pi_v - \pi_\iota)$ weighted by a reflection coefficient ϖ, while the lymphatic drainage in the opposite direction is mainly driven by the drop related to the IFP and lymphatic vessels pressure p_l ([102, 213, 214]). Naturally, this terms are multiplied by two conductivity coefficients, named κ_v and κ_l respectively. The constitutive equation (5.4), where ϕ_F and ϕ_{F0} severally connote the current and the initial fluid volume fractions, introduces other characteristic poroelastic constants, in particular C^{eff} is the the effective compressibility factor in which the porosity φ and the fluid bulk modulus $K^{(F)}$ are also included (the fluid is supposed to be incompressible, so that $1/K^{(F)} \to 0$), and M^{-1} is the inverse of the Biot modulus, expressed as

$$M^{-1} = C^{eff}\left(1 - \mathbf{A} : \mathbf{B}\right),$$
$$\mathbf{B} = \frac{1}{C^{eff}}\, \mathsf{S} : \mathbf{A} = \frac{1}{C^{eff}}\left(\mathsf{S} - \mathsf{S}^{(m)}\right) : \mathbf{I} \tag{5.6}$$

In (5.6) further appears the Skempton compliance difference tensor $\mathbf{B}$, that reduces to $\mathbf{B} = (B/3)\,\mathbf{I}$ because of isotropy, with $B = \left(1/K - 1/K^{(m)}\right)/C^{eff}$, tending to unity for fluid-saturated materials, as well as for $K^{(m)}$ approaching to $K^{(F)}$, wheter or not the fluid and the matrix are assumed incompressible, in this case being the porosity φ actually uneffective. Introducing the undrained elastic constants as

$$\mathsf{S}^{(u)} = \mathsf{S} - \mathsf{S} : (\mathbf{A} \otimes \mathbf{B}) \tag{5.7}$$

and by also invoking isotropy, the scalar Biot effective stress coefficient A got in equation (5.3) can be expressed in terms of undrained and drained constants and the Skempton coefficient B

$$\mathsf{S}^{(u)} = \mathsf{S} - \frac{A\,B}{3}\mathsf{S} : (\mathbf{I} \otimes \mathbf{I}) = \mathsf{S} - \frac{A\,B}{3}\frac{1 - 2\nu}{E}\,(\mathbf{I} \otimes \mathbf{I})$$
$$A = \frac{3}{B}\frac{\left(\nu^{(u)} - \nu\right)}{(1 - 2\nu)\left(1 + \nu^{(u)}\right)} \tag{5.8}$$

Then, by focusing on a spherically symmetric case in a way to have the deformations $(5.1)_2$ be written as $\mathbf{E} = diag\left\{\partial u / \partial r,\, u/r,\, u/r\right\}$ and the multiplier $\gamma = diag\left\{\gamma_r,\, (1 - \gamma_r)/2,\, (1 - \gamma_r)/2\right\}$, the stress-strain-pore pressure constitutive equations $(5.2)_1$ take the form

$$\begin{cases} \sigma_r = \frac{E}{(1+\nu)(1-2\nu)} \left((1-\nu)\,\frac{\partial u}{\partial r} + 2\nu\frac{u}{r} - \left(\nu + (1-2\nu)\,\gamma_r\right) g \right) - \frac{3}{B}\frac{\left(\nu^{(u)}-\nu\right)}{(1-2\nu)\left(1+\nu^{(u)}\right)}\,p, \\[2mm] \sigma_\theta = \sigma_\phi = \frac{E}{(1+\nu)(1-2\nu)} \left(\frac{u}{r} + \nu\frac{\partial u}{\partial r} - \frac{1}{2}\left(1-(1-2\nu)\,\gamma_r\right) g \right) - \frac{3}{B}\frac{\left(\nu^{(u)}-\nu\right)}{(1-2\nu)\left(1+\nu^{(u)}\right)}\,p \end{cases}$$

<div align="right">(5.9)</div>

in agreement with works both by Rice ([161]) and Araujo ([13]), respectively with regard to the characterization of porous materials and the anisotropic expansion of linear elasticity through a fixed prescribed growth-strain distribution. Similarly, by starting from the definition of the isotropic Skempton coefficient B, an analogous reasoning let to simply obtain that $C^{eff} = A/KB = 9\left(\nu^{(u)} - \nu\right)/B^2 E\left(1+\nu^{(u)}\right)$, so that the constitutive relation for fluid content ζ in $(5.4)_1$ combined with the expression of the Biot modulus given by $(5.6)_1$ becomes

$$\zeta = \frac{3}{B}\frac{\left(\nu^{(u)}-\nu\right)}{(1-2\nu)\left(1+\nu^{(u)}\right)}\,(\epsilon - g) + \frac{9\left(\nu^{(u)}-\nu\right)}{B^2 E\left(1+\nu^{(u)}\right)}\left(1 - \frac{\left(\nu^{(u)}-\nu\right)}{(1-2\nu)\left(1+\nu^{(u)}\right)}\right)p \qquad (5.10)$$

with $\epsilon = tr\left(\mathbf{E}\right)$, the latter also showing the growth g effectively playing a role against the increase of fluid fraction, but it is actually the associated growth dynamics introduced in the following revealing this as the consequence of an effective consumption, modeled as a resource sharing/fight dilemma and actually interpreted as a predation by the cells. The ulterior advantage of having adopted this notation lies into the fact that equations (5.8) and (5.10) need only four elastic constants E, ν, $\nu^{(u)}$ and B, that can be easily accessible in Literature, also with reference to biological tissues (see for example [65]).

The poroelastic constitutive equations (5.9) and (5.10) involve the growth strain function $g = g\left(\mathbf{\Phi}\right)$, $\mathbf{\Phi}$ here being the vector collecting the volumetric fractions of the species involved in the dynamics –in this case represented by the healthy and tumor cells and the ECM, say ϕ_H, ϕ_T and ϕ_M– and g representing an inelastic growth term that is responsible of the current net generation of the species at each time t. As a consequence, the poroelastic field equations $(5.2)_2$ and (5.5) naturally result coupled with the species mass balances in the form

$$\begin{cases} \nabla \cdot \boldsymbol{\sigma} = \mathbf{0} \\[1mm] \frac{\partial \zeta}{\partial t} - \nabla \cdot \left(\frac{\mathbf{K}}{v_F}\nabla p\right) = \Gamma_F \\[1mm] \frac{\partial \mathbf{\Phi}}{\partial t} = \mathbf{\Gamma}_g \end{cases} \qquad (5.11)$$

where $\mathbf{\Gamma}_g$ represents the vector of the net species rates, actually explaining the way in which the species interact. For this purpose, by focusing on the competition between cancer and healthy cells interacting with the ECM to survivor in the common environment by challenging for the same resources, Volterra-Lotka (VL) equations –largely used in literature to model cell-cell and cell-immune system interactions ([75, 99]) due to the widely recognized contribution that evolutionary game theory as well as population ecology can give in understanding and predicting the behavior and the structure of a heterogeneous cells population ([208, 212]) also in complex environments, like the tissue-level microenvironments– have been here employed to describe

the dynamics among the species. The mutual inhibiting inter-species parameter is thus just related to the weight that each species exerts on the other one, modifying the growth rates through non zero dimensionless competition terms. Equations $(5.11)_3$ can be then explicitly given in the form

$$
\begin{cases}
\frac{\partial \phi_T}{\partial t} = \Gamma_T = \phi_F\, \gamma_T\, \phi_T \left(1 - \alpha_{TT}\phi_T - \alpha_{TH}\phi_H - \alpha_{TM}\phi_M\right) \\[3mm]
\frac{\partial \phi_H}{\partial t} = \Gamma_H = \phi_F\, \gamma_H\, \phi_H \left(1 - \alpha_{HT}\phi_T - \alpha_{HH}\phi_H - \alpha_{HM}\phi_M\right) \\[3mm]
\frac{\partial \phi_M}{\partial t} = \Gamma_M = \beta_T\phi_T + \beta_H\phi_H - \delta_M\phi_M \left(\alpha_{MT}\phi_T + \alpha_{MH}\phi_H\right)
\end{cases}
\tag{5.12}
$$

By observing equations $(5.12)_1$ and $(5.12)_2$ it can be noticed that they look like the classical diffusive VL-like ones, while the proliferation rate (i.e. the measure of converting available resources into replication capability) is here directly proportional to the variable fluid content $\phi_F = \phi_{F0} + \zeta$. In this sense the fluid is a feeding-like term which enters explicitly in the definition of the payoff functions of the cells populations rates unlike the classical competitive equations, in which species are supposed to have food indefinitely. The current food-provison term actually multiplies the inner growth rates γ_T and γ_H, penalized through the VL-coefficients α_{IJ}, with $\{I, J\} = \{T, H, M\}$, representing for $I = J$ a self-inhibiting term, whereas for $I \neq J$ they provide the effects of the mutual inter-species inhibitions. The third equation simply reproduces the balance of ECM in which biochemical differences between healthy and tumor ECM components are neglected and therefore the resulting overall ECM fraction, ϕ_M, dynamically depends on the synthesis and Matrix Degrading Enzymes (MDEs) processes promoted by cells, through the production characteristic rates β_T and β_H, and the loss rate δ_M, weighted by the coefficients α_{MT} and α_{MH}.

At this point, it is worth noting that classical poroelastic field equations $(5.11)_1$ shall be adopted provided that $\mathbf{u}$ as well as the stresses σ_{ij} produce infinitesimal changes in this quasi-stationary problem, and also that the volumetric growth term g keeps adequately small; however one should first ascertain what is a small deformation dealing with growing tumor, as suggested by [78], and this sounds valid especially in case growth is not an *a priori* assigned parameter but is instead the result of interior dynamics, that autonomously evolve once the external and initial conditions are given.

With reference to tumor spheroids made by a central nucleus and a surrounding hollow sphere with radii a and b, provided with a rigid internal inclusion with radius $r_i \to 0$ in order to avoid singularities, under the hypothesis of isotropic linear elasticity and under the further simplifying assumptions both of isotropic growth, which means $\gamma_r = 1/3$, and isotropic constant permeability, which gives $\mathbf{K}/v_F = k_F\mathbf{I}$, the equations (5.3) and (5.5) reduce to those of a spherically symmetric problem in which the poroelastic variables are those obtained (5.9) and (5.10), and a fully coupled system (5.11) is derived, involving an essential set of measurable parameters and five variables - say $\{u, p, \phi_T, \phi_H, \phi_M\}$-, being the sole radial non zero displacement component and all the unknown functions depending upon r and time t. In particular, one has:

$$\begin{cases} \frac{\partial}{\partial r}\left(\left(\frac{\partial u}{\partial r}+2\frac{u}{r}\right)-\left(\frac{1+\nu}{1-\nu}\right)\gamma_r g-\frac{A}{3K}\left(\frac{1+\nu}{1-\nu}\right)p\right)=0 \\[2em] \frac{\partial\zeta}{\partial t}=k_F\frac{1}{r^2}\frac{\partial}{\partial r}\left(r^2\frac{\partial p}{\partial r}\right)+\kappa_v\left(p_v-p-\varpi\left(\pi_v-\pi_\iota\right)\right)-\kappa_l\left(p-p_l\right) \\[2em] \frac{\partial\phi_T}{\partial t}=\phi_F\,\gamma_T\,\phi_T\left(1-\alpha_{TT}\phi_T-\alpha_{TH}\phi_H-\alpha_{TM}\phi_M\right) \\[2em] \frac{\partial\phi_H}{\partial t}=\phi_F\,\gamma_H\,\phi_H\left(1-\alpha_{HT}\phi_T-\alpha_{HH}\phi_H-\alpha_{HM}\phi_M\right) \\[2em] \frac{\partial\phi_M}{\partial t}=\beta_T\phi_T+\beta_H\phi_H-\delta_M\phi_M\left(\alpha_{MT}\phi_T+\alpha_{MH}\phi_H\right) \end{cases} \qquad (5.13)$$

where the net growth strain term (assuming that the constituents have the same density) can be defined in terms of the solid constituents as:

$$g=\phi_T+\phi_H+\phi_M-\phi_{T0}+\phi_{H0}+\phi_{M0} \qquad (5.14)$$

analogously to the variation of fluid content ζ, the additional subscript 0 indicating the volumetric fractions of tumor and healthy cells and matrix, respectively, at the conventional initial time $t=0$. To take into account the mechanically-coupled processes affecting growth, the coefficients appearing in the VL equations (5.12) are thought to be dependent on the mechanical stress in the way explained in the section below.

5.3.1.1 *Physical meaning and estimation of both poroelastic parameters and VL coefficients*

- *Poroelastic Parameters*:

Once the ordinary set of poroelastic constants adopted in writing the problem (5.13) have largely been discussed before, the source/sink term appearing in equation (5.13)$_2$ involve the use of two conductivity parameters. The first one, κ_v is proportional to both the hydraulic permeability of the blood vessel wall L_v and the vascular surface area per unit volume S_v/V, and it is here considered to be constant since no effects of vascularization have been taken into account at this point, so that the vascular surface can be supposed homogeneously distributed within the overall volume. However, there is a wide Literature ([102]) reporting the distinction of tumor and healthy vascular permeability. The other conductivity parameter κ_l is instead related to the effectiveness of the lymphatic drainage within the tissues. It is known that within a tumor there are no functional absorbing lymphatics due to the fact that ordinary lymphatic drainage mechanisms are altered and then the interstitial fluid pressure rises to values that are proportional to the vascular pressure. The draining lymphatics density tends in fact to decrease in the early stages mainly due to the action of MDEs over-produced by tumor cells ([214]) and also tumor cell induced-stress such as tumor overcrowding can cause lymphatic collapse since the lymphatic vessels pressures is generally low.

Moreover, cancer metastatic cells tend to invade lymphatic vessels and lymphnodes space (however metastasis is here not treated). The transition from neoplasic tissue to normal tissue typical values of $\kappa_l = L_l S_l / V$, L_l and S_l / V being respectively the lymphatic vessel permeability and the lymphatic surface area per unitvolume, is then modeled through a decreasing function by assuming κ_l linearly decreasing with the tumor fraction variation:

$$\kappa_l = \left(1 - \left(\phi_T - \phi_{T0}\right)\right)\kappa_{ln} \qquad (5.15)$$

with κ_{ln} being an assigned constant denoting the nominal value of drainage conductivity in normal tissues. Naturally κ_l multiplies the pressure drop $p - p_l$, with p_l constant. In the same way κ_v multiplies the Starling's gradient $p_v - p - \varpi\left(\pi_v - \pi_\iota\right)$. The term p_v represents the microvascular net pressure (MVP) inside the blood vessels (the effective pressure is considered due to the fact that vessels can locally be both afferent and efferent), that in normal conditions exceeds the pressure in IF space and promotes the movement of fluid toward the latter. The hydrostratic gradient $p_v - p$ is countered by the colloidal osmotic pressure gradient $\left(\pi_v - \pi_\iota\right)$ related to the plasma proteins, multiplied by a reflection coeffient ϖ that takes into account the selectivity of the vessels pores, here assumed constant.

- *Volterra-Lotka Parameters*

In standard VL models all the coefficients are assumed to be constant because the food chain is simulated by assuming that preys can access to indefinite reserves of food, reproducing and being preyed by predators at a constant rate. On the other hand, to realistically describe the competitive dynamics among cell species and ECM in tumor spheroids, two main phenomena cooperate to require varying coefficients in the VL equations (5.12). The first one is that in biological tissues nutrients are delivered by fluids which in poroelastic models obey the fluid balance equation (5.5) and whose content is generally neither spatially uniform nor constant in time and can be explicitly accounted through the term $\phi_F = \phi_{F0} + \zeta$. Additionally, some VL parameters also implicitly vary with space and time through the hydrostatic stress level perceived by cells, $\sigma^{hyd} = tr\left(\boldsymbol{\sigma}\right)/3$, which directly acts to modulate the intrinsic proliferation rates of the cell species. Accordingly, the rate of tumor cells and healthy cells in (5.12)$_1$ and (5.12)$_2$ are then influenced by the presence of the mutual competition term α_{HT} and α_{TH} that weight the way a species is influenced by the presence of the other one, while the explicit form of the characteristic growth parameters γ_T and γ_H can be constructed to take into account the effect of hydrostatic stress. This assumption derives from the fact that the local stress is known to induce latency in cell development known as diapause ([3, 158]), a reversible non-proliferating state during which the cell metabolism is very low and making this way the cells aggregates not to expand over a certain size so reaching a standstill of proliferation, whose reasons are not completely clear yet as well as the way of re-activation. This mechanism, of phenotypic origin and having crucial role in tissue homeostasis for regeneration and growth in normal conditions, is also evidently preserved by cancer cells, entering an inactive and clinically asymptomatic state thanks to which cancer cell are capable also to regulate or at least delay the achievement of the apoptotic state when critical conditions are achieved, in this way becoming a concrete possibility for the tumor itself to control its growth and to undergo dormancy as long as the environmental con-

ditions are again favorable to progression, as in the case of the angiogenic dormancy in which cancer cells are not inactive although they look clinically asymptomatic, until adequate vascularization restores their growth potential. This mechanism is also investigated with therapeutic purposes, in order to induce or maintain the dormancy and avoid metastasis ([158]). In particular, from a mechanical standpoint, it can be supposed an interesting connection with the experimental observation according to which high compressive stresses inhibit tumor growth ([83, 137]). Hence, given that the hydrostatic stress affects the intrinsic tumor cell growth rates γ_T and γ_H in a way such that if σ^{hyd} is less than a critical threshold value σ_{cr}^{hyd} , and assumed that cancer cells and healthy cells in the quiescent state are virtually indistinguishable as the former appear as asymptomatic as the latter, it is thought that the respective intrinsic growth rates reduce to a common low growth rate, say γ_q, while if the critical stress value is overcome, growth rate approaches abnormal values typical of cancer cells. The following transition function $S_K \left(\sigma^{hyd}\right)$ has been finally introduced:

$$\gamma_K = \gamma_{K0} S_K = \gamma_{K0} \left(\frac{\gamma_q}{\gamma_{K0}} + \frac{\left(1 - \frac{\gamma_q}{\gamma_{K0}}\right) \exp\left(\chi_\sigma \left(\sigma^{hyd} - \sigma_{cr}^{hyd}\right)\right)}{1 + \exp\left(\chi_\sigma \left(\sigma^{hyd} - \sigma_{cr}^{hyd}\right)\right)} \right), \qquad (5.16)$$

$$\gamma_{K0} = T_K^{-1} ln2$$

where $K = \{T, H\}$, χ_σ is a constant and the corresponding fixed coefficients γ_{T0} and γ_{H0} have been taken depending upon the doubling time T_T and T_H of tumor and healthy cell species, respectively, assumed in the range 17-40 hours ([67] and experimentally determined for two different cell lines (as argued in the following), whereas the quiescent metabolic rate γ_q is a reduced non zero metabolic coefficient resulting from the fact that quiescent cells arrest their division process but not their metabolic activity, because they maintain a basal metabolic rate in presence of nutrients ([54]) and can increase size until optimal environmental conditions occur. Thus, it is assumed that $\gamma_q = \varepsilon_q \gamma_{H0}$, with $\varepsilon_q \ll 1$ being an appropriate reduction coefficient.

The coefficients α_{TM} and α_{HM} are chosen to be constant and represent the weight the ECM exerts in terms of restriction of available space. The cross terms α_{HT} and α_{TH} are instead a measure of the mutual inhibition, while the coefficients α_{TT} and $\alpha_H H$ are self-competition coefficients accounting for the carrying capacity of each cellular species. These coefficients can be considered constant and not affected by the mechanical stress, this because tumor quiescent cells keep their aggressive mutagenic phenotype against normal cells, like their intimate nature was just hidden during quiescence. All these considerations let to describe a sufficiently complex population dynamics with respect to the classical one, being the game of interaction affected by the environmental parameters as well as there possibility of changing the strategy through the modulation of the the intrinsic rates in order to find the fittest way to survive. On the other hand, in this first formulation the variability is in the rate and there is no way of physically discriminating proliferating cells from quiescent cells, and also necrosis as well as angiogenesis have not been modeled, these aspect certainly introducing higher degree of complexity to the equations. Finally, it is worth to note that in the proposed model ECM balance $(5.12)_3$ is also written in a VL-like form, with a production rate that depends on the amount of cells synthesizing ECM components, say distinctly β_T and β_H for cancer and healthy cells, while the

degrading rate δ_M is weighted by the interaction coefficients α_{MT} and α_{MH} which account the way ECM is attacked by the cells lysis, leading to a three-species VL-like competition. The adopted parameters are summarized in Table 6.

5.3.2 *Results of the linear model*

Numerical simulations by means of the commercial package Wolfram Mathematica®([210]). With focus on the linear model, the respect of the hypothesis of small deformations introduced in section implies the analyses of solutions effectively remarking this assumption. As a consequence, since it is expected that the whole growth process would likely generate large deformations on the timescale of the tumor growth, the attention has been here payed on a reduced time window (in relation with the conducted experimental observations), in order to obtain solutions compatible with the linear model assumptions. The latter solutions could not provide the needed long-term information in relation with experimental findings: in this sense, the nonlinear model described in the following sections will be certainly more effective. However, it is worth noting that the linear model results of great engineering interest for the evolutionary problems at hand since it provides a strategy to construct the entire solution by superposing incremental sub-cases, which can be linearly modeled. In this paragraph, given the control volume dimensions via the assignment of the external radius b, a confined *in vivo* growth has been modeled by analyzing a displacement-prescribed case, i.e. $u(b,t) = 0$. In particular, species distributions, pressure and displacement have been prescribed at the starting time $t_i = 0^+$ by giving the following initial conditions:

$$
\begin{aligned}
\phi_M\left(r, t_i\right) = \phi_{M0}, \quad \phi_T\left(r, t_i\right) = \phi_{T0}\, D(r) \\
\phi_H\left(r, t_i\right) = \phi_{H0}(1 - D(r)), \quad p\left(r, t_i\right) = 0, \quad u\left(r, t_i\right) = 0
\end{aligned}
\tag{5.17}
$$

Herein $D(r) = \left(1 + \exp\left(\chi_r\left(r - a\right)/b\right)\right)^{-1}$ is a function adopted to characterize the transition from neoplasic core to the host environment, where χ_r is a proper smoothing coefficient, a is the initial tumor front and the relation $\phi_{T0} > \phi_{H0}$ subsists to take into account internal hyperplasia. In this situation, it was assumed $b = 3a$ as initial geometrical relation between external and internal initial radii of the tumor spheroid. In addition, no Darcy fluxes occur at $r = b$ and $r = r_i$, where also null displacement $u(r_i, t)$ has been provided. Moreover, no accumulated stress has been provided to the body, then a residual stress-free simulation is here considered for the sake of simplicity, and the simulation time has been set to 1 week. These two fact imply that some of the previously discussed phenomena, such as growth inhibition due to mechanical compression, could be not immediately observable as long as the nonlinear model will be treated and simulations could be carried performed over longer time. However, as said, the linear model can be used to construct more elaborated solutions, by iteratively treating linear solutions obtained up to a generic time t_k as a new starting state –including distributions, pressure and internal stress distributions– in order to construct solutions up to the next time $t_{k+1} = t_k + \Delta t$.

By then focusing on the species development, reported in Fig. 43, the tumor species fast accrues its amount in the tumor region, by increasing of approximately the 30%, and slightly starts to invade the surrounding host tissue. In this case, the tumor

amount growth results greater than its invasiveness potential, meaning that the tumor cells –for the assigned initial state– tend to "bulky" proliferate by penalizing the other healthy constituents and by saturating the available space and the nutrients rather than diffusing and increasing its extension. Additionally, the limited migration of the case under discussion can be also attributed to the absence of pre-existing resident compressive stress (here not provided). Experimental observations ([200]) that tumor migration is strongly enhanced by the level of mechanical compression, which induces border cancer cells to augment their motility. In the present case, an "unloaded" environment was imagined, and therefore stress within the spheroid can be considered still sustainable by the internal proliferating cells.
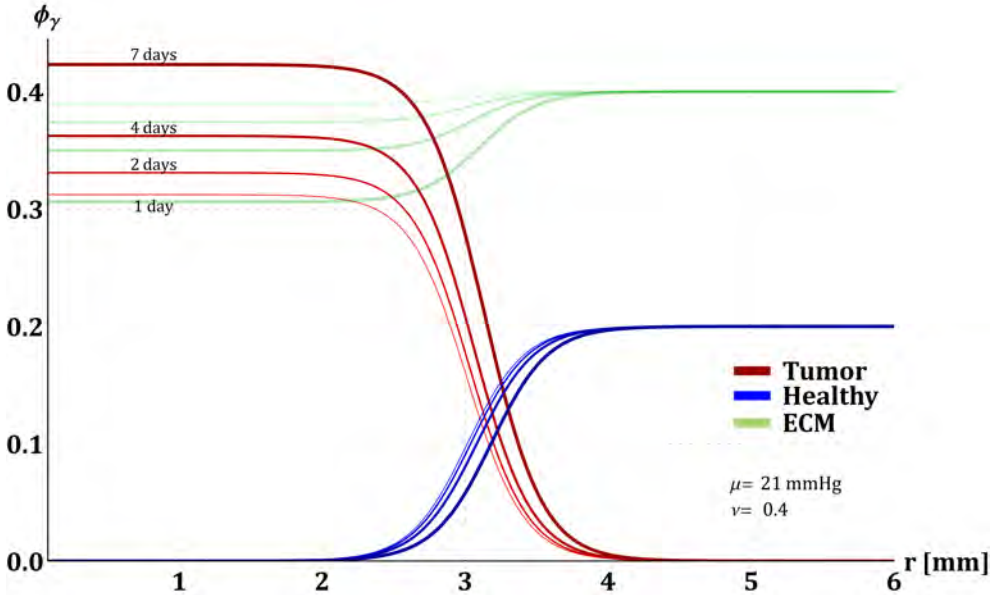
Figure 43: Tumor, healthy and ECM fractions within the control volume at the specified times.

The IFP was predicted to rise within the tumor interior, this generating an outward flux at the tumor-host interface (Fig. 44), and this implies that the tumor interior will be progressively deprived of nutrient exchange due to the IFP barrier, and thus abnormally high IFP significantly contributes to induce potential internal apoptosis and necrosis within tumor spheroids.

Also the IFP combines with the growth term and the elastic response directly derivable from the displacements and the elastic constants to express the effective stress field that build up into the volume. Solid stresses account the tumor accretion by generating internal compression –here approaching 800 kPa, as shown in Fig. 45–, decreasing towards the periphery. In particular, radial stress amplitude slightly decreases and reaches at $r = b$ a value representing the radial reaction exerted against the confinement made by the outer environment, while circumferential stress exhibits a more drastic transition from the intratumoral region to the host healthy tissue, here also exhibiting positive values, probably related to the tissue accommodation in
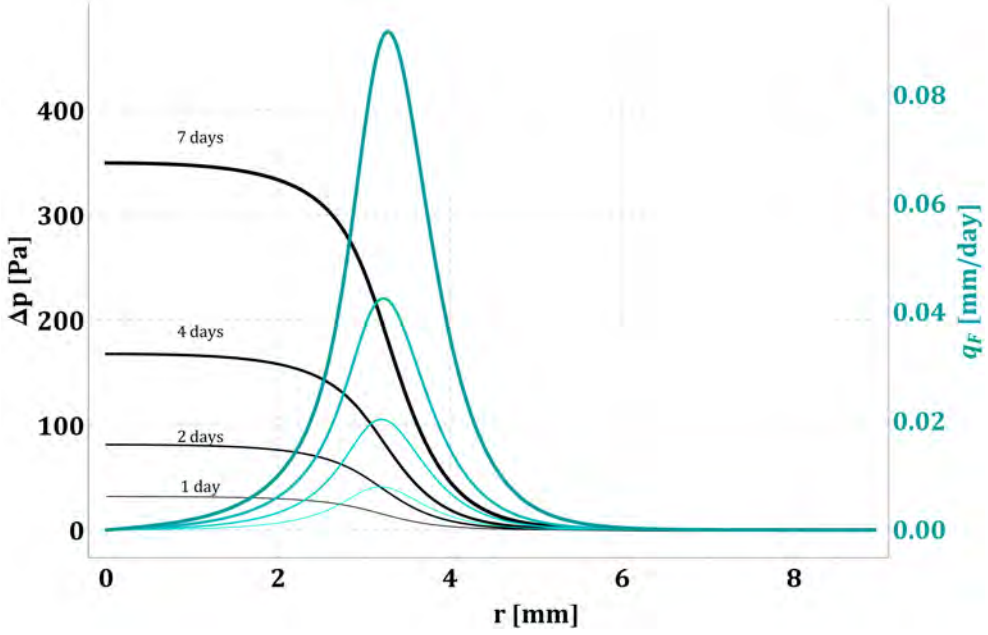
Figure 44: Evaluation of the pressure drop and radial flux at different times.

correspondence of the spheroid expansion, and, proceeding toward the exterior, hoop compression re-occurs as an effect of the peripheral confinement.

As said, the effects of stress accumulation and tumor invasion are long-term effects that can be depicted for enhanced growth process. Therefore, with a sole illustrative purpose to both anticipate the results of the nonlinear model and show at the same time the predictive potential of the full-coupled strategy, two further long-time simulations have been conducted. In particular, different external loading conditions could have different long-term effects on cells growth: therefore, two limiting conditions have been compared by considering a stress-free growth (i.e. $\sigma_{rr}(b) = 0$) and a fully confined growth. Results are summarized in Fig. 46. Here, tumor cells grown in the unconfined case result more invasive than those ones grown in the confined case (Fig. 46A and B). Stresses in the unconfined case achieve approximately 600 Pa within the tumor interior, while confinement induce almost hydrostatic compression increase up to about 2kPa (Fig. 46C, D,E and F).
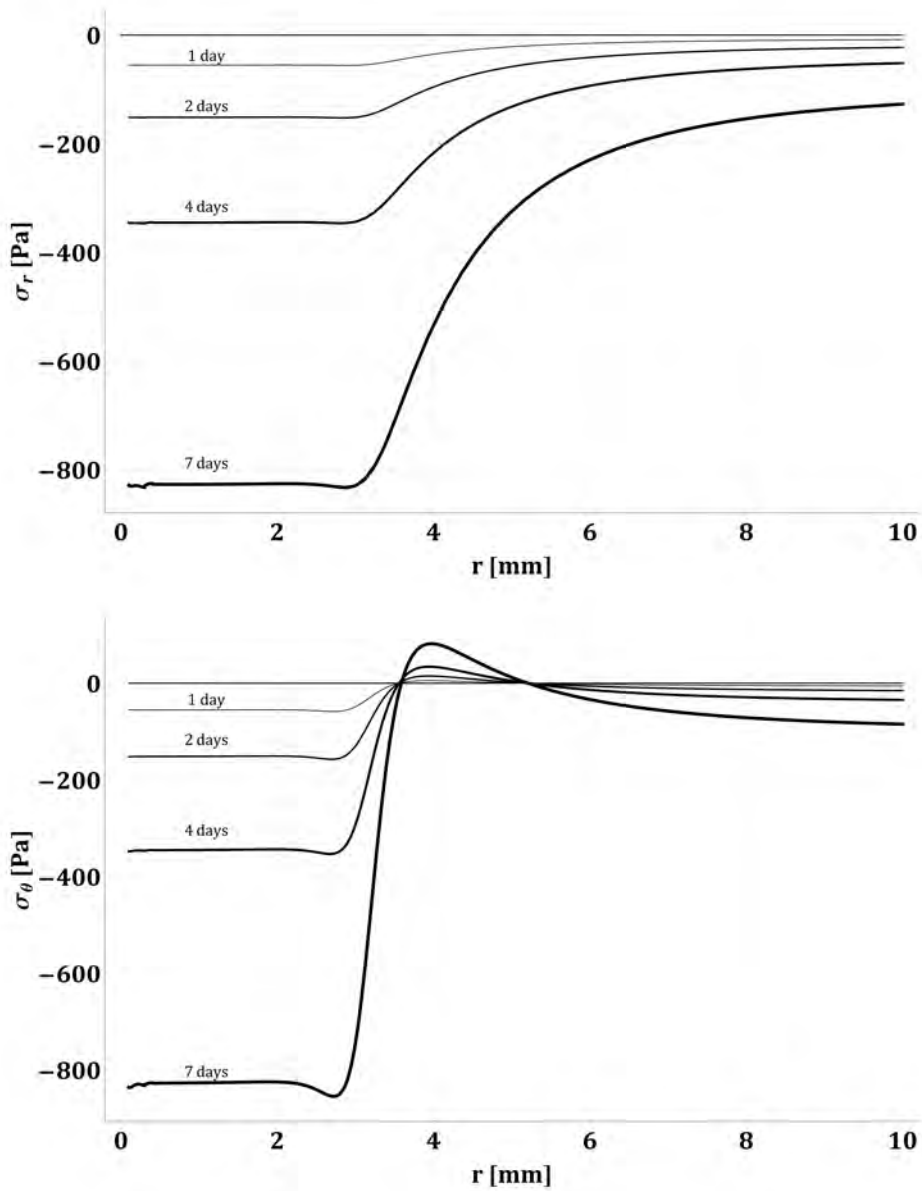
Figure 45: Solid stress obtained from the linear model. (top) Radial Stress. (bottom) Hoop stress.
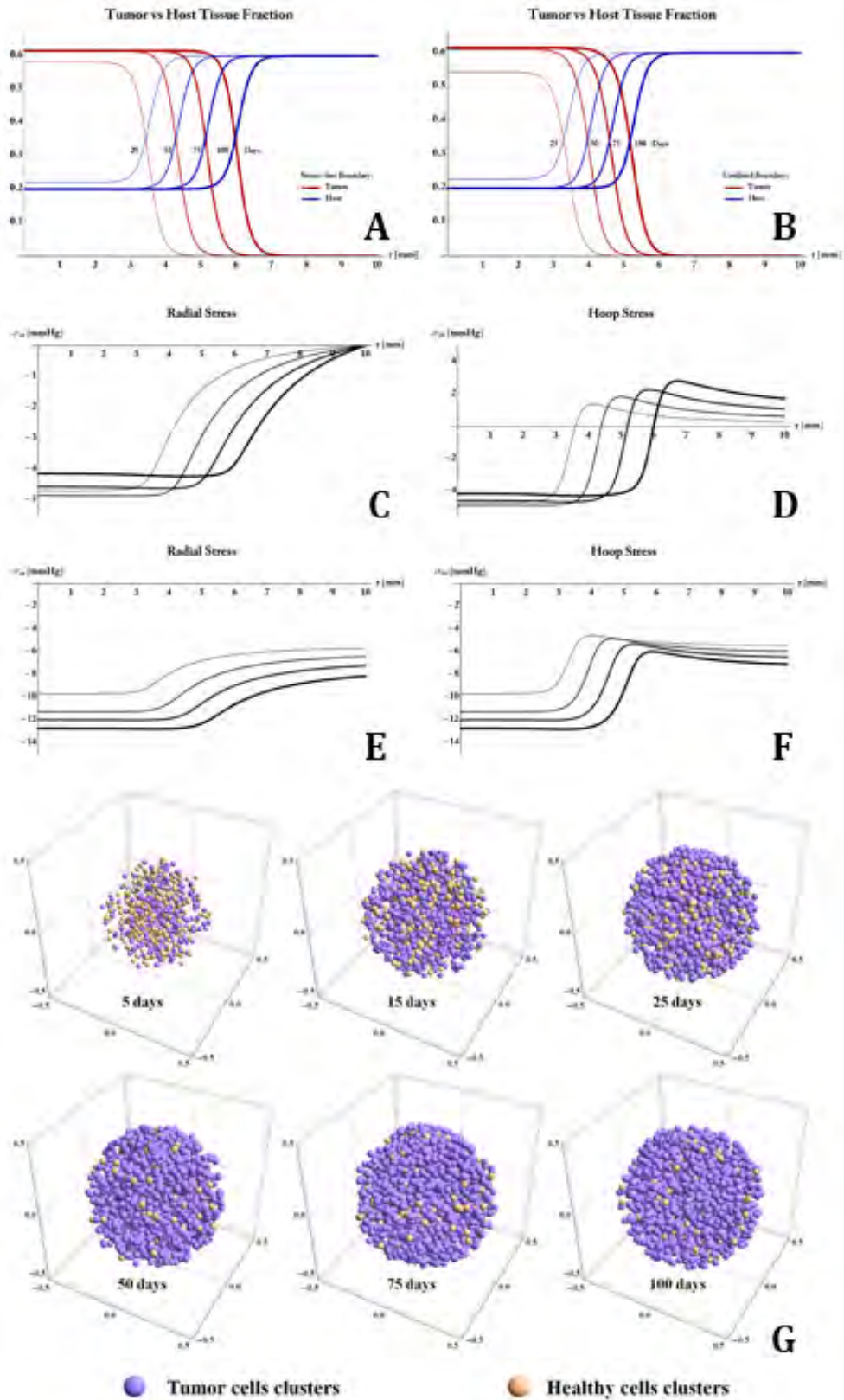
Figure 9. Distribution of tumour and healthy fraction in part of a... Graphs A...

5.4   THE NONLINEAR MCTS MODEL

5.4.1   *Preliminary remarks on the experimental model*

The limitations exhibited by the presented linear model can be overcome by using a nonlinear theory. Also, the integration of the theoretical description with experimental observations introduced hereinafter and derived from both *in vitro* experiments on cancer cells cultures and *in vivo*-implanted tumor spheroids, by means of an animal model, let to even further enhance the previous model. This is done, for example, by observing the growth variability in function of the available nutrients, in order to derive an explicit and more accurate dependence of the growth rate upon the extracellular resources availability and in order to better describe the apoptosis mechanism. For this reason, the nonlinear model has been also enriched by introducing other two constituents, i.e. the nutrient concentration and the apoptotic cells.

Moreover, the experimental observations accompanying the theoretical results developed in the subsequent nonlinear model have been opportunely designed in order to evaluate the dimensional growth and the related mechanical characteristics, in terms of the (direct and inverse) evaluation of the mechanical properties and residual stresses. Then, before presenting the mathematical details of the nonlinear fully coupled MCTS model, some details of the animal model and the experimental procedures are introduced. In particular, two different cell-lines have been adopted:

- Human pancreas cancer cell line MIAPaCa-2, was purchased from American Type Culture Collection (ATCC, Manassas, VA, USA) and grown in Dulbecco's Modified Eagle's medium (DMEM) supplemented with L-glutamine, antibiotics, and 10% heat-inactivated fetal bovine serum (FBS, Gibco/Invitrogen, Grand Island, NY, USA). The cells were maintained at $37°C$ in a humidified atmosphere of 5% CO_2. All experiments were performed with cultures grown for no longer than 6 weeks after recovery from frozen stocks.

- Human Triple Negative Breast cancer cell line MDA-MB.231, was purchased from American Type Culture Collection (ATCC, Manassas, VA, USA) and grown in RPMI1640 medium (DMEM) supplemented with L-glutamine, antibiotics, and 10% heat-inactivated fetal bovine serum (FBS, Gibco/Invitrogen, Grand Island, NY, USA). The cells were maintained at $37°C$ in a humidified atmosphere of 5% CO_2. All experiments were performed with cultures grown for no longer than 6 weeks after recovery from frozen stocks.

Twenty eight-week-old female Foxn$^{nu/nu}$ mice were purchased by Harlan (San Pietro al Natisone, Italy). Mice were housed 5 per cage and maintained on a 12-h light:12-h dark cycle (lights on at 7.00 a.m.) in a temperature-controlled room ($22\pm2°C$) and with food and water ad libitum. The experimental protocols were in compliance with the European Community Council directive (2010/63/EU). Animals were individually identified using numbered ear tags. All experiments were conducted in a biological laminar flow hood. The mice were anesthetized using isoflurane during the high-frequency ultrasound imaging. The anesthetic agent used is Zoletil 100 (Virbac): combination of 50% of Tiletamine and Zolazepam; it is used to 50 mg/kg by adding Atropine sulfate at 0.04 mg/kg, and xilazine 2%. After 2-week of acclimation to the housing conditions, a first group of mice (Mice n.1,...,11) were injected subcutaneously

(s.c.) with a suspension of MDA-MB.231 cells, 1.5×10^6 cells/mouse in the right hind limb in 150 μl of PBS solution. Mice tumor growth was measured biweekly with a digital caliper 2BIOL (Besozzo, Italy) and expressed in terms of surface, volume and measuring two reference diameters.

The experimental protocol provided to sacrifice animals when MDA-MB.231 tumors reached specific nominal sizes: 2 animals at volume of 300 mm^3, 2 animal at volume of 600 mm^3, 2 animals at volume of 900 mm^3 and 2 animals at volume of 1200 mm^3 or when presenting signs of pain. Another group of mice (Mice I,II,III) was instead injected subcutaneously (s.c.) with a suspension of MiaPaCa-2 cells, approximately 2×10^6 cells/mouse, with analogous procedures. Tumors growth was monitored every 5 days by means of caliber (C) and through echography (US). Animals were sacrificed after three weeks and after tumor implantation and organs were dissected and analyzed. All *in vivo* procedures were carried out in accordance with protocols approved by the *European Animal Care and Use Committee*. In the end, time of tumor dissection, each animal was subject to Ultrasound (US) and Magnetic Resonance (MR) imaging.

5.4.1.1 *Imaging and Data Processing*

High-frequency ultrasound imaging

Imaging and measuring of adrenal glands were performed by high-resolution ultrasound imaging system Vevo® 2100 (System Visualsonics, Toronto Canada). It is characterized by high-frequency, high-resolution digital imaging platform with linear array technology and Color Doppler Mode; and is used in preclinical research in a wide range of animal models and applications including cancer, cardiovascular and inflammation, etc. Mice, were anesthetized by isoflourane/O2 (4% for induction and 2, 5% for maintain sedation) and placed in prone position on a temperature-controller surgical table to maintain rectal temperature at 37°C, continual ECG monitoring was obtained via limb electrodes. Tumor dimensions was evaluated by B-Mode (2D) imaging for anatomical visualization, with 22-55 hMHz transducer (operating frequency of 40 MHz, axial resolution 40 μm), with enhanced temporal resolution with frame rates up to 740 fps (in 2D for a 4×4 mm^2 FOV), and enhanced image uniformity with multiple focal zones.

Magnetic resonance imaging

Animals were subjected to magnetic resonance imaging (MRI) at 1.5 T (Magnetom Symphony, Syngo MR 2002B, Siemens, Erlangen, Germany) and a dedicated phased array coil. Mice were placed in a supine, head first position. Axial, sagittal and coronal T2-weighted two-dimensional BLADE images of whole body were obtained. Sequence parameters are: TR/TE 4000/127 msec.; flip angle 150 degrees; slice thickness 2 mm; gap 0 mm; matrix 256x256; FOV 120×120 mm^2; pixel spacing 0.5×0.5 mm^2; acquisition time 4 min). Images assessment was performed in a single reading session for each animals by an expert radiologists. The radiologists, based on T2-weighted images, manually drawn regions of interests (ROI) along contours of tumor, covering the whole lesion with exclusion of peripheral fat, artefacts and blood vessels were drawn over the tumor. The segmentation was done on axial, coronal and sagittal plane and following the segmented volumes (SV) were calculated, for each plane, as
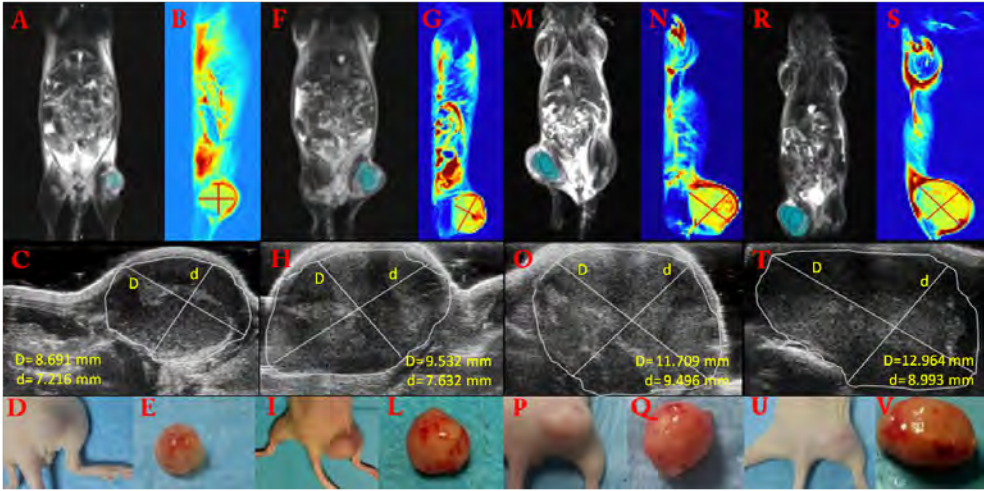
Figure 47: 2D visualization of tumours on mouse n.4, n.9, n.11 and n.1. Coronal and sagittal T2-weighted images, applying intensity colouring maps of mouse n.4 (**A**,**B**), mouse n.9 (**F**,**G**), mouse n.11 (**M**,**N**) and mouse n.1 (**R**,**S**). There were single slice segmentation superimposed on coronal T2 weighted images need to volume calculation. Volumes measured are $231.8mm^3$ (mouse n.4), $504.5mm^3$ (mouse n.9), $818.1mm^3$ (mouse n.11) and $935, 1mm^3$ (mouse n.1), respectively. Ultrasound images (**C**,**H**,**O**,**T**) and tumor specimen images (**D-E**, **I-L**,**P-Q**, **U-V**) were reported for the mouse n.4, n.9, n.11 and n.1, respectively

product between the number of voxels, pixel spacing and slice thickness. The results were reported in term of mean value of three volume measures.

5.4.2 *Imaging results*

Table 4 showed the results of tumor size measures from caliber *in vivo*, *ex vivo*, US and MR imaging. The days indicated in the table represented the days between the inoculation and sacrifice time. MR Imaging was resulted more accurate than US imaging considering the percentage difference of volume measure respect to caliber *ex vivo* volume measure. In fact for MR imaging was obtained a median $\pm$ standard deviation value of $1.9\% \pm 13.8\%$ while for US imaging was obtained a median $\pm$ standard deviation value of $8.7\% \pm 33.8\%$. Figure 47 showed a panel of digital image acquisitions for mouse n.4, n.9, n.11 and n.1. 2D view of MRI allowed a more accurate tumor size estimation and a more accurate interpretation of involvement with adjacent structures (as muscle infiltration) than US imaging. Similar considerations have been made to estimate the morphology of MiaPaCa-2 tumors. In particular, Fig. 48 shows the time development of tumor in Mouse II and the digital processing to accurately evaluate the sample volumes through 3D reconstructions.
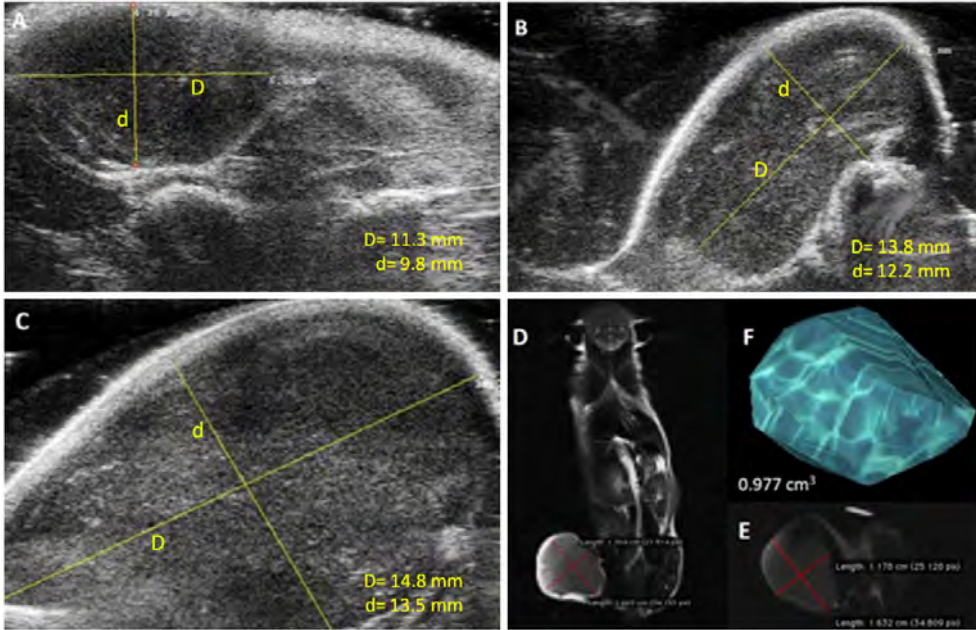
Figure 48: Digital image acquisitions with reference to Mouse II. **A**. Ultrasound image at Time I. **B**. Ultrasound image at Time II. **C**. Ultrasound image at Time III (the yellow lines indicate maximum and minimum diameter); Coronal and Transversal (**D-E**) T1-weighted images (T1-w) at Time III (red lines indicate maximum and minimum diameter); Volumetric image (**F**) obtained by MRI at Time III.

Table 4: Caliber measurements, US measurements ans MRI volumes reconstructions in MDA.MB-231 tumor at different sizes

ID	size	days	US				C vivo				C ex vivo				MR				
			D_{max}	d_{min}	A	V	D_{max}	d_{min}	A	V	D_{max}	d_{min}	A	V	D_{max}	d_{min}	A	V	SV
1	1200	14	14,0	10,5	147,0	771,8	14,1	13,6	165,3	1304,0	12,2	10,1	123,8	627,7	14,5	11,4	165,3	942,2	935,1
6	300	14	11,7	6,9	80,9	279,0	10,5	9,5	76,3	470,0	9,3	8,1	75,5	305,7	10,6	7,2	76,3	274,8	308,9
3	600	21	12,2	6,4	78,2	251,0	13,9	10,5	116,8	761,1	13,8	7,6	104,3	394,1	13,9	8,4	116,8	490,4	403,3
4	300	21	8,7	7,2	62,7	226,5	8,9	8,0	63,2	281,9	7,8	7,2	56,5	203,8	8,1	7,8	63,2	246,4	231,8
7	600	29	16,0	9,0	144,0	648,0	11,5	9,8	91,6	552,2	10,2	8,8	89,8	394,9	10,7	8,6	91,6	392,0	367,5
2	900	40	15,5	10,0	155,0	775,0	13,5	11,6	152,6	908,3	13,5	13,2	178,1	1171,6	15,0	10,2	152,6	778,2	986,3
11	900	40	15,5	10,0	155,0	775,0	13,8	11,8	137,9	960,8	15,2	10,3	156,4	805,2	13,1	10,5	137,9	726,3	818,1
9	600	50	9,5	7,6	72,2	274,4	11,5	10,4	107,9	624,5	10,2	9,6	97,6	467,1	11,6	9,3	107,9	501,6	504,5
10	1200	50	16,0	12,0	192,0	1152,0	16,2	13,2	185,3	1411,3	17,2	12,8	220,5	1411,5	14,2	13,1	185,3	1211,1	1271,3
5	1200	55	13,5	10,0	135,0	675,0	14,4	13,6	168,8	1320,2	13,8	12,3	169,7	1043,9	13,5	12,5	168,8	1054,7	1199,4

5.4.3 *The kinematics of tumor growth in finite deformation*

Let $\mathcal{B}^0$ be a body in its reference configuration and let V^0 be its volume. The growth and the deformation of the elastic body is entirely governed by the body motion $\mathbf{x} = \mathbf{x}\left(\mathbf{X}, t\right)$ that maps the material points $\mathbf{X} \in \mathcal{B}^0$ onto spatial points $\mathbf{x}$ at any time t, so that the overall deformation gradient $\mathbf{F}$ is additionally introduced by accomplishing compatibility with the body particles displacement field $\mathbf{u}\left(\mathbf{X}, t\right) \in C^2\left(\mathcal{B}^0\right)$, thus giving:

$$\mathbf{F} = \frac{\partial \mathbf{x}\left(\mathbf{X}, t\right)}{\partial \mathbf{X}} = \mathbf{I} + \mathbf{u}\left(\mathbf{X}, t\right) \otimes \nabla_{\mathbf{X}} \tag{5.18}$$

where $\otimes$ is the dyadic product and ∇ is the nabla vector, the subscript indicating the coordinates with respect to which the differentiation is performed. By exploiting the polar decomposition theorem, the existence of a proper orthogonal matrix $\mathbf{R} \in \mathbf{Orth}^3_+$ is ensured and introducing the diagonal right stretch tensor $\mathbf{U}$ one has:

$$\mathbf{U} = \lambda_i \left(\hat{\mathbf{N}}_i \otimes \hat{\mathbf{N}}_i^{\mathsf{T}}\right) \qquad \mathbf{F} = \mathbf{R}\mathbf{U} = \lambda_i \left(\hat{\mathbf{n}}_i \otimes \hat{\mathbf{N}}_i^{\mathsf{T}}\right) \tag{5.19}$$

where λ_i and $\hat{\mathbf{N}}_i$ are respectively the principal stretches and the eigenvectors of $\mathbf{U}$ (the summation symbol over $i = 1, 2, 3$ being subtended), while $\hat{\mathbf{n}}_i = \mathbf{R}\hat{\mathbf{N}}_i$ determines the rotation of the eigenbasis in the current configuration (the superscript T indicating the transpose of the tensor matrix representation). By adopting the multiple natural configuration approach introduced by [164] and in following more recent inherent works ([48]), the deformation gradient is assumed to be the result of a growth tensor and an elastic tensor that *de facto* combine in a multiplicative manner in order to give back (5.18), so that one can read:

$$\mathbf{F} = \mathbf{F}_e\,\mathbf{F}_g\,\mathbf{F}_s \tag{5.20}$$

Herein, a further *starving* deformation gradient $\mathbf{F}_s$ is formally introduced in order to take into account the fact that, in principle, one could not simply choose as reference configuration an initial *stress-free* configuration, but rather a state in which residual stress have been previously imprisoned in the body. However, for the sake of simplicity, in what follows it is assumed that $\mathbf{F}_s = \mathbf{I}$. As a consequence, the body is first supposed to undertake a growth process that drives the latter towards a grown intermediate configuration, say $\mathcal{B}^g$. In this configuration, the material particles occupy the position $\mathbf{x}^g\left(\mathbf{X}, t\right) \in \mathcal{B}^g$ and their motion can be described through an appropriate growth tensor $\mathbf{F}^g$. Assuming that the growth is isotropic, the polar decomposition of $\mathbf{F}_g$ leads to write:

$$\mathbf{U}_g = \lambda_g \left(\hat{\mathbf{N}}_i \otimes \hat{\mathbf{N}}_i^{\mathsf{T}}\right) \qquad \mathbf{F}_g = \mathbf{R}_g\mathbf{U}_g = \lambda_g \left(\hat{\mathbf{N}}_{gi} \otimes \hat{\mathbf{N}}_i^{\mathsf{T}}\right) = \lambda_g\,\mathbf{I} \tag{5.21}$$

with $\lambda_g = J_g^{\frac{1}{3}}$, $J_g = \det \mathbf{U}_g = dV_g/dV_0$ denoting the relative volume change with respect to the initial configuration, whereas $\hat{\mathbf{N}}_{gi} = \mathbf{R}_g\hat{\mathbf{N}}_i$ defines the rotation on each eigenvector $\hat{\mathbf{N}}_i$ in the configuration $\mathcal{B}^g$. During the growth process the body is also supposed to be unloaded, in this way the (inelastic) strain contribution being exclusively caused by the volumetric change induced by the growth itself. However,

the introduction of this intermediate configuration also implies the need of discerning separately the contribution of volumetric growth and the densification that can combine together to furnish the growth seen as overall local mass addition/removal. Coherently with the idea of a body system as a multiphasic continuum, this approach allows to translate the concept of growth –seen as flow of material particles entering (or leaving) the system– into an equivalent geometrical deformation of an infinitesimal volume element within the body, the mass flows being so interpreted as intrinsic growth rates of the living species. However, as well-known, the growth strain alone does not completely describe the body motion since the growth process is supposed stress-free and, in general, it could not ensure compatibility of the intermediate configuration since the infinitesimal volume elements grow independently from each other, as conceptually represented in Fig. 49. For this reason, the body must experience an elastic strain which permits to adapt the response to prescribed boundary conditions (i.e. the external mechanical loads and/or the given constraints) as well as to compatibilize the grown elements by kindling suitable self-equilibrated (residual) stresses within the body. Then, the elastic strain $\mathbf{F}_e$ maps the points $\mathbf{x}^g \in \mathcal{B}^g$ onto the actual configuration $\mathbf{x} \in \mathcal{B}$ and, through the already adopted decomposition, gives:

$$\mathbf{U}_e = \lambda_{ei} \left(\hat{\mathbf{N}}_{gi} \otimes \hat{\mathbf{N}}_{gi}^\mathsf{T} \right) \qquad \mathbf{F}_e = \mathbf{R}_e \mathbf{U}_e = \lambda_{ei} \left(\hat{\mathbf{n}}_i \otimes \hat{\mathbf{N}}_{gi}^\mathsf{T} \right) \qquad (5.22)$$

$\mathbf{U}_e$ then denoting the principal elastic stretch seen in the grown configuration. By combining the right stretch tensors introduced in (5.21) and (5.22), the baptized total stretch tensor $\mathbf{U}$ appearing in (5.18) can be determined by considering the right Cauchy-Green tensor:

$$\mathbf{C} = \mathbf{F}^\mathsf{T} \mathbf{F} = \mathbf{U}^2 = \mathbf{U}_g^\mathsf{T} \left(\mathbf{R}_g^\mathsf{T} \mathbf{U}_e^\mathsf{T} \mathbf{U}_e \mathbf{R}_g \right) \mathbf{U}_g = \mathbf{U}_g^\mathsf{T} \overset{\circ}{\mathbf{U}}_e^2 \mathbf{U}_g \qquad (5.23)$$

with $\overset{\circ}{\mathbf{U}}_e^2 = \mathbf{R}_g^\mathsf{T} \mathbf{U}_e^2 \mathbf{R}_g$ thus representing the back rotated version of $\mathbf{U}_e$ reported to the reference configuration. This also let to write:

$$\mathbf{U} = \sqrt{\mathbf{U}_g^\mathsf{T} \overset{\circ}{\mathbf{U}}_e^2 \mathbf{U}_g} \qquad (5.24)$$

Also, the orthogonal rotation matrix $\mathbf{R}$ can be expressed as $\mathbf{R} = \mathbf{R}_e \mathbf{R}_g$.
For the problem at hand, that is a MCTS under uniform boundary conditions, a spherically symmetric geometry is introduced, so that $\mathbf{X} = \{R, \Theta, \Phi\}$, the field variables depending exclusively on R. A spherical body is then considered by simply setting an external radius R_o delimiting the control volume and an inner radius $R_i \to 0$. Furthermore, spherical symmetry ensures that the deformation gradient $\mathbf{F}$ can be conveniently referred to its principal coordinates:

$$\mathbf{F} = \text{Diag}\{\lambda_r \quad \lambda_\theta \quad \lambda_\theta\} \qquad (5.25)$$

In addition, the forms of the deformation gradient (5.25) and of the growth tensor (5.21) imply that the elastic tensor $\mathbf{F}_e$ is also diagonal:

$$\mathbf{F}_e = \mathbf{F}\,\mathbf{F}_g^{-1} = \text{Diag} \left\{ \frac{\lambda_r}{\lambda_g} \quad \frac{\lambda_\theta}{\lambda_g} \quad \frac{\lambda_\theta}{\lambda_g} \right\} \qquad J_e = J J_g^{-1} \qquad (5.26)$$

$J = \det \mathbf{F}$ and $J_e = \det \mathbf{F}_e$ being the Jacobians of the transformations.
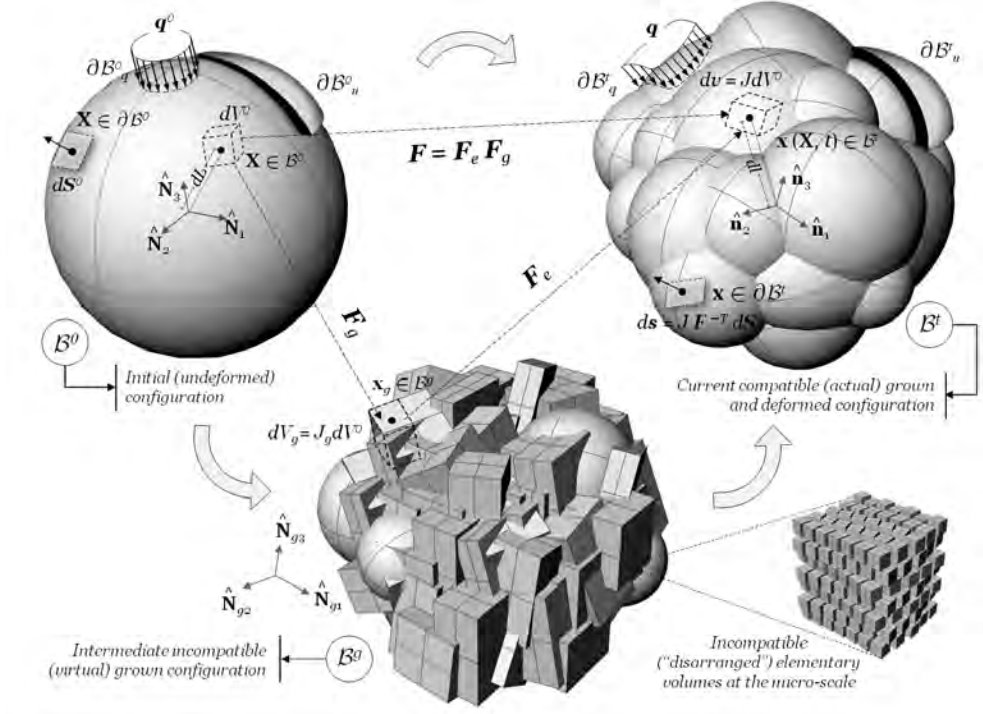
Figure 49: Illustration of the kinematics of growth in finite strain by adopting a multiplicative decomposition of the deformation gradient $\mathbf{F}$ into a growth part $\mathbf{F}_g$ mapping the body points onto an intermediate and generally incompatible configuration and an elastic part $\mathbf{F}_e$ which moves the body toward the current compatible (grown) configuration, which is also subjected to external load-induced deformations.

5.4.4 *Hencky strain measure and associated growth strain*

It is well-known that the finite deformation theory provides general strain measures, generated by the Seth-Hill formula ([84]), recalled from Chapter 1:

$$\mathbf{E}^{(m)} = \frac{1}{2m}\left(\left(\mathbf{F}^{\mathsf{T}}\mathbf{F}\right)^m - \mathbf{I}\right) = \frac{1}{2m}\left(\mathbf{C}^m - \mathbf{I}\right) = \frac{1}{2m}\left(\mathbf{U}^{2m} - \mathbf{I}\right) \tag{5.27}$$

where $\mathbf{C}$ the right Cauchy-Green tensor. In the present work, the Hencky's logarithmic strain measure is adopted, in such a way obtaining:

$$\mathbf{H} := \mathbf{E}^{(0)} = \lim_{m \to 0} \mathbf{E}^{(m)} = \frac{1}{2}\ln\left(\mathbf{F}^{\mathsf{T}}\mathbf{F}\right) = \frac{1}{2}\ln\mathbf{C} = \ln\mathbf{U} \tag{5.28}$$

The reason of this albeit legitimate choice is motivated by several advantages, first of all the possibility of extending the natural properties of the logarithm –i.e. the additive decomposition and the power law– to the logarithmic isotropic tensor function, in this way reducing the nonlinear multiplicative decomposition of the deformation gradient into the linear superposition of elastic and inelastic (growth-associated) strain contributions. In fact, by recalling eq. (5.24), one has:

$$\mathbf{H} = \ln \mathbf{U} = \ln \mathbf{U}_g + \ln \overset{\circ}{\mathbf{U}}_e = \mathbf{H}_g + \overset{\circ}{\mathbf{H}}_e \qquad (5.29)$$

where the back rotated tensor $\overset{\circ}{\mathbf{H}}_e$ is here adopted in order to account the coaxiality of the three Hencky strain tensors, the relationship $\overset{\circ}{\mathbf{H}}_e = \mathbf{R}_g^\mathsf{T} \mathbf{H}_e \mathbf{R}_g$ deriving from both the position introduced in eq. (5.23) and the properties of the logarithmic isotropic tensor function. In particular, if the spherical symmetry is assumed, one has that $\overset{\circ}{\mathbf{H}}_e$ and $\mathbf{H}_e$ coincide. Also, by introducing the spatial velocity gradient $\mathbf{L} = \partial \dot{\mathbf{x}} / \partial \mathbf{x} = \dot{\mathbf{F}} \mathbf{F}^{-1}$ and $\mathbf{D} = \text{sym}(\mathbf{L})$, which represent the incremental deformations, the diagonalized structure let to write

$$\dot{\mathbf{H}} = \sum_{i=1}^{3} \frac{\dot{\lambda}_i}{\lambda_i} \hat{\mathbf{N}}_i \otimes \hat{\mathbf{N}}_i^\mathsf{T} = \mathbf{R}^\mathsf{T} \mathbf{dR} = \mathbf{D} \qquad (5.30)$$

This also provides a simplified intuitive interpretation of $\mathbf{H}$ as the time summation of incremental deformations, a particularly suitable standpoint when dealing with evolutionary and incremental problems, in this way proposing a solution to the issue suggested by Graziano and Preziosi [78] through the adoption of a particular nonlinear deformation measure that simplifies the complexity of the problem related to the presence of multiplicative stretches because of its properties, being also effectively interpreted as an incremental deformation process at the limit. It is worth to highlight that the Eulerian description of the deformation process can be argued in a completely analogous manner. In fact, by introducing the left stretch tensor $\mathbf{V} = \mathbf{RUR}^\mathsf{T}$, the left Cauchy-Green tensor, under the decomposition (5.20), can be written as:

$$\mathbf{b} = \mathbf{FF}^\mathsf{T} = \mathbf{V}^2 = \mathbf{V}_e \mathbf{R}_e \mathbf{V}_g^2 \mathbf{R}_e^\mathsf{T} \mathbf{V}_e^\mathsf{T} = \mathbf{V}_e \check{\mathbf{V}}_g^2 \mathbf{V}_e^\mathsf{T}, \qquad (5.31)$$

$$\mathbf{V} = \sqrt{\mathbf{V}_e \check{\mathbf{V}}_g^2 \mathbf{V}_e^\mathsf{T}} = \lambda_i \hat{\mathbf{n}}_i \otimes \hat{\mathbf{n}}_i^\mathsf{T} \qquad (5.32)$$

$\check{\mathbf{V}}_g$ denoting a push-forward operation of the growth left stretch throughout the current basis. Then the eulerian Hencky strain is defined as

$$\mathbf{h} = \ln \mathbf{V} = \ln \mathbf{V}_e + \ln \check{\mathbf{V}}_g = \mathbf{h}_e + \check{\mathbf{h}}_g \qquad (5.33)$$

Obviously, it is immediate to verify that $\mathbf{H}$ and $\mathbf{h}$ are linked each other by the relationship:

$$\mathbf{H} = \mathbf{R}^\mathsf{T} \mathbf{hR} \qquad (5.34)$$

This also implies that, for a generic isotropic and scalar valued tensor function $\varphi(\cdot)$, one has $\varphi(\mathbf{H}) = \varphi(\mathbf{h})$. In addition, it is possible to bring back to the linear additive formulation $\mathbf{E} = \mathbf{E}_e + \mathbf{E}_g$ by simply considering a first order approximation of (5.29) for both growth and elastic small stretches.

5.4.5 *The hyperelastic potential for MCTS solid phase*

To derive suitable and thermodynamically consistent constitutive assumptions, let us first introduce a geometrically nonlinear strain energy density in the form (see, for example, [11, 27, 174, 215]):

$$\psi_{Hyp}\left(\mathbf{H}_e\right) = \frac{1}{2}\,\mathbf{H}_e : \mathbb{C}_0 : \mathbf{H}_e, \qquad \mathbb{C}_0 > 0 \tag{5.35}$$

so that the (back-rotated) work-conjugate Kirchhoff stress $\boldsymbol{\tau}$ results to be linearly dependent on $\mathbf{H}_e$, as also reported by [86] (in this context the elastic aliquot is considered by depriving the total strain $\mathbf{H}$ of the anelastic growth term $\mathbf{H}_g$):

$$\boldsymbol{\tau}_e = \mathbb{C}_0 : \mathbf{H}_e \tag{5.36}$$

where $\mathbb{C}_0 = 2G\,\mathbb{I} + \Lambda\,\mathbf{I} \odot \mathbf{I}$ represents the (positive definite) tangential stiffness tensor, with G and Λ being the Lamé moduli[2]. Additionally, it is here proposed to enrich the elastic strain energy density (5.35), commonly adopted in problems involving the logarithmic strain measure, in order to take into account the constitutive nonlinearities typically exhibited by biological tissues, that are normally captured by exponential laws. To do this, the well-known Fung exponential constitutive model ([69]) has been extended by replacing the elastic strain tensor $\mathbf{E}_e$ with the general Hill's expression given by (5.27) in order to obtain a bilinear-exponentiated Hencky potential:

$$\psi_{Hyp}\left(\mathbf{E}_e^{(m)}\right) = \frac{1}{2}\,\mathbf{E}_e^{(m)} : \mathbb{A} : \mathbf{E}_e^{(m)} + \frac{c}{2}\left(\exp\left(\mathbf{E}_e^{(m)} : \mathbb{B} : \mathbf{E}_e^{(m)}\right) - 1\right) \tag{5.37}$$

so that the case $m \to 0$ leads to the elastic strain energy density effectively adopted to model the solid part response:

$$\psi_{Hyp}\left(\mathbf{H}_e\right) = \frac{1}{2}\,\mathbf{H}_e : \mathbb{A} : \mathbf{H}_e + \frac{c}{2}\left(\exp\left(\mathbf{H}_e : \mathbb{B} : \mathbf{H}_e\right) - 1\right) \tag{5.38}$$

in which the fourth-order tensors $\mathbb{A}$, $\mathbb{B}$ and the scalar c are material parameters. The consistency conditions for (5.38) read:

$$\psi_{Hyp}\big|_{\mathbf{H}_e \to 0} = 0$$

$$\frac{\partial \psi_{Hyp}}{\partial \mathbf{H}_e}\bigg|_{\mathbf{H}_e \to 0} = \left(\mathbb{A} : \mathbf{H}_e + c\mathbb{B} : \mathbf{H}_e\, e^{(\mathbf{H}_e : \mathbb{B} : \mathbf{H}_e)}\right)|_{\mathbf{H}_e \to 0} = \mathbf{0} \tag{5.39}$$

$$\frac{\partial^2 \psi_{Hyp}}{\partial \mathbf{H}_e \partial \mathbf{H}_e^{\mathsf{T}}}\bigg|_{\mathbf{H}_e \to 0} = \left(\mathbb{A} + (\mathbb{B} + (\mathbf{H}_e : \mathbb{B}) \odot (\mathbb{B} : \mathbf{H}_e))\, c\, e^{(\mathbf{H}_e : \mathbb{B} : \mathbf{H}_e)}\right)|_{\mathbf{H}_e \to 0} =,$$

$$= \mathbb{A} + c\mathbb{B}$$

The $\odot$ operator denoting the standard tensor product between second order tensors. Then, eq. (5.39)$_3$ reproduces the tangential stiffness tensor $\mathbb{C}_0$ appearing in eq. (5.35)

---

2 More precisely, the relation between the Kirchhoff stress and the Hencky strain should account the presence of a structure tensor, as also in detail reported in Chapter 1. In this case, this fabric results in the identity because of the symmetric and diagonal structure of the deformation tensor $\mathbf{H}_e$.

in terms of the material parameters $\mathbb{A}$, $\mathbb{B}$ and c, so that one can assume –due to isotropy– that the latter tensor quantities present an analogous structure, i.e. $\mathbb{A} = a_1 \mathbb{I} + a_2 \mathbf{I} \odot \mathbf{I}$ and $\mathbb{B} = b_1 \mathbb{I} + b_2 \mathbf{I} \odot \mathbf{I}$, the energy (5.38) reducing to:

$$\psi_{Hyp}\left(\mathbf{H}_e\right) = \frac{1}{2}\, a_1 tr\left(\mathbf{H}_e^2\right) + a_2 tr\left(\mathbf{H}_e\right)^2 + \frac{c}{2}\left(e^{\left(b_1 tr\left(\mathbf{H}_e^2\right) + b_2 tr\left(\mathbf{H}_e\right)^2\right)} - 1\right) \qquad (5.40)$$

This also requires $\mathbb{A} + c\mathbb{B}$ be positive definite, and –for the particular form (5.40)– the respect of the conditions $a_1 + c\, b_1 > 0$ and $a_1 + 3a_2 + c\left(b_1 + 3b_2\right) > 0$ in any fitting procedure of experimental data for the determination of the material constants. In this manner, a nonlinear fitting procedure has been carried out in order to match the experimental data resulting from an uniaxial compression test performed on tumor samples in order to experimentally derive the tumor effective mechanical response. Results shown in Fig. , in which simple compression tests performed both on Mia-PaCa2 and MDA.MB231 tumor samples are reported, clearly show how the Hencky enriched law introduced is highly capable of fitting experimentally observed mechanical behavior. The effectiveness of the choice of the hyperelastic potential ψ_{Hyp} slected to represent the elastic/conservative part of the "actual" response of the overall biological (tumor mass) material is shown in Figure 50, where a very good agreement between the experimental points and the theoretical predictions can be seen.
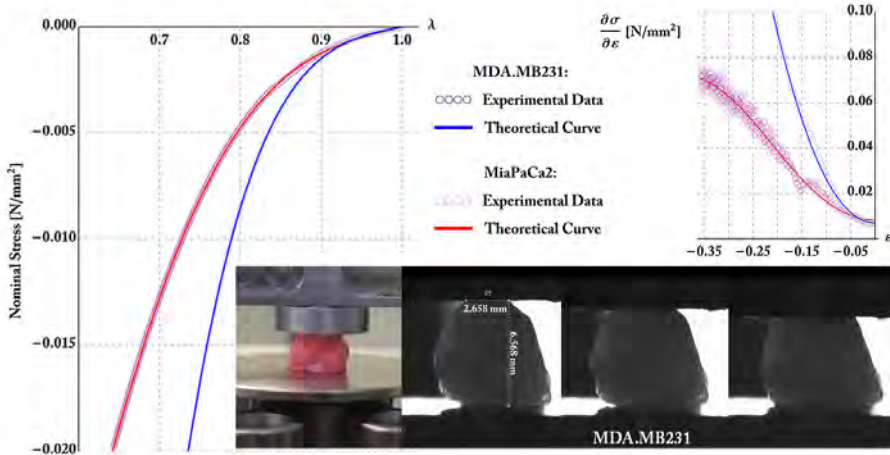
Figure 50: Uniaxial compression test of a tumor specimen. (A) Comparison between experimental data and fitting performed by making use of both a classical Hencky stress-strain curve and the proposed modified Fung-like Hencky law. (B) A picture showing the biological sample positioned in the load cell to perform the laboratory test. (C) Evaluation of the experimentally measured tangent stiffness (Young moduli varying with strain) fitted by means of the proposed Fung-like model.

Table 5: Material coefficients obtained from mechanical tests on MiaPaCa-2 and MDA.MB231 tumor samples.

Material Coeffcient→ Cell Line↓	a_1 [MPa]	a_2 [MPa]	c [MPa]	b_1 [-]	b_2 [-]
MiaPaCa-2	0.0226992	1.17955	0.00310748	-5.52926	1.65771
MDA-MB.231	0.0662486	3.22843	0.0153308	-4.04314	1.72176

5.4.6 *Effective stress and fluid-strain-pore pressure in poroelastic media undergoing large deformations*

In the classical poroelastic approach the saturated porous continuum is composed by a solid part, namely the skeleton, enriched with a fluid phase which flows within the interstitial spaces when the pore network is connected. The presence of the fluid phase thus introduces a further stress contribution, here indicated as interstitial fluid pressure p (IFP). In this framework, the displacement field $\mathbf{u}\left(\mathbf{X}, t\right)$ is referred to the skeleton, so that $\mathbf{F}$ in (5.18) represents its deformation gradient. As a consequence, the motion of the skeleton can be naturally thought as the result of the (intrinsic) elastic response of the solid material and the contribution of the fluid pressure. This let to write the Terzaghi effective stress given as the uncoupled sum of the elastic stress and the IFP, the validity of which is also provided in finite strain regime (see e.g. the work [29]). Therefore, one can write the purely elastic and isotropic Cauchy stress tensor as:

$$\boldsymbol{\sigma} = \boldsymbol{\sigma}^{eff} - \alpha\left(p - p_0\right)\mathbf{I} \tag{5.41}$$

with $\boldsymbol{\sigma}^{eff}$ denoting the effective stress connected with the material effective constitutive response, in this case provided by the conservative potential introduced by (5.40); in addition, $\alpha\mathbf{I}$ and p_0 respectively indicate the isotropic Biot effective stress tensor and the IFP reference pressure. In this way, after neglecting the body forces and inertia terms, the conservation of linear momentum in the reference configuration requires:

$$\nabla_{\mathbf{X}} \cdot \mathbf{P} = \mathbf{0} \tag{5.42}$$

the second order tensor $\mathbf{P}$ being the first Piola-Kirchhoff stress (e.g. the nominal stress), which is considered the work-conjugate tensor of the skeleton deformation gradient $\mathbf{F}$ and thus actually representing the Lagrangian form for the state of the skeleton. It can be shown (see the Appendix B for more details) that the stress tensor $\mathbf{P}$ is related both to the hyperelastic strain energy density describing the effective response of the body and to the IFP through a constitutive relation completely analogous to the Terzaghi decomposition (5.41) which reads as:

$$\mathbf{P} = J_g \mathbf{F}_e^{-\mathsf{T}} \frac{\partial \psi_{Hyp}}{\partial \mathbf{H}_e} \mathbf{F}_g^{-\mathsf{T}} - J\alpha\left(p - p_0\right)\mathbf{F}^{-\mathsf{T}} \tag{5.43}$$

where the expression $\boldsymbol{\tau}_e = \partial \psi_{Hyp} / \partial \mathbf{H}_e$ playing the role of the effective Kirchhoff stress for the porous material (with respect to the grown configuration), in analogy

with linear constitutive equation (5.36) that is commonly adopted when the Hencky strain measure is employed. This additive decoupling –deriving from the conservation of the Terzaghi's effective stress principle in finite strain regime– reasonably suggests the possibility of adopting a decoupled potential for the fluid and the solid part, giving in this manner a suitable expression for the poroelastic potential from which one can properly derive the stress constitutive equation, as well as the other poroelastic fluid-strain-IFP constitutive relation. Details are reported in Appendix A at the end of the Chapter.

In fact –with regard to the variation in fluid content for the fluid-saturated poroelastic body at hand– a fluid content-elastic strain-IFP constitutive equation can be explicitly derived, as also reported by [106]. In particular, the current fluid content at time t can be defined in terms of the kinematics of the mixtures, i.e. in terms of the fluid mass per unit volume of the reference configuration, that is here $\rho_F = J\varrho_F\phi_F$, with ϕ_F and ϱ_F being respectively volume fraction and its true density (fluid mass per unit fluid volume). The following differential state equation is then introduced:

$$d\rho_F = J\varrho_F\left(\alpha dh_e + C^{eff}dp\right) = J\varrho_F\left(\alpha\,dh_e + \left(\frac{1}{M} + \frac{\phi_F}{K_F}\right)dp\right) \qquad (5.44)$$

in which isothermal condition have been considered, $h_e = tr\left(\mathbf{H}_e\right) = \mathbf{H}_e : \mathbf{I}$, while C^{eff} is the effective compressibility factor containing both M and K_F, respectively the Biot and the fluid bulk moduli. Also, the hypothesis of fluid incompressibility (considering ϱ_F constant) leads the incremental fluid fraction variation be defined as:

$$d\left(J\phi_F\right) = J\left(\alpha\,dh_e + \frac{1}{M}dp\right) \qquad (5.45)$$

The above relationship can be further simplified by considering moderate variations of the fluid, in this way obtaining:

$$J\phi_F = \phi_F^0 + J\alpha\,h_e + JM^{-1}\left(p - p_0\right) \qquad (5.46)$$

in this way providing a relationship analogous to those of classical linear poroelasticity, as also discussed by [46], in which ϕ_F^0 is the initial fluid fraction.

The fluid balance equation already introduced in (5.11) is then rewritten, under large deformations, in the following way:

$$\frac{d\rho_F}{dt} + J\nabla_{\mathbf{x}}\cdot\mathbf{q}_F = J\Gamma_F, \quad \Gamma_F = \kappa_v\left(p_v - p - \varpi\left(\pi_v - \pi_\iota\right)\right) - \kappa_l\left(p - p_l\right) \qquad (5.47)$$

where $\mathbf{q}_F$ still denotes the fluid vector flux and Γ_F is the source/sink term (fluid mass supply per unit volume) introduced as a measure of fluid interchange from the leaky capillaries to the absorbing lymphatic vessels within the interstitial space at the microcirculation level, modeled as in (5.13). By taking into account the relationship (5.46), the conservation equation (5.47) becomes:

$$J\left(\alpha\frac{dh_e}{dt} + \frac{1}{M}\frac{dp}{dt}\right) + J\nabla_{\mathbf{x}}\cdot\mathbf{q}_F = J\Gamma_F$$
$$\left(\alpha\frac{dh_e}{dt} + \frac{1}{M}\frac{dp}{dt}\right) + J^{-1}\nabla_{\mathbf{X}}\cdot\mathbf{Q}_F = \Gamma_F \qquad (5.48)$$

where $\mathbf{Q}_F = J\mathbf{F}^{-1}\mathbf{q}_F$ is the material flux vector (i.e. per unit reference area). Furthermore, the vector flux $\mathbf{q}_F$ is supposed to obey Darcy's law, so that $\mathbf{q}_F = -v_F^{-1}\mathbf{k}\nabla_\mathbf{x}p$, with v_F denoting the fluid viscosity and $\mathbf{k}$ the intrinsic permeability symmetric tensor in the current frame of reference. Thus, by further including the transformations $\nabla_\mathbf{x}(\cdot) = \mathbf{F}^{-\mathsf{T}}\nabla_\mathbf{X}(\cdot)$ and $J\mathbf{k} = \mathbf{F}\,\mathbf{k}_0\,\mathbf{F}^\mathsf{T}$, the explicit Lagrangian expression of (5.48) is:

$$\left(\alpha\frac{dh_e}{dt} + \frac{1}{M}\frac{dp}{dt}\right) - (Jv_F)^{-1}\nabla_\mathbf{X}\cdot(\mathbf{k}_0\nabla_\mathbf{X}p) = \Gamma_F \tag{5.49}$$

in this way obtaining the second poroelastic field equation for the IFP, with the operator $d(\cdot)/dt$ representing material derivative. The pressure equation (5.49) still exhibits the source/sink term Γ_F, modeled according to the Starling's law, reported in equaton (5.47). Herein, κ_v is proportional to both the hydraulic permebility of the blood vessel wall L_v and the vascular surface area per unit volume S_v/V, and it is here considered to be constant since no effects of vascularization have been taken into account, so that the vascular surface can be supposed homogeneously distributed within the overall volume. However, there is a wide Literature ([102]) reporting the distinction of tumor and healthy vascular permeability. The other conductivity parameter κ_l is instead related to the effectiveness of the lymphatic drainage within the tissues. It is known that within a tumor there are no functional absorbing lymphatics due to the fact that ordinary lymphatic drainage mechanisms are altered and then the interstitial fluid pressure rises to values that are proportional to the vascular pressure. The draining lymphatics density tends in fact to decrease in the early stages mainly due to the action of MDEs over-produced by tumor cells ([214]) and also tumor cell induced-stress such as tumor overcrowding can cause lymphatic collapse since the lymphatic vessels pressures is generally low. Moreover, cancer metastatic cells tend to invade lymphatic vessels and lymphnodes space (however metastasis is here not treated). The transition from neoplasic tissue to normal tissue typical values of $\kappa_l = L_lS_l/V, L_l$ and S_l/V being severally the lymphatic vessel permeability and the lymphatic surface area per unit volume, is then thought to be affected by the presence of tumor cells, in this case represented by their fraction ϕ_T. Furthermore, it is assumed the lymphatic conductivity to be locally affected also by the apoptotic cell fractions, namely ϕ_A since the apoptotic material is removed by filtration through the lymphatic space itself. In particular, for the sake of simplicity, it is assumed that this parameter decreases linearly with tumor fraction, i.e.:

$$\kappa_l = \kappa_{l0}\left(1 - \left(\phi_T + \phi_A - \phi_T^0 - \phi_A^0\right)\right) \tag{5.50}$$

being ϕ_T^0 and ϕ_A^0 the initial tumor and apoptotic fractions, where κ_{l0} is the unperturbed lymphatic hydraulic conductivity. In this model, both lymphangiogenesis and angiogenesis as well as vascular collapse phenomena have not been taken into account, and thus κ_v has been considered constant. Moreover, the IFP is assumed to be initially at equilibrium, and this implies that the reference pressure p_0 results to be $p_0 = (\kappa_v(p_v - \varpi(\pi_v - \pi_\iota)) + \kappa_{l0}p_l)/(\kappa_v + \kappa_{l0})$,. The other ordinary poroelastic constants, in accord with the structure of relationship (5.10), have been evaluated by explotiting the well known expressions also proposed by Rice ([161]) and Cowin ([46]) and are reported below:

$$\alpha = \frac{3}{B}\frac{\left(\nu^{(u)}-\nu\right)}{(1-2\nu)\left(1+\nu^{(u)}\right)} \tag{5.51}$$

$$\frac{1}{M} = \frac{9\left(\nu^{(u)}-\nu\right)}{B^2 E\left(1+\nu^{(u)}\right)}\left(1-\frac{\left(\nu^{(u)}-\nu\right)}{(1-2\nu)\left(1+\nu^{(u)}\right)}\right) \tag{5.52}$$

where B is the material Skempton coefficient that tends to unity for saturated biological material, $\nu^{(u)}$ is the undrained Poisson ratio, whereas E and ν are the tangential Young modulus and Poisson's ratio.

5.4.7 *Nutrients*

The poroelastic problem here discussed applied to a biological continuum differs from the classical known also because the fact that the fluid phase is known to transport molecular solutes that represent the feeding or the enhancer of the cell population metabolism, so playing an essential to the growth mechanism their digestion actually provides the cells of the required energy. It is here imagined that this energy derives from a single nutrient species dissolved within the fluid because of simplicity. For this reason, if e_n is the specific energy provided by a single mole of nutrient species $n\left(\mathbf{x}\left(\mathbf{X},t\right),t\right)$, by assuming there is direct proportionality between the burning energy and the nutrients, i.e. $\mathcal{E} = e_n n$ with e_n assumed constant, the balance of energy is obviously linked to that of the nutrients according to:

$$\int_{V(t)} \mathcal{E}dV = \int_{V(t)} \left(\frac{d\mathcal{E}}{dt} + \mathcal{E}\nabla_{\mathbf{x}}\cdot\mathbf{v}\right)dV = E_0 + \Psi_0 - \int_{V(t)} \mathcal{E}_{cons}dV$$

$$\frac{d}{dt}\int_{V(t)} \mathcal{E}dV = \int_{V(t)} \left(\frac{d\mathcal{E}}{dt} + \mathcal{E}\nabla_{\mathbf{x}}\cdot\mathbf{v}\right)dV = -\frac{d}{dt}\int_{V(t)} \mathcal{E}_{cons}dV$$

$$\frac{d}{dt}\int_{V(t)} ndV = \int_{V(t)} \left(\frac{dn}{dt} + n\nabla_{\mathbf{x}}\cdot\mathbf{v}\right)dV = -\frac{d}{dt}\int_{V(t)}\int_{t_0}^{t} n\Gamma_{cons}d\tau dV \tag{5.53}$$

$$\frac{d\left(Jn\right)}{dt} = -Jn\Gamma_{cons}, \quad \Gamma_{cons} = \chi_\gamma\left(\phi_\gamma - \phi_\gamma{}^0\right), \qquad \forall V\left(t\right) \subseteq \mathcal{B}$$

In (5.53) a constant total energy E_0 and a constant boundary flux Ψ_0 have been introduced, whereas $\mathcal{E}_{cons}$ represents the aliquota of energy consumed, which is given by the time integral of a consumption term, here modeled as a first order reaction in terms of the nutrients n through a consumption rate Γ_{cons} depending on the tumor and healthy cells volumetric fractions (discussed in the subsequent section and denoted respectively by the subscripts $\gamma = T$ and $\gamma = H$), in a way to have $\Gamma_{cons}\left(t = 0^+\right) = 0$. In addition, the overall quantity of nutrient must account that the latter are dissolved in the fluid phase, so that it is hypothesized that the moles of nutrients n depend simultaneously both on a concentration function, say η, and the fluid fraction ϕ_F. By substituting $n = \eta\phi_F$ into the last of (5.53) one has:

$$\frac{d\left(Jn\right)}{dt} = -Jn\Gamma_{cons}$$

$$\frac{d\left(J\phi_F\eta\right)}{dt} = -J\phi_F\eta\Gamma_{cons} \qquad (5.54)$$

$$\left(J\phi_F\right)\frac{d\eta}{dt} + \eta\frac{d\left(J\phi_F\right)}{dt} = -J\phi_F\eta\Gamma_{cons}$$

in which the quantity $J\phi_F$ is then replaced with relationship (5.46).

The poroelastic equations above introduced, precisely given by equations (5.42) and (5.49), also enriched by the presence of the nutrients through equation (5.54), are naturally coupled with the evolution equations describing the behaviour of the solid matrix, modeled as a heterogeneous phase in which the main constituents are the tumor cells, the healthy cells and the extra-cellular matrix. Their interlaced activity, promoted/inhibited by both the environmental conditions in terms of available space and mechanical stress as well as by the presence/lack of available nutrients carried by the fluid phase, is responsible of the growth of the heterogeneous tissue. This both permits to define the growth strain intervening in the balance equations presented without prescribing any growth function, and moreover causes the rise of the residual stresses imprisoned within the tissue structure that have been recently experimentally observed for example by [192]. The next section is thus dedicated to the derivation of these evolutionary laws, by translating the cell-cell and the cells-ECM interaction occurring at a micro-scale level to the continuum macro-scale with the help of a multiphasic approach.

5.4.8 *Solid Species Equations*

The recent Literature provides formulations on the mechanics of solids with a growing mass establishing a constitutive connection between the evolution equations describing the mass exchange and the kinematic related strain, the most of these taking into exam a homogeneous body undergoing the growth process, see e.g. the review article by Kuhl ([118]), or the extensive analysis by Lubarda and Hoger ([127]), or even the outline involving multiple growing constituents suggested by Schmid et al. ([176]). Also, a mixture theory-based formulation of tissue interstitial growth to describe the change in mass of a solid heterogeneous body even in the light of a poroelastic approach has been recently illustrated by Cowin and Cardoso ([49]). Here, the problem focuses on the definition of the interspecific interactions among the species (introduced above) which can be recognized in the growth process of a multicell tumor spheroid.

Therefore, by considering the RVE of a body in a generic configuration k, with the aim of defining a suitable growth strain for the porous body with multiple biological constituents, the following useful quantities taken into account within the text sections are reported ([176]):

- the *total* density $\rho^{(k)}$:

$$\rho^{(k)} = \frac{dm^{(k)}}{dV^{(k)}} \qquad (5.55)$$

- the *partial* density for each constituent γ:

$$\rho_\gamma{}^{(k)} = \frac{dm_\gamma^{(k)}}{dV^{(k)}} \tag{5.56}$$

- the *true* density for each constituent γ:

$$\varrho_\gamma{}^{(k)} = \frac{dm_\gamma^{(k)}}{dV_\gamma^{(k)}} \tag{5.57}$$

- the constituent volume fraction $\phi_\gamma^{(k)}$ defined as:

$$\phi_\gamma^{(k)} = \frac{dV_\gamma^{(k)}}{dV^{(k)}} \tag{5.58}$$

By combining equations (5.56), (5.57) and (5.58) it immediately follows that:

$$\rho_\gamma^{(k)} = \frac{dm_\gamma^{(k)}}{dV^{(k)}} = \frac{dm_\gamma^{(k)}}{dV_\gamma^{(k)}} \frac{dV_\gamma^{(k)}}{dV^{(k)}} = \varrho_\gamma^{(k)} \phi_\gamma^{(k)} \tag{5.59}$$

whereas the total density can be expressed as:

$$\rho^{(k)} = \frac{dm^{(k)}}{dV^{(k)}} = \frac{1}{dV^{(k)}} \sum_\gamma dm_\gamma^{(k)} = \sum_\gamma \frac{dm_\gamma^{(k)}}{dV^{(k)}} = \sum_\gamma \rho_\gamma^{(k)} = \sum_\gamma \varrho_\gamma^{(k)} \phi_\gamma^{(k)} \tag{5.60}$$

By means of relation (5.59) the *change of density* expressing the densification (or conversely the the "rarefaction") between two different body states (h) and (k) can be easily computed for the single constituent

$$\frac{\rho_\gamma^{(k)}}{\rho_\gamma^{(h)}} = \frac{\varrho_\gamma^{(k)} \phi_\gamma^{(k)}}{\varrho_\gamma^{(h)} \phi_\gamma^{(h)}} \tag{5.61}$$

as well as referring to the total change of density if (5.60) is employed, i.e.

$$\frac{\rho^{(k)}}{\rho^{(h)}} = \frac{\sum_\gamma \varrho_\gamma^{(k)} \phi_\gamma^{(k)}}{\sum_\gamma \varrho_\gamma^{(h)} \phi_\gamma^{(h)}} \tag{5.62}$$

The hypothesis of constant true density implies that equation (5.62) can be rewritten for a body state k with respect to the initial configuration as:

$$\frac{\rho^{(k)}}{\rho^0} = \frac{\sum_\gamma \phi_\gamma^{(k)}}{\sum_\gamma \phi_\gamma^0} \tag{5.63}$$

with k denoting for the application in exam either the growth path which drives the body from the reference $\mathcal{B}^0$ configuration to the grown configuration $\mathcal{B}^g$ or the

adaptative (elastic) deformation path towards the current configuration at time t, namely $\mathcal{B}^t$. It is worth noting that (5.63) implies that the body grows without keeping a constant total density along the growth/resorption path and thus the total solid mass exchange will obviously results into the combined densification and volume effects:

$$\frac{dm^{(k)}}{dm^0} = \frac{\rho^{(k)}\, dV^{(k)}}{\rho^0\, dV^0} = \frac{\sum\limits_{\gamma} \phi_\gamma^{(k)}}{\sum\limits_{\gamma} \phi_\gamma^0} \frac{dV^{(k)}}{dV^0} = J_k \frac{\sum\limits_{\gamma} \phi_\gamma^{(k)}}{\sum\limits_{\gamma} \phi_\gamma^0} \tag{5.64}$$

where eq. (5.63) together with condition (5.71) have been used, while $J_k = dV^{(k)}/dV^0 = \det(\mathbf{F}_k)$ represents the volume change given by the Jacobian of the deformation gradient associated with the mapping toward the configuration k.

By focusing on the specific problem, the solid constituents involved in the growth process, described in the current configuration by their volumetric fractions ϕ_γ on a continuum scale, are namely: the tumor and the healthy cell species, namely T and H, the extra-cellular phase which is denoted with M, whereas the apoptotic cells fraction is indicated by A. As anticipated, the way of describing their rate is strictly guided by their phenotype –in the case of the cells– and by the way the cells interact with the environment, for the ECM. Here, these interactions are modeled through a modified Volterra-Lotka (VL) model, largely used in Literature to describe cell-cell interactions ([75, 99, 108, 124, 125, 212]), in which the inter-species coefficients are not constants as in the classical population models assuming constant feeding and free space, but instead vary as an effect of the changes of the environment in terms of mechanical sensing and nutrient supply. It is in fact reasonably assumed that cells do not compete each other as in a pure predator-prey logic, rather they compete for the same resources and for the shared space. In addition, the mutual inhibiting inter-species parameters are thus related to the weight that each species exerts on the other one, modifying the growth rates through non zero competition terms. The evolution equations for the solid mass constituents are obtained by imposing the conservation principle and also accounting that the solid masses are related to the volume elements through the equation $dm_\gamma = \varrho_\gamma\, \phi_\gamma\, dV$. Therefore, by considering the current volume fractions at time t one has:

$$dm_\gamma = dm_\gamma^0 + dm_\gamma^{gen}$$
$$\varrho_\gamma\, \phi_\gamma\, dV = \varrho_\gamma\, \phi_\gamma^0\, dV^0 + \int_{t_i}^{t} \varrho_\gamma\, \phi_\gamma\, \Gamma_\gamma\, dV\, d\tau \tag{5.65}$$
$$\frac{d}{dt}\left(J\phi_\gamma\right) = J\, \phi_\gamma\, \Gamma_\gamma$$

that represents the Lagrangian form of conservation of mass for the generic constituent γ, where a suitable intrinsic source and sink term Γ_γ has been introduced, which explicitly contains interaction inter-specific terms as well as other parameters that directly influence the growth dynamics. The rates Γ_γ in equation (5.65) are here reported:

$$
\begin{cases}
\Gamma_T = \gamma_T \left(1 - \alpha_{TT}\phi_T - \alpha_{TH}\phi_H - \alpha_{TM}\phi_M\right) - \delta_T \\
\Gamma_H = \gamma_H \left(1 - \alpha_{HT}\phi_T - \alpha_{HH}\phi_H - \alpha_{HM}\phi_M\right) - \delta_H \\
\Gamma_M = \left(\beta_T\phi_T + \beta_H\phi_H\right)\phi_M^{-1} - \delta_M \left(\alpha_{MT}\phi_T + \alpha_{MH}\phi_H\right) \\
\Gamma_A = \delta_T\phi_T + \delta_H\phi_H - \delta_A\phi_A
\end{cases}
\tag{5.66}
$$

where, to take into account the mechanically-activated processes occurring during growth, the coefficients γ_T, γ_H and α_{IJ} appearing in the VL rates (5.66) inserted into equations (5.65) are thought to be dependent both on the mechanical stress, analogously to the linear model. However, provided the considerations already discussed in the linear case, there is here the need to specify what stress measure has been adopted for expressing cells mechano-sensing. To do this, it is supposed that cells rates are affected by the spherical part of the Piola-Kirchhoff stress in the intermediate configuration $\mathcal{B}^g$ in agreement with [127], which is here obtained as $P_e^{sph} = tr\left(\mathbf{P}_e\right)/3$, with $\mathbf{P}_e = J_g^{-1}\mathbf{F}_e^{\mathsf{T}}\mathbf{P}\mathbf{F}_g^{\mathsf{T}}$. This environmental elastic stress directly acts to modulate the intrinsic proliferation rates of the cell species.

In addition, the coupling with the fluid ϕ_F that had been postulated in equation (5.12), has been here opportunely replaced by the more specific coupling with nutrient concentration delivered by the interstitial fluid. This implies that cells growth rate is assumed to be proportional to the nutrient concentration η in the way that the rate is maximum when nutrients are abundant and decreases in case of their depletion. In particular, a standard Michaelis-Menten type dependence has been chosen, identically for both the cells for the sake of simplicity. Furthermore, constant apoptosis is assumed for healthy cells, whereas tumor apoptosis peaks where nutrients are absent and decreases to a minimum value for plenty nutrient concentration, according to the fact that tumor cells are known to evade apoptosis.

Hence, given that the hydrostatic stress affects the intrinsic tumor cell growth rates γ_T and γ_H in a way such that if P_e^{sph} is less than a critical threshold value P_{cr}^{sph}, and assumed that cancer cells and healthy cells in the quiescent state look practically asymptomatic ([158]), it is thought that the respective intrinsic growth rates reduce to a common low growth rate, say γ_Q. Dually, if the critical stress value is overcome, growth rate approaches abnormal values typical of cancer cells. All these considerations lead to re-write the functional forms for the tumor and healthy cells intrinsic rates γ_T and γ_H appearing in equations (5.66)$_1$ and (5.66)$_2$:

$$
\gamma_K = \gamma_{K0} \left(\frac{\eta/\eta_0}{a_\eta + b_\eta\,\eta/\eta_0}\right) S_K(\Delta P)
\tag{5.67}
$$

with a_η and b_η being the coefficients of the Michaelis-Menten term related to the nutrients consumption and η_0 a baseline nutrient concentration. These coefficients have been determined by observing the variations of intrinsic growth rates of both the cells species on the basis of the nutrients availability. In fact, a slight dependence of the cells growth capability upon the nutrients abundance within the environment has been preliminarily studied. Specifically, by looking at Fig. 51, an increase of the replicating potential of both *in vitro* cultured MiaPaCa-2 cells and MDA.MB-231 cells occurred by augmenting the quantity of FBS (Fetal-Bovine-Serum) in the culture medium. For the sake of simplicity, this particular feature has been supposed to

likely transpire also *in vivo* on the basis of the nutrients accessibility.
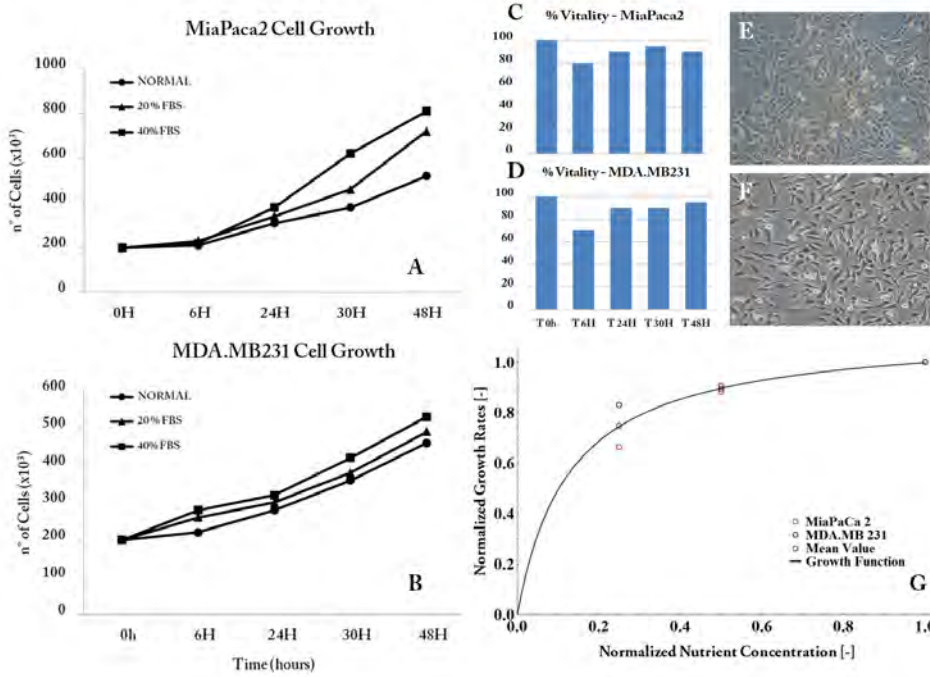
Figure 51: (**A**,**B**) Growth curves of cells species obtained *in vitro* by varying the percentage of Fetal Bovine Serum of the medium. (**C**,**D**) Cells vitality measurements in normal medium. (E,F) Image of the *in vitro* cell cultures. (**G**) Construction of a suitable growth curve describing the functional dependence of the growth rate upon the nutrient availability.

Furthermore, these curve let to obtain experimentally a mean estimation of the intrinsic growth rates of the cell lines. In fact, from the trends above illustrated, the MiaPaCa-2 and the MDA cells mean doubling times are respectively 24 hours and 35 hours. With reference to the stress-dependent factor in equation (5.67), the form of relationship appearing in equation (5.16) has been preserved, with the sole difference of substituting the Cauchy stress of the linear case with the nonlinear stress $\mathbf{P}_e$:

$$S_K(\Delta P) = \frac{\gamma_Q}{\gamma_{K0}} + \left(1 - \frac{\gamma_Q}{\gamma_{K0}}\right) \frac{\exp\left(\chi_P\left(P_e^{sph} - P_{cr}^{sph}\right)\right)}{1 + \exp\left(\chi_P\left(P_e^{sph} - P_{cr}^{sph}\right)\right)} \qquad (5.68)$$

where $\gamma_{K0} = T_K^{-1} \ln 2$ and $K = \{T, H\}$, γ_{K0} being the intrinsic growth coefficient depending upon the cells' doubling time that is specific for the cell line under exam. The quiescent metabolic rate γ_Q is a reduced metabolic coefficient resulting from the fact that quiescent cells arrest their division process but not their activity, because they maintain a basal metabolic rate in presence of nutrients ([54]) until optimal environmental conditions occur. Thus, it is assumed that $\gamma_Q = \varepsilon_Q \gamma_{K0}$, with ε_Q being

an appropriate reduction coefficient.

The coefficients α_{TM} and α_{HM} are chosen to be constant and represent the weight the ECM exerts in terms of restriction of available space. The cross terms α_{HT} and α_{TH} are instead a measure of the mutual inhibition, while the coefficients α_{TT} and α_{HH} are self-competition which wheight the influence that the cells can exert on their similar and account for the carrying capacity of each cellular species. These coefficients can be likely considered constant, in virtue of the fact that tumor quiescent cells are supposed to keep their aggressive mutagenic phenotype against normal cells, like their intimate nature was just hidden during quiescence. All these considerations let to describe a sufficiently complex population dynamics with respect to the classical one, being the game of interaction affected by the environmental parameters as well as there possibility of changing the strategy through the modulation of the the intrinsic rates in order to find the fittest way to survive. On the other hand, in this first formulation the variability is in the rate and there is no way of physically discriminating proliferating cells from quiescent cells, and also necrosis as well as angiogenesis have not been modeled, these aspect certainly introducing higher degree of complexity to the equations.

The third rate in (5.66) simply represents the net balance of ECM in which biochemical differences between healthy and tumor ECM components are neglected and therefore the resulting overall ECM fraction, ϕ_M, dynamically depends on the synthesis and Matrix Degrading Enzymes (MDEs) processes promoted by cells through the production coefficients β_T and β_H and the lysis coefficients α_{MT} and α_{MH}. In conclusion, following an analogous reasoning, the loss rates δ_K are assumed to be dependent on the nutrients deficiency, in particular their lack accentuating the aggregates rate of apoptosis:

$$\delta_K = \delta_{K0} \frac{c_\eta}{c_\eta + \eta/\eta_A} \tag{5.69}$$

c_η being a proper function parameter and η_A being a critical nutrient concentration above which apoptosis rate rises.

5.4.9 *Definition of the growth strain*

The solid body is supposed undergoing volumetric isotropic growth, leading to a diagonal mapping between the reference configuration and the grown configuration, so that the isotropic growth stretch for growth strain tensor (5.21) can be written as:

$$d\mathbf{x}^g = \mathbf{F}_g \, d\mathbf{X}, \qquad \mathbf{F}_g = \lambda_g \, \mathbf{I}, \qquad \lambda_g = J_g^{\frac{1}{3}} \tag{5.70}$$

In searching a suitable expression for the volumetric growth it is taken into account that the body under exam is here thought as a porous heterogeneous continuum made of a certain number of solid constituents with a perfusant filling the interstitial cavities, capable of flowing through the latter. The recent Literature provides several formulations on the mechanics of solids with a growing mass establishing a constitutive connection between the evolution equations describing the mass exchange and the kinematic related strain, the most of these taking into exam a homogeneous body undergoing the growth process, see e.g. the review article [118], or the extensive analysis by [127], or even the outline involving multiple growing constituents suggested by

[176]. Also, a mixture theory-based formulation of tissue interstitial growth to describe the change in mass of a solid heterogeneous body even in the light of a poroelastic approach has been recently illustrated in [49]. Here, the problem focuses on the definition of the interspecific interactions among the species (introduced above) which can be distinctly recognized in the growth process of a multicell tumor spheroid. Along the growth path of the deformation process the solid species accrue or reasorb enhanced by the nutrients contained within the fluid phase, the growth then determining the rise of an adaptive solid strain that, together with the action of a pore-pressure field, also drives the perfusion of the fluid, whose characterization is here accounted by means of the poroelasticity approach. Any increase/decrease of fluid volume due to inflow/outflow can in fact be considered a poroelastic effect, like a "sponge-like" swelling which follows the skeleton deformations. Moreover, by focusing on the specific application, for example, although the fluid is doubtless an enhancer of the growth of the cells populations inhabiting the solid, is not a self-reproducing, i.e. growing, constituent and also it is not directly consumed by cell themselves because cells feeds the nutrients dissolved within the fluid and its movement is exclusively an elastic effect. For these reasons, the growth process is assumed to be entirely the responsibility of the solid phase, and so it is assumed that the volume change can be completely determined by the solid growth under the assumption of a dense structure (e.g. by supposing the solid phase to be present at each material point). In a completely opposite way, the solid constituents mass achieved at the end of the growth process is assumed to preserve on the elastic adaptation path. In particular, the partial masses of the constituents in the grown configuration and in the current configuration are assumed to coincide. This hypothesis is stronger than assuming an unchanging overall mass, because the latter could potentially keep the same as a result of the partial masses changes which in some way balance each other. Thus, to sum up the speech, by indicating by $\mathcal{S}$ the set of solid constituents (i.e. the tumor and healthy cells and the ECM constituents) and with F the fluid one, the two following hypotheses are introduced:

- for $\gamma \in \mathcal{S}$, $dm_\gamma^0 \neq dm_\gamma^g$ and $dm_\gamma^g = dm_\gamma$

- for the fluid species, $dm_F^0 = dm_F^g$ and $dm_F^g \neq dm_F$.

In the framework of multiple configurations description, it is likely to introduce the following simplifying hypothesis: all the solid constituents are characterized by the same *constant true densities* (e.g. the constituent unit mass per unit volume of the constituent itself), that is

$$\varrho_\gamma^{(k)} = \varrho, \qquad \forall \gamma \text{ and for each configuration } (k). \tag{5.71}$$

This hypothesis is supposed reasonable both because the biological constituents have very similar true densities each other and the latter does not significantly change either after a growth process or in response to a mechanical insult, so giving back the fact that the change of density depends exclusively on the volumetric rearrangement (i.e. on the fractions) of the constituents after volumetric growth or after a mechanically-induced volumetric change. By using formula (5.57), under the hypothesis of constant true density for the solid constituents , one has that $dm_\gamma^{(k)} = \varrho \, dV_\gamma^{(k)}$ for each configuration (k) of the deformation process. In this way, by also account-

ing fluid incompressibility in what follows, the partial mass gain for each constituent results to coincide with the normalized volume change:

$$\xi_\gamma^{(k)} = \frac{dm_\gamma^{(k)}}{dm_\gamma^0} = \frac{\varrho\, dV_\gamma^{(k)}}{\varrho\, dV_\gamma^0} = \frac{dV_\gamma^{(k)}}{dV_\gamma^0}, \qquad \xi_\gamma^0 = 1\,\forall\gamma \tag{5.72}$$

The total volume change due to growth is then obtained as

$$J_g = \frac{dV^g}{dV^0} = \sum_\gamma \frac{dV_\gamma^g}{dV^0} = \sum_\gamma \frac{dV_\gamma^g}{dV_\gamma^0}\frac{dV_\gamma^0}{dV^0} = \sum_\gamma \xi_\gamma^g\,\phi_\gamma^0 = \sum_\gamma \frac{dm_\gamma^g}{dm_\gamma^0}\,\phi_\gamma^0 \tag{5.73}$$

herein the hypotheses made about the partial masses lead to:

$$J_g = \sum_\gamma \frac{dm_\gamma^g}{dm_\gamma^0}\,\phi_\gamma^0 = \sum_{\gamma\in\mathcal{S}} \frac{dm_\gamma}{dm_\gamma^0}\,\phi_\gamma^0 + \phi_F^0 \tag{5.74}$$

and also ascertaining that, by mean of equations (??) and (??) and taking constant true density

$$\frac{dm_\gamma}{dm_\gamma^0} = \frac{\rho_\gamma\, dV}{\rho_\gamma^0\, dV^0} = \frac{\varrho\,\phi_\gamma\, dV}{\varrho\,\phi_\gamma^0\, dV^0} = J\,\frac{\phi_\gamma}{\phi_\gamma^0} \tag{5.75}$$

After that it follows that:

$$J_g = J\sum_{\gamma\in\mathcal{S}}\phi_\gamma + \phi_F^0 \tag{5.76}$$

By exploiting the fluid saturation condition (also used to define poroelastic relationships) one gets

$$J_g = 1 + \sum_{\gamma\in\mathcal{S}}\left(J\phi_\gamma - \phi_\gamma^0\right)$$

$$\lambda_g = \left(1 + \sum_{\gamma\in\mathcal{S}}\left(J\phi_\gamma - \phi_\gamma^0\right)\right)^{\frac{1}{3}} \tag{5.77}$$

The above result can be expressed in its rate form by considering the mass conservation principle (5.65), in this way obtaining a comprehensive balance equation for pure volumetric growth:

$$\frac{dJ_g}{dt} = \sum_{\gamma\in\mathcal{S}}\frac{1}{\rho_\gamma^0}\frac{d}{dt}\left(J\rho_\gamma\phi_\gamma\right) = \sum_{\gamma\in\mathcal{S}}\frac{d}{dt}\left(J\phi_\gamma\right) = J\sum_{\gamma\in\mathcal{S}}\phi_\gamma\,\Gamma_\gamma = J_g r_g \tag{5.78}$$

in which $r_g = J_e \sum_{\gamma\in\mathcal{S}}\phi_\gamma\,\Gamma_\gamma$ is a net volumetric generative term in the current configuration and referred to the grown configuration by means of the jacobian J_e.

- *Remark*:

The derived growth induced strain (5.77) let to write the deformation term by means of the Hencky strain measure, say:

$$h_g = \frac{1}{3} \ln(J_g) = \frac{1}{3} \ln \left(1 + J \sum_{\gamma \in \mathcal{S}} \phi_\gamma - \sum_{\gamma \in \mathcal{S}} \phi_\gamma^0 \right) \tag{5.79}$$

In case of small strain[3], this expression reduces to:

$$\epsilon_g = \frac{1}{3} \sum_{\gamma \in \mathcal{S}} \left(\phi_\gamma - \phi_\gamma^0 \right) = \gamma_r \, g \tag{5.80}$$

that is the relationship that had been used in the linear model (see equation (5.14)).

5.4.9.1 *Stresses and Growth in the nonlinear MCTS*

The hypothesis of a spherically symmetric problem is here maintained by writing all the variables of the problem as a function of the sole radial material coordinate R in a space-time frame $\{R, t\} \in \mathbb{R}^+ \times \mathbb{R}^+$. More specifically, the variables involved reduce to: the radial displacement u, the interstitial fluid pressure p, the nutrient concentration η and the solid constituents volume fractions ϕ_γ denoting the tumor cells, the healthy cells, the apoptotic cells and the ECM fractions. Then the MCTS can be modeled as a multiphasic spheroid –immersed in a host multiphasic crown– in which the interaction between the biological constituents (at the microscale) can be described at the continuum scale by means of their volumetric fractions, the solid ones constituting the porous tissue network, as sketched in Fig. 52. In particular, R ranges from an internal inclusion with radius $R_i \to 0^+$ to an external radius R_e (where mechanical tractions and boundary condition are imposed), while the time t starts at a conventional starting time $t_i = 0^+$, by setting a three weeks simulation for both the theoretical case and the MiaPaCa cells, compatibly with the duration of the experiments regarding this cell-line, while, because of the different experimental protocol adopted for the MDA.MB-231 cell-line, numerical solutions were calculated up to 50 days. The simulations, numerically performed by means of the NDSolve package furnished by the computational software *Mathematica*®([210]), consider the growth of a tumor nucleus with a given initial radius equal to a infiltration at the time t_i and surrounded by the external host crown with R_e.

---

3 This case highlights how the hypothesis of small strain, in order to make the current configuration coincide with the initial one, has to be separately valid for both the total strain and the growth strain. In other words, it is not possible to provide a large growth strain and combine it with a suitable elastic strain in order to obtain small total deformations.
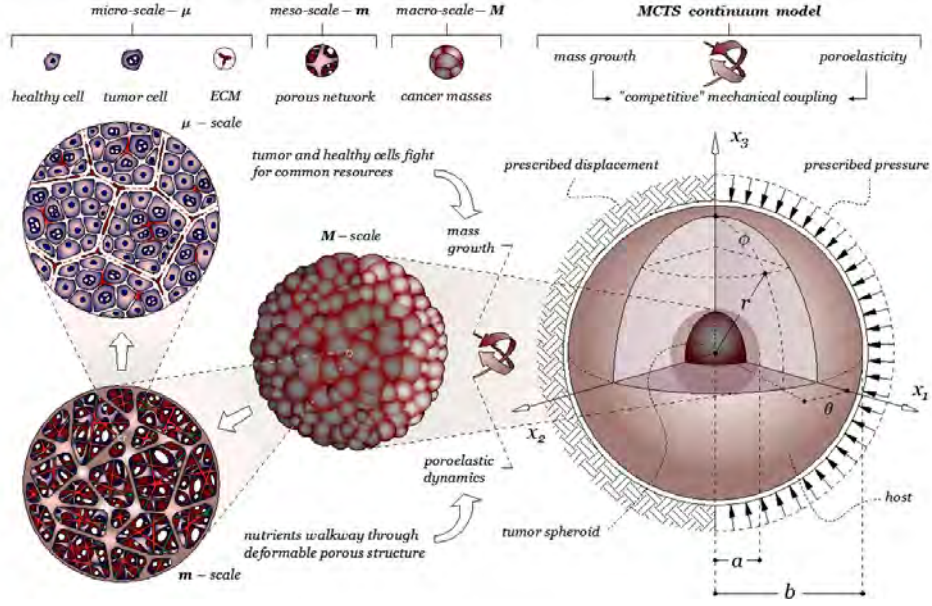
Figure 52: Sketch of the mathematical modeling of the MCTS. The focus is on the different scales in order to highlight the roles of the several constituents in determining the modeled phenomena at the tissue scale.

The entire system of PDEs describing the problem illustrated in Fig. 52 then reads:

$$
\begin{cases}
\frac{\partial P_{RR}}{\partial R} + \frac{2}{R}\left(P_{RR} - P_{\Theta\Theta}\right) = 0 \\[2mm]
\alpha\,\frac{dh_e}{dt} + \frac{1}{M}\frac{dp}{dt} - \frac{k_F}{J R^2}\frac{\partial}{\partial R}\left(R^2 \frac{\partial p}{\partial R}\right) = \Gamma_F \\[2mm]
\phi_F \frac{d\eta}{dt} + \eta\left(\alpha\,\frac{dh_e}{dt} + \frac{1}{M}\frac{dp}{dt}\right) = -\phi_F \eta \Gamma_{cons} \\[2mm]
\frac{1}{J}\frac{d(J\phi_T)}{dt} = \phi_T \Gamma_T \\[2mm]
\frac{1}{J}\frac{d(J\phi_H)}{dt} = \phi_H \Gamma_H \\[2mm]
\frac{1}{J}\frac{d(J\phi_M)}{dt} = \phi_M \Gamma_M \\[2mm]
\frac{1}{J}\frac{d(J\phi_A)}{dt} = \phi_A \Gamma_A
\end{cases}
\tag{5.81}
$$

in the unknown variables $\{u, p, \eta, \phi_T, \phi_H, \phi_M, \phi_A\}$.

Initial and Boundary Conditions. The initial conditions at $t_i = 0^+$ have been assigned by setting a constant ECM initial fraction ϕ_M^0 and a baseline nutrient concentration η_0, while the cells volume fraction distribution have been determined by estimating the tumor nucleus initial radius a from the number of tumor cells injected N_c (approximately 2×10^6 cells in the experiments conduced) as $R_c \left(N_c P_f^{-1} \right)^{1/3}$, R_c representing the tumor cell radius ([121]) and $P_f = 0.68$ being a packaging factor calculated under the simplifying hypothesis of rigid spheres. The given initial distribution within the observed area is supposed to be $\phi_T^0 = \tilde{\phi}_T \Pi(R)$, with $\Pi(R) = \exp(-R/\sqrt{2}a)^2$ being a chosen starting profile and $\tilde{\phi}_T$ its amplitude representing the tumor cells fraction within the volume. In an opposite manner, the healthy cells fraction distribution results $\phi_H^0 = \tilde{\phi}_H (1 - \Pi(R))$, while null apoptotic fraction is also assigned. Furthermore, the saturation condition let to automatically write ϕ_F^0. The IFP is set at its reference value p_0 and also null initial displacement u have been supposed. With reference to the boundary conditions, no internal and external fluxes respectively towards the inner inclusion and the skin overlying layer have been assigned, i.e. $\partial p / \partial R = 0$ both for $R = R_i$ and $R = R_e$. In addition, the internal inclusion is thought to be motionless, i.e. $u = 0$ at $R = R_i$ for each time. At the external boundary $R = R_e$, different illustrative cases of theoretical and practical interest have been analyzed. In particular, the simulations performed refer to:

- a stress-free condition, simulating an unconfined growth case, i.e. $\sigma_{rr}|_{R_e} = 0$.

- a stress-prescribed condition, to analyze the effect of a (constant) environmental pressure on the growth, to meet recent experimental evidences according to which mechanical stress impairs tumor spheroids proliferation ([137, 138, 198]). Interestingly, theses studied *in viro* showed that an isotropic environmental stress ranging from 500 Pa up to 10 kPa can actually reduce cell proliferation and volume expansion, and showed that a compression between 2 and 5 kPa is sufficient to reduce the spheroids volumes (with reference to the unstressed spheroid growth). Therefore, in order to analyze the sensitivity of the model at hand in terms of the influence of the stress conditions on the growth of the tumor spheroid, a confined problem has been also studied, by applying a constant confining compression $\sigma_{rr}(r_e) = -p_{ext}$.

- to find a correlation with the experimental model in the most faithful manner, it is finally imagined that, at the external boundary, the growing MCTS feels the contact with a skin-like layer. This hypothesis have been introduced in order to mimic the possibility of the growing spheroid of exchanging forces with an overlying elastic layer, also directly observing that the animals skin appeared to be more tensed around the grown tumor (see Fig. 53). Therefore, assuming that the deformation process is entirely governed by the evolution of the spheroid, that consequently provokes also the elastic stretching of the skin-like layer, and that the latter layer exhibits a linear constitutive behavior with the true strain, the continuity of the radial Cauchy stresses at $R = R_e$, i.e. $\sigma_{rr}|_{R_e} = \sigma_{rr}^{skin}|_{R_e}$ as well as the coincidence of the hoop stretches, that is $\lambda_{\Theta\Theta}|_{R_e} = \lambda_{\Theta\Theta}^{skin}|_{R_e}$, are then required. If the skin layer is assumed nearly incompressible, one can finally write a leakage-like boundary condition, by imposing the continuity of the normal stresses. In terms of the nominal stresses it
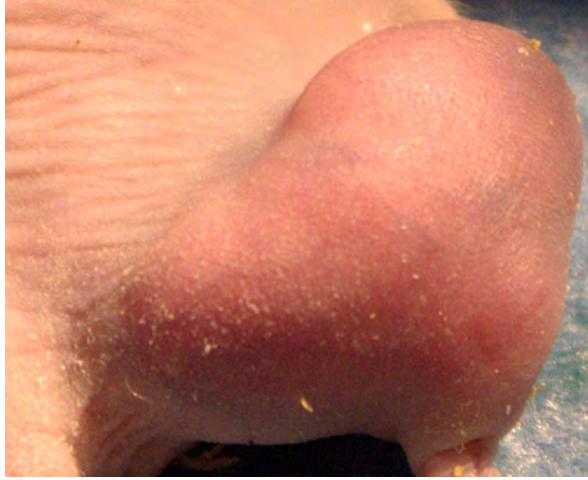
Figure 53: Detail showing the stretched skin layer surrounding the grown tumor in contrast with the more lapse and wrinkled skin appearing in the other "unperturbed" anatomic regions.

results $P_{RR}|_{R_e} = -4G^s \left(1 + u\left(R_e\right) R_e^{-1}\right)^2 \ln\left(1 + u\left(R_e\right) R_e^{-1}\right)$, where G^s is the skin shear modulus.

5.4.10 *Numerical solutions of the MCTS model*

The modeling of the here presented Volterra-Lotka dynamics between tumor and host fractions let to get knowledge about the tumor aggressiveness in terms of the tumor fraction growth, i.e. of its amount and invasion level within the control volume. As shown in Fig. 54, the result of this competition leads the tumor cells be prevailing into the environment, consequently occupying the most of the available space and thus automatically inhibiting the growth of normal cells. In particular, with reference to the unconfined growth case, tumor invasion appears highly aggressive: the combination between growth dynamics and free-stress condition, which also implies free-expansion capability, abet the MCTS to invade almost all the available space, causing the host tissue fraction pauperization. By referring to a stress-prescribed case, the combination of the VL growth kinetics with mechano-sensing processes makes the MCTS aggressiveness effectively reduces in terms of invasiveness radius and presents enhanced apoptosis, in good agreement with the aforementioned experimental works.

Tumor species invasion and stretch together determine the expansion of the tumor volume and consequently, the push of the external environment. This interaction is reasonably accompanied by the development of mechanical forces at the interface region. By looking for example at the unconfined case, one can see that, at three weeks, the most of the environment has been invaded by the tumor species, which forms a compact hyperproliferative spheroid of about 9 mm in radius, as shown in Fig. 55, thus almost entirely pervading the initial healthy volume. Furthermore, Fig. 55 additionally shows the presence of a non zero net (e.g. deviatoric, in the particular case) stress arising at the tumor/host interface, which well represents the previously hypothesized

interface exchange of mechanical stress. The presence deviatoric stress peaks also suggests that growth –that is a dissipation process– could locally be associated to plastic phenomena, related to a reorganization of the cells and compression in the surrounding tissue. Moreover, as also suggested by Ambrosi et al. ([9]), this interface stress could be also related to the formation of a sort of peri-tumoral capsule, since the motion of the expanding tumor spheroid drags and compress the communicating ECM layers.

The growth term and the fluid pressure actually combine with the effective stress in order to express the solid stress field that builds up into the MCTS, which plays a non-negligible role in many phenomena related to the growth of the multicell spheroid, from the influence that mechanical stress exerts on tumor expansion to the adverse importance in determining central necrosis processes, vascular collapse and representing a stress-induced drug-barrier. By focusing on the analysis of these stresses (Fig. 56), it emerges that its hydrostatic stress (Fig. 56B) is predicted to be almost completely compressive in the inner spheroid due to the adverse regime of hyperplasia, to which is related the almost completely hydrostatic stress distributions (see Fig. 56A and C). As anticipated, the latter stresses also represent a mechanical barrier for the perfusants to enter the interior of the tumor, an hypothesis largely put forward in literature, according to which tumor hypertension and high intratumoral IFP (Fig. 56D) can actually compromise the interstitial transport of macromolecules towards the tumor interior and cause a diversion of biological fluids towards the periphery due to the pressure drop at the tumor/host boundary. The aggressive growth of the internal tumor spheroid also determines the push of the surrounding host crown which experiences a positive hydrostatic stress at the tumor-host interface. At the tumor front, where proliferation occurs, a quick rise of hydrostatic stress can be in fact observed, which settles on values (positive, in this case) accounting the thrust of the internal volumetric growth as well as the effects of the absence of an external confinement and actually indicating a deformation of the surrounding tissue. Also the hoop stress shows a similar behavior, see Fig. 56C, and clearly indicates the accumulation of the stress necessary for the compatibilization of the tissue growing elementary volumes during the growth process. The storage of this compressive eigenstress, here exclusively determined by the inner growth dynamics, may be manifested in different ways, for example by acting on the tissue integrity, in order to catch the effects of the its sudden release. For instance, recent literature works analyze the accumulation of residual stress in the tumor spheroid interior (see e.g. [191] and [192]) by engraving the explanted tumor spheroid and estimating the growth-induced stress stored within the tissue from the opening of the slit, as well as by observing the bending of the cut interfaces which then would result no more compatible each other along the discontinuity surface.

In this sense, a less invasive way to determine the accumulation of the growth associated stress could be certainly more effective in order to also account the time evolution that accompanies the accrual of the *in situ* residual stresses. A direct measurement would also consider the compression aliquota induced by the presence surrounding tissues (which instead disappears when the tumor is removed, causing a partial relaxation of the tissue), this representing a further pre-stress that would contribute to the stress-related unfavorable phenomena previously described. In addition, a direct experimental *in loco* estimation, that could be efficiently supported by the present the-

oretical results, can have a key role in modulating the *ad hoc* design of mechanically driven drug delivery therapies. In fact, one could also think to model a further coupling in order to include the effects of therapeutic agents on cells proliferation. This could be likely predicted, for example, by explicitly including in the present evolutionary model the alterations of cells metabolism due to the (direct) interaction with drugs, modeled as a further chemical antagonist species into the VL dynamics. Moreover, the recent literature deeply emphasizes in understanding the role of the mechanical interaction between the growing tumor spheroid and a (stressed) surrounding environment, focusing both on the role of stresses exerted by the tumor grown in a stressed environment (see for example [83]) and on the possibility of inhibiting spheroids proliferation potential as an effect of applied mechanical stresses, see e.g. [137, 138, 198]. As seen, results shown (assuming p_{ext} 2 kPa and 3 kPa) are effectively able to capture a mechanically-induced reduction of the tumor growth of the spheroid in a constrained (compressed) environment, see the bottom panel Fig. 54. Accordingly, the stresses are obviously affected by the external pressure. In particular, 57 (here referred to the case $p_{ext} = 2$ kPa) shows everywhere compressive distributions along the radius, with higher internal compression and weaker stress gradients at the interface. In fact, the host tissue practically feels a hydrostatic compression, that equals the external confinement. As a consequence, the external pressure transparently transfers to the tumor boundary, where Cauchy stresses start to increase towards the tumor center, approaching in this case values of about 5 kPa and thus slightly higher than both the external loads and to the corresponding stresses in the unconfined case (Fig. 56).

Tumor vs Host Tissue Fraction - Unconfined growth
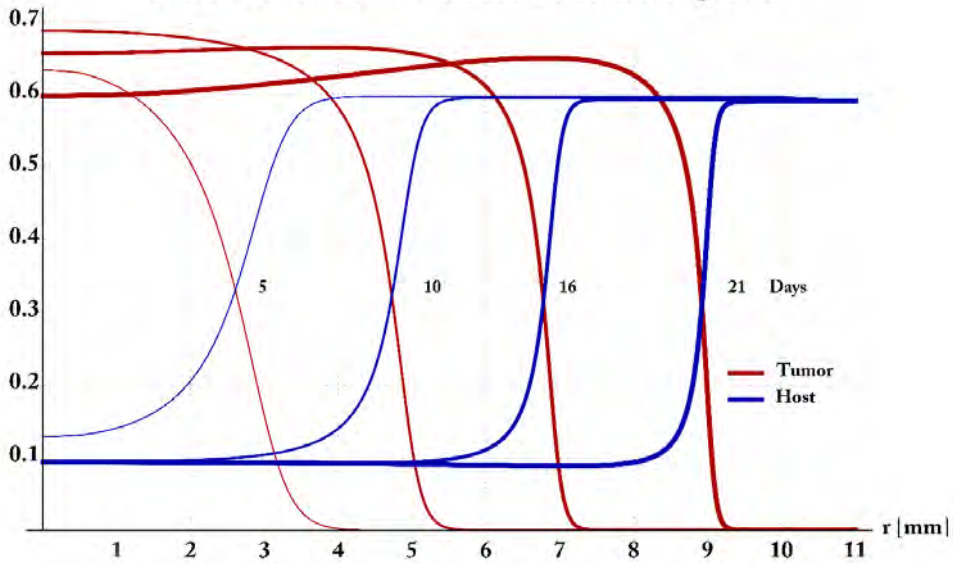
Tumor vs Host Tissue Fraction - Stress prescribed growth
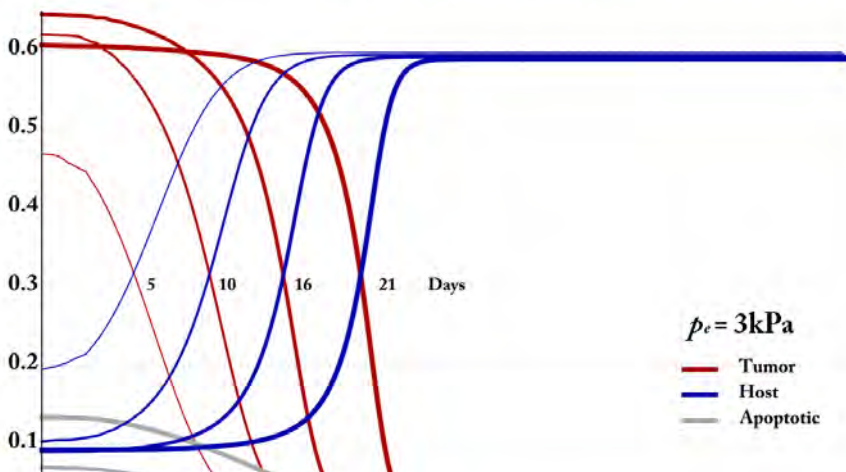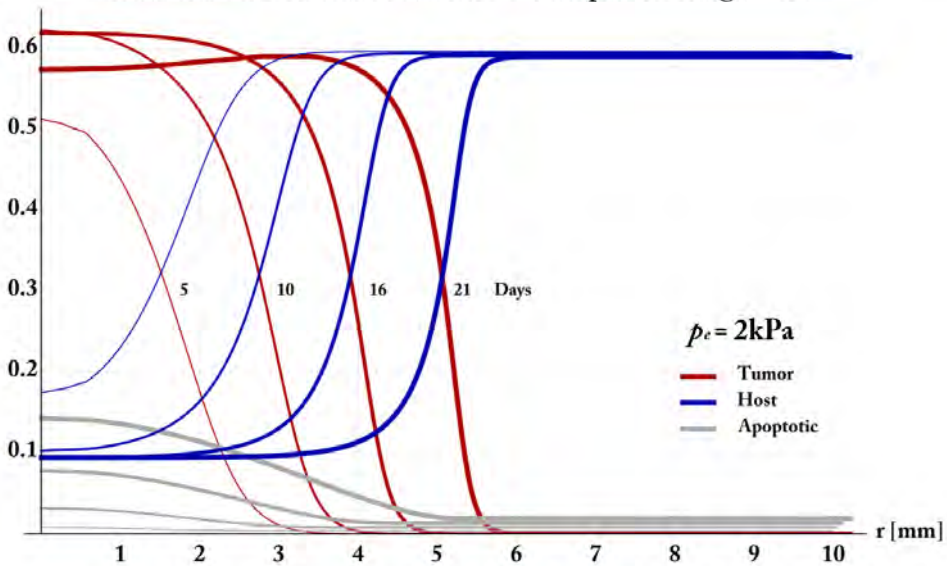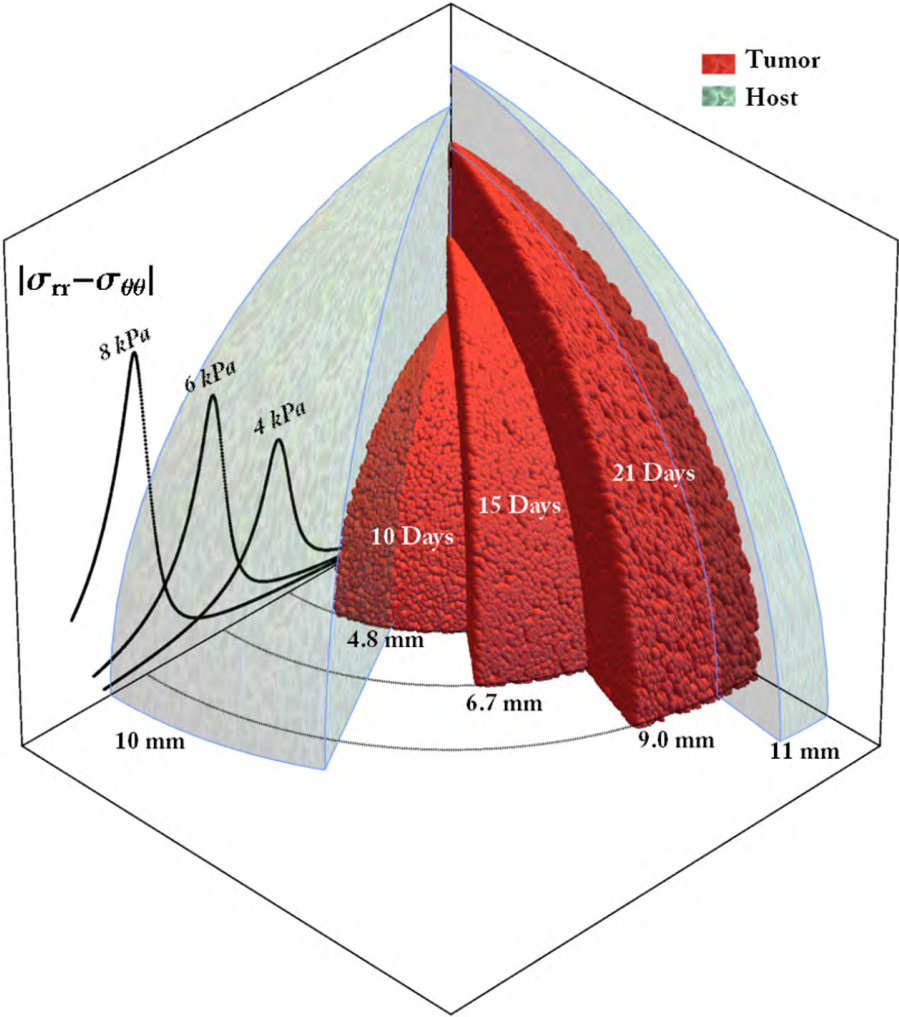
Figure 55: Invasion of the tumor spheroid in the healthy region and representation of the associated non-zero interface stress
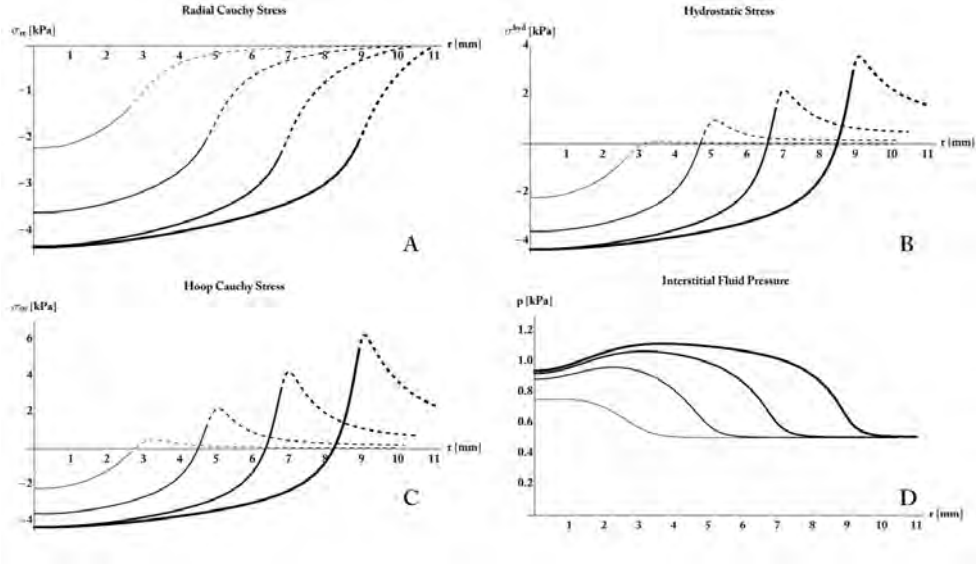
Figure 56: Evolution of the Cauchy stress components at different times. **A**. Radial stress. **B**. Hydrostatic stress. **C**. Circumferentisl stress. **D**. Interstitial Fluid Pressure
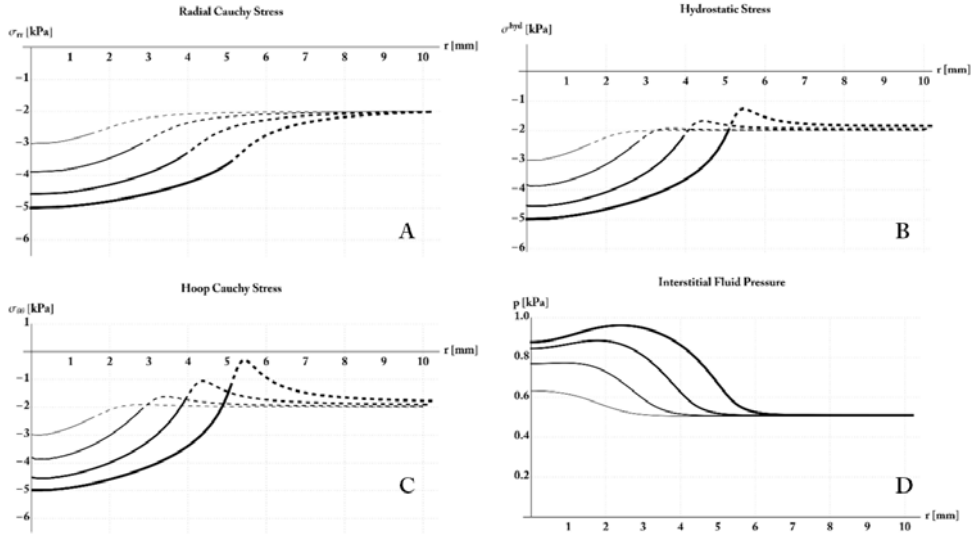
Figure 57: Stress of the spheroid when a compression of 2 kPa is applied. **A**. Radial stress. **B**. Hydrostatic stress. **C**. Circumferentisl stress. **D**. Interstitial Fluid Pressure

5.4.11 *Comparison of theoretical and experimental results*

Focusing on the third set of simulations, the main results, emerging from the numerical solution of problem (5.81) when matched with experimental observations, certainly lie in the possibility of predicting the growth of the tumor species –the MiaPaCa-2 and MDA.MB-231 cell lines in the case at hand– and thus also obtaining the level of invasion of the tumor in the host tissue. In fact, by referring to Fig. 59, it can be seen how the tumor internal phase grows in time by consequently occupying a significant portion of the available domain. More specifically, MiaPaCa-2 cell line seems to growth and invade host tissue faster than the breast cancer counterpart. In fact, approximately 7 mm are achieved in a three-weeks period, while MDA.MB-231 cell line has a slightly greater variability, but averagely implies 40 days to achieve the same dimensions. This also implies that MDA tumor cells interior are progressively more deprived of nutrients because they result to be in a hypoxic region longer than pancreatic cells and also feel constant compression in such region: as a consequence, the percentage of apoptosis in the tumor inner layers is more enhanced, and this metabolic/stress-driven alteration actually makes the MCTS exhibit a non-proliferative core surrounded by a proliferating ring of tumor MDA cells (see e.g. 59). This results in complete agreement with the experimental evidences according to which mechanical stress accumulation produces enhances central apoptosis, with the MCTSs *de facto* exhibiting proliferating cells rings in the peripheric regions which have been also experimentally observed in the present Literature, see e.g. the work by Cheng et al., [38] (however, proprietary hystological analysis to evaluate caspase-3 activity should be properly conducted in order to find an exact correlation with the theoretical model outcomes).

This can be interpreted as the overall result of both the inter-specific VL dynamics explicitly included in the model between the tumor and the host tissue species and the effect of the other environmental variables affecting the growth process, as well as the external conditions to which the body is subjected which derive from the biological structures in contact with the tumor. In particular, from Fig. 59 information about the composition of the phases (in terms of percentage of cells, ECM and fluid) as well as a quantitative observation of the invasiveness can be readily derived. Also, the theoretically predicted growth curve related to the time progress of the tumors radius seems to be in good agreement with the experimental data, in terms of experimentally measured dimensions; the complete set of experimental measure is reported to Table 4, while the comparison between numerical simulations and experimental findings is synthetically shown in Fig. 60.

As previously discussed, the growth of the MCTS is connected the genesis of *in situ* internal stresses. These stresses account for both the internal pressure exerted by the growing mass and the elastic compatibilization of the grown volume, as well as the elastic deformation because of the external mechanical stimuli. In absence of external loads, the stress within the body is expressively related to the internal inelastic deformation, i.e. it is the expression of the mechanical force exerted by the growing tissue elements. In the present case, the numerical results serve also the introduction of the elastic confinement aimed to simulate the tension exchange with the skin layer and the spheroid will thus project an external radial reactive tension, which is not constant as in the previous section, but its magnitude evolves with the tumor development (in this sense, it is more realistic to think this mechanical
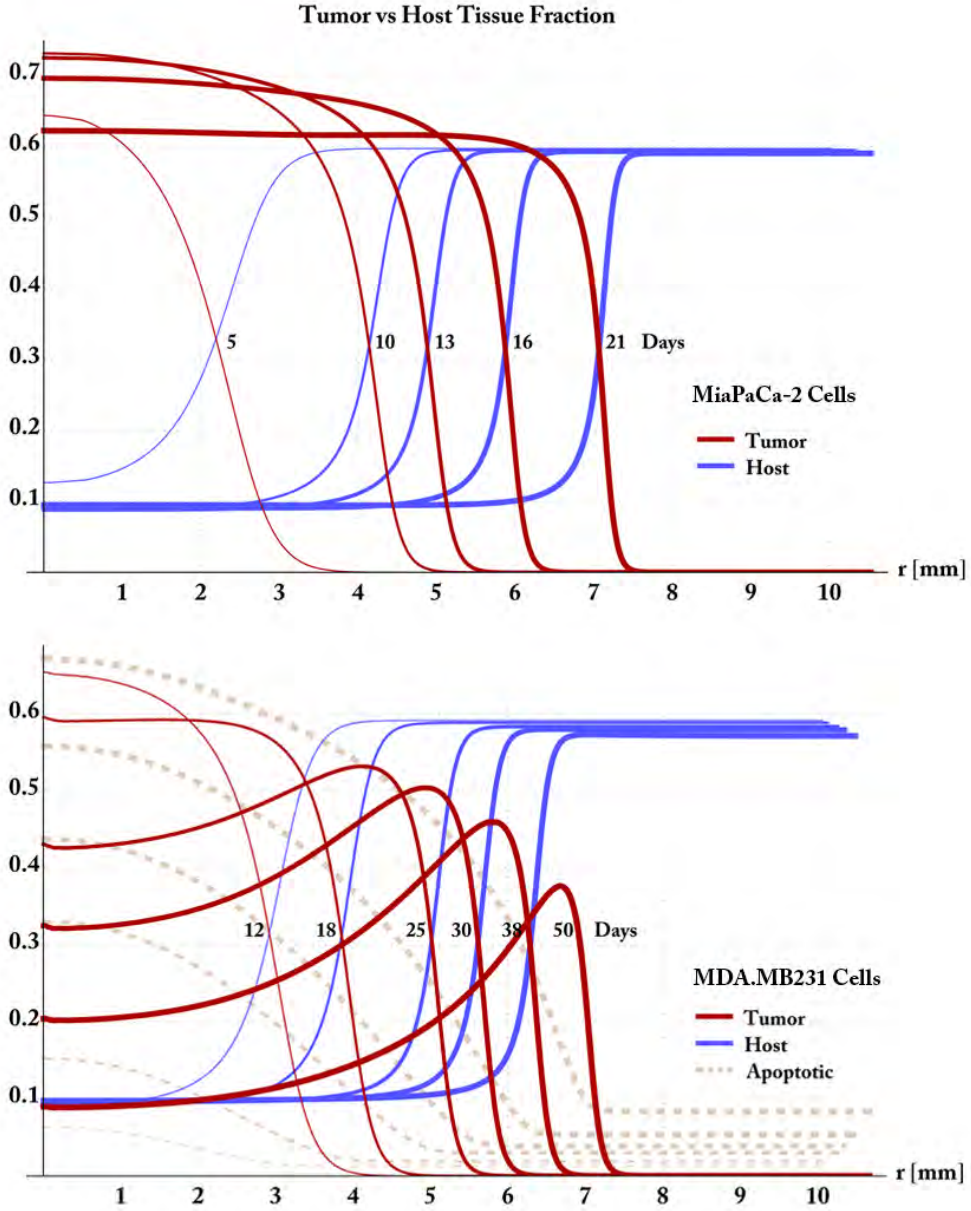
Figure 58: Tumor fraction vs host fraction in MiaPaCa-2 (top) and MDA.MB-231 (bottom) cell lines

interaction as a progressively increasing reaction rather than a constant pressure, in terms of consequences on tumor spheroid growth kinetics). Fot both the cells, the analysis of the radial stresses show the progressive accumulation of a slightly variable radial compression which is quantitatively more enhanced (and uniform) in the tumor region. The combination of radial and circumferential solid stresses –the case of MDA-
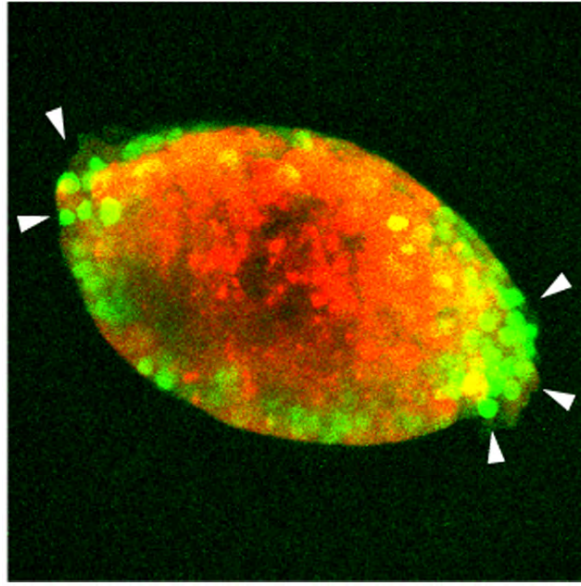
Figure 59: Cancer cell spheroid (red) showing that proliferative zone (green) concentrates towards the periphery, while proliferation is suppressed in the regions of higher mechanical stress, where apoptosis is induced. *Image from Cheng et al. [38]*, doi:10.1371/journal.pone.0004632.g003.

MB231 cells is illustrated in Fig.61– gives an internal hydrostatic state of stress that attains, in this case, a value of 8 kPa (about 60 mmHg) inside the tumor and slightly decreases toward the periphery, where the proliferation front advances because of the minor resistance. Also the host surrounding crown is consequently radially constrained, and it is additionally compressed by the external increasing reaction.

The circumferential Cauchy stresses in Fig.61 show a quantitatively similar trend to the radial stresses in the inner layers; however, a sharper gradient occurs at the interface at each time, provoking also peri-tumoral circumferential positive tensions before relaxing and re-approaching compressive values due to the host external confinement. Also, MiaPaCa-2 tumors exhibited very similar behavior in terms of mechanical stress, as shown in 62, with internal compression equal to approximately 4 kPa.

Importantly, it is widely accepted ([191]) that residual stress are a general feature of avascular tumor spheroids, i.e. human tumors accumulate growth-induced mechanical stress in an analogous manner with respect to the animal models here presented. Accordingly, this enhanced approach combining VL dynamics, hyperelasticity of the biological samples under exam and fluid contribution are able to reproduce the most of the stress characteristics that Jain et al.([191]) have described in their works. They in fact demonstrated that accumulated solid stress ranged in the interval 2-19 kPa and presents circumferential distributions with intratumoral compression and peripheral tensions. In the case just discussed, the presence of the host tissue crown and the external confinement would dimish the latter feature, but it can be somehow restored –in order to investigate the mechanical properties of the tumor itself– by virtually "explanting" the tumor spheroid, then depriving it of the external layers and compression. Moreover, it could be pairwise interesting to provide the time-evolution of

Tumor Radius [mm]
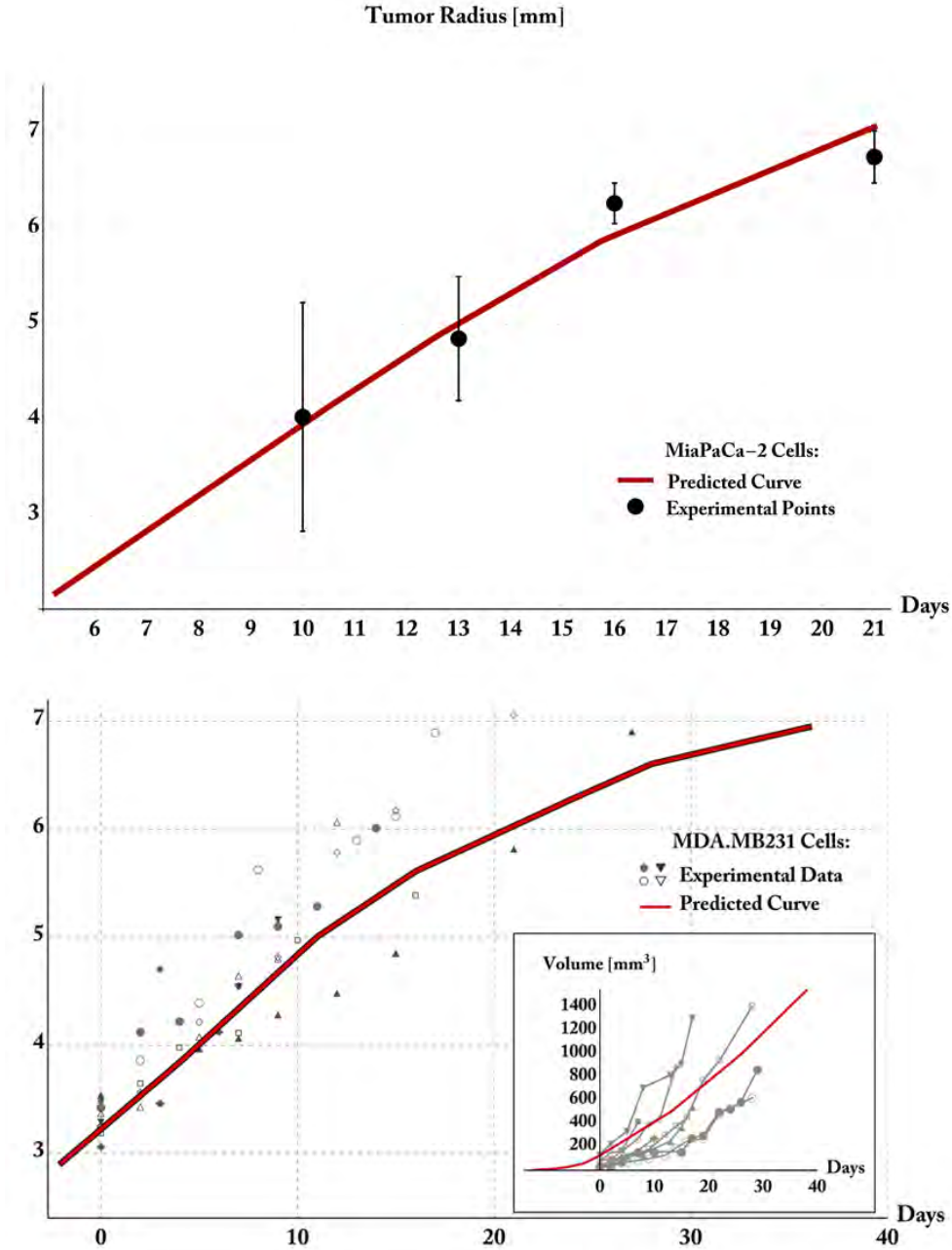
Figure 60: Comparison between the experimenatal size measure and the predicted spheroid redius development obtained from the numerical simulations. (top) MiaPaCa-2 cell line (bottom) MDA.MB-231 cell line.

this stresses combined with the tumor interspecific development, as shown by the present models, and it is thought that growth-induced stress and deformation also affect the material properties of the evolving tissue. In addition, it is possible that

local material properties and resident stress have a close relationship. As anticipated, from a physiological point of view, elevated solid stresses cause compression of blood capillaries and lymphatic vessels. The former is at the bases of the hypoxia and the lack of an adequate level of nutrients and can induce central necrosis, whereas the latter provokes an increase of the interstitial fluid pressure which makes peripheral backflow phenomenona carrying fluids outside the mass more likely to happen. All these factors combined promote tumor progression, invasion and immuno-suppression. As a consequence, the exact knowledge of the *in situ* solid stress combined with the knowledge of evolved material properties of the tissue would furnish a complete view of the tumoral micro-environment in order to obtain several important therapeutic implications, for example in mechanically relaxing tumor compression to control internal permeability, in this way improving the efficacy of drug perfusion and also designing *ad hoc* drug-delivery procedures.

Table 6: Synoptic table of the parameters adopted in the MCTS model (exp.det. = experimentally determined)

Parameter	Value	Unit	Source
Poroelastic/Conductivity parameters			
ν_u	0.49999	[-]	[46, 65]
B	0.9999	[-]	[65]
k_F	4.13×10^{-8}	$\mathrm{cm}^2\mathrm{mmHg}^{-1}\mathrm{d}^{-1}$	[166, 192]
L_p	3.6×10^{-8}	$\mathrm{cm}\ \mathrm{mmHg}^{-1}\mathrm{d}^{-1}$	[166, 192]
S/V	100	cm^{-1}	[102, 166]
κ_{l0}	1.33×10^{-5}	$\mathrm{mmHg}^{-1}\mathrm{d}^{-1}$	[214]
p_v	25	mmHg	[102, 192]
ϖ	0.91	[-]	[102, 192]
$\pi_v - \pi_l$	10	mmHg	[102, 192]
Cells rates and interspecific coefficients			
$T_T = T_H$	24 (MiaPaCa-2) 35 (MDA.MB231)	hours	exp. det.
$\alpha_{TT} = \alpha_{TH} = \alpha_{MH}$	1	[-]	[75, 99, 208]
$\alpha_{HT} = \alpha_{HH}$	3	[-]	[75, 99, 208]
α_{MT}	2	[-]	[75, 99, 208]
β_T	.05	d^{-1}	[37]
β_H	.1	d^{-1}	[37]
$\delta_T = \delta_H$	0.0314 (MiaPaCa) 0.0719 (MDA.MB231)	d^{-1}	[121]
ϵ_q	0.1	[-]	[197]
a_η	0.1	[-]	exp. det.
b_η	0.9	[-]	exp. det.
c_η	0.25	[-]	exp. det.
η_0	10^{-8}	$\mathrm{g\ cm}^{-3}$	[113]
$\tilde{\phi}_T = \tilde{\phi}_H$	0.2	[-]	assumed
$\tilde{\phi}_M$	0.4	[-]	assumed
a	1	mm	exp. det.
G^s	15	kPa	[55]
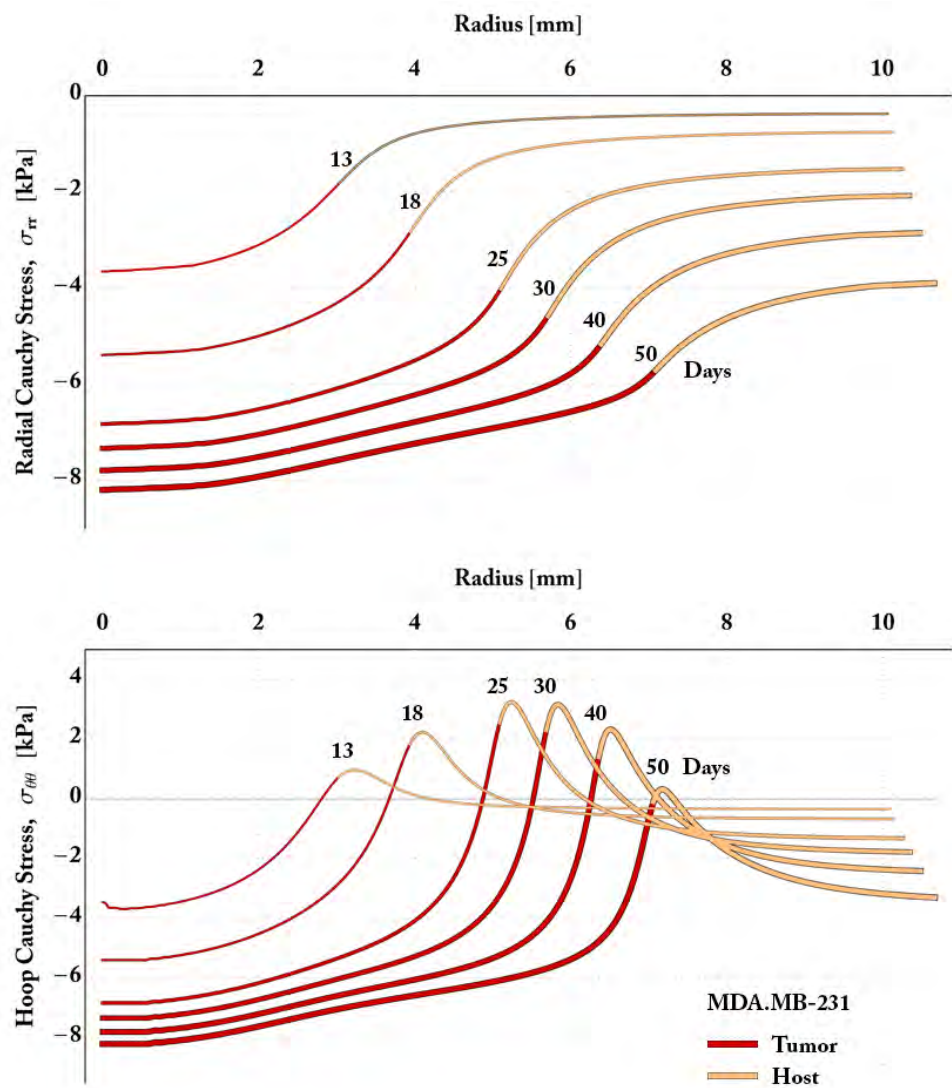
Figure 61: Stresses in the heterogeneous MCTS, MDA.MB-231 cells. (Top) Radial Stress. (Bottom) Circumferential Stress.
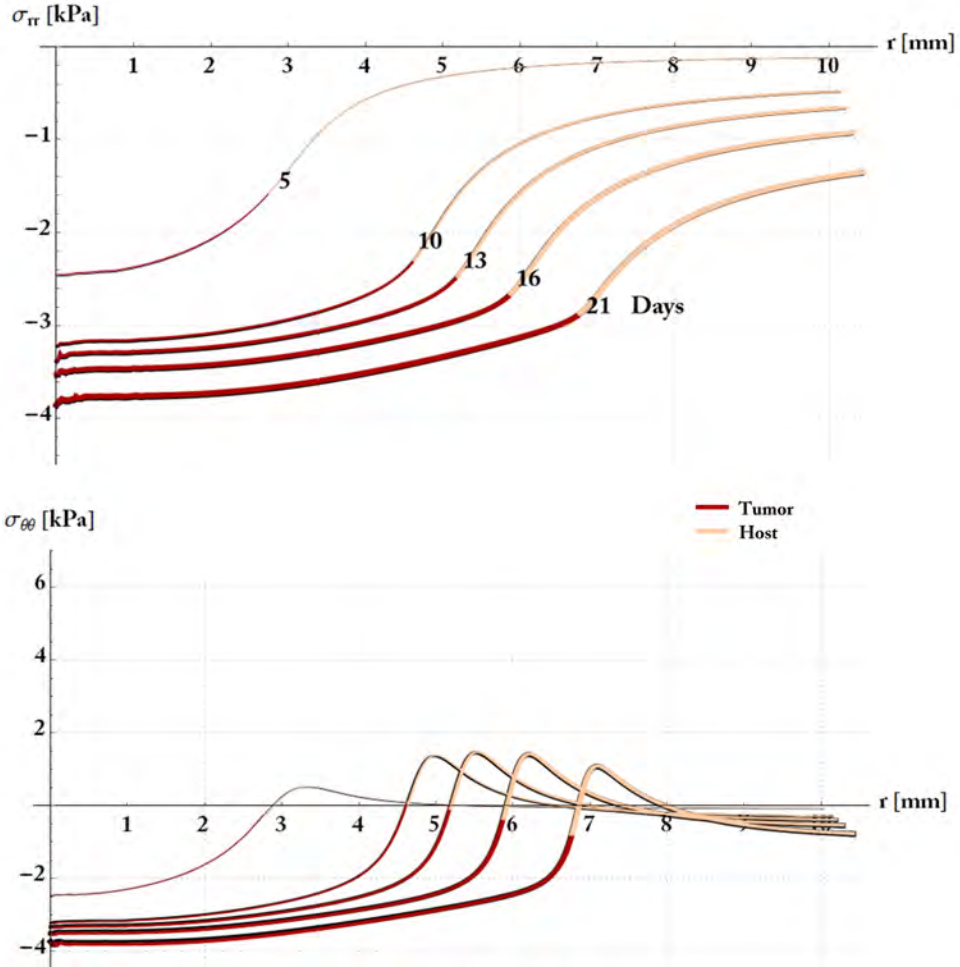
Figure 62: Stresses in the heterogeneous MCTS, MiaPaCa-2 cells. (Top) Radial Stress. (Bottom) Circumferential Stress.

The nonlinear model here presented, which provides a strategy combining interspecific evolution equations aimed to replicate the interaction between the tissue constituents and a poroelastic framework which describes the fluid-solid interplay, leads to the characterization of the growth-induced intratumoral stresses. Such stresses, which are commonly defined as the self-equilibrated stresses in a free-traction body, are known to influence the mechanical behavior of many tissues, as well as of many engineering materials, and can be strongly related to the growth and remodelling processes (see, for example the case of arteries discussed by Fung [69]). As said, in the case of solid tumors, stress seems to concur in many physiological events related to their development, such as internal necrosis and vascular collapse as well as peripheral migration and lymphangiogenesis: this happens by influencing cell proliferation and squeezing, and by altering nutrients and chemicals walkways through mechano-sensing activated inhibition and flow impairment. The role of stress gradients in biological media is in fact critical in promoting cells reconfiguration and motility and, naturally, plays also a driving role in chemicals diffusion within the fluid phase as well as macro-molecules extravasation throughout the *interstitium*. In the case of tumors, there is a wide literature dedicated to the investigation of tumor mechanical micro-environment to establish the nature as well as the causes and the effects of intratumoral residual stresses ([12, 182, 191, 192]), and are aimed also to offer mechanically based hypotheses to prospect intratumoral drug inflow as well as to reduce peritumoral convective flow and thus likely decrease metastasis of cancer cells ([102]). Furthermore, from a kinematic standpoint, the presence of residual stress basically reveals that body growth takes place in an incompatible manner, meaning that the compatible observable strain of a grown tissue is the combination of an incompatible growth strain (which would cause growth with disruptions) and an incompatible strain due to elastic stress [182], which is then responsible of restoring the geometrical and structural compatibility of the tissue. In the case, the presence of a residual stress manifests through the bending of the tissue halves (see Fig. 63).

This implies that *in loco* residual stress can be revealed, as largely known, by making cuts and by noticing the resulting change in configuration. By virtue of these considerations, several models of tumor growth have been proposed ([165]) and, to date, no direct quantitative measurements of residual stress in solid tumors have been shown, except for indirect estimations performed by measuring the deformation resulting from the opening of the two halves of an excised tumor spheroid after that a partial cut is realized on the mass itself, by then relating the experimental findings with cutting finite element simulations (see the work by Stylianopoulos et al. [191]). This particular behavior has also been qualitatively replicated on a tumor spheroid, by first making a partial cut (up to half the spheroid height) and observing the progressive opening of the slit with the characteristic opening angle, and then performing a complete cutting and observing the curvature of the generated surface, as reported in Fig. 63.

However, it is well-known that residual stress influences the mechanical behavior of the material. Nonzero residual stress field in a traction-free body is necessarily inhomogeneous and anisotropic ([85]), as well as an imposed deformation out of the residually
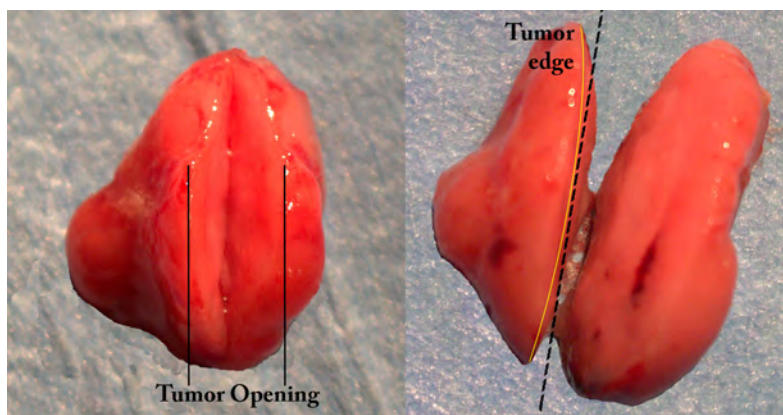
Figure 63: Visualization of the opening angle when a partial cut is performed (left) and of the bending of the tumor spheroid halves in case of a complete cut (right), revealing the presence of residual stress.

stressed configuration can relieve the internal loads at some points and load other points, while a residual stress-free material would be only loaded by such deformation. Also, another essential evidence is that the actual (tangent) material properties can depend on residual stress, and consequently material properties of a homogeneous and isotropic "ground" material can become inhomogeneous and anisotropic as a result of the accumulation of both residual stress and, of course, deformation: therefore, the knowledge of the latter ones together with strain energy density (which measures how much a material point is loaded or unloaded by a given deformation) can comprehensively characterize the global mechanical behavior of a residually stressed body. Nonlinear tumor spheroids are not excluded from these considerations, and it is therefore thought that tangent stiffness can represent a valid candidate to be an indirect way to trace residual stress. Starting from this idea, before presenting further details, the previous sections results have been here summarized for the sake of clarity:

- An enhanced MCTS model has been developed, by proposing a full coupling strategy between the nonlinear mechanical problem and interspecific dynamic, to describe tumor growth kinetics and stress accumulation. Starting from the whole stress distributions (including external loads due to the imposed boundary conditions), an estimation of the residual stress within the sole tumor has been made by considering the stress distribution at each time deprived by the external radial reaction, by assuming the latter to essentially determine a hydrostatic aliquota associated with external load.

- An *in vivo* experimental model has been conducted, by following a size-controlled protocol. The explanted were thus measured in size and mechanically tested in compression. This particular explantation procedure has been designed in order to both trace tumor effective size and obtain time/size-dependent information about the mechanical properties evolution. Hence, the variation of tangent moduli has been experimentally evaluated during tumor development. Also, a reference (small) tumor spheroid was utilized to reconstruct the theoretical nonlinear stress-stretch law.

Starting from these experimental data and theoretical results, in very good agreement between each other in terms of resulting tumor size growth, a correlation between the theoretically obtained stress and deformation and the experimentally determined tangent moduli is then investigated. Therefore, the residual stress-modified elastic coefficients have been all analytically estimated by adopting a well-known *small-on-large* strategy, which has the advantage to explicitly emphasize the prestress contribution with respect to the deformation contribution in tangent matrix calculation, and by taking into account both induced transverse isotropy and inhomogeneous variation (with respect to the radius) of the stiffness coefficients. To reproduce *in silico* the provided mechanical tests, mechanical properties have been inserted in an appropriate FE model, by simulating a sphere compression between two parallel rigid plates: in this way, stress-strain curves have been numerically derived and compared with experimental findings.

5.5.1 *The small-on-large approach*

The established constitutive equations accounting for growth and elastic deformation at each time let to obtain the different stress measures. In particular, given the elastic second PK stress tensor $\mathbf{S}_e$, the following relations among the various stress tensors are here recalled (see Chapter 1):

$$\mathbf{S}_e = 2\frac{\partial \psi_e}{\partial \mathbf{C}_e} = 2\mathbf{F}_g\frac{\partial \psi_e}{\partial \mathbf{C}}\mathbf{F}_g^\mathsf{T} = 2\mathbf{F}_g\mathbf{S}\mathbf{F}_g^\mathsf{T} \tag{5.82}$$

$$\mathbf{P} = J_g\mathbf{F}_e\mathbf{S}_e\mathbf{F}_g^{-\mathsf{T}} \tag{5.83}$$

$$\boldsymbol{\tau} = J_g\mathbf{F}_e\mathbf{S}_e\mathbf{F}_e^\mathsf{T} = J_g\mathbf{F}\mathbf{S}\mathbf{F}^\mathsf{T} \tag{5.84}$$

$$\boldsymbol{\sigma} = J_e^{-1}\mathbf{F}_e\mathbf{S}_e\mathbf{F}_e^\mathsf{T} = J_e^{-1}\mathbf{F}\mathbf{S}\mathbf{F}^\mathsf{T} \tag{5.85}$$

With the aim of evaluating the tangent stiffness of the tumor body tensor at each time stage, the presence of non-trivial resident stretch –and stress– has to be taken into account. These quantities in fact are known to affect the evaluation of the material properties. It is then here supposed that the tangent moduli to be estimable by means of a *small on large* procedure, in which a small strain (the one related to the testing of the material properties) can be superimposed to the (large) finite strain at a certain time t. This strategy can be somehow viewed as a generalization of the well known evaluation of the elastic modulus of a cord under constant tension, and its formulation has been encountered in many classical elasticity works (see for example [85, 151, 199]) as well as more recent biomechanical works ([15]). By focusing on this specific application, the growth and compatibilization processes occurring in tumor development will likely imply that the incremental material parameters will depend on the history of growth-induced stresses and deformations at time t.

By identifying the body motion at time t with the deformation gradient $\mathbf{F}(t)$, a further (small) gradient is then applied, say $\mathbf{F}^* = \mathbf{I} + \mathbf{H}^*$, where $\mathbf{H}^* = \partial \mathbf{u}^*/\partial \mathbf{x}\,(\mathbf{X}, t)$ is the gradient of the additional displacement $\mathbf{u}^*$, which drives the body to a new current configuration (the system will move towards this configuration at a certain time t^*). The displacement gradient can be obviously decomposed into its symmetric and skew-symmetric parts, i.e. $\mathbf{H}^* = \mathbf{E}^* + \mathbf{\Omega}^*$, which respectively denote the infinitesimal strain

and rotation tensors in case of small deformations. Therefore, a new *small-on-large* deformation gradient $\mathbf{F}(t^*)$ can be defined by means of the standard multiplicative decomposition as $\mathbf{F}(t^*) = \mathbf{F}^*\mathbf{F}(t)$. Starting from this position, the stress $\boldsymbol{\tau}(t^*)$ can be expressed by starting from the knowledge of the stress at time t and the deformation gradient. In particular, by denoting the quantities at time t with the subscript 0, and provided that $J^* \to 1$, the constitutive relation $(5.82)_{3,4}$ let to write

$$\boldsymbol{\sigma}^* = J_{e0}^{-1}\mathbf{F}^*\mathbf{F}_0 \left(\mathbf{S}_0 + \frac{\partial \mathbf{S}}{\partial \mathbf{C}}\Big|_{\mathbf{C}_0} : (\mathbf{C} - \mathbf{C}_0) \right) \mathbf{F}_0^\mathsf{T} \mathbf{F}^{*\mathsf{T}} =$$

$$= \mathbf{F}^* \left(\boldsymbol{\sigma}_0 + 4J_{e0}^{-1}\mathbf{F}_0 \frac{\partial^2 \psi_e}{\partial \mathbf{C}\partial \mathbf{C}}\Big|_{\mathbf{C}_0} \mathbf{F}_0^\mathsf{T} : (\mathbf{F}_0^\mathsf{T}\mathbf{E}^*\mathbf{F}_0) \right) \mathbf{F}^{*\mathsf{T}} \qquad (5.86)$$

where $(\mathbf{C} - \mathbf{C}_0) = 2\mathbf{F}_0^\mathsf{T}\mathbf{E}^*\mathbf{F}_0$. Given that $\mathbf{F}^* = \mathbf{I} + \mathbf{H}^*$, the hypothesis of small displacement gradient $\mathbf{H}^*$ leads to

$$\boldsymbol{\sigma}^* \cong \boldsymbol{\sigma}_0 + (\mathbf{I}\,\overline{\otimes}\,\boldsymbol{\sigma}_0 + \boldsymbol{\sigma}_0\,\underline{\otimes}\,\mathbf{I}) : \mathbf{H}^* + 4J_{e0}^{-1}\mathbf{F}_0 \frac{\partial^2 \psi_e}{\partial \mathbf{C}\partial \mathbf{C}}\Big|_{\mathbf{C}_0} \mathbf{F}_0^\mathsf{T} : (\mathbf{F}_0^\mathsf{T}\mathbf{E}^*\mathbf{F}_0) \qquad (5.87)$$

where the non standard tensor products $\overline{\otimes}$ and $\underline{\otimes}$ can be defined by means of the double contraction rules $(\mathbf{X}\,\overline{\otimes}\,\mathbf{Y}) : \mathbf{Z} = \mathbf{X}\mathbf{Z}\mathbf{Y}^\mathsf{T}$ and $(\mathbf{X}\,\underline{\otimes}\,\mathbf{Y}) : \mathbf{Z} = \mathbf{X}\mathbf{Z}^\mathsf{T}\mathbf{Y}^\mathsf{T}$ (see for example [111, 112]). Derivation with respect to $\mathbf{E}^*$ gives the expression of the tangent stiffness matrix:

$$\mathbf{C}^* = \frac{\partial\boldsymbol{\sigma}^*}{\partial \mathbf{E}^*}\Big|_{\mathbf{F}^*\to\mathbf{I}} \cong \mathbf{I}\,\overline{\otimes}\,\boldsymbol{\sigma}_0 + \boldsymbol{\sigma}_0\,\underline{\otimes}\,\mathbf{I} + 4J_{e0}^{-1}(\mathbf{F}_0 \otimes \mathbf{F}_0^\mathsf{T}) \bullet \circ \frac{\partial^2 \psi_e}{\partial \mathbf{C}\partial \mathbf{C}}\Big|_{\mathbf{C}_0} \bullet \circ (\mathbf{F}_0^\mathsf{T} \otimes \mathbf{F}_0) \qquad (5.88)$$

where the double contraction operation "$\bullet\circ$" appearing in (5.88) are defined such that $[\mathbb{X} \bullet \circ \mathbb{Y}]_{ijhk} = X_{imnk}Y_{mjhn}$ ([111, 112]). Therefore, the tangent moduli of a pre-stressed material will account for the presence of such resident stress through a direct linear dependence (as in the simpler linear situation), and a further contribution which depends on the deformation achieved at time t when the small deformation is superimposed. Furthermore, by also considering the symmetry of the deformation tensor $\mathbf{E}^*$ in contracting the tangent stiffness to the Voigt 6×6 usual notation, the position $C_{\alpha\beta} = (C_{ijhk}^* + C_{ijkh}^*)/2$, $\alpha, \beta = \{1,..,6\}$, $i \neq j$ and $h \neq k$, has been automatically employed[4]. With reference to the adopted strain energy function $\psi_e(\mathbf{H}_e)$ (Equation (5.38)), involving the Hencky strain measure $\mathbf{H}_e = \ln(\mathbf{C}_e)/2$, the tangent stiffness is evaluated by means of the chain rule:

$$\mathbf{C}^* = \mathbf{I}\,\overline{\otimes}\,\boldsymbol{\sigma}_0 + \boldsymbol{\sigma}_0\,\underline{\otimes}\,\mathbf{I} +$$
$$+ 4J_{e0}^{-1}\left[(\mathbf{F}_0 \otimes \mathbf{F}_0^\mathsf{T}) \bullet \circ \frac{\partial \mathbf{C}_e}{\partial \mathbf{C}} \bullet \circ \frac{\partial \mathbf{H}_e}{\partial \mathbf{C}_e} \bullet \circ \left(\frac{\partial^2 \psi_e}{\partial \mathbf{H}_e \partial \mathbf{H}_e}\Big|_{\mathbf{H}_{e0}} \right) \bullet \circ \frac{\partial \mathbf{H}_e}{\partial \mathbf{C}_e} \bullet \circ \frac{\partial \mathbf{C}_e}{\partial \mathbf{C}} \bullet \circ (\mathbf{F}_0^\mathsf{T} \otimes \mathbf{F}_0) \right]$$
$$\qquad (5.89)$$

in which the following tensor derivatives have been introduced:

---

[4] For the sake of clarity, full the following second-order tensors representation has been employed: $\mathbf{X} = \{X_{11}, X_{12}, X_{13}, X_{21}, X_{22}, X_{23}, X_{31}, X_{32}, X_{33}\}$; the Voigt notation reduced to $\mathbf{X}_V = \{X_{11}, X_{22}, X_{33}, X_{23}, X_{13}, X_{12}\}$

$$\frac{\partial \mathbf{C}_e}{\partial \mathbf{C}} = \mathbf{F}_g^{-\mathsf{T}} \otimes \mathbf{F}_g^{-1} \tag{5.90}$$

$$\frac{\partial \mathbf{H}_e}{\partial \mathbf{C}_e} = \sum_{i=1}^{3} \frac{1}{2\lambda_{ei}^2} \mathbf{M}_i \otimes \mathbf{M}_i + \sum_{\substack{i,j=1 \\ i \neq j}}^{3} \frac{\ln(\frac{\lambda_{ei}}{\lambda_{ej}})}{\lambda_{ei}^2 - \lambda_{ej}^2} \mathbf{M}_i \otimes \mathbf{M}_j, \tag{5.91}$$

with the second order tensors $\mathbf{M}_i$, $i = \{1, 2, 3\}$ being defined through the eigenvectors $\mathbf{n}_i$ of the configuration at time t (defined in Section 5.4.3), in a way that $\mathbf{M}_i\mathbf{M}_j = \delta_{ij}\mathbf{M}_i$ and $\sum_{i=1}^{3}\mathbf{M}_i = \mathbf{I}$. Therefore, by referring to the spherically symmetric problem described, and adopting the specific constitutive relation (5.40), at each time t a deformation $\mathbf{F}_{e0} = \text{Diag}\{\lambda_{er0}, \lambda_{e\theta0}, \lambda_{e\phi0}\}$ and stress state $\boldsymbol{\sigma}_0 = \text{Diag}\{\sigma_{r0}, \sigma_{\theta0}, \sigma_{\phi0}\}$ can be identified, in which $\lambda_{e\phi0} = \lambda_{e\theta0}$ and $\sigma_{\phi0} = \sigma_{\theta0}$, respectively. The resulting tangent stiffness matrix exhibits transverse isotropy and its independent elastic constants have the following expressions:

$$C_{11} = C^*_{rrrr} =$$
$$= \frac{1}{\lambda_{e\theta0}^2 \lambda_{er0}} \left(a_1 + a_2 + c\, e^Q \left(\frac{1}{4} \left(2b_2 \log \lambda_{e\theta0}^2 + (b_1 + b_2) \log \lambda_{er0}^2 \right)^2 + b_1 + b_2 \right) \right) + 2\sigma_{r0}, \tag{5.92}$$

$$C_{22} = C^*_{\theta\theta\theta\theta} =$$
$$= \frac{1}{\lambda_{e\theta0}^2 \lambda_{er0}} \left(a_1 + a_2 + c e^Q \left(\frac{1}{4} \left((b_1 + 2b_2) \log \lambda_{e\theta0}^2 + b_2 \log \lambda_{er0}^2 \right)^2 + b_1 + b_2 \right) \right) + 2\sigma_{\theta0}, \tag{5.93}$$

$$C_{12} = C^*_{rr\theta\theta} =$$
$$= \frac{4 \left(a_2 + c\, e^Q \left(\frac{1}{4} \left(2b_2 \log \lambda_{e\theta0}^2 + (b_1 + b_2) \log \lambda_{er0}^2 \right) \left((b_1 + 2b_2) \log \lambda_{e\theta0}^2 + b_2 \log \lambda_{er0}^2 \right) + b_2 \right) \right)}{\lambda_{er0}^{-1} (\log^2 \lambda_{er0} - \log^2 \lambda_{e\theta0})^{-1} \left(\lambda_{er0}^2 - \lambda_{e\theta0}^2 \right)^2}, \tag{5.94}$$

$$C_{23} = C^*_{\theta\theta\phi\phi} =$$
$$= \frac{\lambda_{er0}}{\lambda_{e\theta0}^2} \left(a_2 + c\, e^Q \left(\frac{1}{4} \left((b_1 + 2b_2) \log \lambda_{e\theta0}^2 + b_2 \log \lambda_{er0}^2 \right)^2 + b_2 \right) \right), \tag{5.95}$$

$$C_{66} = C^*_{r\theta r\theta} =$$
$$= \frac{\lambda_{er0} \left(a_1 + b_1 c\, e^Q \right) \log^2 \frac{\lambda_{er0}}{\lambda_{e\theta0}}}{\left(\lambda_{er0}^2 - \lambda_{e\theta0}^2 \right)^2} + \frac{a_1 + b_1 c\, e^Q}{4\lambda_{er0}^3} + \frac{1}{2} \left(\sigma_{\theta0} + \sigma_{r0} \right) \tag{5.96}$$

where $Q = b_1 tr(\mathbf{H}_e^2) + b_2(tr(\mathbf{H}_e))^2$, while transverse isotropy further implies that $C^*_{r\phi r\phi} = C^*_{r\theta r\theta}$, $C^*_{rr\phi\phi} = C^*_{rr\theta\theta}$ and $C^*_{\theta\phi\theta\phi} = (C^*_{\theta\theta\theta\theta} - C^*_{\theta\theta\phi\phi})/2$.

It is worth noting that, as a consequence of both the assumed spherically symmetry of the problem at hand and of isotropic growth hypothesis, the obtained transverse isotropy implies that the five elastic contants (5.92)–(5.96) result to be dependent upon five unknown function, i.e. $C_{\alpha\beta} = \mathcal{C}_{\alpha\beta} \left(\sigma_r, \sigma_\theta, \lambda_r, \lambda_\theta, \lambda_g \right)$. Therefore, in principle, the possibility of measuring the entire set of elastic constants (with respect to a previous measure) might permit to locally find a numerical solutions of a closed non linear system, in order to then find stresses and deformations.

With focus on the present application, the distribution of elastic constants within the tumor at different times and accounting for growth, residual stress and deformations, is shown in Fig. 64.

In particular, one can observe from Fig. 64 the $C_{\alpha\beta}$, $\alpha, \beta = \{1, 2, 3\}$ decrease with volume (see also Fig. 65), this being in accord with theoretical evidences demonstrating that resident residual stress can make the body more compliant [104]. Also, one
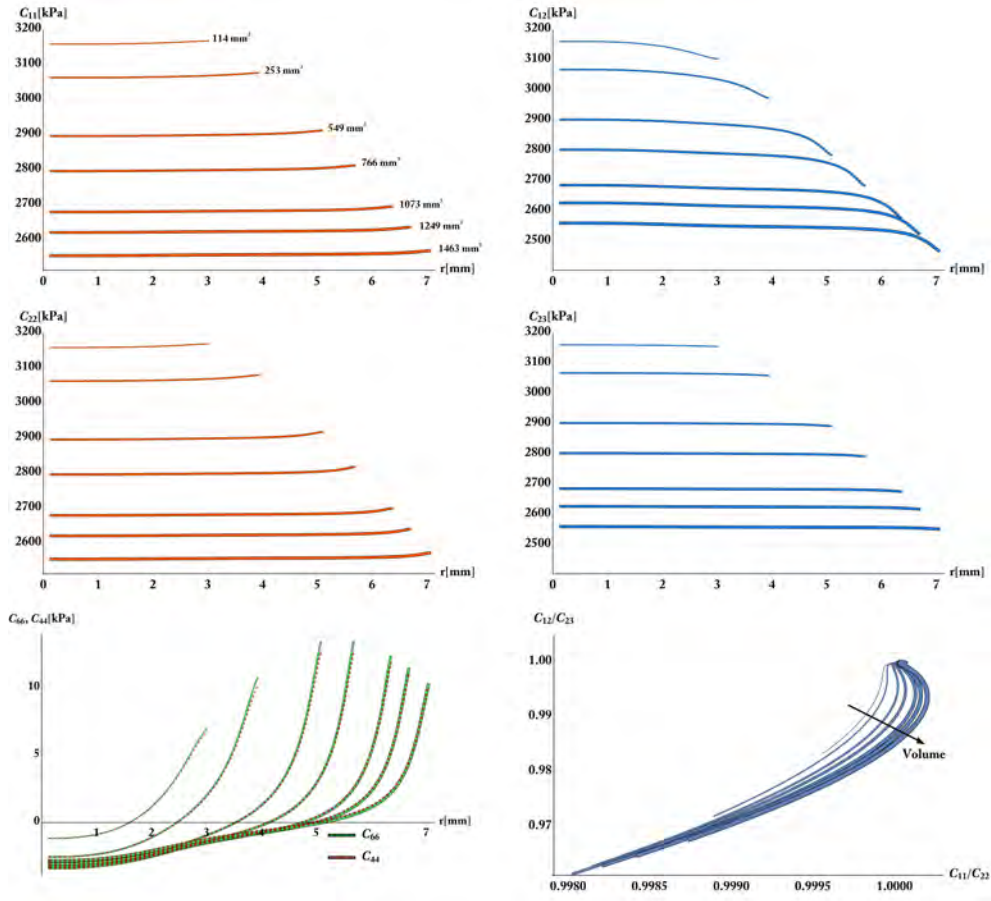
Figure 64: Tangent elastic constants in the MCTSs at different volume size

might hypothesize that this can be considered an overall integration effect –at the tissue scale– of the experimental evidences –at the single-cell scale– according to which cancer cells are more deformable than healthy cells, see e.g. Fraldi et al. [64].

Also, Fig. 64 shows how the tissue actually results a weakly transversely isotropic material. Also, from a quantitative point of view, two main considerations emerge. Perhaps the most evident not ordinary aspect is that radially varying tangent shear moduli exhibit a negative part. This, combined with both weak anisotropy (or, as a matter of fact, an almost isotropic behavior) and a substantial incompressibility (the Poisson's ratios approach 0.5 almost everywhere, especially towards the tumor center), tells us that all the growing tumor inhomogeneous spheroids would exhibit an internal core with negative tangent elastic moduli –thus inherently unstable– and an external ordinary phase (which is stable). Negative stiffness can occur, for example, when deforming a body that stored (or received) energy [119], and so, also in case of the presence of residual stress. However, this unexpected result does not represent a theoretical issue, since the global stability of elastic composites with this particular configuration has been theoretically provided by the works by Drugan and Lakes (see e.g. [57, 114, 120]). Residually stressed tumors seem to replicate this feature, and this
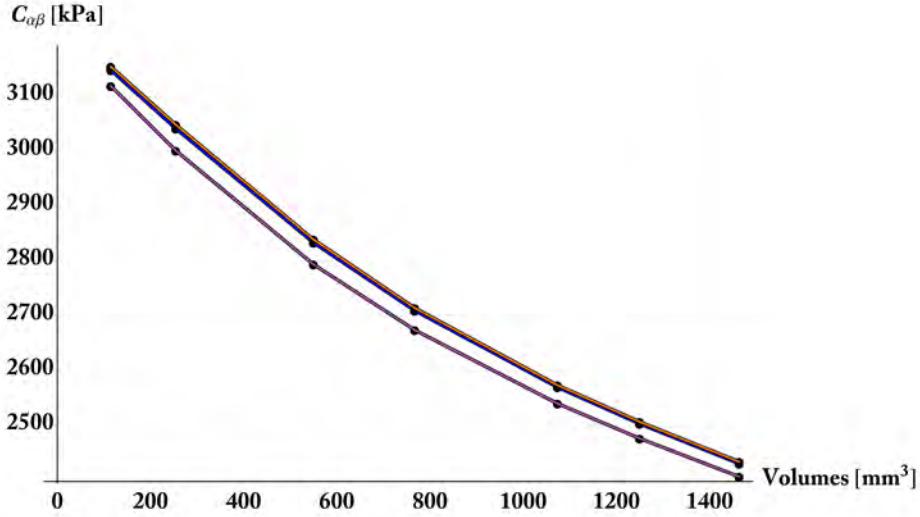
Figure 65: Tangent elastic constants of the superior block as a function of the volume size

tissue softening effect still being in accord with the microscopic cancer cells more compliant structure, in the sense that to further grow and deform under residual compression, tissue locally behaves by intensifying its compliance, and by exhibiting fluid-like behavior.

Another observation to take into account is that the bulk constants are quantitatively very similar each other due to combined weak anisotropy and substantial incompressibility, and this could generate problems in the in-progress finite element procedure (for example, numerical instabilities might occur, the matrix becoming singular). However, the mechanical response of the MCTS due to bulk growth –evaluated by performing a compression test like that one under discussion– mainly involves the volumetric part of the stored energy density, and the respective tangent modulus will be affected by the latter aliquota, rather than the shear tangent response which is minimally implicated. For these reasons, the elastic modulus of interest has been calculated by inverting the superior third-order minor of the tangent stiffness matrix and considering the first compliance constant, i.e. $E = [\mathsf{S}]_{11}^{-1}, \quad \mathsf{S} = \mathbb{C}_{3\times3}^{-1}$, and then passed to the FE model. As seen from Fig. 66, despite the weak anisotropy, the contribution of the volumetric deformation energy makes stiffens the radial response of the material.

As a first implementation, to avoid possible problems related to the presence of the (limited) core with negative Young modulus, the internal core has been in principle substituted by an internal incompressible phase with sufficiently low Young modulus (approaching that one of the first layer with positive modulus).

5.5.2 *Finite Element modeling*

Finite Element simulations have been developed with the aim to evaluate the mechanical response of the MCTS subjected to uniaxial compression, by essentially investigating the influence that growth, deformation and residual stress can have in
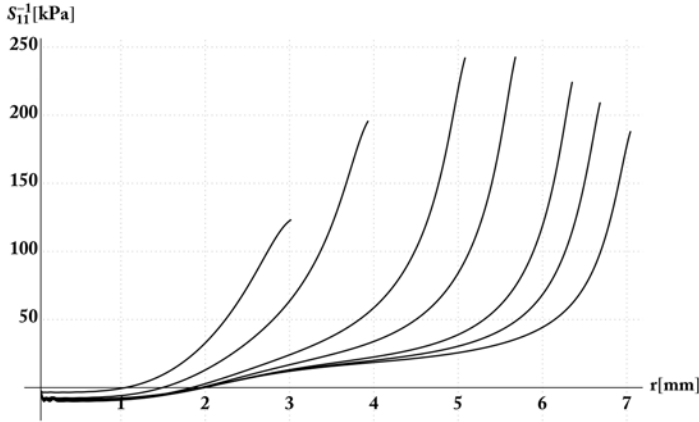
Figure 66: Tangent Young moduli obtained from the compliance matrix at different tumor dimensions.

determining the effective elastic behavior of the material, given in terms of tangent properties. Hence numerical models have been considered, each one being representative (in size and internal elastic properties) of an explanted MTCS according to the experimental protocol summarized in table Table 4. Each numerical simulation aims to reproduce the experimental mechanical compression test performed on *ex vivo* spheroidal tumors. The simulation has been conducted with the aid of the commercial FEM-based code Ansys® ([1]). Since the soft tissue samples under exam exhibit high deformability properties, to simulate the compression action of a rigid plate on them particular attention is required in modeling the dynamics of the contact. This implies the introduction of both geometrical and body contacts-related nonlinearities. For this purpose, an *ad hoc* custom made Ansys procedure, written in APDL parametric language, has been developed to reconstruct all FE models.

In order to reduce the computational efforts and gain advantage in performing several nonlinear analyses, only one-eighth of the sphere has been considered, taking into account the appropriate symmetric boundary conditions (see Fig. 67-left). As already said, to practically avoid numerical instabilities, a spherical cavity has been provided at the center of each sphere and negative YM cores have been replaced by an elastic phase with an high incompressibility and very low stiffness (see Fig. 67-right). By referring to the animal model measurements (see Table 4) and simulated sizes, different spherical geometries have been generated by considering the experimentally-derived external radii and maintaining the same central void (Fig. 67-bottom).

The geometrical models of both rigid plate and hollow sphere have been meshed by means of about 10.000 standard hexahedral elements - SOLID185 - and almost 11.500 nodes with three degrees of freedom for each node, while, to simulate the non linear contact, the external spherical cap and the bottom surface of the plate have been meshed with contact-target elements (CONTA170 TARGE175 respectively). Efforts have been devoted to characterize the tangent stiffness of each numerical simulation of spheroid compression, in which isotropic elastic properties take into account the resident residual stress. Each spherical model has been divided into a wider external spherical region, in which the Young modulus varies radially according to the
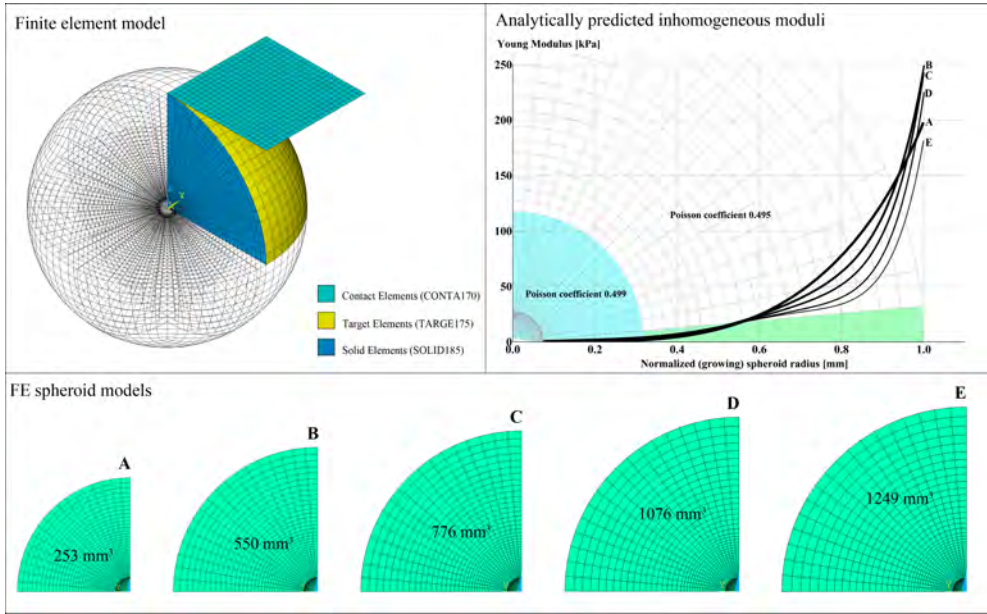
Figure 67: (Top-left) Representation of the FEM modeled uniaxial test. (Top-right) Schematic representation of the assignment of radially varying material properties to the sphere elements. (Down) Considered volumes.

analytically defined law and the Poisson's ratio is equal to $\nu = 0.495$, and a limited central core in which the Young modulus was assumed constant and equal to the lower modulus of the communicating previous zone, with and a more incompressible characteristic, say $\nu = 0.499$ (see Fig. 67-right). Each analysis simulates a compression along z-axes, and was realized by imposing a displacement to the plate of about one-tenth of the external radius of the sphere. A displacements sequence of the compression simulation is reported in the Fig. 68, in which it is also possible to appreciate the effect of the contact confinement and the resultant reactive stress state developing the spheroid at various deformations.

For each numerical substep the reaction force F_z has been evaluated and, together with the computed deformation ϵ_z, a force-deformation curve for each spheroid has been obtained. Finally, these numerical results have been put in direct comparison with the experimental dataset, finding a good agreement between them as reported in Fig. 69. This agreement is more evident in terms of tangent moduli, as highlighted in Fig. 70. Actually, the good agreement between experimental results and the coupled analytic/Finite element strategy let to consider this procedure a reliable and less invasive technique to investigate the nature of residual stress and stored energy within tumor masses in a way to preserve their integrity, as well as to convincingly validate the results given by the hyperelastic/VL model also in terms of predicted mechanical features.
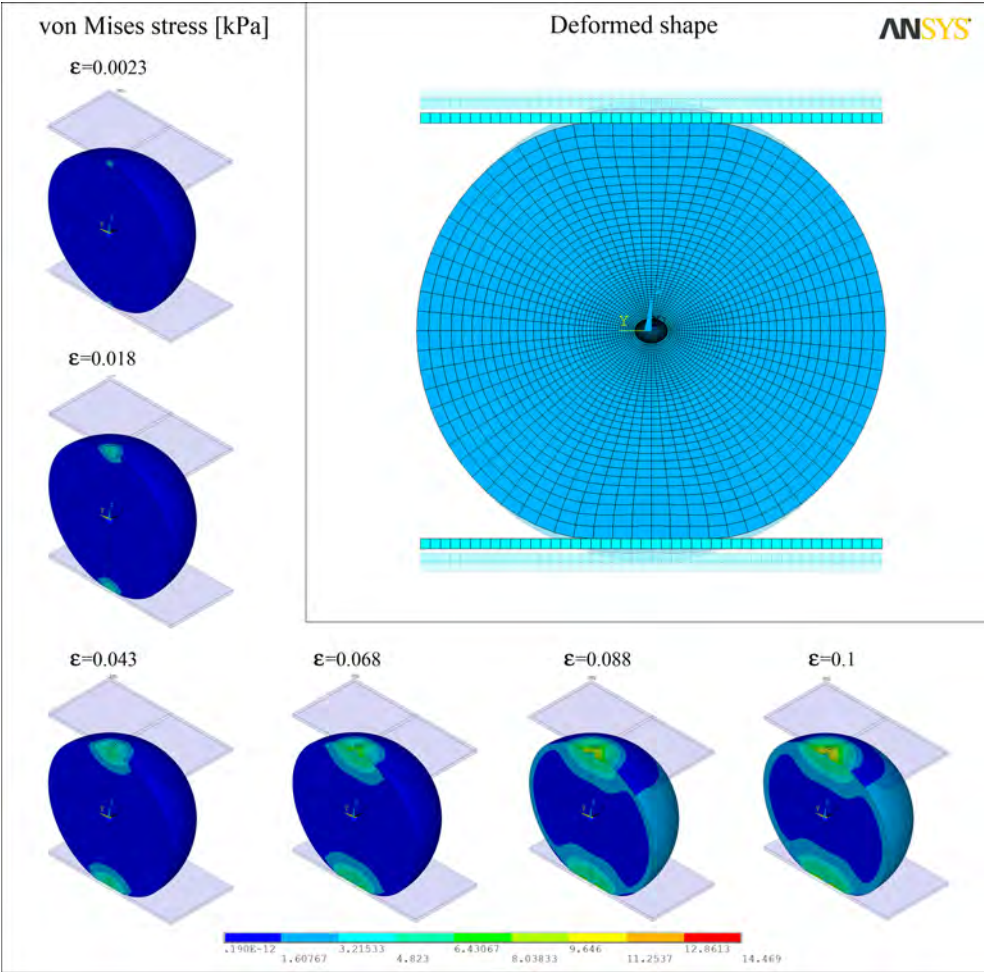
Figure 68: (Top-left) Representation of the FEM modeled uniaxial test. (Top-right) Schematic representation of the assignment of radially varying material properties to the sphere elements. (Down) Considered volumes.
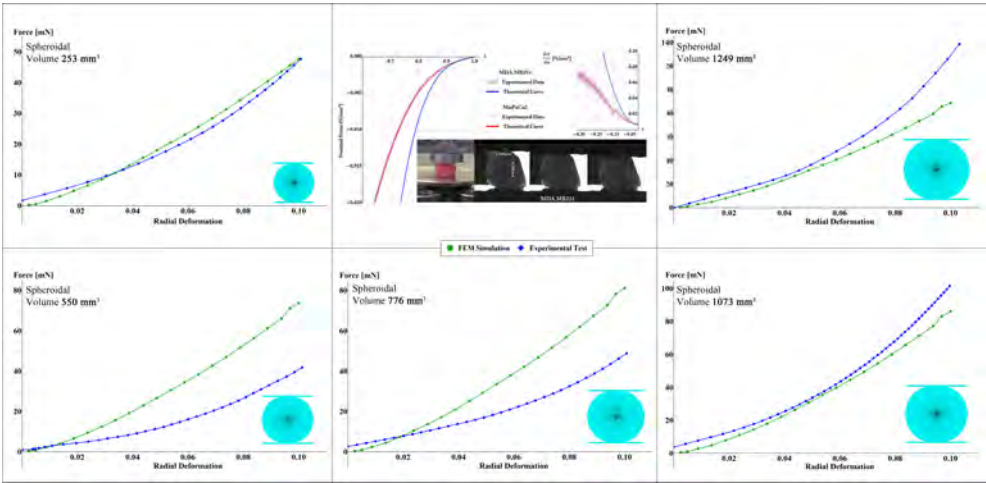
Figure 69: Experimental (blue points) and numerically obtained (green points) force-deformation curves in direct comparison for each MCTS. (Middle) fitting of two experimental dataset with the hyperelastic law adopted in the analytical model
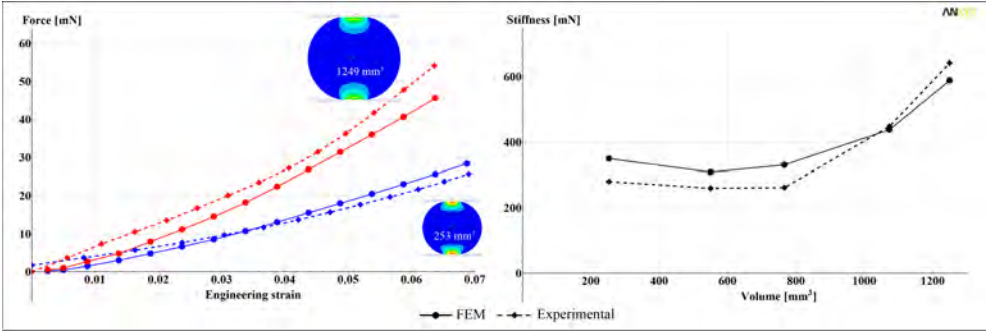
Figure 70: Experimental (dashed line) and numerically obtained (continuous line) development of the tangent moduli as a function of the tumor sizes.

APPENDIX A

Mathematical Details for the derivation of the Strain Energy Density and of the solid stress:

The total mechanical energy can be defined from the referential volumetric energy density ψ_0 as well as from the volumetric energy density ψ, respectively related to the configurations $\mathcal{B}^0$ and $\mathcal{B}^g$ and connected each other by (also provided by Ganghoffer, [72]):

$$\int_{V^0} \psi_0(\mathring{\mathbf{H}}_e, \rho_F) dV^0 = \int_{V^g} \psi\left(\mathbf{H}_e, \rho_F\right) dV^g = \int_{V^0} J_g \psi\left(\mathbf{H}_e, \rho_F\right) dV^0 \tag{A.1}$$

the relationship $\psi_0 = J_g \psi$ being useful in the following. Apart from the elastic strain, both of them are supposed to depend explicitly also on the fluid content $\rho_F = J_{\varrho F} \phi_F$ as discussed in section 5.4.6. By neglecting thermal terms contributions, the dissipation inequality can be written as ([7]):

$$\int_V \boldsymbol{\sigma} : \mathbf{D}\, dV - \int_{\partial V} \mu\, \mathbf{q}_F \cdot \mathbf{n}\, dS \geq \frac{d}{dt} \int_{V^0} J_g \psi\, dV^0 \tag{A.2}$$

which can be expressed by means of localization theorem as:

$$J\boldsymbol{\sigma}\left(\mathbf{x}\left(\mathbf{X}, t\right), t\right) : \mathbf{D} - \nabla_{\mathbf{X}} \cdot \left(\mu\, \mathbf{Q}_F\right) \geq \frac{d\, J_g \psi}{dt} \tag{A.3}$$

where, in (A.2) and (A.3), μ denotes the fluid chemical potential and $\mathbf{Q}_F = J\mathbf{q}_F\mathbf{F}^{-\mathsf{T}}$ is the referential flux vector, while the tensor $\mathbf{D} = \operatorname{sym}(\dot{\mathbf{F}}\mathbf{F}^{-1})$ is the symmetrical velocity gradient. The fluid conservation equation $(5.47)_1$ returns the relation:

$$\frac{d\rho_F}{dt} + \nabla_{\mathbf{X}} \cdot \mathbf{Q}_F = J\Gamma_F \tag{A.4}$$

so that a simple manipulation of (A.3) by also accounting (A.4) gives:

$$\mathbf{P} : \dot{\mathbf{F}} - \mathbf{Q}_F \cdot \nabla_{\mathbf{X}}\mu - \mu J \Gamma_F + \mu\, \dot{\rho}_F \geq \psi \dot{J}_g + J_g \frac{\partial \psi}{\partial \mathbf{H}_e} : \dot{\mathbf{H}}_e + J_g \frac{\partial \psi}{\partial \rho_F} \dot{\rho}_F \tag{A.5}$$

where the symmetry of the Cauchy stress tensor and the identity $J\boldsymbol{\sigma} : \mathbf{D} = J\boldsymbol{\sigma} : \mathbf{L}$ have been used, this giving $J\boldsymbol{\sigma}\mathbf{F}^{-\mathsf{T}} : \dot{\mathbf{F}} = \mathbf{P} : \dot{\mathbf{F}}$. Terms in equation (A.5) can be reorganized keeping in mind the multiplicative decomposition of the deformation gradient (5.20) and by applying the Jacobi formula and the chain rule respectively on the first term and the second term of the right side, in this way having:

$$\left(\mathbf{P}\,\mathbf{F}_g^{\mathsf{T}} - J_g\mathbf{F}_e^{-\mathsf{T}} \frac{\partial \psi}{\partial \mathbf{H}_e}\right) : \dot{\mathbf{F}}_e + \left(\mu - J_g \frac{\partial \psi}{\partial \rho_F}\right) \dot{\rho}_F + \left(\mathbf{F}_e^{\mathsf{T}}\mathbf{P} - J_g\psi\mathbf{F}_g^{-\mathsf{T}}\right) : \dot{\mathbf{F}}_g +$$
$$- \mathbf{Q}_F \cdot \nabla_{\mathbf{X}}\mu - J\mu\Gamma_F \geq 0 \tag{A.6}$$

From which it is immediately obtained through the standard application of the Coleman's method ([44]) on the first two brackets that:

$$\mathbf{P} = J_g \mathbf{F}_e^{-\mathsf{T}} \frac{\partial \psi}{\partial \mathbf{H}_e} \mathbf{F}_g^{-\mathsf{T}} = \mathbf{F}_e^{-\mathsf{T}} \frac{\partial \psi_0}{\partial \overset{\circ}{\mathbf{H}}_e} \mathbf{F}_g^{-\mathsf{T}} \tag{A.7}$$

and

$$\mu = J_g \frac{\partial \psi}{\partial \rho_F} = \frac{\partial \psi_0}{\partial \rho_F} \tag{A.8}$$

in which it is assumed that the growth deformation term associated with the solid species does not depend explicitly on the elastic deformation and the fluid content. In addition, the respect of the dissipation inequality (A.7) is fulfilled by adopting for the fluid flux and the fluid source term structures of the type $\mathbf{Q}_F = -\mathbf{k}_0 \nabla_{\mathbf{X}} \mu$, with $\mathbf{k}_0$ being a positive definite permeability tensor, and Γ_F proportional to $-\mu$ through a positive conductivity parameter, which in the case of an incompressible fluid can be represented for instance by Darcy law and Starling equation respectively, given by the equations $(5.47)_2$ encountered in section 5.4.6. The last remaining term in equation (A.7) is actually connected to the dissipation processes due to growth, the Eshelby-like stress $\mathbf{\Sigma} = \mathbf{F}_e^{\mathsf{T}} \partial \psi_0 / \partial \mathbf{F}_e - \psi_0 \mathbf{I}$ being related to the material (configurational) forces arising because of the domain changes (see e.g. [7, 72, 149]) and conjugated to $\mathbf{L}_g = \dot{\mathbf{F}}_g \mathbf{F}_g^{-1}$.

The potential ψ_0 has to be made explicit then also in the light of the poroelastic approach here adopted. In this context the Terzaghi decomposition is frequently used in order to express the stress in terms of the solid stress/deformation and interstitial fluid pressure, the validity of this uncoupling in finite strain regime having also been discussed in Literature (see e.g. the work [29]). This (partial) change of arguments can be perceived by introducing a strain energy density which is dual to that one introduced in equation (A.1), by means of a Legendre transform, performed in what follows on the referential energy for the sake of clarity. Additionally, a general decomposition for the latter is introduced, in a way that the potential ψ_0, connected with the skeleton response, can be intuitively derived from the effective response of the material (described by the hyperelastic law proposed in section 5.4.5) by subtracting a second potential taking into account the sole fluid response. Hence:

$$\psi_0 = \psi_{Hyp,0}(\overset{\circ}{\mathbf{H}}_e) - \psi_{F,0}(\overset{\circ}{\mathbf{H}}_e, \rho_F) \tag{A.9}$$

Hence, a variation of ψ_0 gives:

$$d\psi_0 = \frac{\partial \psi_0}{\partial \overset{\circ}{\mathbf{H}}_e} : d\overset{\circ}{\mathbf{H}}_e + \frac{\partial \psi_0}{\partial \rho_F} d\rho_F = \overset{\circ}{\boldsymbol{\tau}}_e : d\overset{\circ}{\mathbf{H}}_e + \mu \, d\rho_F \tag{A.10}$$

so that by subtracting the variation $d(\mu \, \rho_F) = \mu \, d\rho_F + \rho_F \, d\mu$ one obtains:

$$d\psi_0^* = \overset{\circ}{\boldsymbol{\tau}}_e : d\overset{\circ}{\mathbf{H}}_e - \rho_F \, d\mu \tag{A.11}$$

with $\partial \psi_0 / \partial \overset{\circ}{\mathbf{H}}_e = \partial \psi_0^* / \partial \overset{\circ}{\mathbf{H}}_e$ and

$$\psi_0^*(\overset{\circ}{\mathbf{H}}_e, \mu) = \psi_{Hyp,0}(\overset{\circ}{\mathbf{H}}_e) - \psi_{F,0}^*(\overset{\circ}{\mathbf{H}}_e, \mu) = \psi_0 - \mu \, \rho_F \tag{A.12}$$

Furthermore, a constitutive relationship for the fluid content is derived since:

$$\rho_F = -\frac{\partial \psi_0^*}{\partial \mu} = \frac{\partial \psi_{F,0}^*}{\partial \mu} \tag{A.13}$$

The latter also implying that:

$$d\rho_F = -\frac{\partial}{\partial \mu}(d\psi_0^*) = -\frac{\partial \overset{\circ}{\boldsymbol{\tau}}_e}{\partial \mu} : d\overset{\circ}{\mathbf{H}}_e + \frac{\partial \rho_F}{\partial \mu} d\mu = J\varrho_F\,\boldsymbol{\alpha} : d\overset{\circ}{\mathbf{H}}_e + J\varrho_F^2\, C^{eff} d\mu \tag{A.14}$$

in which the positions $\partial\overset{\circ}{\boldsymbol{\tau}}_e/\partial\mu = \partial^2\psi_0^*/\partial\mu\partial\overset{\circ}{\mathbf{H}}_e = -J\varrho_F\boldsymbol{\alpha}$ and $\partial\rho_F/\partial\mu = -\partial^2\psi_0^*/\partial\mu^2 = J\varrho_F^2 C^{eff}$ have been introduced. The coefficients $\boldsymbol{\alpha}$ and C^{eff} are denoted respectively as Biot effective stress tensor and Biot effective compressibility modulus, multiplied by the Jacobian J in order to take into account their material expression. As known, their physical meaning have been largely elucidated in the poroelasticity Literature (see e.g. the pioneering work by [23] as well as other more recent works such as [45]. By further considering an incompressible fluid (i.e. by considering ϱ_F constant and an elevated fluid bulk modulus) and by assuming isotropy, equation (A.14) reduces to the constitutive relationship (5.45):

$$d\left(J\phi_F\right) = J\left(\alpha dh_e + M^{-1} dp\right) \tag{A.15}$$

where the fluid chemical potential definition $\mu = \mu_0 + \varrho_F^{-1}\left(p - p_0\right)$ has been implied. The relationships (A.14) and (A.15) can be further simplified by considering moderate variations of the fluid, in a way to write:

$$\rho_F = \rho_F^0 + J\varrho_F\boldsymbol{\alpha} : \overset{\circ}{\mathbf{H}}_e + J\varrho_F^2 M^{-1}\left(\mu - \mu_0\right) \tag{A.16}$$

or

$$J\phi_F = \phi_F^0 + J\alpha\, h_e + JM^{-1}\left(p - p_0\right) \tag{A.17}$$

being $\rho_F^0 = \varrho_F\phi_F^0$. As a consequence, by considering (A.16) and (A.13), a direct integration returns that:

$$\psi_{F,0}^*(\overset{\circ}{\mathbf{H}}_e, \mu) = \rho_F^0\left(\mu - \mu_0\right) + J\varrho_F\left(\mu - \mu_0\right)\boldsymbol{\alpha} : \overset{\circ}{\mathbf{H}}_e + J\frac{\varrho_F^2}{2M}\left(\mu - \mu_0\right)^2 \tag{A.18}$$

so that the poroelastic uncoupled potential can be derived from (A.12) as:

$$\psi_0^*(\overset{\circ}{\mathbf{H}}_e, \mu) = \psi_{Hyp,0}(\overset{\circ}{\mathbf{H}}_e) - \rho_F^0\left(\mu - \mu_0\right) - J\varrho_F\left(\mu - \mu_0\right)\boldsymbol{\alpha} : \overset{\circ}{\mathbf{H}}_e +$$
$$- J\frac{\varrho_F^2}{2M}\left(\mu - \mu_0\right)^2 \tag{A.19}$$

from which, accounting also (A.1), it follows that the Kirchhoff stress can be also given by the Terzaghi decomposition:

$$\overset{\circ}{\boldsymbol{\tau}}_e = J_g\frac{\partial\psi_{Hyp}}{\partial\mathbf{H}_e} - J\varrho_F\left(\mu - \mu_0\right)\boldsymbol{\alpha} \tag{A.20}$$

and, consequentially, the first Piola-Kirchhoff elastic stress is written, also provided isotropy and fluid incompressibility, according to (A.7):

$$\mathbf{P} = \mathbf{F}_e^{-\mathsf{T}} \overset{\circ}{\boldsymbol{\tau}}_e \mathbf{F}_g^{-\mathsf{T}} = J_g \mathbf{F}_e^{-\mathsf{T}} \frac{\partial \psi_{Hyp}}{\partial \mathbf{H}_e} \mathbf{F}_g^{-\mathsf{T}} - J\alpha \left(p - p_0 \right) \mathbf{F}^{-\mathsf{T}} \qquad (\text{A.21})$$

APPENDIX B

Thermodynamic forces associated to the linear growth model:

The theoretical model introduced in the previous sections combines the classical poroelastic field equations with linear growth through the direct (full) coupling with a suitable dynamical system –whose motion follows the Volterra-Lotka logic– in order to express the inelastic deformation due to volumetric growth as a result of the net interaction of the biological solid species. It could pairwise interesting for this reason to make some thermodynamic considerations in order to derive from a dissipation principle both the constitutive assumptions and determine an expression for the thermodynamic forces the model conjugated to state variables, as well as the conditions which ensure both the global stability and the thermodynamic consistence of the system in a linear theoretical framework. The latter can be seen as a multi-component system, in which the solid constituents are denoted by a subscript $i \in \mathcal{S}$, while the fluid one is indicated by the subscript $i = F$. However, the high water content in the so-called solid species let to assume a constant true density – say ϱ– for each constituent, so that the total density of the system remains unchanged:

$$\rho = \rho_S + \rho_F = \sum_{i \in \mathcal{S}} \varrho\, \phi_i + \varrho\phi_F = \varrho \qquad (\text{B.1})$$

since the sum of all the volumetric fractions gives unity (in what follows, the subscript i will exclusively refer to the solid constituents and the hypothesis of constant density will be hold true). Also, growth, which is described as an inelastic process, inevitably implies the presence of a dissipation. For this reason, the free energy density ψ is here expressed as the sum of a reversible energy aliquota, which is linked to the purely (poro)elastic contribution, and a dissipative term, which is instead function of the solid growing species , in a way to write:

$$\psi = \psi_e \left(\mathbf{E}_e, \phi_F \right) + \psi_g \left(\phi_i \right) \qquad (\text{B.2})$$

In particular, under the hypothesis of an isothermal process, the balance of energy can be made explicit by introducing a specific and metabolic energy contribution, say ϵ_g which is directly responsible of the growth process g. Hence, the first principle explicitly reads:

$$\int_{\mathcal{V}} \rho \, \frac{dU}{dt} \, dv = \int_{\mathcal{V}} \boldsymbol{\sigma} : \mathbf{D} \, dv + \int_{\mathcal{V}} \varepsilon_g \, \dot{g} \, dv \qquad (\text{B.3})$$

U and $\mathcal{V}$ being the internal energy per unit mass and the volume measure, respectively. Also, $\mathbf{v}$ is the velocity vector and $\mathbf{D} = sym(\mathbf{v} \otimes \nabla)$ is the symmetrical velocity gradient. Analogously, the second principle can be instead expressed by introducing a thermodynamic force f_g conjugated to the rate $\dot{g}$ –representing a volumetric rate of

entropy supply– and a conductive rate of entropy supply due to the fluid flux vector, in a way to have:

$$\int_{\mathcal{V}} \frac{dS}{dt} \rho \, dv \geq \int_{\mathcal{V}} f_g \, \dot{g} \, dv + \int_{\partial \mathcal{V}} \mu_F \, \mathbf{q}_F \cdot d\mathbf{A} \tag{B.4}$$

By subtracting equation (B.4) from (B.3), and identifying the free energy per unit volume defined in (B.2) as $\psi = \rho(U - S)$, the dissipation inequality can be readily obtained:

$$\int_{\mathcal{V}} \boldsymbol{\sigma} : \mathbf{D} \, dv - \int_{\partial \mathcal{V}} \mu_F \, \mathbf{q}_F \cdot d\mathbf{A} + \int_{\mathcal{V}} \varepsilon_g \, \dot{g} \, dv - \int_{\mathcal{V}} f_g \, \dot{g} \, dv \geq \frac{d}{dt} \int_{\mathcal{V}} \psi \, dv \tag{B.5}$$

where $\mu_F = \rho_F^{-1}(p - p_0)$ is the fluid chemical potential. To further express the former equation in a local form, the Gauss theorem is applied on the second member of the left side of (B.5), while the chain rule on the right side, with ψ given by (B.2). It results:

$$\boldsymbol{\sigma} : \mathbf{D} - \nabla \mu_F \cdot \mathbf{q}_F - \mu_F \, \nabla \cdot \mathbf{q}_F + \varepsilon_g \, \dot{g} - f_g \, \dot{g} \geq \frac{\partial \psi_e}{\partial \mathbf{E}_e} : \dot{\mathbf{E}}_e + \frac{\partial \psi_e}{\partial \phi_F} \, \dot{\phi}_F + \sum_i \frac{\partial \psi_g}{\partial \phi_i} \, \dot{\phi}_i \tag{B.6}$$

The terms in equation (B.6) can be then collected by invoking both the strain additive decomposition of the deformations under isotropy, i.e. $\mathbf{E} = \mathbf{E}_e + (g/3)\mathbf{I}$, and the fluid continuity equation (5.5):

$$\left(\boldsymbol{\sigma} - \frac{\partial \psi_e}{\partial \mathbf{E}_e} \right) : \dot{\mathbf{E}}_e + \left(p - p_0 - \frac{\partial \psi_e}{\partial \phi_F} \right) \dot{\phi}_F - \nabla \mu_F \cdot \mathbf{q}_F - (p - p_0)\Gamma_F +$$
$$+ \left(\sigma^{hyd} + \epsilon_g - f_g \right) \dot{g} - \nabla_{\boldsymbol{\phi}} \psi_g \cdot \dot{\boldsymbol{\phi}} \geq 0 \tag{B.7}$$

from which one gets the following constitutive assumptions for the ordinary poroelastic variables

$$\boldsymbol{\sigma} = \frac{\partial \psi_e}{\partial \mathbf{E}_e},$$
$$p = p_0 + \frac{\partial \psi_e}{\partial \phi_F} \tag{B.8}$$

In addition, relation (B.7) results satisfied by taking a Darcy type flux vector $\mathbf{q}_F = -\mathbf{K}\nabla \mu_F$ (with $\mathbf{K} > 0$) and by opportunely introducing a fluid source term such that $\Gamma_F \propto p_0 - p$ (which is expressed by the Starling law in (5.5)). In order to introduce explicit constitutive assumptions and obtain a suitable expression for the linear elastic potential as a function of the ordinary poroelastic variable –the strain tensor and the interstitial pressure, according to the most of the classical models ([46])– a Legendre transform is performed on ψ_e in a way to have a partially dual energy:

$$\psi_e^* (\mathbf{E}_e, p) = \psi_e (\mathbf{E}_e, \phi_F) - \phi_F(p - p_0) \tag{B.9}$$

By further considering its differential form and accounting $(B.8)_2$ one has the identity:

$$d\psi_e^* = \frac{\partial \psi_e}{\partial \mathbf{E}_e} : d\mathbf{E}_e - \phi_F\, dp = \frac{\partial \psi_e^*}{\partial \mathbf{E}_e} : d\mathbf{E}_e + \frac{\partial \psi_e^*}{\partial p}\, dp, \qquad (B.10)$$

from which

$$\frac{\partial \psi_e}{\partial \mathbf{E}_e} = \frac{\partial \psi_e^*}{\partial \mathbf{E}_e} \quad \text{and} \quad \phi_F = -\frac{\partial \psi_e^*}{\partial p} \qquad (B.11)$$

Equation $(B.11)_2$ together with $(B.9)$ then let to obtain the explicit constitutive relation $(5.4)_1$ for the fluid content by linearizing the incremental fluid fraction $d\phi_F$, thus having

$$\phi_F = \phi_{F0} + \mathbf{A} : \mathbf{E}_e + M^{-1}(p - p_0) \qquad (B.12)$$

in which $\mathbf{A} = -\partial^2 \psi_e^*/\partial \mathbf{E}_e \partial p$ and $M^{-1} = -\partial^2 \psi_e^*/\partial p^2$, and ϕ_{F0} being the initial fluid fraction at zero elastic strain and at the reference pressure p_0. Hence, the substitution of (**??**) into $(B.11)_2$ and a direct integration of with respect to p gives:

$$\psi_e^* = \hat{\psi}\left(\mathbf{E}_e\right) - \phi_{F0}(p - p_0) - (p - p_0)\mathbf{A} : \mathbf{E}_e - \frac{1}{2M}(p - p_0)^2 \qquad (B.13)$$

where the introduced energy density term $\hat{\psi}$ can be interpreted as the effective energy aliquota, the one connected to the displacement gradient. In a linear isotropic framework, this naturally coincides with the quadratic elastic St. Venant-Kirchhoff strain energy density, i.e.:

$$\hat{\psi} = \frac{1}{2}\,\mathbf{E}_e : \mathbb{C} : \mathbf{E}_e \qquad (B.14)$$

with $\mathbb{C} = \partial^2 \psi_e^*/\partial \mathbf{E}_e^2 = 2\mu\mathbb{I} + \lambda\mathbf{I} \odot \mathbf{I}$ being the isotropic fourth order stiffness tensor, in a way that, together with the relation $(B.8)_1$, the Terzaghi stress $(5.1)_3$ is immediately derivable.

Once dealt about the elastic potential, in the light of the specific constitutive assumptions that have been introduced, the reduced dissipation inequality $(B.7)$ reads:

$$\left(\sigma^{hyd} + \epsilon_g - f_g\right)\dot{g} - \nabla_{\boldsymbol{\phi}}\psi_g \cdot \dot{\boldsymbol{\phi}} \geq 0 \qquad (B.15)$$

These terms are clearly not independent, since the growth function g is related to the species vector by (5.14). However, they singularly carry different information for the system at hand and, for this reason, the conditions of their positivity is separately analyzed. The first term actually associates the growth volumetric strain to both mechanical and metabolic factors, from which one obtains that the thermodynamic driving force conjugated to the growth can be expressed as $f_g = \sigma^{hyd} + \epsilon_g$ (this can be seen as a linear expression of an Eshelbian stress previously discussed for the nonlinear case). This relation also qualitatively suggests that growth takes place in presence of available and adequate metabolic resources, in a way to sustain growth also in a stressed (e.g. compressed) environment, in which growth could be likely inhibited. The respect of $(B.15)$ would in fact imply that the lack of metabolites (nutrients), as well as the simultaneous presence of unfavorable compressive state of stress would

either arrest the growth or cause a resorption process, which is still in agreement with the sign of (B.15). Furthermore, this coupling term (less intuitive than the other ones) can be seen as an effective cross-talk between the purely mechanical part of the problem and the biological one, which focuses on the kinematic description of the growth, and in this sense also authorizes the possibility of establishing the "two-way" feedback mechanism already discussed. In particular, one can assume a direct influence of the mechanical stress on the growth, here modeled by introducing non-constant VL coefficients as above discussed, which have been explicitly built as a (positive) function of the hydrostatic stress in a way to enforce the mechanical inhibition of the proliferative potential of cell species in a compressed environment.

The last term in (B.15) deals instead with the condition $\dot{\psi}_g = \nabla_{\boldsymbol{\phi}} \psi_g \cdot \dot{\boldsymbol{\phi}} \leq 0$, which is strongly connected to the ecological stability of the species dynamics. In particular, the condition emerged represents the well-known Lyapunov stability criterion ([129]) which relates the stability of a certain stationary point of the ecosystem to the existence of a positive-definite Lyapunov function in the positive octant of the phase field, that vanishes at the equilibrium points and such that its time derivative is locally negative semidefinite in a neighborhood of the candidate attractor point(s). Inequality (B.15) then actually states a substantial equivalence between the thermodynamical and dynamical stability of the multi-species system, in the light of the fact that the entropy principle can be attributed to the study of the stability of the Lyapunov function of the generalized VL system at hand, a key parallel for the present application that has been also deeply investigated –without considering mechanical coupling– in the field of ecological modeling recent literature (see, for example, the work by Chakrabarti and Ghosh - [36]). For these reasons, compatibly with the Lyapunov stability theorem assessments, one can suppose that, in the neighborhood of an equilibrium point $\boldsymbol{\phi}^*$, the dissipation potential can assume the following expression:

$$\psi_g\left(\phi_i, \phi_i^*\right) = \sum_{i=\{T,H,M\}} \left(\phi_i - \phi_i^*\right) + \phi_i^* \ln\left(\frac{\phi_i^*}{\phi_i}\right),$$

$$\dot{\psi}_g = \sum_{i=\{T,H,M\}} \left(\phi_i - \phi_i^*\right) \Gamma_i \tag{B.16}$$

which is very similar to the Boltzmann entropy formula. In order to define a specific dissipation function for the species, the study of the stationary points is then required.

Equilibria

Then, with the aim to discuss the stability of the system (5.13) in a simpler way, it is here proposed of separating the first two poroelastic nonhomogeneous PDEs from the multispecies equations on the basis of their characteristic times. In fact, apart from the static momentum equation, the poroelastic equations are intrinsically governed by the speed of the elastic medium (that is proportional to $\sqrt{K/\varrho}$) and by the rise/decay times of the pressure $\tau_p^+ \approx (\kappa_v M)^{-1}$ and $\tau_p^- \approx (\kappa_l M)^{-1}$, that are of the order of the seconds/fraction of seconds. On the other hand, cells dynamics processes will adapt nearby their attractors presumably in a slower manner, because of both the greater biological intrinsic proliferation times –of the order of the day– and the VL mutual

interactions. In other words, by condensing the poroelastic field variables within the vector $\mathfrak{S} = \{u, p\}$, the dynamic-coupled differential equations (5.13) posed in the way

$$\begin{cases} L(\mathfrak{S}, \dot{\mathfrak{S}}) = \mathbf{\Pi}\,(\mathfrak{S}, \boldsymbol{\phi}) \\ \dot{\boldsymbol{\phi}} = \mathbf{\Gamma}\,(\mathfrak{S}, \boldsymbol{\phi}) \end{cases} \tag{B.17}$$

presents the fast variables $\mathfrak{S}$ and slow variables $\boldsymbol{\phi}$, since regardless of how time can be scaled, so that the relative rates will verify the condition $\| \dot{\mathfrak{S}} \|_\infty \gg \| \dot{\boldsymbol{\phi}} \|_\infty$. Hence, for rescaled times t' comparable with the rate of $\mathfrak{S}$, one can obtain a fast subsystem FS corresponding to

$$\begin{cases} L(\mathfrak{S}, \dot{\mathfrak{S}}) = \mathbf{\Pi}\,(\mathfrak{S}, \boldsymbol{\phi}; t') \\ \dot{\boldsymbol{\phi}} = 0 \end{cases} \tag{B.18}$$

and, for rescaled t'' compatible with the (slowest) characteristic time of the species, a slow subsystem SS is

$$\begin{cases} L(\mathfrak{S}, \dot{\mathfrak{S}}) = 0 \\ \dot{\boldsymbol{\phi}} = \mathbf{\Gamma}\,(\mathfrak{S}, \boldsymbol{\phi}; t'') \end{cases} \tag{B.19}$$

The dynamics of the original system can be explained in terms of the respective fast and slow subsystems. This procedure also validates the adoption of a decoupled potential in (B.2), with the functions ψ_e and ψ_g being independent of the species vector and of the poroelastic variables, respectively. Since $\boldsymbol{\phi}$ are fixed in the FS, the growth term is quasi static in time t', so that the problem would reduce to a classic poroelastic problem with a constant growth strain, whose stability is guaranteed the ellipticity of the poroelastic classical problem. At the slow time scales, the conditions (B.19) let to study the dynamics of the species, during longer time intervals, for fixed quantities $\mathfrak{S}$.

By following this way of reasoning, at sufficiently slow time scales t'' the state variables $\mathbf{E}_e$ and ϕ_F of the coupled potential (B.2) can be assumed to hold at a certain constant value, say $\{\overline{\mathbf{E}}_e, \overline{\phi}_F\}$ (or, equivalently, $\{\overline{\mathbf{E}}_e, \overline{p}\}$), in a way that condition (B.15) can be rewritten as:

$$\nabla_{\boldsymbol{\phi}} \psi_g \cdot \frac{\partial \boldsymbol{\phi}}{\partial t''}\big|_{(\overline{\mathbf{E}}_e, \overline{p})} \leq 0 \tag{B.20}$$

Thus, also by virtue of the theorem proposed by Tuljapurkar (see [193]), this condition is equivalent to study the local stability of the species motion around a given equilibrium point $\boldsymbol{\phi}^*$ in the phase space delimited by the tetrahedron $\mathfrak{I} = \{(\phi_T, \phi_H, \phi_M) \in \mathbb{R}^3_{\geq 0} : \phi_T + \phi_H + \phi_M < 1 - \overline{\zeta}(\overline{\mathbf{E}}_e, \overline{p})\}$. In addition, it is noticed that the localization of the entropy inequality naturally implies the study of the stability of the local species time trajectories, that is to say the requirement –at each point P of the open domain Ω– of the ordinary condition:

$$\begin{aligned} &\forall\, \epsilon > 0 \text{ and } \forall P \in \Omega \\ &\exists\, \delta(\epsilon) > 0 : \|\boldsymbol{\phi}|_{t''=0^+} - \boldsymbol{\phi}^*\| < \delta \ \rightarrow\ \|\boldsymbol{\phi}|_{t'' \geq 0^+} - \boldsymbol{\phi}^*\| < \epsilon \end{aligned} \tag{B.21}$$

Thus, considering the specific case of a radially symmetric problem, by introducing a non-dimensional variable $z = r/b - c\gamma_{T0}t''$, the focus is on the following non-dimensional subsystem:

$$
\begin{cases}
-c\frac{d\phi_T}{dz} = q\left(\overline{\mathbf{E}}_e, \overline{p}\right)\phi_T\left(1 - \alpha_{TT}\phi_T - \alpha_{TH}\phi_H - \alpha_{TM}\phi_M\right) \\[2mm]
-c\frac{d\phi_H}{dz} = q\left(\overline{\mathbf{E}}_e, \overline{p}\right)\tilde{\gamma}_{H0}\phi_H\left(1 - \alpha_{HT}\phi_T - \alpha_{HH}\phi_H - \alpha_{HM}\phi_M\right) \\[2mm]
-c\frac{d\phi_M}{dz} = \tilde{\beta}_T\phi_T + \tilde{\beta}_H\phi_H - \tilde{\delta}_M\phi_M\left(\alpha_{MT}\phi_T + \alpha_{MH}\phi_H\right)
\end{cases}
\tag{B.22}
$$

in which tilde denotes the initial rates divided by γ_{T0}, while the function $q > 0$ takes into account the influence of the (mechanical) coupling parameter, which are fixed at the slow time scales. The positivity of the latter can be assumed by observing that (5.16) is a positive function, together with the adoption of a linear porosity law which ensures small porosity variations, avoiding in this way a complete saturation of the pore space. Moreover, the non-dimensional constant c does not influence the search of equilibrium points, and thus one can assume $c = -1$ in what follows for the sake of simplicity. Equations (B.22) clearly represent a three-species system, that let to determine in a more direct way both the physically/biologically consistent equilibrium points and the physically/biologically consistent trajectories lying in the domain $\mathfrak{I}$. This is also guaranteed by considering positive initial conditions for the species, which ensures that the positive octant is invariant and that all trajectories of motion keep bounded in this $(0, \mathbb{R}^+) \times (0, \mathbb{R}^+) \times (0, \mathbb{R}^+)$, as shown by Itik ([99]). These two lemmas can be reported for completeness:

Lemma 1. With all positive initial conditions, the solutions of the system (B.22) lie in $(0, \mathbb{R}^+) \times (0, \mathbb{R}^+) \times (0, \mathbb{R}^+)$. This follows by observing that each coordinate hyper-plane is invariant.

Lemma 2. The solutions of (B.22) with initial values in $(0, \mathbb{R}^+) \times (0, \mathbb{R}^+) \times (0, \mathbb{R}^+)$ are bounded from above in $(0, \mathbb{R}^+) \times (0, \mathbb{R}^+) \times (0, \mathbb{R}^+)$ for all $t \geq 0$.

Then, starting from (B.22), the Jacobi matrix $\mathcal{J}_\Gamma = \nabla_\phi\Gamma$ of the linearized system results to be (tildes are omitted for clarity):

$$
\mathcal{J}_\Gamma =
\begin{bmatrix}
q(1 - \alpha_{TH}\phi_H - \phi_M\alpha_{TM} - 2\phi_T\alpha_{TT}) & -q\alpha_{TH}\phi_T & -q\alpha_{TM}\phi_T \\
-q\alpha_{HT}\phi_H & q(1 - 2\alpha_{HH}\phi_H - \alpha_{HM}\phi_M - \alpha_{HT}\phi_T) & -q\alpha_{HM}\phi_H \\
\beta_T - \alpha_{MT}\phi_M & \beta_H - \alpha_{MH}\phi_M & -\alpha_{MH}\phi_H - \alpha_{MT}\phi_T
\end{bmatrix}
\tag{B.23}
$$

Steady state points are founded by posing $\Gamma = \mathbf{0}$. The physically admissible points which can potentially occur describe the following exclusive situations of interest:

1. Cells fractions extinction. This first situation is depicted by three equilibrium points, and it can be written as $\phi_1^* = \{\phi_{T1}^* = 0, \phi_{H1}^* = 0, \phi_{M1}^*\}$, with ϕ_{M1}^* being determined in the first two cases respectively as $1/\alpha_{HM}$ and $1/\alpha_{TM}$, while it is undetermined in the third of them. Then, the first two cases are included in the

last one and only the point $\phi_1^* \subset \mathfrak{J}$ can be analyzed. Basically, this equilibrium state points out that, in the instant in which cells trajectories approach cells extinction, matrix will remain unchanged (this derives also from the fact that no self-degradation had been provided).

2. Healthy fraction dominance. It is associated to the steady state ϕ_2^* with expression

$$\left\{ \phi_{T2}^* = 0, \phi_{H2}^* = \frac{1}{\alpha_{HH}} \left(1 - \frac{\beta_H \alpha_{HM}}{\delta_M \alpha_{MH}} \right), \phi_{M2}^* = \frac{\beta_H}{\delta_M \alpha_{MH}} \right\} \qquad \text{(B.24)}$$

and would correspond to a system in its healthy stage, without invading tumor.

3. Tumor fraction dominance. The equilibrium point –say ϕ_3^*– is given by

$$\left\{ \phi_{T3}^* = \frac{1}{\alpha_{TT}} \left(1 - \frac{\beta_T \alpha_{TM}}{\delta_M \alpha_{MT}} \right), \phi_{H3}^* = 0, \phi_{M3}^* = \frac{\beta_T}{\delta_M \alpha_{\mathrm{MT}}} \right\} \qquad \text{(B.25)}$$

and it is associated to a complete tumor stage.

4. Solid species coexistence. These (two) points have an articulate expression in terms of model coefficients, so let them be denoted simply as $\phi_4^* = \{\phi_{T4}^*, \phi_{H4}^*, \phi_{M4}^*\}$ and $\phi_5^* = \{\phi_{T5}^*, \phi_{H5}^*, \phi_{M5}^*\}$ not to burden the speech.

With reference to parameters adopted (see table Table 6), a situation of strong dominance occurs for the tumor species. The introduction of the aggressive tumor species with a fitness function that, in relation to the modified coefficients, possesses a strategy prevailing on the healthy counterpart, *de facto* turns the ECM-healthy cell coexistence (i.e. in absence of tumor species) into an unstable equilibrium state. In particular, the insurgence of a predator species within the ecosystem possessing the given characteristics heavily affects the normal system homeostasis. In other words, provided that points in 1) and 4) have no physical interest for the consideration at hand (in particular, equilibria 4) do not give acceptable states), one can see that the tumor presence generates an unstable direction in correspondence of point 2). The eigenvalues associated to points 2) and 3) –say $\mathbf{y}_2$ and $\mathbf{y}_3$– are:

$$\mathbf{y}_2 = \mathcal{J}_\Gamma(\phi_2^*) = \left\{ -\frac{q \left(\delta_M \alpha_{MH} - \beta_H \alpha_{HM} \right)}{\delta_M \alpha_{MH}}, -\frac{\delta_M \alpha_{MH} - \beta_H \alpha_{HM}}{\alpha_{HH}}, \right.$$
$$\left. \frac{q \left(-\beta_H \alpha_{HH} \alpha_{TM} + \beta_H \alpha_{HM} \alpha_{TH} + \alpha_{HH} \delta_M \alpha_{MH} - \delta_M \alpha_{MH} \alpha_{TH} \right)}{\alpha_{HH} \delta_M \alpha_{MH}} \right\} \qquad \text{(B.26)}$$

$$\mathbf{y}_3 = \mathcal{J}_\Gamma(\phi_3^*) = \left\{ -\frac{q \left(\delta_M \alpha_{MT} - \beta_T \alpha_{TM} \right)}{\delta_M \alpha_{MT}}, -\frac{\delta_M \alpha_{MT} - \beta_T \alpha_{TM}}{\alpha_{TT}}, \right.$$
$$\left. \frac{q \left(-\alpha_{HM} \beta_T \alpha_{TT} - \alpha_{HT} \delta_M \alpha_{MT} + \alpha_{HT} \beta_T \alpha_{TM} + \delta_M \alpha_{MT} \alpha_{TT} \right)}{\delta_M \alpha_{MT} \alpha_{TT}} \right\} \qquad \text{(B.27)}$$

The projections in the phase space of Fig. 71A and B respectively show equilibria ϕ_2^* and ϕ_3^* in their planes, i.e. $\phi_T = 0$ and $\phi_H = 0$. In particular, focusing on Fig. 71A , the projections of phases trajectories in the plane $\phi_T = 0$ exhibit a convergent trend towards the point ϕ_2^*; this means that the plane $\phi_T = 0$ constitutes a stable subspace

for state 2., described by the two dimensional stable subspace $\mathcal{E}_2 = span\{\mathbf{v}_{21}, \mathbf{v}_{22}\}$, where $\mathbf{v}_{21}$ and $\mathbf{v}_{22}$ are the eigenvectors corresponding to the eigenvalues $\mathbf{y}_2$ with negative real part. In particular, the third eigenvalue y_{23} has positive real part by substituting the adopted coefficients and also given that the function q is strictly positive, and thus generates an unstable direction $\mathbf{v}_{23}$ according to the first Lyapunov stability theorem (here denoted by means of the red arrow in Fig. 71A and C). Therefore, the effect of tumor strategy, as highlighted in Fig. 71C, is to "divert" trajectories from the healthy subspace towards the tumor stage. Furthermore, it results that $\Re\{y_3\} < 0$, and consequently ϕ_3^* is a stable attractor (Fig. 71B and Fig. 71D).
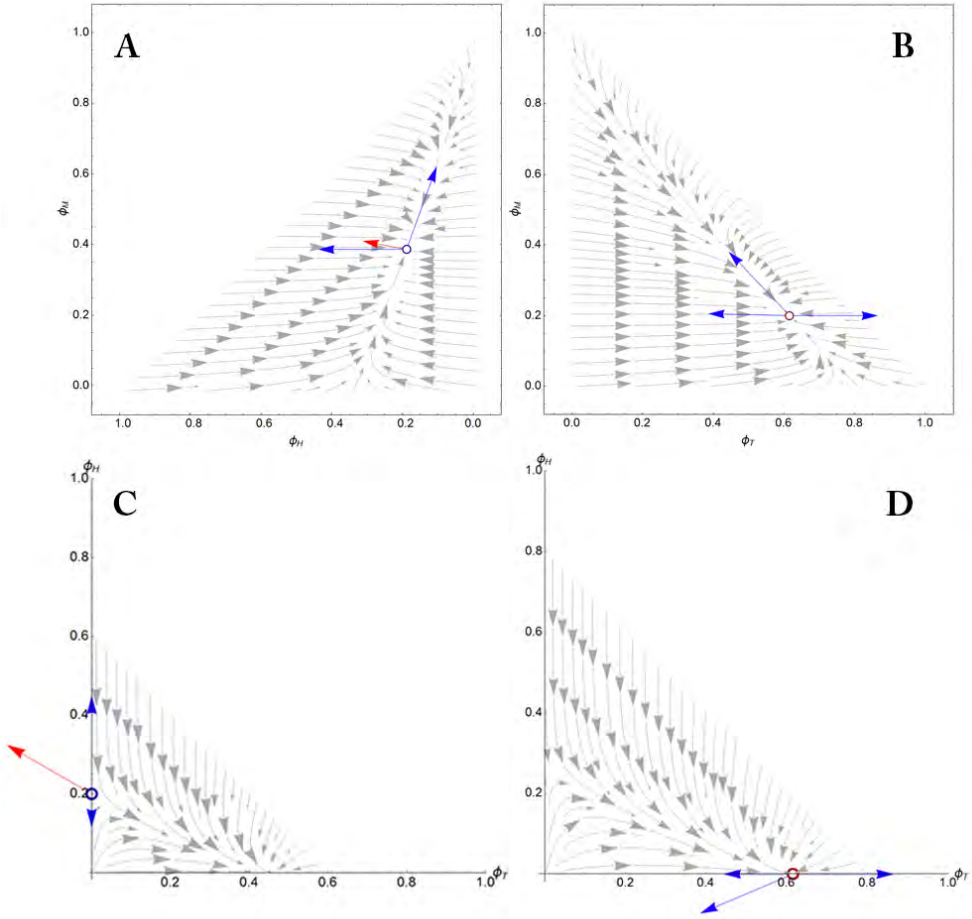
Figure 71: **A**. Representation (projection) of the phase portrait in the plane $\phi_T = 0$, with focus on the equilibrium point ϕ_2^*. **B**. Representation of the phase in the plane $\phi_H = 0$, that evidences the equilibrium point ϕ_3^*. **C**. Projection of the phase portrait in the plane $\phi_M = \phi_{M2}*$. The stable manifolds (blue arrows) directed in direction $\phi_T = 0$ and the unstable manifold (red arrow) driving trajectories towards the tumor invasion stage are here clearly distinguishable. **D**. Tumor dominance stage, constituting a stable attractor.

Naturally, these considerations are related to the chosen set of coefficients. The variation of the coefficients α_{IJ}, δ_I and β_I may generate scenarios, in which altered dynamics may occur exhibiting different stable attractors –like those ones related to the cells cohexistence that additionally include oscillating patterns here not obtained, or the one related to the tumor extinction in which the healthy species is able to survive to a given *ad hoc* treatment– also in presence of a tumor-type fitness function in the species rates. All the coefficient must in fact be interpreted as the translation of the microscopic interactions between cells and between cells and ECM, and this implies that the coefficients themselves may be actually the net result of multiple reactions-based processes that occur at a subcellular scale. There could be therefore the possibility of modelling the latter interaction by considering a more realistic multiscale approach in which chemical species actually work as intermediate regulators of the cross-talks among populations at the tissue scale. In this way also the interaction between tumor and immune system could be considered by also introducing perturbation of these mechanisms, in particular by explicitly inserting antagonist species like drugs in order to analyze the variations of the tumor strategy coefficients and capture possible changes into the system fate, by operatively prospecting the possibility to determine a metamorphosis of the biosystem asymptotic behavior.

In this Research work different biomechanical topics have been analyzed. In particular, the different themes have been treated with increasing complexity, by progressively including new phenomena and tracing new strategies in order to faithfully describe some important cells interspecific dynamics and the way they determine macroscopic tissue growth and residual stresses. Different key aspects and cues on the physics of development growing tumors, from the modelling of a multi-cell environment through the eclectic adoption of behavioral scheme of the Volterra-Lotka approach to their direct relationship with harboring intratumoral stresses and the mechanical response of the tumor tissue, have been harvested in Chapter 5 in order to furnish a faithful model of tumor complex dynamics, believing that a logical scheme (those one of the VL population dynamics) could have been able to describe a chaotic event such as the occurrence of a tumor disease. However, although some important feature depending on direct competition between cancer and healthy cells have been elucidated, other important aspects remain to date partially excluded. Among these, there is the possibility to include the oncogenic potentials of some immune cells or the aggressiveness of malignant cells which become malignant as a result of *mutation processes*, thus even further from the classical evolutionary logic. Also, the coupling with chemical species could be enriched in order to replicate a more complex environment in which the interspecific coefficients themselves can be viewed as the result of the chemical pathways through which cells communicating with the environment, in this way realizing a more structured and multiscale model. Alterations of the equilibria of the system could be analyzed by considering the introduction of antagonist chemical species in order to investigate their effectiveness on the cells proliferation potential as well as in terms of their capability of perfusing withing the tuor interstitium. In the field of therapy, other applications could be investigated, based on the possibility of mechanically targeting tumor cells aggregates through selected resonant ultra-sounds stimulations. The strategy proposed can be of course applied also in the other fields of the research presented. In fact, starting from the results obtained in Chapter 4, the full coupling could be used to enhance biomechanical models of arterial walls by integrating diffusion/reaction-based cell dynamics into macroscopic description of growth, remodeling and mechanics of the vessel structure, by exploiting the feedback from histological analyses and the *ad hoc* designed biaxial experimental tests to characterize the constitutive behavior of vessel structures. Also, the integrated Finite Element simulations would allow to force numerical algorithms to replicate *in vivo* responses, by reconstructing detailed 3D geometries of anatomic districts of interest with the help of imaging techniques. In this way FE-guided topology optimization would be coupled with enhanced biomechanical strategies to improve the biomechanical synergy between the vessel and the prostheses, realized with optimized materials and micro-structure.

Finally, all these activities, apart from the degree of detail with which have been presented throughout the Thesis work, are motivated by a common denominator: the attempt to contribute to pave the way –by means of enlarged multidisciplinary and

multiphysic perspective which is nowadays necessary in the contemporary Research–
to unloose, at least partially, the Gordian knot of the knowledge of the microcosm of
the living materials, in the belief they can be described through the simple principle
that govern the macro-systems around us.

ACKNOWLEDGEMENTS

Part IV

BIBLIOGRAPHY

BIBLIOGRAPHY

[1] *ANSYS Mechanical User's Guide.* Release 15.0. ANSYS, Inc. 2013.

[2] William P. Adams. ?Capsular Contracture: What is It? What Causes It? How Can It Be Prevented and Managed?? In: *Clinics in Plastic Surgery* 36.1 (2009), pp. 119–126. DOI: 10.1016/j.cps.2008.08.007.

[3] Julio a Aguirre-Ghiso. ?Models, mechanisms and clinical evidence for cancer dormancy.? In: *Nature reviews. Cancer* 7.11 (2007), pp. 834–846. ISSN: 1474-175X. DOI: 10.1038/nrc2256.

[4] Victor Alastrué, Estefanía Peña, Miguel Ángel Martínez, and Manuel Doblaré. ?Assessing the Use of the "Opening Angle Method" to Enforce Residual Stresses in Patient-Specific Arteries.? In: *Annals of Biomedical Engineering* 35.10 (2007), pp. 1821–1837. DOI: 10.1007/s10439-007-9352-4.

[5] Victor Alastrué, Estefanía Peña, Miguel Ángel Martínez, and Manuel Doblaré. ?Experimental study and constitutive modelling of the passive mechanical properties of the ovine infrarenal vena cava tissue.? In: *Journal of Biomechanics* 41.14 (2008), pp. 3038 –3045. ISSN: 0021-9290. DOI: http://dx.doi.org/10.1016/j.jbiomech.2008.07.008.

[6] D. Ambrosi and F. Guana. ?Stress-Modulated Growth.? In: *Mathematics and Mechanics of Solids* 12.3 (2005), pp. 319–342. DOI: 10.1177/1081286505059739.

[7] D Ambrosi and A Guillou. ?Growth and dissipation in biological tissues.? In: *Continuum Mechanics and Thermodynamics* 19.5 (2007), pp. 245–251. DOI: http://dx.doi.org/10.1007/s00161-007-0052-y.

[8] D. Ambrosi and F. Mollica. ?On the mechanics of a growing tumor.? In: *International Journal of Engineering Science* 40.12 (2002), pp. 1297–1316. ISSN: 00207225. DOI: 10.1016/S0020-7225(02)00014-9.

[9] D. Ambrosi, L. Preziosi, and G. Vitale. ?The interplay between stress and growth in solid tumors.? In: *Mechanics Research Communications* 42 (2012), pp. 87–91. DOI: 10.1016/j.mechrescom.2012.01.002.

[10] D Ambrosi et al. ?Perspectives on biological growth and remodeling.? In: *Journal of the Mechanics and Physics of Solids* 59.4 (2011), pp. 863–883. ISSN: 0022-5096. DOI: http://dx.doi.org/10.1016/j.jmps.2010.12.011.

[11] L. Anand. ?On H. Hencky's Approximate Strain-Energy Function for Moderate Deformations.? In: *Journal of Applied Mechanics* 46.1 (1979), p. 78. DOI: 10.1115/1.3424532.

[12] R. P. Araujo and D. L S McElwain. ?The nature of the stresses induced during tissue growth.? In: *Applied Mathematics Letters* 18.10 (2005), pp. 1081–1088. ISSN: 08939659. DOI: 10.1016/j.aml.2004.09.019.

[13] R. Araujo. ?A history of the study of solid tumour growth: the contribution of mathematical modelling.? In: *Bulletin of Mathematical Biology* (2004). DOI: 10.1016/s0092-8240(03)00126-5.

[14] T. Aybek, M. Sotiriou, T. Wohleke, A. Miskovic, A. Simon, M. Doss, S. Dogan, G. Wimmer-Greinecker, and A. Moritz. ?Valve opening and closing dynamics after different aortic valve-sparing operations.? In: *J. Heart Valve Dis.* 14.1 (2005), pp. 114–120.

[15] S. Baek, R.L. Gleason, K.R. Rajagopal, and J.D. Humphrey. ?Theory of small on large: Potential utility in computations of fluid–solid interactions in arteries.? In: *Computer Methods in Applied Mechanics and Engineering* 196.31-32 (2007), pp. 3070–3078. DOI: 10.1016/j.cma.2006.06.018.

[16] Steven D. Bain and Ted S. Gross. ?Structural Aspects of Bone Resorption.? In: *Topics in Bone Biology.* Springer Science + Business Media, pp. 58–66. DOI: 10.1007/1-84628-016-8__4.

[17] Peter D Ballyk, Colin Walsh, Jagadish Butany, and Matadial Ojha. ?Compliance mismatch may promote graft–artery intimal hyperplasia by altering suture-line stresses.? In: *Journal of Biomechanics* 31.3 (1997), pp. 229–237. DOI: 10.1016/s0197-3975(97)00111-5.

[18] Erika M. Bastos, Miguel S. Neto, Maria Teresa S. Alves, Élvio B. Garcia, Rafael A. Santos, Thaís Heink, Juliana B. Pereira, and Lydia M. Ferreira. ?Histologic Analysis of Zafirlukast's Effect on Capsule Formation Around Silicone Implants.? In: *Aesth Plast Surg* 31.5 (2007), pp. 559–565. DOI: 10.1007/s00266-006-0257-7.

[19] B. P. Bengtson. ?Complications, reoperations, and revisions in breast augmentation.? In: *Clin Plast Surg* 36.1 (2009), pp. 139–156.

[20] K. Berger and L. R. Sauvage. ?Late fiber deterioration in Dacron arterial grafts.? In: *Ann. Surg.* 193.4 (1981), pp. 477–491.

[21] Olivier Michel Bical, Jérome Héran, Bernard Thébault, and François Funck. ?Pseudoaneurysm following Dacron replacement of the ascending aorta.? In: *European Journal of Cardio-Thoracic Surgery* 35.3 (2009), pp. 536–536. DOI: 10.1016/j.ejcts.2008.12.013.

[22] Davide Bigoni. *Nonlinear Solid Mechanics.* Cambridge University Press (CUP), 2009. DOI: 10.1017/cbo9781139178938.

[23] M. A. Biot. ?General Theory of Three-Dimensional Consolidation.? In: *J. Appl. Phys.* 12.2 (1941), p. 155. DOI: 10.1063/1.1712886.

[24] Eugene D Boland, Branch D Coleman, Catherine P Barnes, David G Simpson, Gary E Wnek, and Gary L Bowlin. ?Electrospinning polydioxanone for biomedical applications.? In: *Acta Biomaterialia* 1.1 (2005), pp. 115–123. ISSN: 1742-7061. DOI: http://dx.doi.org/10.1016/j.actbio.2004.09.003.

[25] Y. Boucher and R. K. Jain. ?Microvascular pressure is the principal driving force for interstitial hypertension in solid tumors: Implications for vascular collapse.? In: *Cancer Research* 52.18 (1992), pp. 5110–5114. ISSN: 00085472.

[26] S. Brinkhues. ?Modeling and simulation of arterial walls with focus on damage and residual stresses.? PhD thesis. Universitat Duisburg-Essen, 2012.

[27] O. T. Bruhns, H. Xiao, and A. Meyers. ?Constitutive inequalities for an isotropic elastic strain-energy function based on Hencky's logarithmic strain tensor.? In: *Proceedings of the Royal Society of London A: Mathematical, Physical and Engineering Sciences* 457.2013 (2001), pp. 2207–2226. ISSN: 1364-5021. DOI: `10.1098/rspa.2001.0818`.

[28] Pascal R. Buenzli, Peter Pivonka, and David W. Smith. ?Bone refilling in cortical basic multicellular units: insights into tetracycline double labelling from a computational model.? In: *Biomechanics and Modeling in Mechanobiology* 13.1 (2013), pp. 185–203. DOI: `10.1007/s10237-013-0495-y`.

[29] Patrick de Buhan, Xavier Chateau, and Luc Dormieux. ?The constitutive equations of finite strain poroelasticity in the light of a micro-macro approach.? In: *European Journal of Mechanics - A/Solids* 17.6 (1998), pp. 909–921. ISSN: 09977538. DOI: `10.1016/S0997-7538(98)90501-0`.

[30] H. Byrne. ?Modelling solid tumour growth using the theory of mixtures.? In: *Mathematical Medicine and Biology* 20.4 (2003), pp. 341–366. DOI: `10.1093/imammb20.4.341`.

[31] et al C. Cascone. ?Modelli di diffusione di specie in ambienti frammentati.? In: (2003).

[32] M.S. Cabrera, C.W.J. Oomens, C.V.C. Bouten, A.J.J.C. Bogers, S.P. Hoerstrup, and F.P.T. Baaijens. ?Mechanical analysis of ovine and pediatric pulmonary artery for heart valve stent design.? In: *Journal of Biomechanics* 46.12 (2013), pp. 2075 –2081. ISSN: 0021-9290. DOI: `http://dx.doi.org/10.1016/j.jbiomech.2013.04.020`.

[33] Thierry Carrel. ?The autograft inclusion: An obligatory step to avoid late failure following the Ross procedure?? In: *The Journal of Thoracic and Cardiovascular Surgery* 149.2 (2015), S53–S54. DOI: `10.1016/j.jtcvs.2014.09.023`.

[34] Thierry Carrel, Markus Schwerzmann, Friedrich Eckstein, Thierry Aymard, and Alexander Kadner. ?Preliminary results following reinforcement of the pulmonary autograft to prevent dilatation after the Ross procedure.? In: *The Journal of Thoracic and Cardiovascular Surgery* 136.2 (2008), pp. 472–475. DOI: `10.1016/j.jtcvs.2008.02.004`.

[35] M Centola, A Rainer, C Spadaccio, S De Porcellinis, J A Genovese, and M Trombetta. ?Combining electrospinning and fused deposition modeling for the fabrication of a hybrid vascular graft.? eng. In: *Biofabrication* 2.1 (Mar. 2010), p. 14102. ISSN: 1758-5090 (Electronic). DOI: `10.1088/1758-5082/2/1/014102`.

[36] C.G. Chakrabarti and Koyel Ghosh. ?Non-equilibrium thermodynamics of ecosystems: Entropic analysis of stability and diversity.? In: *Ecological Modelling* 220.17 (2009), pp. 1950–1956. DOI: `10.1016/j.ecolmodel.2009.04.055`.

[37] M. A. J. Chaplain. ?Mathematical modelling of the loss of tissue compression responsiveness and its role in solid tumour development.? In: *Mathematical Medicine and Biology* 23.3 (2006), pp. 197–229. DOI: `10.1093/imammb/dql009`.

[38]   Gang Cheng, Janet Tse, Rakesh K Jain, and Lance L Munn. "Micro-environmental mechanical stress controls tumor spheroid size and morphology by suppressing proliferation and inducing apoptosis in cancer cells." In: *PloS one* 4.2 (2009), e4632. ISSN: 1932-6203. DOI: 10.1371/journal.pone.0004632.

[39]   Matthias Chiquet. "Regulation of extracellular matrix gene expression by mechanical stress." In: *Matrix Biology* 18.5 (1999), pp. 417–426. DOI: 10.1016/s0945-053x(99)00039-6.

[40]   J Chlupac, E Filova, and L Bacakova. "Blood vessel replacement: 50 years of development and tissue engineering paradigms in vascular surgery." In: *Physiol Res* 58 (2009), Suppl 2: S119–139.

[41]   C J Chuong and Y C Fung. "Three-dimensional stress distribution in arteries." eng. In: *Journal of biomechanical engineering* 105.3 (Aug. 1983), pp. 268–274. ISSN: 0148-0731 (Print).

[42]   G. P. Clagett, J. M. Salander, W. L. Eddleman, S. Cabellon, J. R. Youkey, D. W. Olson, J. E. Hutton, and N. M. Rich. "Dilation of knitted Dacron aortic prostheses and anastomotic false aneurysms: etiologic considerations." In: *Surgery* 93.1 Pt 1 (1983), pp. 9–16.

[43]   J. M. Clark and S. Glagov. "Transmural organization of the arterial media. The lamellar unit revisited." In: *Arteriosclerosis, Thrombosis, and Vascular Biology* 5.1 (1985), pp. 19–34. DOI: 10.1161/01.atv.5.1.19.

[44]   Bernard D. Coleman and Morton E. Gurtin. "Thermodynamics with Internal State Variables." In: *The Journal of Chemical Physics* 47.2 (1967), pp. 597–613. DOI: 10.1063/1.1711937.

[45]   Olivier Coussy. *Mechanics and Physics of Porous Solids*. Wiley-Blackwell, 2010. DOI: 10.1002/9780470710388.

[46]   S C Cowin and S B Doty. *Tissue Mechanics*. Springer, 2007.

[47]   S. C. Cowin and D. H. Hegedus. "Bone remodeling I: theory of adaptive elasticity." In: *Journal of Elasticity* 6.3 (1976), pp. 313–326. DOI: 10.1007/bf00041724.

[48]   Stephen C. Cowin. "Continuum kinematical modeling of mass increasing biological growth." In: *International Journal of Engineering Science* 48.11 (2010), pp. 1137–1145. ISSN: 00207225. DOI: 10.1016/j.ijengsci.2010.06.008.

[49]   Stephen C. Cowin and Luis Cardoso. "Mixture theory-based poroelasticity as a model of interstitial tissue growth." In: *Mechanics of Materials* 44 (2012), pp. 47–57. ISSN: 01676636. DOI: 10.1016/j.mechmat.2011.07.005.

[50]   Yannis F. Dafalias and Zacharias Pitouras. "Stress field in actin gel growing on spherical substrate." In: *Biomechanics and Modeling in Mechanobiology* 8.1 (2007), pp. 9–24. DOI: 10.1007/s10237-007-0113-y.

[51]   Tirone E. David, Susan Armstrong, Cedric Manlhiot, Brian W. McCrindle, and Christopher M. Feindel. "Long-term results of aortic root repair using the reimplantation technique." In: *The Journal of Thoracic and Cardiovascular Surgery* (2012), pp. 1–4. DOI: 10.1016/j.jtcvs.2012.11.075.

[52] Tirone E. David, Susan Armstrong, Cedric Manlhiot, Brian W. McCrindle, and Christopher M. Feindel. "Long-term results of aortic root repair using the reimplantation technique." In: *The Journal of Thoracic and Cardiovascular Surgery* 145.3 (2013), S22–S25. DOI: 10.1016/j.jtcvs.2012.11.075.

[53] Tirone E. David, Carolyn David, Anna Woo, and Cedric Manlhiot. "The Ross procedure: Outcomes at 20 years." In: *The Journal of Thoracic and Cardiovascular Surgery* 147.1 (2014), pp. 85–94. DOI: 10.1016/j.jtcvs.2013.08.007.

[54] Ralph J. DeBerardinis, Julian J. Lum, Georgia Hatzivassiliou, and Craig B. Thompson. "The Biology of Cancer: Metabolic Reprogramming Fuels Cell Growth and Proliferation." In: *Cell Metabolism* 7.1 (2008), pp. 11–20. DOI: 10.1016/j.cmet.2007.10.002.

[55] S. Derler and L. C. Gerhardt. "Tribology of Skin: Review and Analysis of Experimental Results for the Friction Coefficient of Human Skin." In: *Tribol Lett* 45.1 (2011), pp. 1–27. DOI: 10.1007/s11249-011-9854-y.

[56] Wolfram Dolores, Rainer Christian, Niederegger Harald, Piza Hildegunde, and Wick Georg. "Cellular and molecular composition of fibrous capsules formed around silicone breast implants with special focus on local immune reactions." In: *Journal of Autoimmunity* 23.1 (2004), pp. 81–91. DOI: 10.1016/j.jaut.2004.03.005.

[57] W. J. Drugan. "Elastic Composite Materials Having a Negative Stiffness Phase Can Be Stable." In: *Phys. Rev. Lett.* 98.5 (2007). DOI: 10.1103/physrevlett.98.055502.

[58] Erik Fink Eriksen. "Cellular mechanisms of bone remodeling." In: *Rev Endocr Metab Disord* 11.4 (2010), pp. 219–227. DOI: 10.1007/s11154-010-9153-1.

[59] Dan Fagrell, Anders Berggren, and Erkki Tarpila. "Capsular Contracture around Saline-Filled Fine Textured and Smooth Mammary Implants: A Prospective 7.5-Year Follow-Up." In: *Plastic and Reconstructive Surgery* 108.7 (2001), pp. 2108–2112. DOI: 10.1097/00006534-200112000-00046.

[60] M. Fraldi, F. Carannante, and L. Nunziante. "Analytical solutions for n-phase functionally graded material cylinders under de saint venant load conditions: Homogenization and effects of poisson ratios on the overall stiffness." In: *Composites Part B: Engineering* 45.1 (2013), pp. 1310–1324. ISSN: 13598368. DOI: 10.1016/j.compositesb.2012.09.016.

[61] M. Fraldi and F. Guarracino. "An improved formulation for the assessment of the capacity load of circular rings and cylindrical shells under external pressure. Part 1. Analytical derivation." In: *Thin-Walled Structures* 49.9 (2011), pp. 1054–1061. ISSN: 0263-8231. DOI: http://dx.doi.org/10.1016/j.tws.2011.03.014.

[62] M. Fraldi, L. Esposito, G. Perrella, A. Cutolo, and S. C. Cowin. "Topological optimization in hip prosthesis design." In: *Biomechanics and Modeling in Mechanobiology* 9.4 (2009), pp. 389–402. DOI: 10.1007/s10237-009-0183-0.

[63]   M. Fraldi, L. Nunziante, a. Gesualdo, and F. Guarracino. **?**On the bounding of limit multipliers for combined loading.**?** In: *Proceedings of the Royal Society A: Mathematical, Physical and Engineering Sciences* 466.2114 (2010), pp. 493–514. ISSN: 1364-5021. DOI: 10.1098/rspa.2009.0240.

[64]   M. Fraldi, A. Cugno, L. Deseri, K. Dayal, and N. M. Pugno. **?**A frequency-based hypothesis for mechanically targeting and selectively attacking cancer cells.**?** In: *J. R. Soc. Interface* 12.111 (2015), p. 20150656. DOI: 10.1098/rsif.2015.0656.

[65]   G. Franceschini, D. Bigoni, P. Regitnig, and G.A. Holzapfel. **?**Brain tissue deforms similarly to filled elastomers and follows consolidation theory.**?** In: *Journal of the Mechanics and Physics of Solids* 54.12 (2006), pp. 2592–2620. DOI: 10.1016/j.jmps.2006.05.004.

[66]   Peter Fratzl and Richard Weinkamer. **?**Nature's hierarchical materials.**?** In: *Progress in Materials Science* 52.8 (2007), pp. 1263–1334. ISSN: 0079-6425. DOI: http://dx.doi.org/10.1016/j.pmatsci.2007.06.001.

[67]   J. P. Freyer and R. M. Sutherland. **?**Regulation of growth saturation and development of necrosis in EMT6Ro multicellular spheroids by the glucose and oxygen supply.**?** In: *Cancer Res.* 46.7 (1986), pp. 3504–3512.

[68]   Y C Fung. *Introduction to Bioengineering.* WORLD SCIENTIFIC, 2001. DOI: 10.1142/4183.

[69]   Y Fung. *Biomechanics: mechanical properties of living tissues.* Biomechanics Y. C. Fung. Springer-Verlag, 1981.

[70]   YC Fung and SQ Liu. **?**Changes of zero-stress state of rat pulmonary arteries in hypoxic hypertension.**?** In: *Journal of Applied Physiology* 70.6 (1991).

[71]   Matias Gancedo, Luis Ruiz-Corro, Adriana Salazar-Montes, Ana Rosa Rincón, and Juan Armendáriz-Borunda. **?**Pirfenidone Prevents Capsular Contracture After Mammary Implantation.**?** In: *Aesth Plast Surg* 32.1 (2007), pp. 32–40. DOI: 10.1007/s00266-007-9051-4.

[72]   J.F. Ganghoffer. **?**Mechanical modeling of growth considering domain variation. Part II: Volumetric and surface growth involving Eshelby tensors.**?** In: *Journal of the Mechanics and Physics of Solids* 58.9 (2010), pp. 1434–1459. DOI: 10.1016/j.jmps.2010.05.003.

[73]   J. M. Garcia-Aznar, T. Rueberg, and M. Doblare. **?**A bone remodelling model coupling microdamage growth and repair by 3D BMU-activity.**?** In: *Biomechanics and Modeling in Mechanobiology* 4.2-3 (2005), pp. 147–167. DOI: 10.1007/s10237-005-0067-x.

[74]   K Garikipati. **?**A continuum treatment of growth in biological tissue: the coupling of mass transport and mechanics.**?** In: *Journal of the Mechanics and Physics of Solids* 52.7 (2004), pp. 1595–1625. DOI: 10.1016/j.jmps.2004.01.004.

[75]   Robert a Gatenby. **?**Population Ecology Issues in Tumor Growth Population Ecology Issues in Tumor Growth.**?** In: *Cancer Research* 51.10 (1991), pp. 2542–2547.

[76]   Klika V Goriely A. *Current challenges in the mechanobiology of growth*. Tech. rep. Banff International Research Station, 2012.

[77]   Jason M. Graham, Bruce P. Ayati, Sarah A. Holstein, and James A. Martin. ?The Role of Osteocytes in Targeted Bone Remodeling: A Mathematical Model.? In: *PLoS ONE* 8.5 (2013). Ed. by Luc Malaval, e63884. DOI: 10.1371/journal.pone.0063884.

[78]   L. Graziano and L. Preziosi. ?Mechanics in Tumor Growth.? In: *Modeling of Biological Materials*. Springer Science + Business Media, 2007, pp. 263–321. DOI: 10.1007/978-0-8176-4411-6_7.

[79]   Morton E. Gurtin, Eliot Fried, and Lallit Anand. *The Mechanics and Thermodynamics of Continua*. Cambridge University Press (CUP), 2009. DOI: 10.1017/cbo9780511762956.

[80]   Mohamed Ben Hamouda and Naziha Atti. ?Comparison of growth curves of lamb fat tail measurements and their relationship with body weight in Babarine sheep.? In: *Small Ruminant Research* 95.2-3 (2011), pp. 120–127. DOI: 10.1016/j.smallrumres.2010.10.001.

[81]   Y. Han, S. C. Cowin, M. B. Schaffler, and S. Weinbaum. ?Mechanotransduction and strain amplification in osteocyte cell processes.? In: *Proceedings of the National Academy of Sciences* 101.47 (2004), pp. 16689–16694. DOI: 10.1073/pnas.0407429101.

[82]   I. Hariton, G. deBotton, T.C. Gasser, and G.A. Holzapfel. ?Stress-driven collagen fiber remodeling in arterial walls.? In: *Journal of Biomechanics* 39 (2006), S317. DOI: 10.1016/s0021-9290(06)84245-4.

[83]   G Helmlinger, P a Netti, H C Lichtenbeld, R J Melder, and R K Jain. ?Solid stress inhibits the growth of multicellular tumor spheroids.? In: *Nature biotechnology* 15.8 (1997), pp. 778–783. ISSN: 1087-0156. DOI: 10.1038/nbt0897-778.

[84]   R. Hill. ?On constitutive inequalities for simple materials.? In: *Journal of the Mechanics and Physics of Solids* 16.5 (1968), pp. 315–322. DOI: 10.1016/0022-5096(68)90018-5.

[85]   Anne Hoger. ?On the determination of residual stress in an elastic body.? In: *Journal of Elasticity* 16.3 (1986), pp. 303–324. DOI: 10.1007/bf00040818.

[86]   Anne Hoger. ?The stress conjugate to logarithmic strain.? In: *International Journal of Solids and Structures* 23.12 (1987), pp. 1645–1656. ISSN: 00207683. DOI: 10.1016/0020-7683(87)90115-6.

[87]   G.A. Holapfel. *Nonlinear Solid Mechanics: A Continuum Approach for Engineering*. Wiley, 2000.

[88]   G. A. Holzapfel. ?Determination of layer-specific mechanical properties of human coronary arteries with nonatherosclerotic intimal thickening and related constitutive modeling.? In: *AJP: Heart and Circulatory Physiology* 289.5 (2005), H2048–H2058. DOI: 10.1152/ajpheart.00934.2004.

[89]   G A Holzapfel and R W Ogden. *Mechanics of Biological Tissue*. Springer, 2006.

[90] Gerhard A Holzapfel and Ray W Ogden. ?Constitutive modelling of arteries.? In: *Proceedings of the Royal Society of London A: Mathematical, Physical and Engineering Sciences* 466.2118 (Apr. 2010), pp. 1551–1597.

[91] GerhardA. Holzapfel, ThomasC. Gasser, and RayW. Ogden. ?A New Constitutive Framework for Arterial Wall Mechanics and a Comparative Study of Material Models.? English. In: *Journal of elasticity and the physical science of solids* 61.1-3 (2000), pp. 1–48. ISSN: 0374-3535. DOI: 10.1023/A:1010835316564.

[92] Jurgen Horer et al. ?Neoaortic root diameters and aortic regurgitation in children after the Ross operation.? eng. In: *The Annals of thoracic surgery* 88.2 (Aug. 2009), 594–600; discussion 600. ISSN: 1552-6259 (Electronic). DOI: 10.1016/j.athoracsur.2009.04.077.

[93] Ingber DE Huang S. ?Cell tension, matrix mechanics, and cancer development.? In: *Cancer Cell* 8.3 (2005), pp. 175–6. DOI: doi:10.1016/j.ccr.2005.08.009.

[94] J D Humphrey. *Cardiovascular Solid Mechanics.* Springer-Verlag New York, 2002. DOI: 10.1007/978-0-387-21576-1.

[95] C.V. Ioannou, N. Stergiopulos, A.N. Katsamouris, I. Startchik, A. Kalangos, M.J. Licker, N. Westerhof, and D.R. Morel. ?Hemodynamics induced after acute reduction of proximal thoracic aorta compliance.? In: *European Journal of Vascular and Endovascular Surgery* 26.2 (2003), pp. 195–204. DOI: 10.1053/ejvs.2002.1917.

[96] Christos V. Ioannou, Denis R. Morel, Asterios N. Katsamouris, Sofia Katranitsa, Irena Startchik, Afksentios Kalangos, Nico Westerhof, and Nikos Stergiopulos. ?Left Ventricular Hypertrophy Induced by Reduced Aortic Compliance.? In: *J Vasc Res* 46.5 (2009), pp. 417–425. DOI: 10.1159/000194272.

[97] Hanna Isaksson, Corrinus C. van Donkelaar, Rik Huiskes, and Keita Ito. ?A mechano-regulatory bone-healing model incorporating cell-phenotype specific activity.? In: *Journal of Theoretical Biology* 254.3 (2008), p. 717. DOI: 10.1016/j.jtbi.2008.07.003.

[98] Giorgio Israel and Ana Millán Gasca. *The Biology of Numbers.* Springer Science + Business Media, 2002. DOI: 10.1007/978-3-0348-8123-4.

[99] Mehmet Itik and Stephen P. Banks. ?Chaos in a three dimensional cancer model.? In: *International Journal of Bifurcation and Chaos* 20.01 (2010), pp. 71–79. DOI: 10.1142/s0218127410025417.

[100] M. Itskov. ?The Derivative with respect to a Tensor: some Theoretical Aspects and Applications.? In: *ZAMM* 82.8 (2002), pp. 535–544. ISSN: 1521-4001. DOI: 10.1002/1521-4001(200208)82:8<535::AID-ZAMM535>3.0.CO;2-U.

[101] Jeffrey G Jacot, Ibrahim Abdullah, Michael Belkin, Marie Gerhard-Herman, Peter Gaccione, Joseph F Polak, Magruder C Donaldson, Anthony D Whittemore, and Michael S Conte. ?Early adaptation of human lower extremity vein grafts: wall stiffness changes accompany geometric remodeling.? eng. In: *Journal of vascular surgery* 39.3 (Mar. 2004), pp. 547–555. ISSN: 0741-5214 (Print). DOI: 10.1016/j.jvs.2003.09.045.

[102]   Rakesh K. Jain, Ricky T. Tong, and Lance L. Munn. "Effect of vascular normalization by antiangiogenic therapy on interstitial hypertension, peritumor edema, and lymphatic metastasis: Insights from a mathematical model." In: *Cancer Research* 67.6 (2007), pp. 2729–2735. ISSN: 00085472. DOI: 10.1158/0008-5472.CAN-06-4102.

[103]   Robert L. Jilka. "Biology of the basic multicellular unit and the pathophysiology of osteoporosis." In: *Med. Pediatr. Oncol.* 41.3 (2003), pp. 182–185. DOI: 10.1002/mpo.10334.

[104]   B. E. Johnson and A. Hoger. "The Use of Strain Energy to Quantify the Effect of Residual Stress on Mechanical Behavior." In: *Mathematics and Mechanics of Solids* 3.4 (1998), pp. 447–470. DOI: 10.1177/108128659800300405.

[105]   Arseniy Karkach. "Trajectories and models of individual growth." In: *Demographic Research* 15 (2006), pp. 347–400. DOI: 10.4054/demres.2006.15.12.

[106]   Ali Karrech, Thomas Poulet, and Klaus Regenauer-Lieb. "Poromechanics of saturated media based on the logarithmic finite strain." In: *Mechanics of Materials* 51 (2012), pp. 118–136. DOI: 10.1016/j.mechmat.2012.03.011.

[107]   H.K. Khalil. *Nonlinear Systems.* Prentice Hall, 1996.

[108]   Ardeshir Kianercy, Robert Veltri, and Kenneth J Pienta. "Critical transitions in a game theoretic model of tumour metabolism." In: *Interface focus* 4.4 (2014), p. 20140014. ISSN: 2042-8898. DOI: 10.1098/rsfs.2014.0014.

[109]   Sang-Hoon Kim, ChoHay Mun, Youngmee Jung, Sang-Heon Kim, Dong-Ik Kim, and SooHyun Kim. "Mechanical properties of compliant double layered poly(L-lactide-co-ϵ-caprolactone) vascular graft." English. In: *Macromolecular Research* 21.8 (2013), pp. 886–891. ISSN: 1598-5032. DOI: 10.1007/s13233-013-1095-5.

[110]   Shin Y. Kim, Thomas J. Hinkamp, William R. Jacobs, Robert C. Lichtenberg, Harold Posniak, and Roque Pifarré. "Effect of an inelastic aortic synthetic vascular graft on exercise hemodynamics." In: *The Annals of Thoracic Surgery* 59.4 (1995), pp. 981–989. DOI: 10.1016/0003-4975(95)00068-v.

[111]   O. Kintzel. "Fourth-order tensors–tensor differentiation with applications to continuum mechanics. Part II: Tensor analysis on manifolds." In: *ZAMM* 86.4 (2006), pp. 312–334. DOI: 10.1002/zamm.200410243.

[112]   O. Kintzel and Y. Başar. "Fourth-order tensors – tensor differentiation with applications to continuum mechanics. Part I: Classical tensor analysis." In: *ZAMM* 86.4 (2006), pp. 291–311. DOI: 10.1002/zamm.200410242.

[113]   Kanchi Lakshmi Kiran, Devaraj Jayachandran, and S. Lakshminarayanan. "Mathematical modelling of avascular tumour growth based on diffusion of nutrients and its validation." In: *Can. J. Chem. Eng.* 87.5 (2009), pp. 732–740. DOI: 10.1002/cjce.20204.

[114]   D.M. Kochmann and W.J. Drugan. "Dynamic stability analysis of an elastic composite material having a negative-stiffness phase." In: *Journal of the Mechanics and Physics of Solids* 57.7 (2009), pp. 1122–1138. DOI: 10.1016/j.jmps.2009.03.002.

[115] E.W. Kopf and A.J. Lotka. ?Elements of Physical Biology.? In: *Journal of the American Statistical Association* 20.151 (1925), p. 452. DOI: 10.2307/2965538.

[116] J. Kováčik. ?Correlation between Young's modulus and porosity in porous materials.? English. In: *Journal of Materials Science Letters* 18.13 (1999), pp. 1007–1010. ISSN: 0261-8028. DOI: 10.1023/A:1006669914946.

[117] E. Kuhl and P. Steinmann. ?Mass- and volume-specific views on thermodynamics for open systems.? In: *Proceeding of the Royal Society of London* 459.2038 (2003), pp. 2547–2568. ISSN: 1364-5021. DOI: 10.1098/rspa.2003.1119.

[118] Ellen Kuhl. ?Growing matter: A review of growth in living systems.? In: *Journal of the Mechanical Behavior of Biomedical Materials* 29 (2014), pp. 529–543. DOI: 10.1016/j.jmbbm.2013.10.009.

[119] R. S. Lakes, T. Lee, A. Bersie, and Y.C. Wang. ?xtreme damping in composite materials with negative-stiffness inclusions.? In: *Nature* (2001). DOI: http://dx.doi.org/10.1038/35069035.

[120] R.S. Lakes and W.J. Drugan. ?Dramatically stiffer elastic composite materials due to a negative stiffness phase?? In: *Journal of the Mechanics and Physics of Solids* 50.5 (2002), pp. 979–1009. DOI: 10.1016/s0022-5096(01)00116-8.

[121] James J. Lee, Justin Huang, Christopher G. England, Lacey R. McNally, and Hermann B. Frieboes. ?Predictive Modeling of In Vivo Response to Gemcitabine in Pancreatic Cancer.? In: *PLoS Comput Biol* 9.9 (2013). Ed. by Mark S. Alber, e1003231. DOI: 10.1371/journal.pcbi.1003231.

[122] Vincent Lemaire, Frank L. Tobin, Larry D. Greller, Carolyn R. Cho, and Larry J. Suva. ?Modeling the interactions between osteoblast and osteoclast activities in bone remodeling.? In: *Journal of Theoretical Biology* 229.3 (2004), pp. 293–309. DOI: 10.1016/j.jtbi.2004.03.023.

[123] Jianying Li, Haiyan Li, Li Shi, Alex S.L. Fok, Cemal Ucer, Hugh Devlin, Keith Horner, and Nick Silikas. ?A mathematical model for simulating the bone remodeling process under mechanical stimulus.? In: *Dental Materials* 23.9 (2007), pp. 1073–1078. DOI: 10.1016/j.dental.2006.10.004.

[124] David Liao and Thea D Tlsty. ?Evolutionary game theory for physical and biological scientists. II. Population dynamics equations can be associated with interpretations.? In: *Interface Focus* 4.4 (2014), pp. 20140038–20140038. ISSN: 2042-8898. DOI: 10.1098/rsfs.2014.0038.

[125] David Liao and Thea D. Tlsty. ?Evolutionary game theory for physical and biological scientists. II. Population dynamics equations can be associated with interpretations.? In: *Interface Focus* 4.4 (2014), pp. 20140038–20140038. ISSN: 2042-8898. DOI: 10.1098/rsfs.2014.0038.

[126] Shuyang Lu, Peng Zhang, Xiaoning Sun, Feirong Gong, Shouguo Yang, Li Shen, Zheyong Huang, and Chunsheng Wang. ?Synthetic ePTFE Grafts Coated with an Anti-CD133 Antibody-Functionalized Heparin/Collagen Multilayer with Rapid in vivo Endothelialization Properties.? In: *ACS Applied Materials & Interfaces* 5.15 (2013), pp. 7360–7369. DOI: 10.1021/am401706w.

[127] V A Lubarda and A Hoger. **?**On the mechanics of solids with a growing mass.**?** In: *International Journal of Solids and Structures* 39.18 (2002), pp. 4627–4664. ISSN: 0020-7683. DOI: http://dx.doi.org/10.1016/S0020-7683(02)00352-9.

[128] V.A. Lubarda. **?**Constitutive theories based on the multiplicative decomposition of deformation gradient: Thermoelasticity, elastoplasticity, and biomechanics.**?** In: *Applied Mechanics Reviews* 57.2 (2004), pp. 95–108. DOI: 10.1115/1.1591000.

[129] A. M. Lyapunov. **?**The general problem of the stability of motion.**?** In: *International Journal of Control* 55.3 (1992), pp. 531–534. DOI: 10.1080/00207179208934253.

[130] HAJIME MAETA and MOTOKAZU Hori. **?**Effects of a lack of aortic "windkessel" properties on the left ventricle.**?** In: *Jpn Circ J* 49.2 (1985), pp. 232–237. DOI: 10.1253/jcj.49.232.

[131] P.S. Malchesky. **?**Artificial Organs 2012: a year in review.**?** In: *Artificial Organs* 37.3 (2013), pp. 324–349. DOI: 10.1111/aor.12057.

[132] Koichi Matsuo and Naoko Irie. **?**Osteoclast–osteoblast communication.**?** In: *Archives of Biochemistry and Biophysics* 473.2 (2008), pp. 201–209. DOI: 10.1016/j.abb.2008.03.027.

[133] Geard Maugin. *Configurational Forces.* Chapman and Hall/CRC, 2010. DOI: 10.1201/b10356.

[134] G. Patrick Maxwell and Allen Gabriel. **?**The Evolution of Breast Implants.**?** In: *Plastic and Reconstructive Surgery* 134 (2014), 12S–17S. DOI: 10.1097/prs.0000000000000348.

[135] Luis G. Melo, Massimiliano Gnecchi, Christopher A. Ward, and Victor J. Dzau. **?**Vascular Remodeling in Health and Disease.**?** In: *Cardiovascular Medicine.* Springer Science + Business Media, 2007, pp. 1541–1565. DOI: 10.1007/978-1-84628-715-2_74.

[136] G. Molea, F. Schonauer, G. Bifulco, and D. D'Angelo. **?**Comparative study on biocompatibility and absorption times of three absorbable monofilament suture materials (Polydioxanone, Poliglecaprone 25, Glycomer 631).**?** In: *British Journal of Plastic Surgery* 53.2 (2000), pp. 137–141. DOI: 10.1054/bjps.1999.3247.

[137] Fabien Montel et al. **?**Stress Clamp Experiments on Multicellular Tumor Spheroids.**?** In: *Phys. Rev. Lett.* 107.18 (2011). DOI: 10.1103/physrevlett.107.188102.

[138] Fabien Montel, Morgan Delarue, Jens Elgeti, Danijela Vignjevic, Giovanni Cappello, and Jacques Prost. **?**Isotropic stress reduces cell proliferation in tumor spheroids.**?** In: *New Journal of Physics* 14 (2012). ISSN: 13672630. DOI: 10.1088/1367-2630/14/5/055008.

[139]   M. J. Moreno, A. Ajji, D. Mohebbi-Kalhori, M. Rukhlova, A. Hadjizadeh, and M. N. Bureau. ?Development of a compliant and cytocompatible micro-fibrous polyethylene terephthalate vascular scaffold.? In: *Journal of Biomedical Materials Research Part B: Applied Biomaterials* 97B.2 (2011), pp. 201–214. DOI: 10.1002/jbm.b.31774.

[140]   Bahrami AR. Naderi H Matin MM. ?Review paper: critical issues in tissue engineering: biomaterials, cell sources, angiogenesis, and drug delivery systems.? In: *Journal of Biomaterials Applications* 26.4 (2011), pp. 383–417. DOI: 10.1177/0885328211408946.

[141]   Francesco Nappi, Cristiano Spadaccio, Clotilde Castaldo, Franca Di Meglio, Daria Nurzynska, Stefania Montagnani, Massimo Chello, and Christophe Acar. ?Reinforcement of the pulmonary artery autograft with a polyglactin and polydioxanone mesh in the Ross operation: experimental study in growing lamb.? eng. In: *The Journal of heart valve disease* 23.2 (Mar. 2014), pp. 145–148. ISSN: 0966-8519 (Print).

[142]   Francesco Nappi, Cristiano Spadaccio, Pierre Fouret, Nadjib Hammoudi, Juan Carlos Chachques, Massimo Chello, and Christophe Acar. ?An experimental model of the Ross operation: Development of resorbable reinforcements for pulmonary autografts.? In: *The Journal of Thoracic and Cardiovascular Surgery* 149.4 (July 2015), pp. 1134–1142. DOI: 10.1016/j.jtcvs.2014.12.056.

[143]   Francesco Nappi, Angelo Rosario Carotenuto, Donato Di Vito, Cristiano Spadaccio, Cristophe Acar, and Massimiliano Fraldi. ?Stress-shielding, growth and remodeling of pulmonary artery reinforced with copolymer scaffold and transposed into aortic position.? In: *Biomechanics and Modeling in Mechanobiology* (2015). DOI: 10.1007/s10237-015-0749-y.

[144]   Francesco Nappi, Cristiano Spadaccio, Massimo Chello, and Christophe Acar. ?The Ross procedure: Underuse or under-comprehension?? In: *The Journal of Thoracic and Cardiovascular Surgery* 149.5 (July 2015), pp. 1463–1464. DOI: 10.1016/j.jtcvs.2015.01.021.

[145]   Francesco Nappi, Cristiano Spadaccio, Nawwar Al-Attar, and Christophe Acar. ?The Ross procedure at the crossroads: Lessons from biology: Is Dr Ross's dream concluded?? In: *International Journal of Cardiology* 178 (2015), pp. 37–39. ISSN: 0167-5273. DOI: http://dx.doi.org/10.1016/j.ijcard.2014.10.134.

[146]   B. S. Noble, N. Peet, H. Y. Stevens, A. Brabbs, J. R. Mosley, G. C. Reilly, J. Reeve, T. M. Skerry, and L. E. Lanyon. ?Mechanical loading: biphasic osteocyte survival and targeting of osteoclasts for bone destruction in rat cortical bone.? In: *AJP: Cell Physiology* 284.4 (2002), pp. C934–C943. DOI: 10.1152/ajpcell.00234.2002.

[147]   Juha-Pekka Nuutinen, Claude Clerc, Raija Reinikainen, and Pertti Törmälä. ?Mechanical properties and in vitro degradation of bioabsorbable self-expanding braided stents.? In: *Journal of Biomaterials Science, Polymer Edition* 14.3 (2003), pp. 255–266. DOI: 10.1163/156856203763572707.

[148]   R.W. Ogden. *Nonlinear Elastic Deformations.* Dover Publications, 1997.

[149]   Tobias Olsson and Anders Klarbring. ?Residual stresses in soft tissue as a consequence of growth and remodeling: application to an arterial geometry.? In: *European Journal of Mechanics - A/Solids* 27.6 (2008), pp. 959–974. ISSN: 0997-7538. DOI: http://dx.doi.org/10.1016/j.euromechsol.2007.12.006.

[150]   Lawrence Perko. *Differential Equations and Dynamical Systems.* Springer US, 1996. DOI: 10.1007/978-1-4684-0249-0.

[151]   Gianpietro Del Piero. ?Some properties of the set of fourth-order tensors, with application to elasticity.? In: *Journal of Elasticity* 9.3 (1979), pp. 245–261. DOI: 10.1007/bf00041097.

[152]   Giuseppe Pisani, Raffaele Scaffa, Ornella Ieropoli, Edoardo M. Dell'Amico, Daniele Maselli, Umberto Morbiducci, and Ruggero De Paulis. ?Role of the sinuses of Valsalva on the opening of the aortic valve.? In: *The Journal of Thoracic and Cardiovascular Surgery* 145.4 (2013), pp. 999–1003. DOI: 10.1016/j.jtcvs.2012.03.060.

[153]   N. Poeppl, S. Schreml, F. Lichtenegger, A. Lenich, M. Eisenmann-Klein, and L. Prantl. ?Does the Surface Structure of Implants Have an Impact on the Formation of a Capsular Contracture?? In: *Aesth Plast Surg* 31.2 (2007), pp. 133–139. DOI: 10.1007/s00266-006-0091-y.

[154]   J. L. Del Pozo et al. ?Pilot Study of Association of Bacteria on Breast Implants with Capsular Contracture.? In: *Journal of Clinical Microbiology* 47.5 (2009), pp. 1333–1337. DOI: 10.1128/jcm.00096-09.

[155]   Lukas Prantl, Stephan Schreml, Stefan Fichtner-Feigl, Nina P??ppl, Marita Eisenmann-Klein, Hartmut Schwarze, and Bernd F??chtmeier. ?Clinical and Morphological Conditions in Capsular Contracture Formed around Silicone Breast Implants.? In: *Plastic and Reconstructive Surgery* 120.1 (2007), pp. 275–284. DOI: 10.1097/01.prs.0000264398.85652.9a.

[156]   Luigi Preziosi and Andrea Tosin. ?Multiphase modelling of tumour growth and extracellular matrix interaction: Mathematical tools and applications.? In: *Journal of Mathematical Biology* 58.4-5 (2009), pp. 625–656. ISSN: 03036812. DOI: 10.1007/s00285-008-0218-7.

[157]   V. Quaglini, S. Mantero, and T. Villa. ?Mechanical properties of breast periprosthetic capsules and the correlation to capsule contracture.? In: *J Appl Biomater Biomech* 3.3 (2005), pp. 184–191.

[158]   Aparna C. Ranganathan, Alejandro P. Adam, and Julio A. Aguirre-Ghiso. ?Opposing Roles of Mitogenic and Stress Signaling Pathways in the Induction of Cancer Dormancy.? In: *Cell Cycle* 5.16 (2006), pp. 1799–1807. DOI: 10.4161/cc.5.16.3109.

[159]   Mikael C Rechtsman, Frank H Stillinger, and Salvatore Torquato. ?Negative Poisson's Ratio Materials via Isotropic Interactions.? In: *Phys. Rev. Lett.* 101.8 (2008), p. 85501. DOI: 10.1103/PhysRevLett.101.085501.

[160]   Jiu-Sheng Ren. ?Growth and residual stresses of arterial walls.? In: *Journal of Theoretical Biology* 337 (2013), pp. 80–88. DOI: 10.1016/j.jtbi.2013.08.008.

[161]   James R. Rice and Michael P. Cleary. **?**Some basic stress diffusion solutions for fluid-saturated elastic porous media with compressible constituents.**?** In: *Rev. Geophys.* 14.2 (1976), p. 227. DOI: 10.1029/rg014i002p00227.

[162]   G. Riepe et al. **?**Long-term in vivo alterations of polyester vascular grafts in humans.**?** In: *European Journal of Vascular and Endovascular Surgery* 13.6 (1997), pp. 540–548. DOI: 10.1016/s1078-5884(97)80062-7.

[163]   Francis Robicsek and Mano J Thubrikar. **?**Role of sinus wall compliance in aortic leaflet function.**?** In: *The American Journal of Cardiology* 84.8 (1999), pp. 944–946. DOI: 10.1016/s0002-9149(99)00475-0.

[164]   Edward K Rodriguez, Anne Hoger, and Andrew D McCulloch. **?**Stress-dependent finite growth in soft elastic tissues.**?** In: *Journal of Biomechanics* 27.4 (1994), pp. 455–467. ISSN: 0021-9290. DOI: http://dx.doi.org/10.1016/0021-9290(94)90021-3.

[165]   Tiina Roose, S. Jonathan Chapman, and Philip K. Maini. **?**Mathematical Models of Avascular Tumor Growth.**?** In: *SIAM Rev.* 49.2 (2007), pp. 179–208. DOI: 10.1137/s0036144504446291.

[166]   Tiina Roose, Paolo A. Netti, Lance L. Munn, Yves Boucher, and Rakesh K. Jain. **?**Solid stress generated by spheroid growth estimated using a linear poroelasticity model.**?** In: *Microvascular Research* 66.3 (2003), pp. 204–212. DOI: 10.1016/s0026-2862(03)00057-8.

[167]   DonaldN. Ross. **?**Replacement of aortic and mitral valves with a pulmonary autograft.**?** In: *The Lancet* 290.7523 (1967), pp. 956–958. DOI: 10.1016/s0140-6736(67)90794-5.

[168]   Corrado Rubino, Vittorio Mazzarello, Francesco Farace, Francesco D???Andrea, Andrea Montella, Grazia Fenu, and Gian Vittorio Campus. **?**Ultrastructural Anatomy of Contracted Capsules Around Textured Implants in Augmented Breasts.**?** In: *Annals of Plastic Surgery* 46.2 (2001), pp. 95–102. DOI: 10.1097/00000637-200102000-00001.

[169]   Marc D. Ryser, Svetlana V. Komarova, and Nilima Nigam. **?**The Cellular Dynamics of Bone Remodeling: A Mathematical Model.**?** In: *SIAM J. Appl. Math.* 70.6 (2010), pp. 1899–1921. DOI: 10.1137/090746094.

[170]   Marc D Ryser, Nilima Nigam, and Svetlana V Komarova. **?**Mathematical Modeling of Spatio-Temporal Dynamics of a Single Bone Multicellular Unit.**?** In: *Journal of Bone and Mineral Research* 24.5 (2009), pp. 860–870. DOI: 10.1359/jbmr.081229.

[171]   Marcos A Sabino, Susana González, Leni Márquez, and José L Feijoo. **?**Study of the hydrolytic degradation of polydioxanone PPDX.**?** In: *Polymer Degradation and Stability* 69.2 (2000), pp. 209–216. ISSN: 0141-3910. DOI: http://dx.doi.org/10.1016/S0141-3910(00)00062-8.

[172]   Henryk J. Salacinski, Sean Goldner, Alberto Giudiceandrea, George Hamilton, Alexander M. Seifalian, Alan Edwards, and Robert J. Carson. **?**The Mechanical Behavior of Vascular Grafts: A Review.**?** In: *Journal of Biomaterials Applications* 15.3 (2001), pp. 241–278. DOI: 10.1106/NA5T-J57A-JTDD-FD04.

[173] Malisa Sarntinoranont, Frank Rooney, and Mauro Ferrari. ?Interstitial stress and fluid pressure within a growing tumor.? In: *Annals of Biomedical Engineering* 31.3 (2003), pp. 327–335. ISSN: 00906964. DOI: 10.1114/1.1554923.

[174] B. Schieck and H. Stumpf. ?The appropriate corotational rate, exact formula for the plastic spin and constitutive model for finite elastoplasticity.? In: *International Journal of Solids and Structures* 32.24 (1995), pp. 3643–3667. DOI: 10.1016/0020-7683(95)00007-w.

[175] S Schlesinger. ?Zafirlukast (Accolate): A new treatment for capsular contracture.? In: *Aesthetic Surgery Journal* 22.4 (2002), pp. 329–336. DOI: 10.1067/maj.2002.126753.

[176] H. Schmid, L. Pauli, A. Paulus, E. Kuhl, and M. Itskov. ?Consistent formulation of the growth process at the kinematic and constitutive level for soft tissues composed of multiple constituents.? In: *Computer Methods in Biomechanics and Biomedical Engineering* 15.5 (2012), pp. 547–561. DOI: 10.1080/10255842.2010.548325.

[177] G. Sciumé, S. Shelton, C. T. Gray W. G.and Miller, F. Hussain, M. Ferrari, P. Decuzzi, and B. A. Schrefler. ?A multiphase model for three-dimensional tumor growth.? In: *New Journal of Physics* 15 (2013). DOI: doi:10.1088/1367-2630/15/1/015005.

[178] Christine M. Scotti, Jorge Jimenez, Satish C. Muluk, and Ender A. Finol. ?Wall stress and flow dynamics in abdominal aortic aneurysms: finite element analysis vs. fluid–structure interaction.? In: *Computer Methods in Biomechanics and Biomedical Engineering* 11.3 (2008), pp. 301–322. DOI: 10.1080/10255840701827412.

[179] S.A. Sell, M.J. McClure, D.C. Knapp, B.H. Walpoth, D. G. Simpson, and G. L. Bowlin. ?Electrospun polydioxanone-elastin blends: potential for bioresorbable vascular grafts.? In: *Biomed Mater* 1 (2006), pp. 72–80. DOI: 10.1088/1748-6041/1/2/004.

[180] Malakh Shrestha, Hassina Baraki, Ilona Maeding, Sebastian Fitzner, Samir Sarikouch, Nawid Khaladj, Christian Hagl, and Axel Haverich. ?Long-term results after aortic valve-sparing operation (David I).? In: *European Journal of Cardio-Thoracic Surgery* (2011). DOI: 10.1016/j.ejcts.2011.04.012.

[181] A. Sionkowska. ?Current research on the blends of natural and synthetic polymers as new biomaterials: Review.? In: *Progress in Polymer Science* (2011). DOI: 10.1016/j.progpolymsci.2011.05.003.

[182] Richard Skalak, Stephen Zargaryan, Rakesh K. Jain, Paolo A. Netti, and Anne Hoger. ?Compatibility and the genesis of residual stress by volumetric growth.? In: *J. Math. Biol.* 34.8 (1996), pp. 889–914. DOI: 10.1007/bf01834825.

[183] Hiromichi Sonoda, Shin-Ichi Urayama, Keiichi Takamizawa, Yasuhide Nakayama, Chikao Uyama, Hisataka Yasui, and Takehisa Matsuda. ?Compliant design of artificial graft: Compliance determination by new digital X-ray imaging system-based method.? In: *Journal of Biomedical Materials Research* 60.1 (2002), pp. 191–195. ISSN: 1097-4636. DOI: 10.1002/jbm.10055.

[184] Cristiano Spadaccio, Massimo Chello, Marcella Trombetta, Alberto Rainer, Yoshiya Toyoda, and Jorge A Genovese. ?Drug releasing systems in cardiovascular tissue engineering.? eng. In: *Journal of cellular and molecular medicine* 13.3 (Mar. 2009), pp. 422–439. ISSN: 1582-4934 (Electronic). DOI: 10.1111/j.1582-4934.2008.00532.x.

[185] Cristiano Spadaccio, Alberto Rainer, Matteo Centola, Marcella Trombetta, Massimo Chello, Mario Lusini, Elvio Covino, Yoshiya Toyoda, and Jorge A Genovese. ?Heparin-releasing scaffold for stem cells: a differentiating device for vascular aims.? eng. In: *Regenerative medicine* 5.4 (July 2010), pp. 645–657. ISSN: 1746-076X (Electronic). DOI: 10.2217/rme.10.25.

[186] Cristiano Spadaccio, Alberto Rainer, Raffaele Barbato, Massimo Chello, and Bart Meyns. ?The fate of large-diameter Dacron® vascular grafts in surgical practice: are we really satisfied?? eng. In: 168.5 (Oct. 2013), pp. 5028–5029. ISSN: 1874-1754 (Electronic). DOI: 10.1016/j.ijcard.2013.07.165.

[187] Cristiano Spadaccio, Stefania Montagnani, Christophe Acar, and Francesco Nappi. ?Introducing bioresorbable scaffolds into the show. A potential adjunct to resuscitate Ross procedure.? In: *International Journal of Cardiology* 190 (July 2015), pp. 50–52. DOI: 10.1016/j.ijcard.2015.04.098.

[188] Scott L. Spear, Diane K. Murphy, Araceli Slicton, and Patricia S. Walker. ?Inamed Silicone Breast Implant Core Study Results at 6 Years.? In: *Plastic and Reconstructive Surgery* 120.Supplement 1 (2007), 8S–16S. DOI: 10.1097/01.prs.0000286580.93214.df.

[189] P Stelzer, DJ Jones, and RC Elkins. ?Aortic root replacement with pulmonary autograft.? In: *Circulation* 80.5 Pt 2 (1989). ISSN: 0009-7322.

[190] Paul Stelzer. ?The Ross Procedure: State of the Art 2011.? In: *Seminars in Thoracic and Cardiovascular Surgery* 23.2 (2011), pp. 115–123. DOI: 10.1053/j.semtcvs.2011.07.003.

[191] T. Stylianopoulos et al. ?Causes, consequences, and remedies for growth-induced solid stress in murine and human tumors.? In: *Proceedings of the National Academy of Sciences* 109.38 (2012), pp. 15101–15108. DOI: 10.1073/pnas.1213353109.

[192] T. Stylianopoulos, J. D. Martin, M. Snuderl, F. Mpekris, S. R. Jain, and R. K. Jain. ?Coevolution of Solid Stress and Interstitial Fluid Pressure in Tumors During Progression: Implications for Vascular Collapse.? In: *Cancer Research* 73.13 (2013), pp. 3833–3841. DOI: 10.1158/0008-5472.can-12-4521.

[193] S. D. TULJAPURKAR. ?Stability of Lotka Volterra systems.? In: *Nature* 264.5584 (1976), pp. 381–381. DOI: 10.1038/264381a0.

[194] Larry A. Taber. ?Biomechanics of Growth, Remodeling, and Morphogenesis.? In: *Applied Mechanics Reviews* 48.8 (1995), p. 487. DOI: 10.1115/1.3005109.

[195] N. R. Tai, H. J. Salacinski, A. Edwards, G. Hamilton, and A.M. Seifalian. ?Compliance properties of conduits used in vascular reconstruction.? In: *British Journal of Surgery* 87.11 (2000), pp. 1516–1524. ISSN: 1365-2168. DOI: 10.1046/j.1365-2168.2000.01566.x.

[196]   J. J.M. Takkenberg, L. M.A. Klieverik, P. H. Schoof, R.-J. van Suylen, L. A. van Herwerden, P. E. Zondervan, J. W. Roos-Hesselink, M. J.C. Eijkemans, M. H. Yacoub, and A. J.J.C. Bogers. **?**The Ross Procedure: A Systematic Review and Meta-Analysis.**?** In: *Circulation* 119.2 (2008), pp. 222–228. DOI: 10.1161/circulationaha.107.726349.

[197]   Marcus J. Tindall, Louise Dyson, Kieran Smallbone, and Philip K. Maini. **?**Modelling acidosis and the cell cycle in multicellular tumour spheroids.**?** In: *Journal of Theoretical Biology* 298 (2012), pp. 107–115. DOI: 10.1016/j.jtbi.2011.11.009.

[198]   X. Trepat. **?**Forcing Tumor Arrest.**?** In: *Physics* 4 (2011). DOI: 10.1103/physics.4.85.

[199]   C. Truesdell and W. Noll. **?**The Non-Linear Field Theories of Mechanics.**?** In: *The Non-Linear Field Theories of Mechanics.* Springer Science + Business Media, 1965, pp. 1–541. DOI: 10.1007/978-3-642-46015-9_1.

[200]   J. M. Tse, G. Cheng, J. A. Tyrrell, S. A. Wilcox-Adelman, Y. Boucher, R. K. Jain, and L. L. Munn. **?**Mechanical compression drives cancer cells toward invasive phenotype.**?** In: *Proceedings of the National Academy of Sciences* 109.3 (2011), pp. 911–916. DOI: 10.1073/pnas.1118910109.

[201]   A. M. Turing. **?**The Chemical Basis of Morphogenesis.**?** In: *Philosophical Transactions of the Royal Society of London B: Biological Sciences* 237.641 (1952), pp. 37–72. ISSN: 0080-4622. DOI: 10.1098/rstb.1952.0012.

[202]   R. Vandiver and A. Goriely. **?**Differential growth and residual stress in cylindrical elastic structures.**?** In: *Philosophical Transactions of the Royal Society A: Mathematical, Physical and Engineering Sciences* 367.1902 (2009), pp. 3607–3630. DOI: 10.1098/rsta.2009.0114.

[203]   J. Veselý, L. Horný, H. Chlup, T. Adámek, M. Krajíček, and R. Žitný. **?**Constitutive modeling of human saphenous veins at overloading pressures.**?** In: *Journal of the Mechanical Behavior of Biomedical Materials* 45 (2015), pp. 101 – 108. ISSN: 1751-6161. DOI: http://dx.doi.org/10.1016/j.jmbbm.2015.01.023.

[204]   V. Volterra. **?**Una teoria matematica sulla lotta per l'esistenza.**?** In: *Scientia* V (1927), pp. 112–124.

[205]   V. Volterra. **?**Mathematical theory of struggle for existence.**?** In: (1928).

[206]   V. Volterra. **?**Variations and Fluctuations of the Number of Individuals in Animal Species Living Together.**?** In: *Journal du Conseil international pour l'exploration de la mer* (1928).

[207]   Hong Wang, Baohua Ji, X. Sherry Liu, René F. M. van Oers, X. Edward Guo, Yonggang Huang, and Keh-Chih Hwang. **?**Osteocyte-viability-based simulations of trabecular bone loss and recovery in disuse and reloading.**?** In: *Biomechanics and Modeling in Mechanobiology* 13.1 (2013), pp. 153–166. DOI: 10.1007/s10237-013-0492-1.

[208]   Mao Xiang Wang and Pik Yin Lai. **?**Population dynamics and wave propagation in a Lotka-Volterra system with spatial diffusion.**?** In: *Physical Review E - Statistical, Nonlinear, and Soft Matter Physics* 86.5 (2012), pp. 8–15. ISSN: 15393755. DOI: 10.1103/PhysRevE.86.051908.

[209]   Samuel E. Wilson, Richard Krug, Gregory Mueller, and Latresia Wilson. **?**Late Disruption of Dacron Aortic Grafts.**?** In: *Annals of Vascular Surgery* 11.4 (1997), pp. 383–386. DOI: 10.1007/s100169900065.

[210]   Inc. Wolfram Research. *Mathematica*. Wolfram Research, Inc., 2015.

[211]   Chin-Ho Wong, Miny Samuel, Bien-Keem Tan, and Colin Song. **?**Capsular Contracture in Subglandular Breast Augmentation with Textured versus Smooth Breast Implants: A Systematic Review.**?** In: *Plastic and Reconstructive Surgery* 118.5 (2006), pp. 1224–1236. DOI: 10.1097/01.prs.0000237013.50283.d2.

[212]   Amy Wu, David Liao, Thea D Tlsty, James C Sturm, and Robert H Austin. **?**Game theory in the death galaxy: interaction of cancer and stromal cells in tumour microenvironment.**?** In: *Interface focus* 4.4 (2014), p. 20140028. ISSN: 2042-8898. DOI: 10.1098/rsfs.2014.0028.

[213]   Jie Wu, Zu Rong Ding, Yan Cai, Shi Xiong Xu, Gai Ping Zhao, and Quan Long. **?**Simulation of tumor microvasculature and microenvironment response to anti-angiogenic treatment by angiostatin and endostatin.**?** In: *Applied Mathematics and Mechanics (English Edition)* 32.4 (2011), pp. 437–448. ISSN: 02534827. DOI: 10.1007/s10483-011-1428-7.

[214]   Min Wu, Hermann B. Frieboes, Mark A.J. Chaplain, Steven R. McDougall, Vittorio Cristini, and John S. Lowengrub. **?**The effect of interstitial pressure on therapeutic agent transport: Coupling with the tumor blood and lymphatic vascular systems.**?** In: *Journal of Theoretical Biology* 355 (2014), pp. 194–207. DOI: 10.1016/j.jtbi.2014.04.012.

[215]   H. Xiao, O. T. Bruhns, and A. Meyers. **?**Logarithmic strain, logarithmic spin and logarithmic rate.**?** In: *Acta Mechanica* 124.1-4 (1997), pp. 89–105. DOI: 10.1007/bf01213020.

[216]   Shijia Zhao and Linxia Gu. **?**Implementation and validation of aortic remodeling in hypertensive rats.**?** eng. In: *Journal of biomechanical engineering* 136.9 (Sept. 2014), p. 91007. ISSN: 1528-8951 (Electronic). DOI: 10.1115/1.4027939.

[217]   Meital Zilberman and Robert C. Eberhart. **?**DRUG-ELUTING BIORESORBABLE STENTS FOR VARIOUS APPLICATIONS.**?** In: *Annual Review of Biomedical Engineering* 8.1 (2006), pp. 153–180. DOI: 10.1146/annurev.bioeng.8.013106.151418.

[218]   Oscar A. Zimman, Jorge Toblli, Inés Stella, Marcelo Ferder, Leon Ferder, and Felipe Inserra. **?**The Effects of Angiotensin-Converting Enzyme Inhibitors on the Fibrous Envelope around Mammary Implants.**?** In: *Plastic and Reconstructive Surgery* 120.7 (2007), pp. 2025–2033. DOI: 10.1097/01.prs.0000287381.93729.e2.

[219]   Martin Zumsande, Dirk Stiefs, Stefan Siegmund, and Thilo Gross. **?**General analysis of mathematical models for bone remodeling.**?** In: *Bone* 48.4 (2011), pp. 910–917. DOI: 10.1016/j.bone.2010.12.010.

LIST OF FIGURES

LIST OF TABLES